11-1-2019 2:00 PM

# Novel PV Solar Farm Control as STATCOM (PV-STATCOM) for SSR Mitigation in Synchronous Generators and Wind Farms

Reza Salehi Sharafdarkolaee, *The University of Western Ontario*

Supervisor: Varma, Rajiv K., *The University of Western Ontario*
A thesis submitted in partial fulfillment of the requirements for the Doctor of Philosophy degree in Electrical and Computer Engineering
© Reza Salehi Sharafdarkolaee 2019

# Abstract

Transmission lines across the world are extensively compensated by series capacitors to increase their power transfer capacity. However, series compensation can potentially cause subsynchronous resonance (SSR) which can lead to significant damage in shafts of synchronous generators and wind farms. Dynamic reactive power compensators such as STATCOM and SVCs are typically used for mitigation of SSR, but these are quite expensive.

Large scale PV solar farms are growing at a very rapid rate across the world. It is quite likely that they may get installed near synchronous generators or wind farms which are directly or indirectly interfaced with series compensated lines.

For the first time, novel SSR damping controls for the patented technology of PV solar farm controlled as STATCOM (PV-STATCOM) are presented in this thesis for mitigating SSR both during night and day in synchronous generators connected to series compensated lines. The PV-STATCOM successfully mitigates SSR whether the solar farm is located at generator terminals or remotely from it.

New SSR alleviation controls are also developed for PV-STATCOM for mitigating SSR in wind farms connected to series compensated networks, during night and day, irrespective of PV-STATCOM location. The SSR damping controls are based on wind farm generator speed and line current, both of which are locally available signals.

As soon as a system disturbance is detected, the solar farm discontinues its real power generation and makes available its entire inverter capacity for dynamic reactive power exchange as STATCOM, for SSR mitigation. Once subsynchronous oscillations are damped the solar farm utilizes a novel ramp-up technique according to which SSR damping function is kept activated with remaining inverter capacity during power ramp-up. Such a fast ramp-up technique is not envisaged in Grid Codes. The entire process of SSR damping for all cases studied takes less than half a minute.

A novel coordinated control of PV-STATCOM and DFIG based Type 3 wind farms is developed for faster and effective SSR damping, when both are connected to series compensated lines.

MATLAB based eigenvalue analysis validated by nonlinear simulations through SIMULINK and PSCAD software confirm the effectiveness of proposed SSR damping controls.

## Keywords

PV Solar Farm, Solar Energy, Induction Generator (IG)-based Wind Farm, Doubly-Fed Induction Generator (DFIG)-based Wind Farm, Subsynchronous Oscillations (SSO), Subsynchronous Resonance (SSR), Series Compensation, Flexible AC Transmission System (FACTS), Dynamic Reactive Power Compensation, STATCOM, PV-STATCOM, Smart Inverter, Power Ramping.

# Summary for Lay Audience

Because of environmental pollution, energy security, and economic concerns, many large-scale renewable energy sources including PV solar farms and wind farms are being increasingly employed worldwide to satisfy the high-growing demand of world energy consumption. As there are usually considerable distances between large renewable energy systems and load centers, they need to be connected to transmission lines to transfer the generated power to load centers. Therefore, the power transfer capacity of transmission lines needs to be increased in some cases to evacuate these large amounts of power to the grid.

As an alternative to the construction of new and expensive transmission lines, series capacitive compensation is a simple and economic technology to increase power transmission limit of existing transmission lines. Nevertheless, Subsynchronous Resonance (SSR) is a preventing concern for using series capacitive compensation extensively. SSR is an unstable electrical power system condition which resulted in generator shaft failure, power outage, and costly damages to the electricity grid.

Several countermeasures have been investigated and utilized to alleviate SSR since its first occurrence, including flexible AC transmission system (FACTS) devices such as STATCOM and SVC. But these countermeasures are much expensive besides having many installation difficulties.

Nowadays, large-scale PV solar farms with rating in excess of 100 MW are already commissioned and increasingly being developed worldwide which are comparable to transmission level shunt connected FACTS devices such as, Static Var Compensators and STATCOMs.

This thesis presents a novel concept of utilizing PV solar inverter as a FACTS devices STATCOM, termed PV-STATCOM, to alleviate SSR in the series compensated power system on a 24/7 basis. The efficacy of PV-STATCOM SSR alleviation in synchronous generator and wind farms (IG-based and DFIG-based) is demonstrated through various simulations and

studies. Also, SSR alleviation with utilizing PV-STATCOM and DFIG-based wind farm, simultaneously, is presented in this thesis.

The PV-STATCOM involves embedding additional controls with measurement circuitry on the inverters and the electrical/civil infrastructure (buswork, breakers, transformers) of an existing PV solar farm to transform it into a STATCOM. This makes PV-STATCOM at least 50-100 times cheaper than an equivalent size STATCOM to achieve the same goal.

Dedicated to:

*My Parents, My Wife, and My Sisters*

# Acknowledgments

I would like to express my sincere gratitude to my supervisor, Professor Rajiv K. Varma, for his munificent support, motivation, wisdom, and guidance throughout my graduate career at University of Western Ontario. It was a great privilege and honor to work and study under his guidance. He has set an example of excellence as a researcher, mentor, instructor. No words are adequate to express my appreciation to him. I, herewith, can only convey my sincere and warm regards to him.

I would also like to thank Dr. Mehrdad Kermani from the University of Western Ontario, and Dr. Mehrdad Kazerani and Dr. Claudio Canizares from University of Waterloo for valuable and insightful courses they provided.

I would like also to express my profound gratitude to my parents, my wife, and my sisters for providing me with unconditional love, unfailing support, and continuous encouragement throughout my years of study. This accomplishment would not have been possible without their support.

I am extremely grateful to my friends Mohammad, and Sibin for their kind support during my study in University of Western Ontario. Also, I take this opportunity to express my gratefulness to all and sundry who have helped me during this journey.

*Reza Salehi Sharafdarkolaee*

# Table of Contents

# List of Tables

# List of Figures

# List of Appendices

# List of Abbreviations

FSGWT     Fixed-Speed Generator Wind Turbines

ASGWT     Adjustable Speed Generator Wind Turbines

IG       Induction Generator

SG       Synchronous Generator

DFIG      Doubly-Fed Induction Generator

PV       Photovoltaic

SSO      Subsynchronous Oscillations

SSR      Subsynchronous Resonance

IGE      Induction Generator Effect

TI       Torsional Interactions

SSCI      Subsynchronous Control Interaction

ERCOT     Electric Reliability Council of Texas

RSC      Rotor Side Converter

GSC      Grid Side Converter

PMSG     Permanent Magnet Synchronous Generator

WAMS     Wide-Area Measurement System

SCR      Short Circuit Ratio

HVDC     High Voltage DC

HVAC     High Voltage AC

| | |
|---|---|
| FSPC | Frequency Sensitive Power Control |
| FACTS | Flexible AC Transmission System |
| TCSC | Thyristor Controlled Series Compensators |
| GCSC | Gate Controlled Series VAr Compensation |
| UPFC | Unified Power Flow Controller |
| SVC | Static VAr Compensator |
| STATCOM | Static Synchronous Compensator |
| PCC | Point of Common Coupling |
| VSI | Voltage Source Inverter |
| CSI | Current Source Inverter |
| IGBT | Insulated Gate Bipolar Transistor |
| SMES | Superconducting Magnetic Energy Storage |
| POD | Power Oscillation Damping |
| PSS | Power System Stabilizer |
| BESS | Battery Energy Storage Systems |
| DER | Distributed Energy Resource |
| EPS | Electric Power System |
| NERC | North American Electric Reliability Corporation |
| VRT | Voltage Ride-Through |
| FFR | Fast Frequency Response |

| | |
|---|---|
| SPWM | Sinusoidal Pulse Width Modulation |
| SVPWM | Sinusoidal Vector PWM |
| SHE | Selective Harmonic Elimination |
| PLL | Phase Locked Loop |
| PI | Proportional Integral |
| FFT | Fast Fourier Transform |
| MPPT | Maximum Power Point Tracking |
| IRR | Intermittent Renewable Resources |
| GA | Genetic Algorithm |
| OF | Objective Function |

# List of Symbols

| | |
|---|---|
| $F$ | Subsynchronous Frequency (*Hz*) |
| $\theta$ | Angle (*radian*) |
| $\Omega$ | Angular Velocity (*radian/sec*) |
| $R$ | Resistance (*ohm*) |
| $C$ | Capacitor (*Farad*) |
| $L$ | Inductance (*Henry*) |
| $X$ | Reactance (*ohm*) |
| $D$ | Damping Coefficient |
| $K$ | Spring Constant (*Newton. meter/radian*) |
| $H$ | Inertia Constant (*second*) |
| $T$ | Torque (*Newton.meter*) |
| $\psi$ | Flux Linkage (*Weber*) |
| $\xi$ | damping ratio |
| $P$ | Active Power (*Watt*) |
| $Q$ | Reactive Power (*var*) |
| $V$ | Voltage (*Volt*) |
| $I$ | Current (*Ampere*) |

# Chapter 1

# 1    Introduction

It is now well understood that electric power generation with fossil fuels has adverse effects on global climate due to greenhouse gases. In addition to environmental pollution threat, economic concerns, possible shortage of fossil fuels, and world energy policies have resulted in growing utilization of renewable energy sources around the globe. Renewable energy sources constitute sustainable and reliable carbon-free electric energy systems. Renewable energy includes hydro-power, wind power, solar power, ocean wave power, bio-power, geothermal power, etc.

Wind power systems have grown the fastest among renewable energy sources, so far. Substantial improvements in their technology, in addition to the advancement of power electronics, have ended up in bigger sizes, lesser costs and more controllability of wind farms. Nowadays, many large-scale wind farms operate in the world especially in USA, China, India, North Europe, and Germany. Among these, several of them are rated more than 500 MW [1-5]. The mechanical drive train in wind turbines transmits the rotor torque developed by wind power to the electrical generator to produce electrical energy. Wind turbines are categorized into two types based on their speed control system: Fixed-Speed Generator Wind Turbines (FSGWT), and Adjustable Speed Generator Wind Turbines (ASGWT) [6-8]. FSGWT are known as Type 1 or Type 2 wind turbine generators, with the latter having external resistances introduced in their rotor circuits. In FSGWT, the generator rotates at or close to a constant speed regardless of wind speed. FSGWT harvests maximum power at a particular wind speed and delivers the same at the frequency of electrical network connected to the wind farm. This type of wind turbine is equipped with squirrel cage induction generators which are simple to operate. However, Induction Generator (IG) draws inductive reactive power from the grid due to lack of external exciter during its operation, which represents a major disadvantage of the FSGWT systems [9]. The double-cage IG is preferred to single-cage machine due to its high efficiency and low maintenance requirements. In addition, the slip in these machines can vary over a wide range for IG-based wind farms [7, 9-11]. In ASGWT, the maximum aerodynamic efficiency is achieved by keeping the tip speed ratio fairly constant [6, 9]. This type of

turbine has advantages over the FSGWT in terms of lower mechanical stress, improved power quality, high system efficiency, and reduced acoustic noise. Both Synchronous Generator (SG) and the induction generator can be used in ASGWT. One important class of ASGWT is the Doubly-Fed Induction Generator (DFIG) known as Type 3 wind turbine generators. Most wind turbines in Europe and North America use DFIGs (Type 3) or full inverter-based wind turbine generators, known as Type 4 wind turbine generators [7, 11]. However, there are still a significant number of large Type 1 wind farms around the world which use FSGWT, such as Alta Wind Energy Center (1170 MW) in California, USA; Brahmanvel WF (549 MW) in India, Biglow Canyon WF (450 MW) in Oregon, USA; Twin Groves WF (396 MW) in Illinois, USA; Papalote Creek WF (380 MW) in Texas, USA; Clyde WF (350 MW) in UK, Hallett WF (348 MW) in Australia, Maple Ridge WF (321 MW) in New York, USA; Pioneer Prairie WF (300 MW) in Iowa, USA; Tarfaya WF (300 MW) in Morocco, Stateline wind farm (300.96 MW) at the border of Washington and Oregon, Fowler Ridge WF (300.3 MW) in Indiana, USA; Horse Hollow Wind Energy Center (299 MW) in Texas, USA; Lake Bonney Wind Farm (279 MW) in Australia, etc.[1-5].

However, in recent years, solar farms have been receiving more attention in the world and their sizes are growing rapidly. After hydropower and wind power, solar power is the third biggest renewable energy source in the world. The dominant source of this energy is photovoltaic (PV) technology. PV panels are very reliable and need little maintenance because of creating electricity actively and not requiring any types of mechanical parts that can fail. Nowadays, a large number of PV solar farms rated more than 100 MW are already commissioned and increasingly being developed around the world. Some example of PV solar farm are as follows: Tengger Desert Solar Park (1500 MW) in China, Kurnool Ultra Mega Solar Park (1000 MW) in India, Yanchi Solar PV Station (1000 MW) in China, Longyangxia Dam Solar Park (850 MW) in China, Kamuthi Solar Power Project (648 MW) in India, Solar Star I and II (579 MW) in USA, Desert Sunlight Solar Farm and Topaz Solar Farm (550 MW each) in USA; Huanghe Hydropower Golmud Solar Park (500 MW) in China, Charanka Solar Park (345 MW) in India, Agua Caliente Solar Project (295 MW) in Arizona, USA; California Valley Solar Ranch (250 MW) in California, USA [12-14].

As there are usually considerable distances between large renewable energy systems and load centers, they need to be connected to transmission lines to transfer the generated power to load centers. For instance, the 550-MW Desert Sunlight Solar Farm is connected to a transmission line in California [15]. Therefore, power transfer capacity of transmission lines needs to be increased in some cases to evacuate these large amounts of power to the grid. Series capacitive compensation of transmission lines is a simple and economic way to improve the power transfer capacity of existing lines [16, 17]. It is well established that increasing the power transfer capacity of existing lines with series capacitive compensation is considerably less expensive than installing new lines. As an example, ABB performed a study which stated that investment of increasing the power transfer capacity of two existing transmission lines from 1300 MW to 2000 MW utilizing series capacitive compensation is approximately 10 percent of building a third parallel line [18]. However, series capacitive compensation causes Subsynchronous Oscillations (SSO) which if uncontrolled, can potentially cause Subsynchronous Resonance (SSR) resulting in severe damages in shafts of synchronous generators and wind turbine [19-22].

The main objective of this thesis is to propose a novel utilization of PV solar farm inverter as a FACTS device STATCOM, termed PV-STATCOM, to alleviate subsynchronous resonance in steam turbine driven synchronous generator, IG-based windfarm, and DFIG-based farm connected to a series compensated transmission line.

## 1.1  Subsynchronous Resonance (SSR)

Subsynchronous resonance is an electric power system condition where the electric network exchanges energy with the turbine-generator at one or more of the natural frequencies of the combined system below the synchronous frequency of the system [23]. A series capacitive compensation excites the subsynchronous current in the line at an electrical frequency $f_{er}$ given by [23,26]:

$$f_{er} = f_0 \sqrt{\frac{X_c}{X_n}} \qquad (1.1)$$

Where $X_c$ is the reactance of the series capacitor, $X_n$ is the reactance of the line including that of the generator and transformer, $f_0$ is the nominal frequency of the power system. Typically $X_c$ can up-to 50%-70% on $X_n$ , and $f_{er} < f_0$. The subsynchronous currents in the line with frequency of $f_{er}$ result in subsynchronous oscillations in rotor torques and current at the complementary frequency as $f_r$.

$$f_r = f_0 - f_{er} \tag{1.2}$$

This excited rotor current causes subsynchronous armature voltage components which may heighten subsynchronous armature current to produce SSR.

SSR can be divided into following main categories: 1) The Induction Generator Effect (IGE), 2) Torsional Interactions (TI), 3) transient torque, and 4) Subsynchronous Control Interaction (SSCI) [20, 24-26].

## 1.1.1 Induction Generator Effect (IGE)

Induction generator effect occurs due to self-excitation of the electrical system and consists of just electrical system dynamics [22]. A component of rotating *mmf* in the armature air gap with angular velocity $2\pi f_{er}$ is caused by generator armature currents at subsynchronous frequency $f_{er}$. The interaction between this *mmf* and the main field air gap *mmf* generates torques at two frequencies i.e. subsynchronous frequency ($f_0$ - $f_{er}$) and supersynchronous frequency ($f_0$ + $f_{er}$). As the rotating *mmf* is turning slower than the rotor circuit, the resistance to the subsynchronous current viewed from the armature terminal is negative as the slip of the machine viewed as an induction generator is negative. When the magnitude of this negative resistance exceeds the sum of the armature and network resistance at the resonant frequency ($f_{er}$), the armature currents can be sustained or raised. This phenomenon is called induction generator effect [20, 22]. A fairly little torsional interaction happens provided that the generator torsional mode frequency ($f_n$) is different from the subsynchronous torque frequency.

## 1.1.2 Torsional Interaction (TI)

Torsional interaction involves not only the electrical system dynamics but also the mechanical system dynamics. When the electrical system natural frequency and the

frequency of the subsynchronous component of the armature voltage are close, the subsynchronous current creates a rotor torque that is phased to sustain subsynchronous torque. This torque may exceed the inherent mechanical damping of the rotating system. In such cases, the rotor torsional frequencies will be amplified and lead to shaft failure as experienced for the first time at Mohave Plant in Southern California in 1970. This effect which is called torsional interaction is much more significant compared to the induction generator effect [20, 22].

## 1.1.3 Transient Torque

Transient torque is the result of disturbances in the system like faults and switching of lines, etc. These disturbances may cause current oscillations in the system which tend to fluctuate with the natural frequency of the system and may excite the oscillatory torque in the shaft of the generator. In the system with no series capacitor compensation, these transient variations are always dc transients, which decay to zero with a time constant that depends on the ratio of inductance to resistance. But, for the system with series capacitive compensation, the frequency of oscillations depends on the system capacitor and inductance that may align with the natural frequency of the mechanical system. So, there can be a large peak torque due to large disturbance currents which can lead to shaft failure [20, 22].

## 1.1.4 Subsynchronous Control Interaction (SSCI)

Subsynchronous control interactions (SSCI) are mainly due to adverse interactions between the controller of power electronic device (such as HVDC link, SVC, and inverter-based renewable energy sources like DFIG) and series compensated electrical system to which these devices are connected [27-38]. SSCI can even occur in a weak system without series compensation due to the interaction between the controller of inverter and the weak system [27, 30, 32]. SSCI can cause severe damages to power system components as experienced at Electric Reliability Council of Texas (ERCOT) system in 2009 [25, 29].

SSCI does not have well-defined frequencies like other types of SSR since the frequency of oscillations in SSCI depends not only on the configuration of the series compensated transmission line and system parameters but also on power electronics controller

configuration and parameters [39]. Moreover, the oscillations caused by the SSCI may grow faster compared to other types of SSR, since the undamped oscillation in SSCI depends on the electrical and controller interactions, which have a smaller time constant [39].

## 1.2   Subsynchronous Resonance Study Methods

There are several techniques available to simulate and analyze SSR phenomena. The most common techniques are as follows [40]:

a. Frequency scanning
b. Eigenvalue analysis
c. Electromagnetic transient simulation

### 1.2.1 Frequency Scanning

Frequency scanning is an efficient and cost-effective technique for preliminary analysis of subsynchronous resonance. In this technique, the equivalent impedance is computed by looking into the network from a point behind the stator winding of the generator under study, as a function of the frequency [40, 41]. Should there be a frequency at which the reactance is zero and resistance is negative, self-sustaining oscillations at that frequency would be expected due to the induction generator effect [42]. Frequency scanning can sometimes provide information regarding possible problems with torsional interaction and transient torques [42].

### 1.2.2 Eigenvalue Analysis

Eigenvalue analysis is widely used for the study of induction generator effect and torsional interaction. Eigenvalue analysis accurately provides all the natural modes and damping or undamping of the coupled electrical and mechanical system [40]. When only small-signal dynamics of low-frequency (0.1 - 2 Hz) are of concern, e.g. inter-area oscillations, network dynamics are neglected and only machine and controllers' dynamics are considered. When small-signal dynamics of high-frequency (5-180 Hz) are of interest e.g. SSR, the network dynamic model and further details of machine and controller models need to be

incorporated [43]. However, eigenvalue studies get relatively complicated when the system under study has a high number of buses.

Eigenvalue analysis of the system is carried out through linearized model of the power system. The basic procedure of eigenvalue analysis includes [44-46]:

a. Development of a positive sequence model of the power system
b. Modeling of power system components
c. Obtaining the linearized model of the system
d. Calculation of eigenvalues of the system
e. The real part of the eigenvalues demonstrates the positive or negative damping of each mode.
f. The real component of eigenvalues corresponding to the subsynchronous modes of the spring-mass system indicates the severity of torsional interaction
g. The real component of eigenvalues corresponding only to electrical system resonant frequencies reveals the severity of the induction generator effect

In this thesis, the linearization toolbox of MATLAB software is used to obtain the state-space model of study systems and perform eigenvalue analysis.

## 1.2.3 Electromagnetic Transient Simulation

To determine the potential for SSR torque amplification, electromagnetic transient analysis is performed to find the peak transient shaft torque that is to be expected when disturbances, like fault and switching of the lines, take place in a series compensated system [20, 22].

In this thesis, PSCAD/EMTDC and MATLAB/Simulink software are employed to perform electromagnetic transient simulations.

## 1.3   Subsynchronous Resonance in Different Devices

The utilization of series capacitive compensation has increased significantly after the first installation of series capacitive compensation in the world at Ballston, New York in 1928 [47]. However, series capacitive compensation has been known as a cause of SSR in both synchronous and induction generator since 1937 [48].

## 1.3.1 SSR in Synchronous Generator Connected to Series Compensated Transmission Line

SSR did not get much attention until two shaft failures of the Mohave generator in Nevada, USA in 1970 and 1971 [21]. Figure 1.1 depicts the single line diagram of the transmission system in which the Mohave generator plant was connected [21, 49]. The Mohave plant consisted of a cross-compound generation unit located in southern Nevada. In 1970, shaft damage was experienced when opening the circuit breaker in one of two lines connected to the plant led Mohave generator to become radially connected to the southern California Lugo bus through a series compensated transmission line. At that time, the power system operator did not recognize the problem, and the generation unit was placed back in operation after a few months. Consequently, a nearly identical incident occurred one year later, in 1971. It was found that the event experienced in Mohave power plant was due to energy exchange between the series-compensated line and mechanical system of the Mohave power plant. Investigations determined that an electrical resonance at 30.5 Hz produced torque at 29.5 Hz (the 60 Hz compliment frequency), which was nearly coincident with the frequency of the second torsional vibration-mode of the turbine-generator at 30.1 Hz [49].
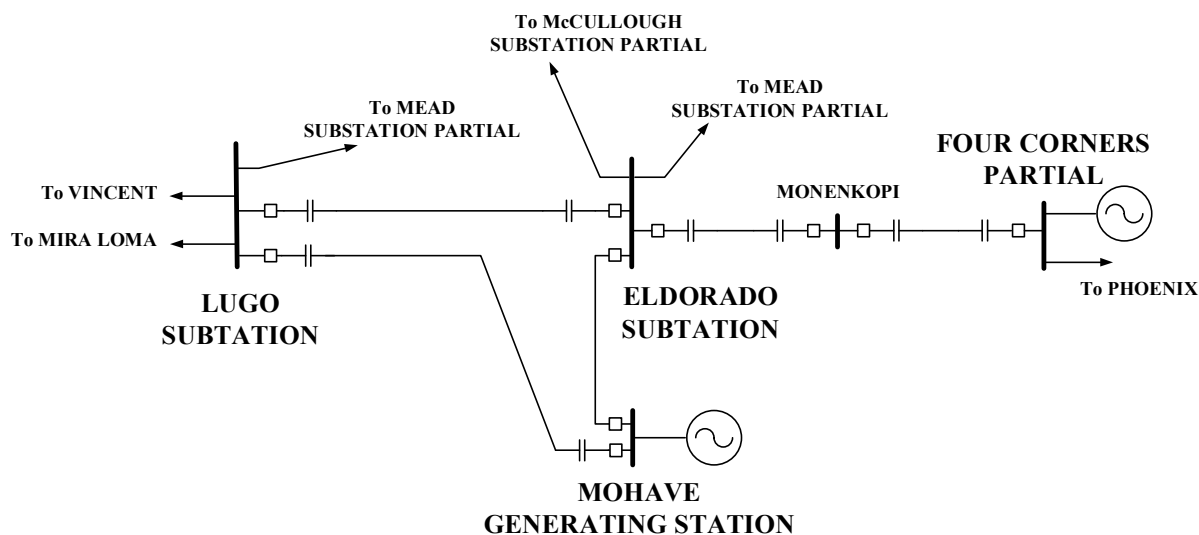


**Figure 1.1: The schematic diagram of the transmission system in which the Mohave generator plant was connected [21, 49]**

Synchronous generator shaft failure due to SSR was also experienced at Vungang I thermal plant, Vietnam, in 2015 [50]. Figure 1.2 shows the single line diagram of the Vungang

plant with 500 kV transmission system [50]. The Vungange I thermal plant consists of two turbines with a total capacity of 1200 MW. To increase the power transfer capability of transmission lines and also stability of the system, the parallel transmission lines between Vungang bus and Danang substation is compensated with the series capacitors, i.e. compensation level of 55%. SSR occurrence in this system on November 24, 2015, caused several large cracks in the generator of the first unit [50].
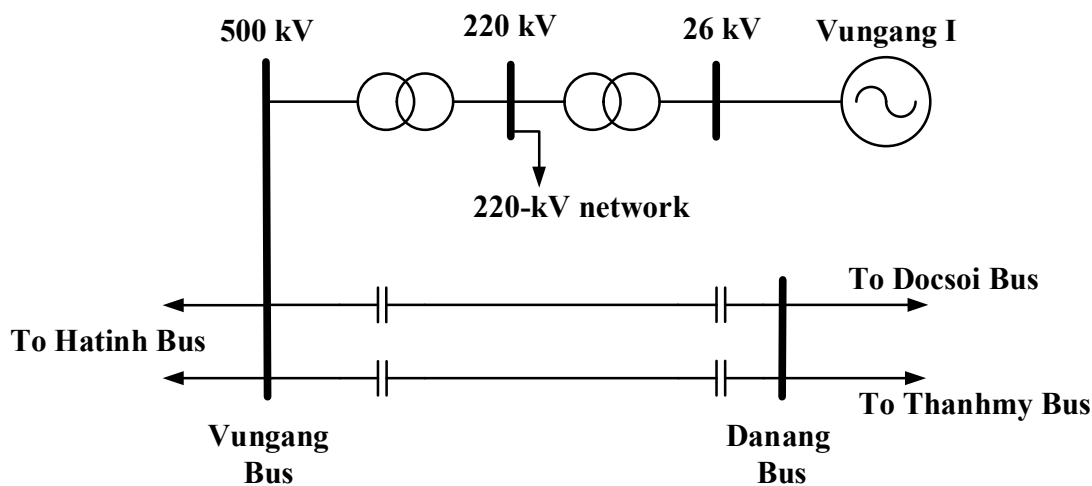


**Figure 1.2: Single line diagram of the Vungang plant with 500 kV transmission system [50].**

## 1.3.2 SSR in Type 1 IG-Based Wind Farms Connected to Series Compensated Transmission Line

To accommodate increased power flow from wind plants, there is a need for a substantial upgrade of grid transmission infrastructures. As described above, series capacitive compensation is a simple cost-effective method to increase the power transfer capacity of lines. However, this series capacitive compensation may potentially produce SSR in induction generator (IG)-based wind turbine generators [51, 52]. An elaborate analytical and simulation-based study of subsynchronous resonance in IG-based wind farm connected to a series-compensated transmission line is reported in [44, 45, 53].

The potential of SSR through a frequency domain model of the IG-based wind farm was studied in [54]. It was established that torsional modes may be excited by an electrical fault in the network, but any unstable torsional interaction was not indicated. IGE is the major

cause of SSR in wind farms interfaced with series-compensated network due to network resonance oscillatory mode. Due to low shaft stiffness (inertia) of the wind turbine drive train, the frequency of torsional modes in wind turbines is in the range of 1 to 3 Hz. In order to create TI in IG-based wind farm, a very high level of series compensation is required which rarely occurs [44, 55, 56].

## 1.3.3 SSR in Type 3 DFIG-based Connected to Series Compensated Transmission Line

DFIG is an important category of variable speed generator wind turbines. Modeling of DFIG based wind farm connected to a series compensated transmission line is presented in [57]. Impact studies of series capacitor and control parameters on SSO through small-signal analysis and time domain simulations were carried out in this paper. Detailed modeling of DFIG based wind farm connected to a series-compensated transmission line was reported in [58-61]. In these papers, small-signal analysis followed by a time domain simulation were performed to examine the SSR conditions.

The wind power industry has become more interested in SSR studies after the two SSR events that occurred in wind farms connected to series-compensated transmission lines in USA [28, 62, 63].

In the Electric Reliability Council of Texas (ERCOT) system in 2009, due to a single line to ground fault in the system and subsequent outage, two large wind farms (485 MW) become radially connected to a 345-kV series-compensated transmission line. Figure 1.3 depicts the single line diagram of the ERCOT grid [39, 63-65]. Series capacitors are located on the transmission lines between following buses: Bus13-Bus16, and Bus 15-Bus 16. The compensation level varies from 50% to 80% [65]. The worst-case scenario in terms of susceptibility to SSR occurs when the wind farm is radially connected to the series compensation capacitor via Bus 2, Bus 3, Bus 8, Bus 13, Bus 16 and Bus 15 while the other lines are open [39]. In 2009, After the fault, once the faulted line was cleared, the wind farm found itself operating radially with the 345-kV transmission line with 50% series compensation. Then, SSCI between the wind turbine generator control and series capacitor got initiated. This led to a fast generation of SSR, causing damage to both the series

capacitor and the wind turbine (as voltage exceeded 2 p.u. before the series capacitor was bypassed) [62, 63, 66].
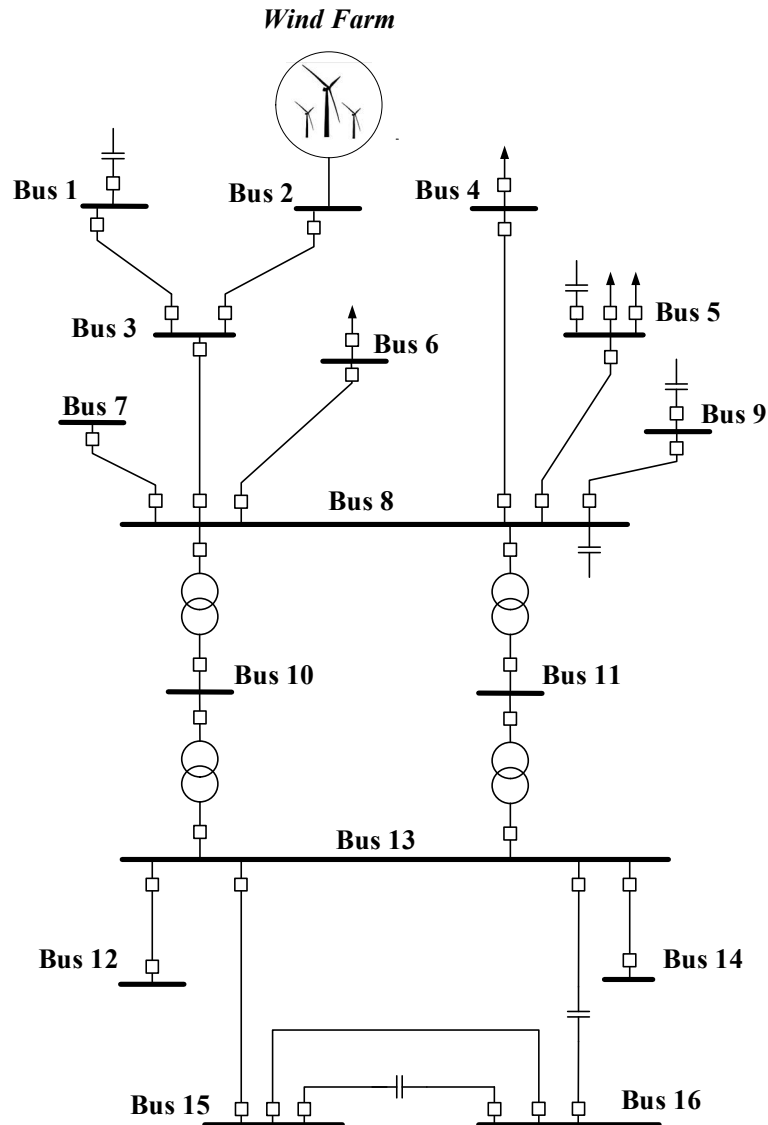


**Figure 1.3 The single line diagram of the ERCOT grid with DFIG-based wind farm at Bus 2 [39, 63-65].**

In 2007, another SSR event in a wind farm took place in Minnesota, USA. Many wind farms are planned and connected to the 345-kV series-compensated transmission line in southwestern Minnesota. In one case, the series compensation level was chosen to be 60% in a 54-mile line. One end of the line was connected to a 150-MW wind farm. Figure 1.4 depicts the single line diagram of the Minnesota system in which the 150-MW wind farm

is connected. During the commissioning process, the switching operation resulted in the radial operation of the wind farm with the series-compensated transmission line. The system tripped due to the flashover in the generator bus duct resulting in the bypass of the series capacitor. This was later confirmed as SSCI that resulted from the interaction of the DFIG controller and series compensated transmission line [67].
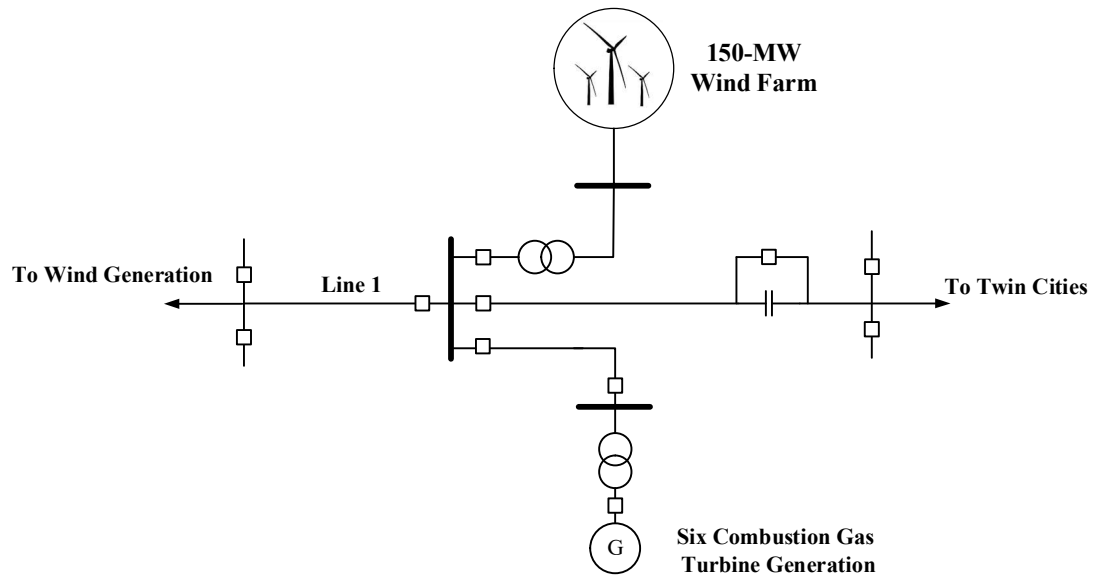


**Figure 1.4: Single line diagram of the Minnesota system in which 150-MW wind farm is connected [67].**

In addition, on December 25, 2012, SSR was observed in wind farms located in Guyuan of North China, which caused many wind turbines to trip [28, 32, 68]. Several similar events happened in subsequent weeks [28]. In [28], it is shown that SSR gets initiated in DFIG-based wind farm connected to series compensated transmission line even if the compensation level is very low (for example 6.67% in the event reported in [28] ). This paper also shows that the controllers of DFIG, especially the controller of Rotor Side Converter (RSC), have a noticeable effect of equivalent impedance of DFIG. Therefore, the controllers of RSC and Grid Side Converter (GSC) greatly affects the damping and frequency of the potential subsynchronous oscillations, which makes DFIGs more vulnerable to SSR [28, 68].

## 1.3.4 SSR in Type 4 PMSG-based Wind Farms Connected to Weak Grids

Recently, SSCI in the Permanent Magnet Synchronous Generator (PMSG)-based windfarm is getting attention [27, 30, 32]. Sustained power oscillations at subsynchronous frequency have been repeatedly captured in PMSG-based wind farm in Xinjiang Uygur Autonomous Region, China, through Wide-Area Measurement System (WAMS), since June 2014, [27]. In this case, there is no series capacitor nearby [27]. The interaction between PMSG-based wind farm and weak ac grid causes a negative-resistance effect for initiating SSCI [27]. In [27], it is shown that the control strategies and parameters of wind farm converter, and Short Circuit Ratio (SCR) which represents strength of the system, play a dominant role in the stability of SSCI mode.

If the frequency of the SSCI mode caused by the interaction of PMSG-based wind farm and weak system, matches the frequency of torsional mode of nearby turbo-generators, it can excite intense torsional vibration in the shaft of turbo-generators. On July 2015 in Xinjiang Uygur Autonomous Region, China, the interaction between PMSG-based wind farm and weak ac system resulted in the excitation of the torsional mode in nearby turbo-generators, which caused three 660-MW generators to trip [27, 32].

## 1.3.5 SSR in Synchronous Generators Connected to HVDC Line

High Voltage DC (HVDC) systems enable bulk power transmission over long distances with higher efficiency and lower electrical losses. HVDC transmission enables secure and stable asynchronous interconnection of power networks that operate on different frequencies. In addition, it provides instant and precise control of the power flow. HVDC systems also have lower environmental impact because they require fewer overhead lines to deliver the same amount of power as High Voltage AC (HVAC) systems [69].

Conventional HVDC systems are based on line-commutated current source converters. They are prone to the problem of commutation failures while operating with weak ac systems. The HVDC converter control can destabilize torsional modes of nearby turbo generators [70]. Torsional interaction between the HVDC link and the turbine generator at Square Butte in North Dakota was first reported in 1980 [70, 71]. Several studies have been performed to identify the cause of interaction and to devise countermeasures for these

subsynchronous oscillations. Experience with the Square Butte DC-link indicated that the rectifier current control loop and the Frequency Sensitive Power Control (FSPC) that was designed to damp interarea oscillations, could cause an undamped 11.5 Hz oscillation under certain operating conditions [70, 71].

As the application of HVDC systems for wind farm interconnection grows, the threat of SSR interaction between wind turbines and HVDC controllers also increases. The potential of SSR in wind farms connected to the HVDC line was shown for the first time in [51].

## 1.4 Methods of SSR Mitigation

Several countermeasures have been investigated and utilized to alleviate subsynchronous resonance (SSR) since its first occurrence in 1971 such as: NGH subsynchronous resonance damping scheme [72, 73], generator excitation control [74-77], Flexible AC Transmission System (FACTS) devices [16, 78-91], energy storage system [92, 93], and using converter of the doubly-fed induction generator (DFIG) system [56, 62, 94-97].

### 1.4.1 SSR Mitigation by Flexible AC Transmission Systems (FACTS)

The concept of preventing SSR in turbine driven synchronous generators through reactive power modulation of shunt connected dynamic reactive power compensators is presented in [77, 98, 99], and actually implemented in [100]. FACTS devices have been utilized for alleviating SSR, through dynamic reactive power compensation. Thyristor Controlled Series Compensators (TCSC) and Gate Controlled Series VAr Compensation (GCSC) [84, 90, 101], Static Synchronous Series Compensator (SSSC) [85-88, 102], Unified Power Flow Controller (UPFC) [103-105], Static VAr Compensator (SVC) [52, 81, 106] , and Static Synchronous Compensator (STATCOM) [82, 83, 91, 107].

### 1.4.1.1 SSR Mitigation by Static Var Compensator (SVC)

SVC is a shunt connected thyristor-based FACTS device which can dynamically exchange either capacitive or inductive currents with the connected power system. SVC current is controlled to regulate specific parameters of the electrical power system (typically bus voltage) [78]. SVC is now considered as a very mature technology. It has been used for reactive power compensation since 1970s [80]. There are multiple applications for SVC

within power systems to: increase power transfer across transmission corridors, mitigate power oscillations, enhance voltage stability margins, improve HVDC converter terminal performance, provide load compensation, etc. SVCs continue to be installed at a large number of locations around the world for providing various benefits to power systems [78].

SVC can be used to control the voltage level at a specific bus with the capability of adding additional damping controls. These can effectively alleviate oscillations in power system such as low frequency interarea oscillations and subsynchronous oscillations [78, 81]. SVC controller consists of three major parts: measurement systems, control components, and power components. The main goal of SVC controller is to maintain the voltage at a predefined voltage reference ($V_{ref}$) at the Point of Common Coupling (PCC). The measurement systems measure the PCC voltage and other power system control signals. The measured signals are passed through filters for use as inputs to various controllers. The error between the reference voltage and measured voltage is fed to the voltage regulator. The voltage regulator generates the required firing angle of thyristor switches to be fired to provide the necessary reactive compensation.

Figure 1.5 illustrates the steady state and dynamic characteristic of an SVC, which describe the variation of SVC bus voltage with SVC current. Although SVC is a voltage regulation device for maintaining constant voltage, a finite slope is incorporated in the dynamic characteristic of an SVC. The slope provides advantages such as substantial reduction of the reactive power rating of the SVC for achieving nearly the same objective, avoiding the SVC from reaching its reactive power limits frequently, facilitating reactive power sharing among multiple compensators operating in parallel.

It should be noted that voltage control alone does not have any capability to provide electrical damping. This objective can be achieved with a separate controller named auxiliary or power swing damping controller, which modulates the bus voltage and thereby introduces system damping. This auxiliary control is based on additional signals such as deviations in power flow, magnitude of line current, bus frequency, or generator speed, etc. The control signals provide information on rotor oscillations which need to be damped. In [81], generator speed is used as control signal for the SVC controller to mitigate SSR. Voltage angle deviation is, likewise, utilized as the control signal to damp the SSR in [106].
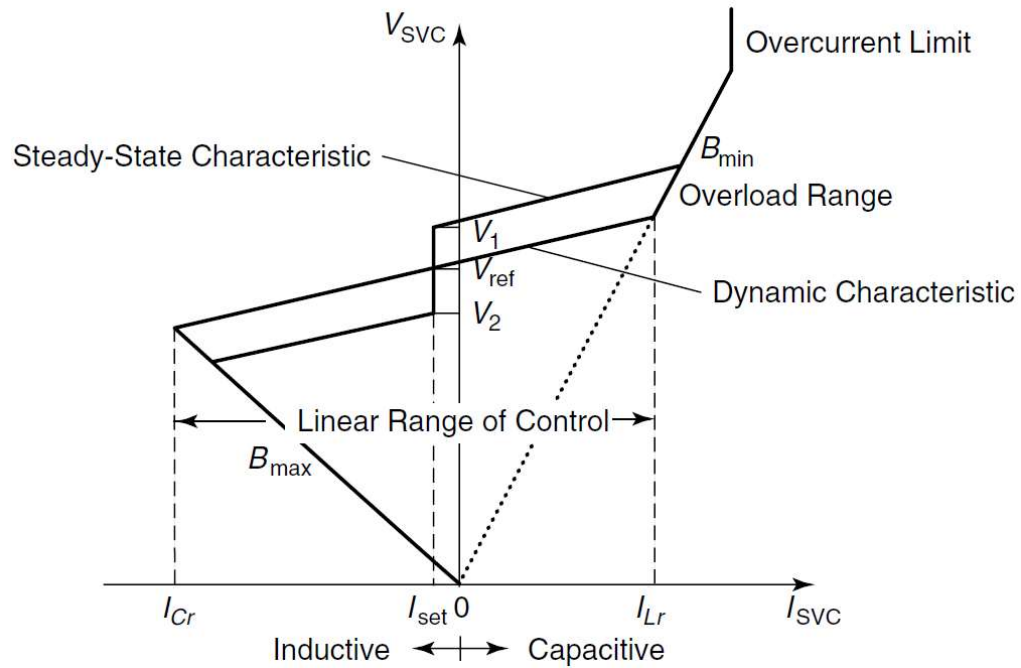
**Figure 1.5: The voltage-current characteristic of the SVC [78]**

## 1.4.1.2    SSR Mitigation by STATCOM

STATCOM is a shunt connected Voltage Source Converter (VSC) with the ability to dynamically control reactive power with rapid response time (typically, 1-2 cycles) [16]. STATCOM uses IGBT, IGCT or GTO as switching devices. In these switches, both switching ON and switching OFF events can be controlled. This gives two degrees of freedom compared to one degree of freedom provided by thyristors in SVCs. This makes STATCOM faster and more effectively controllable than an SVC. STATCOM uses no physical inductor or capacitor for reactive power support, unlike SVC. Modulating the difference between the magnitude of the voltage at STATCOM terminal ($E_S$) and PCC ($V_{PCC}$) causes reactive power exchange in STATCOM. If $E_S > V_{PCC}$, STATCOM acts as a capacitor and inject reactive power to the system. However, if $E_S < V_{PCC}$, STATCOM absorbs reactive power like an inductor.

The main application of STATCOM is to provide dynamic reactive power compensation and regulate the voltage at PCC within acceptable limits. To achieve this goal, the VSC is controlled based on two distinct methods: current-control and voltage-control. The current-control strategy is widely used because of the following advantages: robustness against

variations in the parameters of the VSC and ac system, superior dynamic performance, and higher control precision [108]. The steady state and dynamic characteristics of STATCOM are presented in Figure 1.6. Unlike SVC whose performance degrades with lower bus voltage (Figure 1.5), STATCOM reactive current output does not depend on the voltage at the bus. STATCOM can provide its rated current even at very low bus voltages. Thus, STATCOM is preferred over SVC at buses where the voltage goes too low or drops down very fast [62].

Like SVC, a STATCOM with voltage control alone is unable to damp torsional SSR oscillations and hence an auxiliary damping controller is required [82, 83, 91]. It is possible to mitigate SSR by damping controllers utilizing electrical signals such as rotor speed deviation [82], PCC voltage [83], and line current [91].
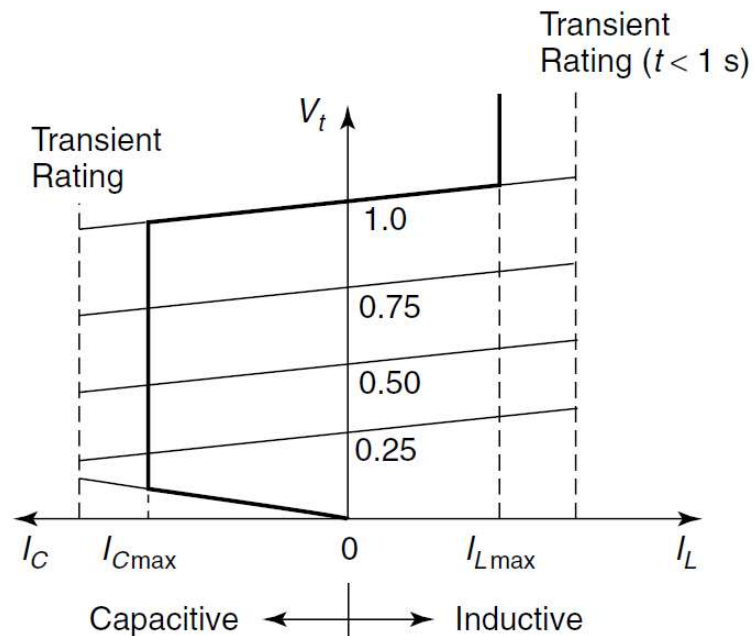


**Figure 1.6: The voltage-current (V-I) characteristic of the STATCOM [78]**

## 1.4.2 SSR Mitigation by Energy Storage Systems

Combination of the energy storage system and voltage source converter can provide a real and reactive power controller device for improving power system stability. Since the first Superconducting Magnetic Energy Storage (SMES) unit was successfully commissioned at the Bonneville Power Administration (BPA) substation in Tacoma, Washington, on

February 1983 [93], several studies have been performed to study on the damping effect of energy storage systems on power systems.

The main components of SMES unit are high-temperature superconductor coil, VSC, and transformer. The superconducting coil is interfaced with a power system through a VSC connected transformer. The SMES current is unidirectional, however, the SMES coil voltage can be varied in a wide range between positive and negative values through the control of firing angles [109, 110].

In [111], the application of a SMES unit to damp SSR through simultaneous control of both active and reactive power in the IEEE First SSR Benchmark system is presented [112]. The control of firing angles provides this ability for the SMES to control both active power and reactive power independently and rapidly in all four quadrant domains. In [93], this application is also employed and verified to alleviate SSR in IEEE Second SSR Benchmark system [113]. A combination of SMES and STATCOM is used to alleviate the SSR in wind farm in [114].

## 1.4.3 SSR Mitigation by Utilizing DFIG Converter

In DFIG, the grid-side converter (GSC) like a STATCOM has the ability to exchange both active and reactive power very rapidly. By controlling this reactive power exchange with the system, SSR can be damped. Studies to investigate the capability of GSCs of a DFIG in mitigating SSR is presented in [56, 62, 96, 115].

The control capability of DFIG converter in alleviating SSR in DFIG-based wind farm is presented in [56]. The subsynchronous damping controller added to GSC in [56] utilizes the voltage across the series capacitor as the control signal.

In [115], a damping controller is proposed for mitigating SSR in DFIG-based windfarm in a modified IEEE First SSR Benchmark system. Residue-based analysis is used to identify an optimum input control signal to the damping controller among three tested signals: 1) generator rotor speed $\omega_r$, 2) line real power $P_{line}$, and 3) voltage across the series capacitor $V_c$. Root-locus method is used to compute the required damping controller gain to stabilize the SSR mode while verifying the residue-based analysis.

A damping controller has been added to the controller of GSC in DFIG-based windfarm to damp SSR in a nearby turbine generator [96]. The effectiveness of the proposed method is demonstrated for a high compensation level (65%) in the IEEE Second SSR Benchmark system.

The damping of SSR in a DFIG-based windfarm in a network similar to ERCOT system is investigated in [62]. In this paper, the damping controller effectiveness is compared for cases: 1) integrated to RSC, and 2) integrated to GSC. The damping controller is designed using multi-input multi-output state-space method to manage several measurements and control inputs. Damping controller integrated with RSC controller provided better damping performance and enhanced robustness against changes in the operating conditions as compared to the damping controller added to GSC controller [62].

## 1.5 Control Interaction among Dynamic Devices

Widespread applications of FACTS devices, HVDC systems, and inverter-based energy sources, has led to concerns of adverse control interactions among them [78, 116-120].

The control interaction between multiple SVCs in the Hydro-Quebec power system has been studied whereas increasing oscillations of 16-Hz frequency are observed in the transient response due to adverse interaction between the SVC controllers [116]. It is further shown in [78] that low short circuit level of ac system in a tightly coupled ac/dc system can cause strong interaction between HVDC and SVC controllers, and they need to be designed in a coordinated manner.

In [117], the potential interaction between a proposed TCSC and existing SVC for the New York State transmission system is investigated. The study results indicate the existence of adverse control interaction between TCSC controller and SVC controller. The control interaction action between multiple TCSCs has been addressed in [118]. The adverse interaction between Power System Stabilizer (PSS) of synchronous generators and Power Oscillation Damping (POD) controller of FACTS devices has been addressed in [119-122].

Subsynchronous and supersynchronous oscillations in voltage and current of the power system in China south grid due to adverse interaction between multiple STATCOMs and

weak ac/dc grid have been reported in [36]. It is shown that the system is normal while only one STATCOM is online, but, when the second STATCOM is put in operation, subsynchronous and supersynchronous oscillations get initiated in the power system.

Therefore, the controllers of dynamic devices need to be coordinated with other controllers to avoid any adverse interaction and onset of power oscillations and subsynchronous oscillations. Coordination of controllers implies simultaneous (not individual) tuning of the parameters of controllers of different devices to ensure overall enhancement in steady state and dynamic performance. Several coordination methods have been investigated in literature which are mostly optimization-based methods [120, 123, 124]. For example, an optimization approach has been applied to minimize the objective function formed from selected eigenvalues of power system state matrix in [120].

## 1.6   Smart PV Inverters

Smart inverters (also known as advanced inverters) provide control of both real and reactive power, either autonomously or in response to signals communicated by system operator [125-128]. Smart inverters are being increasingly implemented on PV solar systems, Battery Energy Storage Systems (BESS), and wind farms to improve power system performance [129-133].

### 1.6.1 Smart inverter functions

Smart inverter functions allow Distributed Energy Resources (DERs) to provide various grid support functions and enhance reliability [134]. Various smart inverter functions such as Volt/Var, Volt/Watt, Frequency Watt, Low/High Voltage Ride-Through, Low/High Frequency Ride-Through, Dynamic Reactive Current, Controlled Active Power Ramping, Soft Start of Distributed Generation Systems have been proposed in [125, 134, 135], and also demonstrated in real distribution and transmission system [136-138].

Various smart inverter applications have been widely reported and studied. FACTS-like performance of wind farm inverter (as STATCOM) by ENERCON wind energy converter has been reported in [139]. In [140], advanced controls of wind system to provide ancillary services to the system have been described. Utilization of wind farm inverter to damp SSR in nearby turbine generator has been studied in [96, 141]. Also, SSR mitigation in DFIG-

based wind farm by adding auxiliary damping controller in wind farm inverter controller has been proposed in [56, 115].

Voltage support and mitigation of overvoltage conditions by reactive power capability of PV inverters has been investigated in [127]. A control scheme has been proposed in [142] to enable local PV distributed generation system to provide reactive power support for mitigation of large voltage variations due to reverse power flow. In [130], a power oscillation damper (POD) is proposed for a large-scale PV system to damp interarea oscillations. PV smart inverter has been used for voltage control in [143, 144]. In the aforementioned papers, the control strategy is mainly based on reactive power modulation.

PV solar farm utilizes voltage source inverter to convert dc power generated by PV arrays into ac power and inject it to the grid. STATCOM, likewise, includes a voltage source inverter to control reactive power exchange with the system and improve the performance of the system. In 2009, a smart PV inverter controller has been proposed to utilize PV solar farm inverter as STATCOM, termed PV-STATCOM in [15, 145-150] based on pending patents [151, 152]. The novel concept of PV-STATCOM will be described later in this chapter.

## 1.6.2 Standards for Grid Integration of PV systems in Power Transmission and Distribution Systems

Inverter-based energy resources such as PV solar farms are being widely installed and/or planned to be installed in power systems. Besides all the benefits of inverter-based DERs, their integration raises several reliability concerns. Therefore, it necessitates the grid codes to be revised for ensuring Voltage and Frequency Ride Through to ensure stable and secure operation of power systems.

The IEEE Standard 1547-2003 [153] was a pioneer Standard for the integration of Distributed Energy Sources (DER), which presented the technical specifications and requirements for integration of distributed sources with a maximum aggregated capacity of 10 MVA to the Electric Power System (EPS). According to IEEE 1547-2003 standard, "The DR shall not actively regulate the voltage at the PCC. The DER shall not cause the Area EPS service voltage at other Local EPSs to go outside the requirements of ANSI

C84.1-1995, Range A." [153]. This standard indicates that the DER shall cease its power generation when fault happens in the system and prohibit DER to provide any function to support the system such as dynamic voltage control. Considering the various technical benefits provided by power electronic controls of inverters, a revised version of IEEE 1547 Standard was published in 2018 [135]. This new IEEE Standard 1547-2018 allows various DER functions for grid support grid including Low/High Voltage Ride-Through and Low/High Frequency Ride-Through. It is clarified that cessation of power generation does not require open contacts which means the cessation of power generation can be achieved by any means that makes real power generation of DER zero such as by increasing the dc side voltage to open circuit voltage of PV panels in PV solar farm. The IEEE 1547-2018 also applies to DERs connected to the distribution system, although the limit of aggregated DER size, i.e. 10 MVA, has been removed [135]. The German grid code, BDEW- 2008 [154], requires DERs including PV solar system and wind farm to support power system during the disturbances by dynamic reactive power exchange [154]. The North American Electric Reliability Corporation (NERC) standard "Reliability Standards for the Bulk Electric Systems of North America" [155] requires the inverter-based power sources to have the capabilities such as of Voltage Ride-Through (VRT), and dynamic reactive power response. A new IEEE P2800 Standard "Standard for Interconnection and Interoperability of Inverter-Based Resources Interconnecting with Associated Transmission Electric Power Systems" is under development for reliable integration of inverter-based resources into the bulk power system, including, but not limited to, voltage and frequency ride-through, active power control, reactive power control, dynamic active power support under abnormal frequency conditions, dynamic voltage support under abnormal voltage conditions, power quality, negative sequence current injection, and system protection [156].

The grid codes still need to be improved and developed to allow various new and emerging smart inverter functions for improving power system performance and reliability.

## 1.7   PV-STATCOM: A New Smart Inverter

Solar farms are typically idle in the night with their entire assets unutilized. In 2009, a new concept of using PV solar farms as STATCOM was proposed [145] which utilized the

entire capacity of solar farm converter at night as a dynamic reactive power compensator STATCOM to regulate grid voltage and facilitate integration of more wind plants into the system without needing any additional voltage-regulating devices. This technology, termed PV-STATCOM, was employed to improve power transfer capacity of existing transmission network in [15, 146, 157] and increase the connectivity of neighboring wind farms in [146] by employing the remaining capacity of the PV inverter during daytime after active power generation, in addition to utilization of the idle capacity of the converter at night. A limitation of this concept was that it could not be applied during noon time or hours when the solar farm was producing its rated power output.

In 2014, a new patented technology was developed to employ the entire capacity of PV inverter as a full STATCOM both during night and anytime during system need in the day [151]. A new PV-STATCOM control was presented in [158], as an outcome of this thesis, for mitigation of SSR in a turbine driven synchronous generator connected to a series compensated transmission line. The PV-STATCOM, connected at generator terminal, utilized the entire capacity of PV inverter for dynamic reactive power control both during night and day for damping SSR.

The PV-STATCOM technology was used in [147] to provide voltage control during critical system need on a 24/7 basis. The performance of the proposed method was investigated with a 10 kVA PV-STATCOM through both EMTDC/PSCAD software and laboratory implementation studies using dSPACE in [147]. The PV-STATCOM technology was successfully installed and demonstrated during night and day on a 10 kW PV solar system for stabilizing a critical induction motor in the utility network of Bluewater Power Distribution Corporation, Sarnia, Ontario, Canada on 13th December 2016 [159, 160].

PV-STATCOM application for controlling steady state voltage and temporary overvoltage's (TOVs) resulting from unsymmetrical faults in the distribution system was investigated in [148]. In [149], PV-STATCOM was used to provide 24/7 functionality as a STATCOM for power oscillation damping and thereby increase the power transfer capacity of systems which exhibit both local inertial and inter-area oscillatory modes. A coordinated application of PV-STATCOM with power system stabilizers (PSSs) for damping power oscillation in power systems was presented in [161]. Concurrent Fast

Frequency Response (FFR) and POD control by PV-STATCOM was proposed in [150] for enhancing both frequency stability and damping of power oscillations.

## 1.7.1 PV-STATCOM Control Concept

Figure 1.7 depicts the typical pattern of the PV solar farm power generation on a sunny day and the remaining reactive power capacity over a 24-hour period. The PV-STATCOM has two modes of operation: i) Partial STATCOM, and ii) Full STATCOM.

### 1.7.1.1    Partial-STATCOM Mode

Partial-STATCOM mode utilizes inverter capacity remaining after real power generation ($P_{PV}$) during daytime for dynamic reactive power control as a STATCOM. Active power generation is the priority of the PV plant in this mode. SSR mitigation is performed without interrupting real power output from the PV plant. This mode is used during daytime typically during early morning and late afternoon.

### 1.7.1.2    Full-STATCOM Mode

In Full-STATCOM mode, reactive power exchange is the priority and the entire capacity of solar inverter is utilized for dynamic reactive power control as a STATCOM. During daytime, if any fault or disturbance is detected in the system and reactive power compensation is needed, the solar farm reduces its output active power to zero and makes its entire inverter capacity available for STATCOM operation. As soon as fault/disturbance is cleared, and consequent instability is damped, the solar farm restores its pre-disturbance power output in a ramped manner. Based on grid codes [135, 154, 155], a gradual increment of $P_{PV}$ is required to prevent the initiation of low-frequency oscillation in the system. During the ramp-up of $P_{PV}$ after SSR alleviation, PV-STATCOM utilizes the unused capacity of VSC and operates in Partial-STATCOM mode to avoid the recurrence of SSO and achieve fast ramp-up. This is a novel functionality during the power ramp-up, which is not specified in existing grid codes. The time taken from power reduction to power restoration at its pre-disturbance level is usually less than a minute. The Full-STATCOM mode can be initiated even when the solar farm is producing its rated power at full noon. During nighttime, the solar farm is typically idle. The Full-STATCOM mode utilizes this

entire inverter capacity to operate as a STATCOM for mitigating SSR. The PV-STATCOM technology thus enables a PV solar farm to function like a STATCOM on a 24/7 basis.

PV-STATCOM autonomously determines its operation mode, between Partial-STATCOM mode and Full-STATCOM mode, based on system requirement and PV solar farm condition.
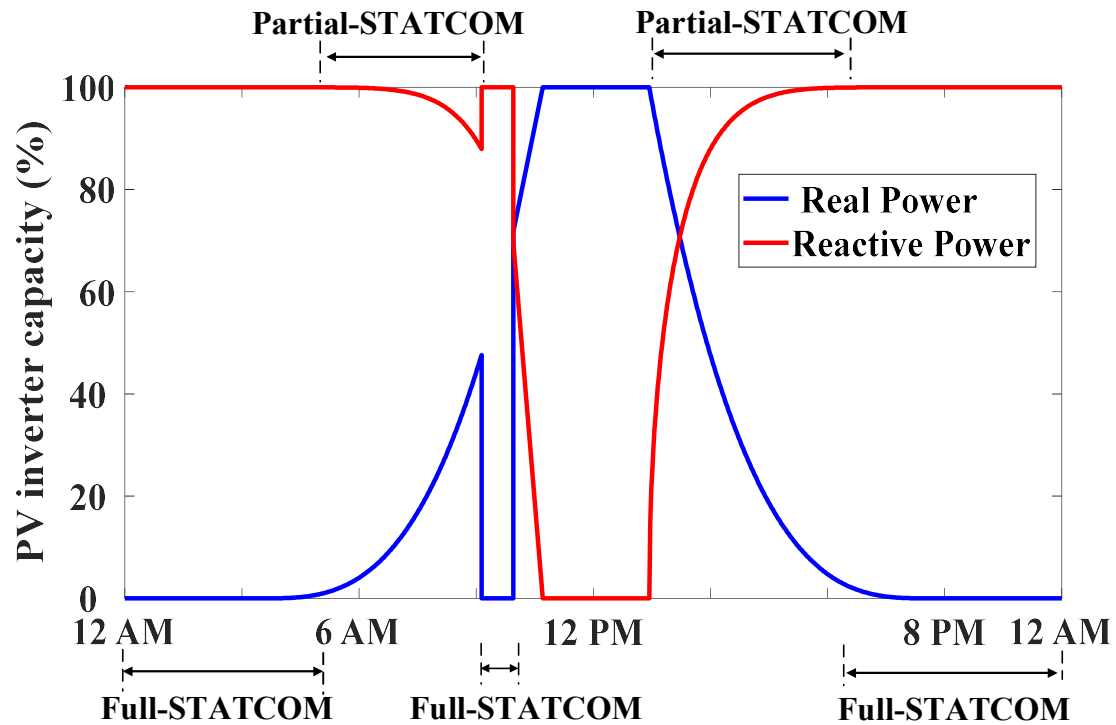


**Figure 1.7:** PV inverter real and reactive power output power as PV-STATCOM over 24-hour duration

## 1.7.2 PV-STATCOM vs Conventional Smart Inverter

The PV-STATCOM is distinct from conventional smart inverters in the following ways:

1) At daytime, PV-STATCOM autonomously determines, once there is a need, to cease active power generation and make available the entire capacity of PV inverter for reactive power exchange. At nighttime, PV inverter is idle, and its entire capacity can be used by PV-STATCOM in Full-STATCOM mode. Therefore, the novel technology of PV-STATCOM enables PV inverter to function as STATCOM on a 24/7 basis. PV-STATCOM provides various STATCOM functions such as

increase in power transfer capacity through power oscillation damping and SSR mitigation. Conventional smart inverters do not provide these functions.

2) PV-STATCOM operates during nighttime whereas conventional smart inverters are not required to operate at the nighttime based on grid codes which are only defined for daytime operation [135, 154, 162].

3) The PV-STATCOM provides voltage control with a response time of 1-2 cycles whereas the conventional voltage control functions such as volt-var, volt-watt, etc respond in 1-2 sec [135].

4) Based on grid codes [135, 154, 155], a gradual increment of real power $P_{PV}$ is required to prevent the initiation of low-frequency oscillations in the system. The PV-STATCOM operates in Partial-STATCOM mode during $P_{PV}$ ramp-up and utilizes the unused capacity of the inverter to prevent any recurrence of disturbances in the system. This allows PV-STATCOM to ramp-up much faster than conventional smart inverters. None of the present grid codes require smart inverters to perform power oscillation damping or voltage control while ramping up.

5) However, since PV-STATCOM provides control of reactive power as smart inverters (although much faster), it comes under the family of smart inverters. Moreover, since it provides various STATCOM functionalities on 24/7 basis it can be considered a new FACTS device.

## 1.7.3 Need for further work

With increasing electrical power generation to meet the load demand, series compensation of lines is expected to be extensively considered as an economical alternative to the construction of new transmission lines, worldwide. This is likely to make the associated generation systems more prone to SSR issues. On the other hand, due to the rapid adoption of renewable energy systems, large-scale PV solar farms and wind farms are increasingly being deployed in transmission systems worldwide. There is a high probability of wind farms and solar farms to be located in close vicinity or even be co-located [163, 164].

Considering the growing developments of large solar farms and their possible connection in series compensated lines, such large solar farms can potentially become candidates for implementation as PV-STATCOM for SSR mitigation both in synchronous generators as well as in wind farms. This SSR alleviation functionality of PV-STATCOM needs to be investigated further.

## 1.8   Scope and Objectives of the Thesis

The scope and objectives of the thesis are described in this section.

### 1.8.1 Scope of the thesis

STATCOM is well-known as an effective countermeasure to alleviate SSR in the power system [82]. New control of PV solar farm as a STATCOM termed PV-STATCOM was presented in [15, 145-150] based on pending patents [151]. PV solar farms with rating over 100 MW are growing rapidly around the world. The likelihood of these PV solar farms to be connected to series compensated transmission lines is high. Furthermore, the sizes of these large-scale PV solar farms are comparable to those of transmission level STATCOMs, therefore they can very well be used as PV-STATCOMs. However, PV-STATCOM for damping SSR has not been investigated so far. Thus, the objective of this thesis is to utilize PV-STATCOM to mitigate SSR in series-compensated transmission systems. Implementation of SSR mitigation functionality on existing PV solar farms can reduce or obviate the need for installing additional expensive FACST devices such as STATCOM and SVC for the same purpose.

### 1.8.2 Objectives of the thesis

The objective of this thesis is to propose a novel economical PV solar system based solution (PV-STATCOM) for damping SSR in synchronous generator and wind farms connected to series compensated lines.

To achieve this objective the following tasks have been identified for this thesis, which eventually lead to the different Chapters of this thesis:

1) Mitigation of SSR in a synchronous generator connected to series compensated line by a PV solar farm as PV-STATCOM located either at generator terminals or at line midpoint

2) Mitigation of SSR in a Type 1 wind farm connected to series compensated line by a PV solar farm as PV-STATCOM located either at wind farm terminals or at line midpoint

3) Control coordination of PV-STATCOM and DFIG-Based Wind Farm for damping of subsynchronous oscillation in a series compensated line

## 1.9   Outline of the Thesis

Chapter 2 presents models of various components of the power system including synchronous generator drive train, induction generator mechanical drive train, doubly-fed induction generator, series-compensated line, PV solar farm, and PV-STATCOM controller.

Chapter 3 investigates the effectiveness of PV-STATCOM in damping SSR in synchronous generator connected to a series compensated transmission line. The study system is a modified IEEE First SSR Benchmark system with PV solar farm connected at generator bus. The generator speed is employed as the control signal for damping controller. Small-signal analysis and electromagnetic transient simulations are utilized to demonstrate the effectiveness of PV-STATCOM in SSR alleviation for all the critical levels of series compensation.

Chapter 4 studies the efficacy of PV-STATCOM in mitigation of SSR in a synchronous generator when the PV system is located remotely from the synchronous generator. Line active power is utilized as the local control signal for damping controller to avoid the communication delay if generator speed were supposed to be chosen as the control signal. Eigenvalue analysis and time domain simulations are employed to validate the PV-STATCOM ability in damping SSR in the synchronous generator for all the critical levels of series compensation.

Chapter 5 deals with the application of PV-STATCOM for damping SSR in IG-based Type 1 wind farm. This control is developed in a modified IEEE First SSR Benchmark system

in which the solar farm may be located at either wind farm terminal or at line midpoint. In this chapter, generator speed and line current signals are utilized as the control signal by damping controller. Modal analysis and electromagnetic transient studies are performed for wide-ranging system conditions to demonstrate PV-STATCOM efficacy in preventing SSR.

Chapter 6 presents the control coordination between PV-STATCOM damping controller and DFIG converter damping controller for SSR mitigation. The study system is derived from the IEEE First SSR Benchmark system with the synchronous generator being replaced by a combination of DFIG-based Type 3 wind farm and PV solar farm. Line current is selected as the control signal for both damping controllers. The Genetic Algorithm (GA) block of MATLAB software is used to develop coordinated damping controller parameters in both DFIG converter and PV-STATCOM.

Chapter 7 presents the conclusions and significance of the thesis. This Chapter also provides suggestions for future research work with PV-STATCOM technology in the are of SSR mitigation.

Chapter 2

# 2 System Modeling

## 2.1 Introduction

This chapter presents the models of various subsystems including synchronous generator and its torsional system, IG-based wind farm, IG mechanical drive train, DFIG-based wind farm, series-compensated line, PV solar farm, and PV-STATCOM controller. The subsynchronous damping controller design procedure is also described in this chapter. All the components of the study system are modeled in both PSCAD/EMTDC and/or MATLAB/Simulink software.

Detailed eigenvalue analysis of SSR phenomena in the modified IEEE First SSR Benchmark system is carried out through the linearization block of MATLAB software. The results are validated through electromagnetic transient simulation studies performed using PSCAD/EMTDC or MATLAB/Simulink software.

## 2.2 Modeling of IEEE First SSR Benchmark System

The IEEE First SSR Benchmark system [112] which is widely used  for SSR studies is chosen as the base study system in this thesis. This system, depicted in Figure 2.1, has been developed for the study of subsynchronous interactions between multi-mass turbine generators and series compensated transmission system [112]. The IEEE First SSR Benchmark system is established based on real parameters taken from the Navajo project [112]. This radial system can produce both self-excitation and transient problems as severe as observed in the actual system [112].  It includes an 892.4-MW steam turbine driven synchronous generator connected to a 500-kV series compensated transmission line through a 26 kV/500 kV transformer [112]. This study system is modified in this thesis based on different case studies with integrated PV solar farm and/or wind farm (IG-based or DFIG-based).
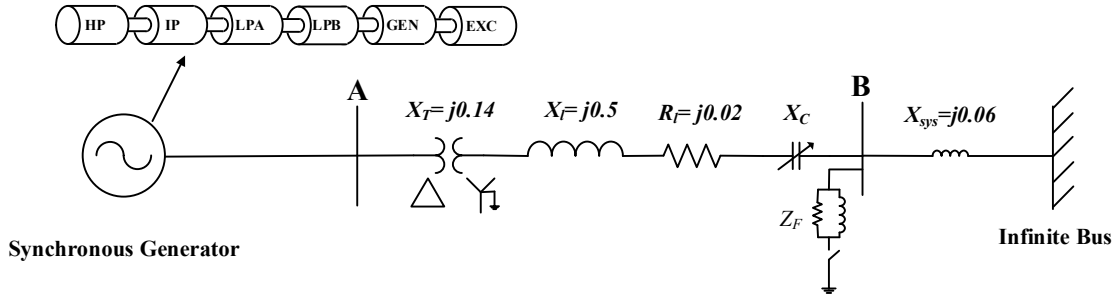
**Figure 2.1: IEEE First SSR Benchmark system**

## 2.2.1 Synchronous Generator Model

The synchronous generator converts mechanical energy to electrical energy and is the main source of real power generation in power systems. The synchronous generator with all phases balanced is represented by a sixth order model in this thesis [165]. Figure 2.2 depicts the schematic diagram of synchronous machine [165] in which *as*, *bs* and *cs* are the stator three-phase windings, *kd* is the *d*-axis damper winding, *fd* is the field winding, *kq1* and *kq2* are the first and second *q*-axis damper winding, respectively; $\theta_r$ is the electrical angle by which the *q*-axis leads the magnetic axis of phase a winding, and $\omega_r$ is the electrical angular velocity.
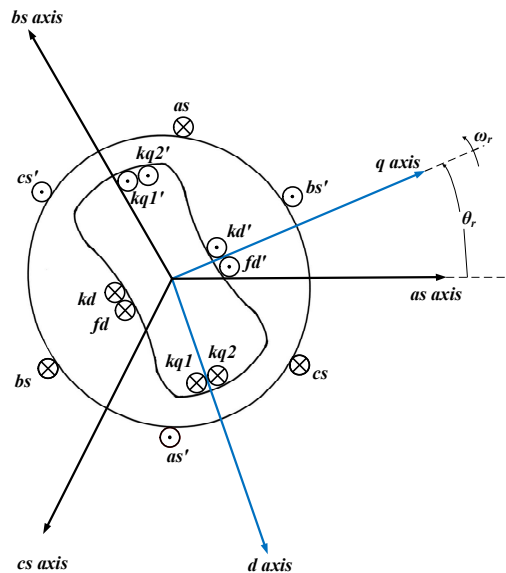


**Figure 2.2: Schematic diagram of a synchronous machine**

The detailed mathematical model of a synchronous generator, per unit model in the *dq-reference* frame, is as follows [165].

$$v_{qs} = -r_s i_{qs} + \frac{\omega_r}{\omega_b} \psi_{ds} + \frac{1}{\omega_b} \frac{d}{dt} \psi_{qs} \tag{2.1}$$

$$v_{ds} = -r_s i_{ds} - \frac{\omega_r}{\omega_b} \psi_{qs} + \frac{1}{\omega_b} \frac{d}{dt} \psi_{ds} \tag{2.2}$$

$$v_{kq1} = r_{kq1} i_{kq1} + \frac{1}{\omega_b} \frac{d}{dt} \psi_{kq1} \tag{2.3}$$

$$v_{kq2} = r_{kq2} i_{kq2} + \frac{1}{\omega_b} \frac{d}{dt} \psi_{kq2} \tag{2.4}$$

$$v_{fd} = r_{fd} i_{fd} + \frac{1}{\omega_b} \frac{d}{dt} \psi_{fd} \tag{2.5}$$

$$v_{kd} = r_{kd} i_{kd} + \frac{1}{\omega_b} \frac{d}{dt} \psi_{kd} \tag{2.6}$$

where $\omega_b$ is the base electrical angular velocity, $v_{qs}$, $v_{ds}$, $i_{qs}$, $i_{ds}$ are the stator $qd$-axis voltages and current, respectively; $v_{kq1}$, $v_{kq2}$, $i_{kq1}$, $i_{kq2}$ are the first and second $q$-axis damper winding voltages and currents, respectively; $v_{fd}$, $i_{fd}$ are the field winding voltage and current, respectively; $v_{kd}$, $i_{kd}$ are the $d$-axis damper winding voltage and current, respectively.

$r_s$ is stator resistance ($p.u.$); $r_{kq1}$, $r_{kq2}$ are resistance of the first and second $q$-axis damper winding ($p.u.$), respectively; and $r_{fd}$, $r_{kd}$ are resistance of the field winding and $d$-axis damper winding ($p.u.$), respectively.

The flux linkage equations are as follows [165]:

$$\psi_{qs} = -X_{ls} i_{qs} + X_{mq}(-i_{qs} + i_{kq1} + i_{kq2}) \tag{2.7}$$

$$\psi_{ds} = -X_{ls} i_{ds} + X_{md}(-i_{ds} + i_{fd} + i_{kd}) \tag{2.8}$$

$$\psi_{kq1} = X_{kq1}i_{kq1} + X_{mq}(-i_{qs} + i_{kq1} + i_{kq2}) \tag{2.9}$$

$$\psi_{kq2} = X_{kq2}i_{kq2} + X_{mq}(-i_{qs} + i_{kq1} + i_{kq2}) \tag{2.10}$$

$$\psi_{fd} = X_{fd}i_{fd} + X_{md}(-i_{ds} + i_{fd} + i_{kd}) \tag{2.11}$$

$$\psi_{kd} = X_{kd}i_{kd} + X_{md}(-i_{ds} + i_{fd} + i_{kd}) \tag{2.12}$$

where $X_{ls}$ is stator leakage reactance (*p.u.*), $X_{kq1}$, $X_{kq2}$ are leakage reactance of the first and second *q*-axis damper winding (*p.u.*), respectively; $X_{fd}$, $X_{kd}$ are leakage reactance of the field winding and *d*-axis damper winding (*p.u.*), respectively; $X_{md}$ is the mutual reactance of the *d*-axis windings (*p.u.*), $X_{mq}$ is the mutual reactance of the *q*-axis windings (*p.u.*).

## 2.2.2 Excitation System Model

IEEE Type DC1 A exciter [166] is utilized to regulate the generator voltage, in this thesis. Figure 2.3 shows the configuration of IEEE Type DC1 A exciter where $V_C$ is generator terminal voltage, $V_{ref}$ is the reference voltage, $V_{UEL}$ is the under-excitation signal, $V_F$ is stabilizing feedback, and $E_{fd}$ is the field voltage. HV gate is just employed in unusual or severe condition to prevent operation that jeopardizes the stability of the synchronous machine or could lead to loss of synchronism due to insufficient excitation [166, 167]. The parameters of the excitation system are presented in Appendix A.
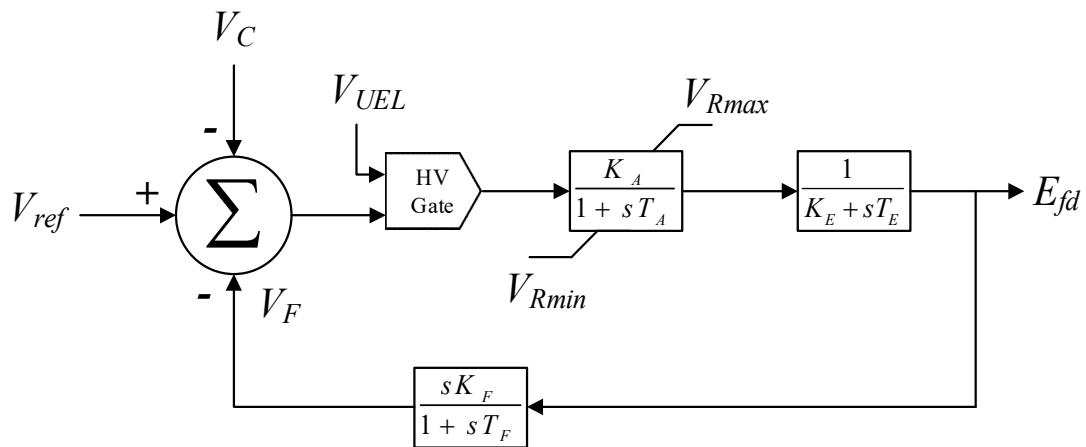


**Figure 2.3: Block diagram of IEEE Type DC1 A exciter**

## 2.2.3 Turbine Generator Mechanical System Model

Turbine Generator (T-G) mechanical system is a complex system, an exact analysis of which may require an advanced continuum model. However, a lumped multi-mass model of this system is adequate for the study of torsional interactions [20]. Figure 2.4 depicts the structure of a typical lumped six mass-spring system model which consists of the High Pressure turbine (HP), the Intermediate Pressure turbine (IP), the low pressure turbines (LPA and LPB), the Generator (GEN), and the exciter (EXC). This multi-mass system has natural resonance frequencies below the system frequency [20]. The torsional mode oscillations are lightly damped, induced by transients due to fault or disturbances in the system [20].
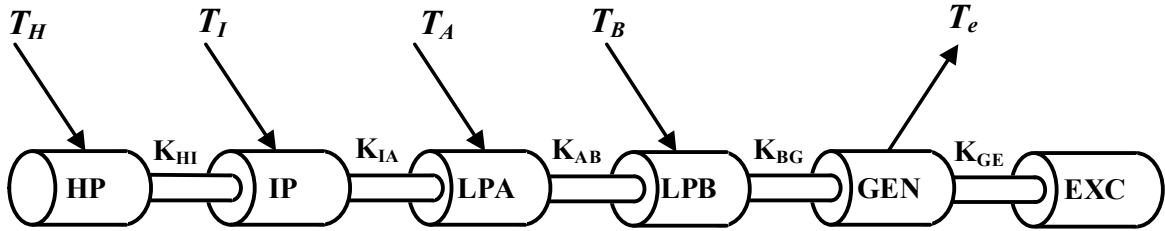


**Figure 2.4: Structure of a typical lumped six mass-spring system model.**

The dynamic equations of the torsional system shown in Figure 2.4 are as follows:

$$\frac{d}{dt}\omega_H = \frac{1}{2H_H}(-D_H\omega_H - D_{HI}(\omega_H - \omega_I) + T_{HP} - T_{HI}) \qquad (2.13)$$

$$\frac{d}{dt}T_{HI} = K_{HI}\omega_b\,(\omega_H - \omega_I) \qquad (2.14)$$

$$\frac{d}{dt}\omega_I = \frac{1}{2H_I}(-D_I\omega_H + D_{HI}(\omega_H - \omega_I) - D_{IA}(\omega_I - \omega_A) + T_{IP} + T_{HI} \\ - T_{IA}) \qquad (2.15)$$

$$\frac{d}{dt}T_{IA} = K_{IA}\omega_b\,(\omega_I - \omega_A) \qquad (2.16)$$

$$\frac{d}{dt}\omega_A = \frac{1}{2H_A}(-D_A\omega_A + D_{IA}(\omega_I - \omega_A) - D_{AB}(\omega_A - \omega_B) + T_{LPA}$$
$$+ T_{IA} - T_{AB}) \tag{2.17}$$

$$\frac{d}{dt}T_{AB} = K_{AB}\omega_b(\omega_A - \omega_B) \tag{2.18}$$

$$\frac{d}{dt}\omega_B = \frac{1}{2H_B}(-D_B\omega_B + D_{AB}(\omega_A - \omega_B) - D_{BG}(\omega_B - \omega_G) + T_{LPB}$$
$$+ T_{AB} - T_{BG}) \tag{2.19}$$

$$\frac{d}{dt}T_{BG} = K_{BG}\omega_b(\omega_B - \omega_G) \tag{2.20}$$

$$\frac{d}{dt}\omega_G = \frac{1}{2H_G}(-D_G\omega_G + D_{BG}(\omega_B - \omega_G) - D_{GE}(\omega_G - \omega_E) - T_e$$
$$+ T_{BG} - T_{GE}) \tag{2.21}$$

$$\frac{d}{dt}T_{GE} = K_{GE}\omega_b(\omega_G - \omega_E) \tag{2.22}$$

$$\frac{d}{dt}\omega_E = \frac{1}{2H_E}(-D_E\omega_E + D_{GE}(\omega_G - \omega_E) + T_{GE}) \tag{2.23}$$

where $H$, $I$, $A$, $B$, $G$, and $E$ indicate HP, IP, LPA, LPB, GEN, and EXC, respectively. The speed of masses is denoted with $\omega_x$ *(p.u.)*, $x = H, I, A, B, G, E$. The damping coefficient of masses are indicated with $D_x$ *(p.u.)*, $x = H, I, A, B, G, E$. $H_x$ (s) is the inertia constant, $x = H, I, A, B, G, E$. $D_{xy}$ *(p.u.)*, $K_{xy}$ *(p.u./rad)*, $T_{xy}$ are the damping coefficient, spring constant, and internal torque between masses, respectively, while $xy = HI, IA, AB, BG, GE$. $T_H$, $T_I$, $T_A$, and $T_B$ indicate the mechanical torque developed by corresponding turbine sections, and $T_e$ *(p.u.)* denotes the electrical torque.

## 2.2.4 Steam Turbine Governor and Model

The steam turbine converts the enthalpy of high-pressure and high-temperature steam to rotating mechanical torque, and consequently to electrical energy by the generator. The governor regulates the generator speed in response to changing load condition to meet the

frequency stability requirement of the grid [168]. Figure 2.5 depicts the block diagram of a 4-mass steam turbine and its governor system which is used in this thesis [167-169]. The parameters of the steam turbine and governor system are presented in Appendix A.
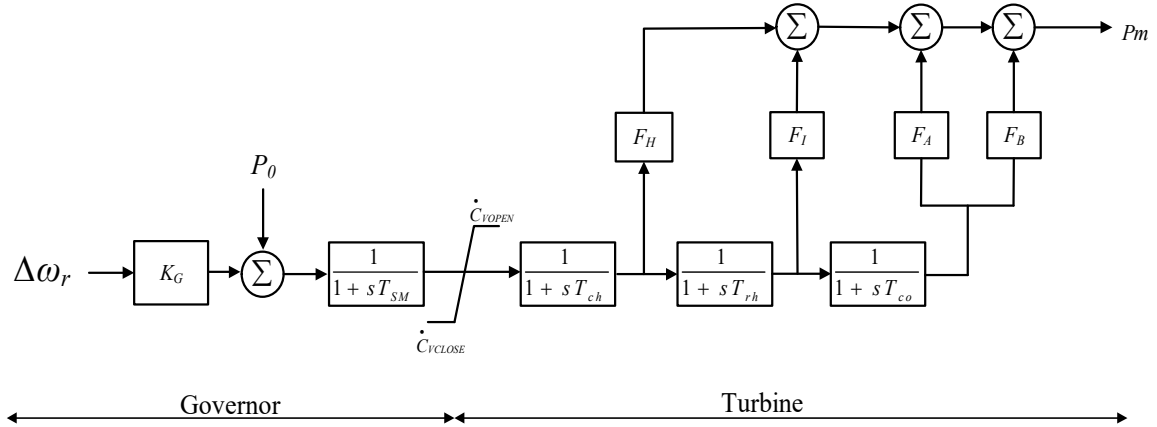


**Figure 2.5: Block diagram of steam turbine and governor system**

## 2.2.5 Series Compensated Transmission Line Model

Figure 2.6 depicts a transmission line model consisting of the series compensated line.
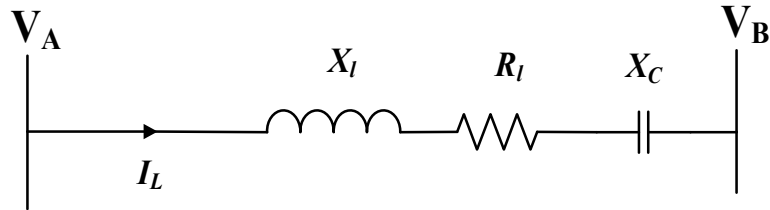


**Figure 2.6: Transmission line with series capacitive compensation**

The dynamic equations of the transmission line in *dq*-reference frame are as follows [58, 61]:

$$\frac{d}{dt}i_{qL} = \omega_b \left( -\frac{R_l}{X_l}i_{qL} - \overline{\omega}_e i_{dL} - \frac{1}{X_l}V_{qc} + \frac{V_{qA} - V_{qB}}{X_l} \right) \qquad (2.24)$$

$$\frac{d}{dt}i_{dL} = \omega_b \left( \overline{\omega}_e i_{qL} - \frac{R_l}{X_l}i_{dL} - \frac{1}{X_l}V_{dc} + \frac{V_{dA} - V_{dB}}{X_l} \right) \qquad (2.25)$$

$$\frac{d}{dt}V_{qC} = \omega_b\left(X_C i_{qL} - \overline{\omega}_e V_{dC}\right) \tag{2.26}$$

$$\frac{d}{dt}V_{dC} = \omega_b\left(X_C i_{qL} + \overline{\omega}_e V_{qC}\right) \tag{2.27}$$

where $R_L$ is the line resistance (*p.u.*), $X_L$ is the reactance of the line inductance (*p.u.*), $X_C$ is the reactance of the series capacitor (*p.u.*), $\omega_b$ is the base speed (377 *rad/s*), $\overline{\omega}_e$ is the rotating synchronous frame frequency (*p.u.*), $V_{qC}$ and $V_{dC}$ are the *qd*-axis voltage across the series capacitor (*p.u.*), $I_{qL}$ and $I_{dL}$ are the *qd*-axis current of the line (*p.u.*), $V_{qA}$ and $V_{dA}$ are the *qd*-axis voltage of Bus A (*p.u.*), $V_{qB}$ and $V_{dB}$ are the *qd*-axis voltage of Bus B (*p.u.*). Considering a three-phase balanced system, the equations related to zero sequence are neglected.

## 2.3  Modeling of Induction Generator (IG)-based Wind Farm

Figure 2.7 shows an IG-based wind farm connected to the infinite bus through a series compensated transmission line [44]. The wind farm is constituted of an aggregation of several identical double-cage induction generators [44, 45], which can be represented by an aggregated model [170-173]. It is assumed that all generators are of the same type, the same size, and are subjected to the same wind speed. To model the dynamics of the mechanical system, an aggregated two-mass wind turbine is considered. Unlike the synchronous generator, the IG does not have any source of excitation and needs to absorb inductive reactive power for its operation. A shunt capacitor ($X_{WF}$) is therefore connected at the terminal of the wind farm to keep its power factor close to unity.
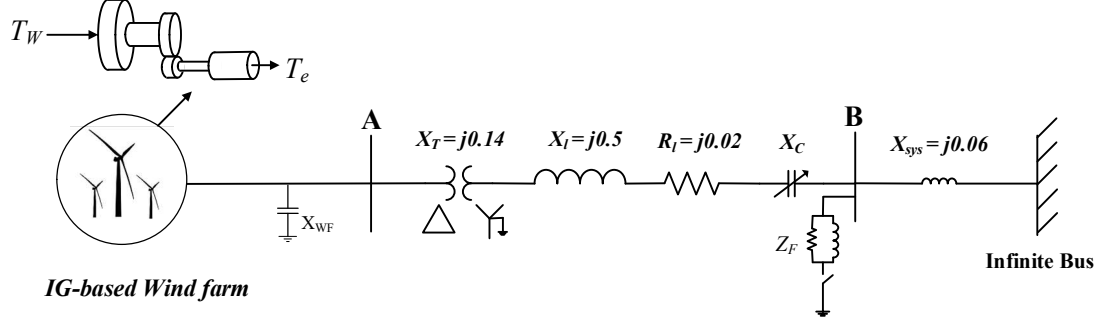
**Figure 2.7: Induction generator (IG)-based wind farm connected to a series compensated system.**

## 2.3.1 Double-Cage Induction Generator Model

The double-cage IG is preferred to the single-cage machine due to its mechanical simplicity, high efficiency, and low maintenance requirements. All commercial induction generators above 5 kW have double-cage rotor [44]. The detailed per unit model of a double-cage induction generator in the *dq-reference* frame is as follows [44, 165].

$$v_{qs} = r_s i_{qs} + \frac{\omega}{\omega_b}\psi_{ds} + \frac{1}{\omega_b}\frac{d}{dt}\psi_{qs} \tag{2.28}$$

$$v_{ds} = r_s i_{ds} - \frac{\omega}{\omega_b}\psi_{qs} + \frac{1}{\omega_b}\frac{d}{dt}\psi_{ds} \tag{2.29}$$

$$v_{qr1} = r_{r1} i_{qr1} + \frac{1}{\omega_b}\frac{d}{dt}\psi_{qr1} + (\frac{\omega - \omega_r}{\omega_b})\psi_{dr1} \tag{2.30}$$

$$v_{dr1} = r_{r1} i_{dr1} - (\frac{\omega - \omega_r}{\omega_b})\psi_{qr1} + \frac{1}{\omega_b}\frac{d}{dt}\psi_{dr1} \tag{2.31}$$

$$v_{qr2} = r_{r2} i_{qr2} + \frac{1}{\omega_b}\frac{d}{dt}\psi_{qr2} + (\frac{\omega - \omega_r}{\omega_b})\psi_{dr2} \tag{2.32}$$

$$v_{dr2} = r_{r2} i_{dr2} - (\frac{\omega - \omega_r}{\omega_b})\psi_{qr2} + \frac{1}{\omega_b}\frac{d}{dt}\psi_{dr2} \tag{2.33}$$

where $\omega_r$ is the rotor speed (*rad/s*), $\omega$ is the synchronous frequency (*rad/s*), $\omega_b$ is the base electrical angular velocity y(*rad/s*), $v_{qs}$, $v_{ds}$, $i_{qs}$, $i_{ds}$ are the stator *dq*-axis voltages and current

(*p.u.*), respectively; $v_{qr1}$, $v_{dr1}$, $i_{qr1}$, $i_{dr1}$ are the first-cage rotor's *dq*-axis voltages and currents (*p.u.*), respectively; $v_{qr2}$, $v_{dr2}$, $i_{qr2}$, $i_{dr2}$ are the second-cage rotor's *dq*-axis voltages and currents (*p.u.*), respectively; $r_s$, $r_{r1}$, $r_{r2}$ are the resistance of stator, first-cage rotor, and second-cage rotor (*p.u.*), respectively. It should be noted that $v_{qr1}$, $v_{dr1}$, $v_{qr2}$, $v_{dr2}$ are zero.

The flux linkage equations are as follows [165]:

$$\psi_{qs} = X_{ls}i_{qs} + X_M(i_{qs} + i_{qr1} + i_{qr2}) \tag{2.34}$$

$$\psi_{ds} = X_{ls}i_{ds} + X_M(i_{ds} + i_{dr1} + i_{dr2}) \tag{2.35}$$

$$\psi_{qr1} = X_{lr1}i_{qr1} + X_M(i_{qs} + i_{qr1} + i_{qr2}) + X_{rM}(i_{qr1} + i_{qr2}) \tag{2.36}$$

$$\psi_{dr1} = X_{lr1}i_{dr1} + X_M(i_{ds} + i_{dr1} + i_{dr2}) + X_{rM}(i_{dr1} + i_{dr2}) \tag{2.37}$$

$$\psi_{qr2} = X_{lr2}i_{qr2} + X_M(i_{qs} + i_{qr1} + i_{qr2}) + X_{rM}(i_{qr1} + i_{qr2}) \tag{2.38}$$

$$\psi_{dr2} = X_{lr2}i_{dr2} + X_M(i_{ds} + i_{dr1} + i_{dr2}) + X_{rM}(i_{dr1} + i_{dr2}) \tag{2.39}$$

where $X_{ls}$ is stator leakage reactance(*p.u.*), $X_{lr1}$, $X_{lr2}$ are first- and second- cage rotors leakage reactance (*p.u.*), respectively; $X_M$ is the mutual reactance between the stator and rotor (*p.u.*), $X_{rM}$ is the mutual reactance between two rotor cages (*p.u.*).

## 2.3.2 Shunt Capacitor Model

As mentioned earlier, the induction generator needs a capacitor at its terminal to operate at unity power factor. Figure 2.8 shows a shunt capacitor. Its dynamic mathematical model in *dq*-frame can be expressed as follows:

$$\frac{d}{dt}v_{qs} = \omega_b(X_{WF}(i_{qs} - i_{qL}) - v_{ds}) \tag{2.40}$$

$$\frac{d}{dt}v_{ds} = \omega_b(X_{WF}(i_{ds} - i_{dL}) + v_{qs}) \tag{2.41}$$

where $X_{WF}$ is the inductance of shunt capacitor ($p.u.$), $i_{qL}$, $i_{dL}$ are line $dq$-axis current ($p.u.$), $v_{qs}$, $v_{ds}$, $i_{qs}$, $i_{ds}$ are the stator $dq$-axis voltages and current ($p.u.$), respectively.

$$V_S$$

$$i_s \qquad i_L$$

$$C_{WF}$$
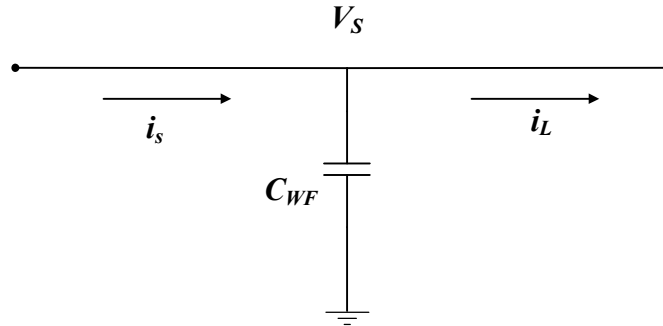
**Figure 2.8: Shunt capacitor model**

## 2.3.3 Drive Train Model

The mechanical system of the wind farm can be modeled with a two-mass system including low-speed turbine and high-speed generator [39, 44].

The dynamic equations of the mechanical system are as follows:

$$\frac{d}{dt}\omega_t = \frac{1}{2H_t}\left(-D_t\omega_t - D_{tg}\left(\omega_t - \omega_g\right) + T_W - T_{tg}\right) \tag{2.42}$$

$$\frac{d}{dt}T_{tg} = K_{tg}\omega_b\left(\omega_t - \omega_r\right) \tag{2.43}$$

$$\frac{d}{dt}\omega_r = \frac{1}{2H_g}\left(-D_g\omega_r + D_{tg}(\omega_r - \omega_t) + T_{tg} - T_e\right) \tag{2.44}$$

where $T_W$ is wind torque ($p.u.$), $T_e$ is the electrical toque ($p.u.$), $\omega_t$ is turbine shaft speed ($p.u.$), $\omega_r$ is generator speed (p.u.), $D_t$ and $D_g$ are damping coefficients of turbine and generator ($p.u.$) respectively; $D_{tg}$ is the damping coefficient between turbine and generator ($p.u.$), and $H_t$ and $H_g$ are the inertia constants of turbine and generator ($s$).

## 2.4 Modeling of Doubly-Fed Induction Generator (DFIG)-based Wind Farm

Figure 2.9 depicts the doubly-fed induction generator (DFIG)-based wind farm connected to a series compensated transmission line [39, 58]. Similar to the IG-based wind farm, the DFIG-based wind farm is an aggregation of several identical DFIG-based wind farm. The DFIG-based windfarm includes a wound-rotor induction generator, and two partial scale voltage source converters: rotor-side converter (RSC) and grid-side converter (GSC) [9]. The RSC and GSC are approximately rated as 30% of nominal generator power [9]. In Figure 2.9, $X_{tg}$ denotes the reactance of GSC transformer. In the following sections, the DFIG-based wind farm model including a wind turbine, an induction generator, RSC controller, GSC controller, and capacitor of DC link between two converters are represented.

### 2.4.1 Wound-Rotor Induction Generator Model

The main difference between the wound-rotor induction generator and squirrel-cage induction generator is that the electrical characteristic of the rotor can be controlled from outside, and its voltage can be impressed by RSC in DFIG-based wind farm [174]. The detailed mathematical model of a wound-rotor induction generator in the $dq$-reference frame is as follows [39, 58, 165]:
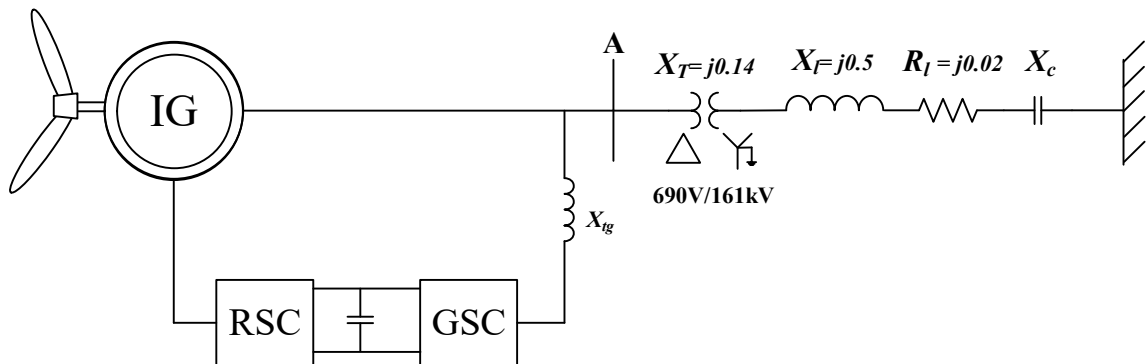


**Figure 2.9: Doubly-fed induction generator (DFIG)-based wind farm connected to a series compensated system.**

$$v_{qs} = r_s i_{qs} + \frac{\omega}{\omega_b}\psi_{ds} + \frac{1}{\omega_b}\frac{d}{dt}\psi_{qs} \tag{2.45}$$

$$v_{ds} = r_s i_{ds} - \frac{\omega}{\omega_b}\psi_{qs} + \frac{1}{\omega_b}\frac{d}{dt}\psi_{ds} \tag{2.46}$$

$$v_{qr} = r_r \ i_{qr} + \frac{1}{\omega_b}\frac{d}{dt}\psi_{qr} + (\frac{\omega - \omega_r}{\omega_b})\psi_{dr} \tag{2.47}$$

$$v_{dr} = r_r \ i_{dr} - (\frac{\omega - \omega_r}{\omega_b})\psi_{qr} + \frac{1}{\omega_b}\frac{d}{dt}\psi_{dr} \tag{2.48}$$

where $\omega_r$ is the rotor speed (*rad/s*), $\omega$ is the synchronous frequency (*rad/s*), $\omega_b$ is the base electrical angular velocity y(*rad/s*), $v_{qs}$, $v_{ds}$, $i_{qs}$, $i_{ds}$ are the stator *dq*-axis voltages and current (*p.u.*), respectively; $v_{qr1}$, $v_{dr1}$, $i_{qr1}$, $i_{dr1}$ are the rotor's *dq*-axis voltages and currents (*p.u.*), respectively; $r_s$, $r_r$ are the resistance of stator, and rotor (*p.u.*), respectively.

The flux linkage equations are as follows [39, 58, 165]:

$$\psi_{qs} = X_{ls}i_{qs} + X_M(i_{qs} + i_{qr}) \tag{2.49}$$

$$\psi_{ds} = X_{ls}i_{ds} + X_M(i_{ds} + i_{dr}) \tag{2.50}$$

$$\psi_{qr} = X_{lr}i_{qr} + X_M(i_{qs} + i_{qr}) \tag{2.51}$$

$$\psi_{dr} = X_{lr}i_{dr} + X_M(i_{ds} + i_{dr}) \tag{2.52}$$

where $X_{ls}$ is stator leakage reactance (*p.u.*), $X_{lr}$ is rotor leakage reactance (*p.u.*), respectively; $X_M$ is the mutual reactance between the stator and rotor winding (*p.u.*).

## 2.4.2 RSC and GSC Controller

Figure 2.10 depicts the block diagram of the RSC controller and GSC controller [39, 58]. In Figure 2.10, $T_e$ denotes the electrical torque, $Q_S$ indicates the reactive power output of stator, $V_{DC}$ is the dc-link voltage, and $V_S$ denotes the voltage at stator terminal. In DFIG-based wind farm, as shown in Figure 2.10, RSC is responsible for controlling the electrical

torque, or rotor speed, and power factor at the stator terminal, or $Q_S$, whereas GSC controls the dc-link voltage and stator terminal voltage [39]. The reference of electrical torque ($T_{e\text{-}ref}$) can be calculated based on wind speed to obtain the optimal torque [39, 58]. In this thesis, the reactive power reference ($Q_{s\text{-}ref}$) is chosen zero to obtain unity power factor at the stator output.
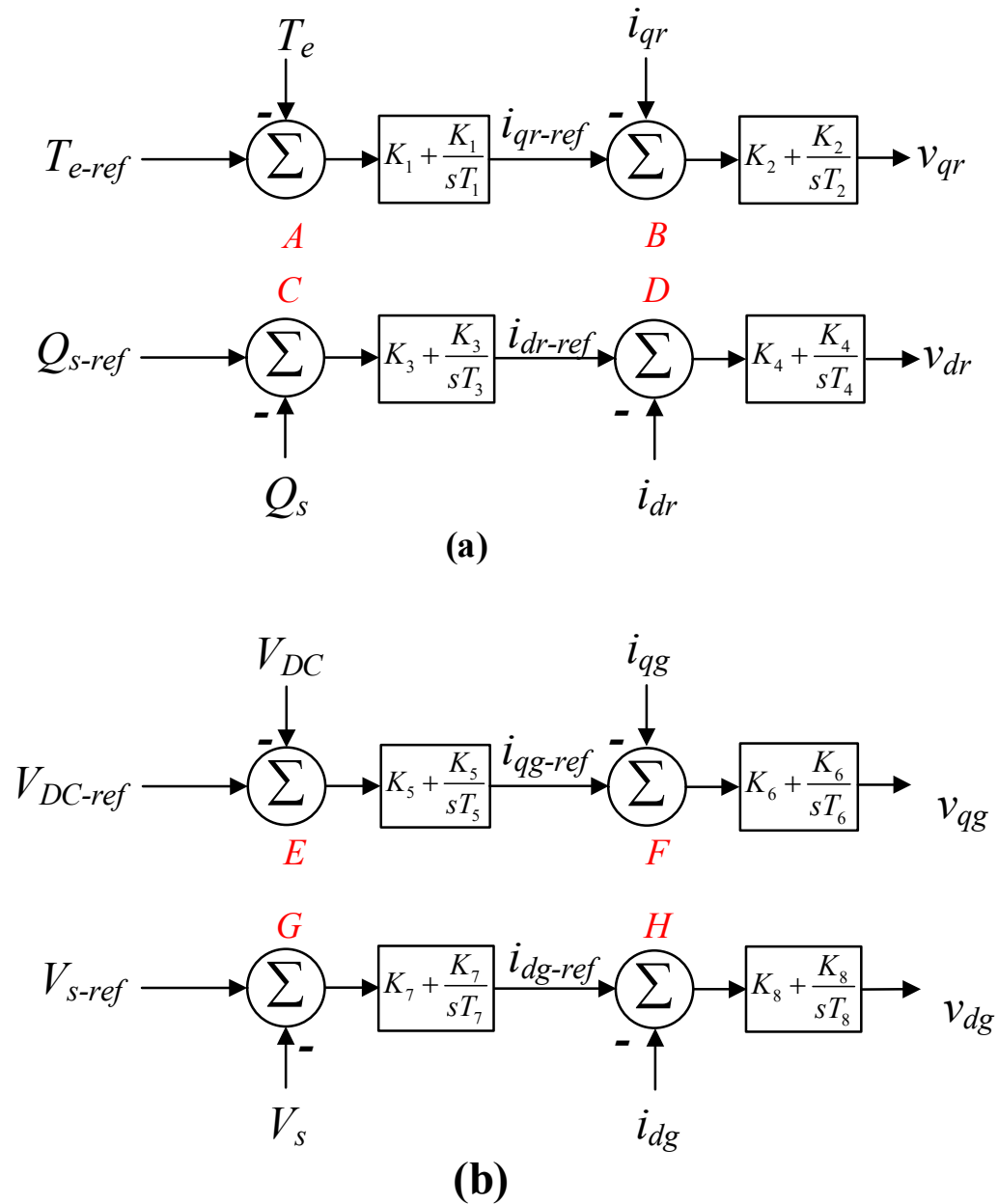


**Figure 2.10: a) RSC controller block diagram   b) GSC controller block diagram**

## 2.4.3 DC Link Model

The capacitor between the RSC and GSC enables decoupled control of two converters [9]. Figure 2.11 depicts the dc-link model. The dynamic mathematical model of dc-link of DFIG can be expressed as follows [39, 58]:

$$-Cv_{DC}\frac{dv_{DC}}{dt} = P_r + P_g \tag{2.53}$$

where $P_r$ in RSC active power (MW), $P_g$ is the GSC active power (MW), $C$ is the dc-link capacitor ($\mu$F), $V_{DC}$ is the dc-link voltage (V).
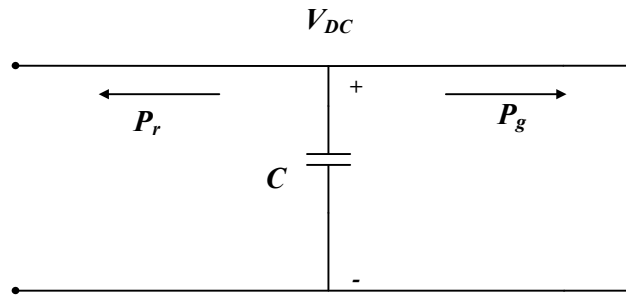


**Figure 2.11: DFIG dc-link model**

## 2.4.4 Drive Train Model

The mechanical system model of the DFIG-based wind turbine is same as the mechanical system model of IG-based wind farm which has been described in section *2.3.3.*

## 2.5  Modeling of PV Solar System

Photovoltaic (PV) solar system converts solar irradiance into electricity using semiconducting material used in solar panels. Figure 2.12 depicts the PV solar system connected at the point of common coupling (PCC) including solar panels, inverter, filter, and step-up transformer. The different part of PV solar system and its control system will be explained in the following sections.
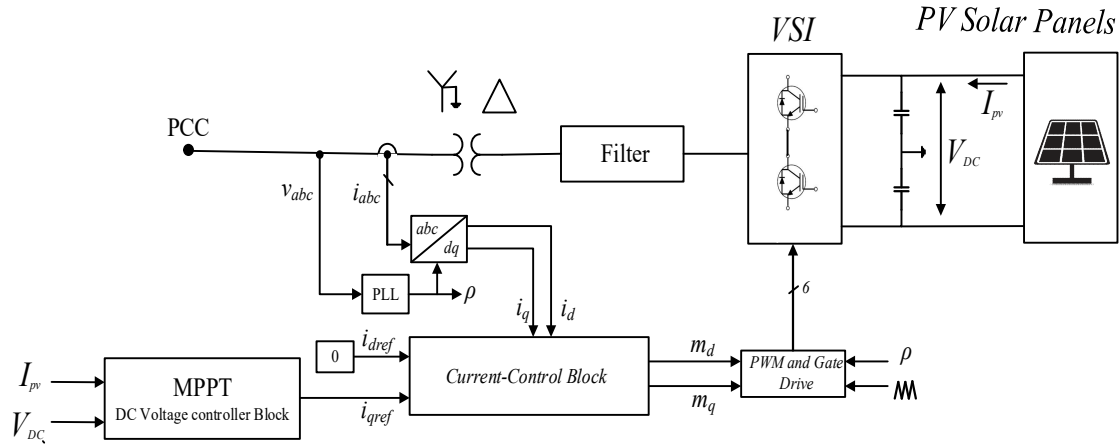
**Figure 2.12: PV solar farm connected at PCC**

## 2.5.1 PV Solar Panel

PV cell, also called solar cell, converts sunlight directly into electricity. The process of converting light (photons) to electricity (voltage) is called the PV effect which was first discovered in 1839 [175]. Due to low output power and voltage, the PV cells need to be connected in series and parallel configuration, called PV panel or PV module, to provide more output power. The output power of a PV panel is nonlinearly influenced by two main factors: solar radiation and temperature [176]. As shown in [176], The increase in solar radiation results in a nonlinear increment in PV panel output while the increment of temperature leads to a nonlinear decrease in PV panel output. Figure 2.13 depicts typical I-V and P-V characteristics of a PV panel for a particular amount of solar radiation and temperature. As shown in Figure 2.13, there is a specific value of voltage at which the output power of the PV panel is maximum ($P_{MAX}$). This voltage is called the maximum power point voltage ($V_{MPP}$).
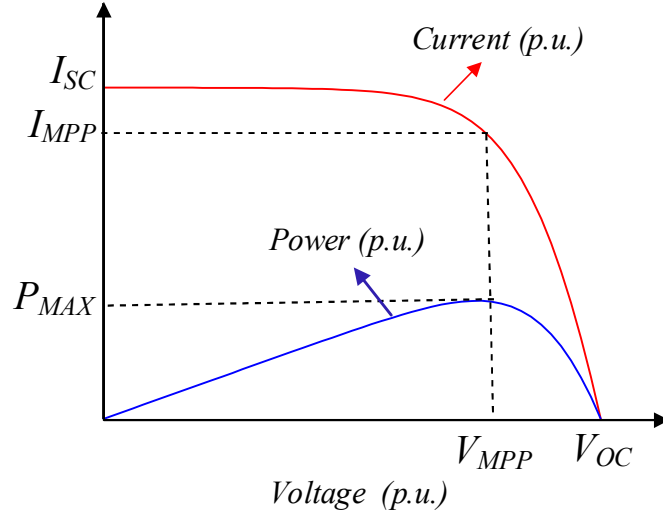
**Figure 2.13: Typical PV solar panel output current and power**

Figure 2.14 depicts the equivalent circuit of the PV cell [176, 177]. This circuit consists of an ideal current source, an antiparallel diode, equivalent parallel resistance ($R_{sh}$), and equivalent series resistance ($R_S$). In Figure 2.14, G denotes the solar radiation, $T$ indicates the temperature, $I_{ph}$ is the photo current, $I_{PV}$ is the cell current, and $V_{PV}$ is the PV cell voltage. As mentioned earlier, the PV panel consists of PV cells in series and parallel configuration. Considering $N_S$ as the number of PV cells in series and $N_P$ the number of PV cells connected in parallel, the output voltage and current of PV panel can be expressed as $V = N_s \times V_{PV}$ and $I = N_P \times I_{PV}$, respectively. The output current of the PV panel can be obtained as follows [176]:

$$I = N_P I_{ph} - N_P I_0 \left[ e^{\frac{q\left(\frac{V_{PV}}{N_s} + R_S \frac{I}{N_P}\right)}{nkT}} - 1 \right] - \frac{N_P V_{PV} + N_S R_s I}{N_S N_P R_{sh}} \qquad (2.54)$$

where $q$ is the charge of the electron ($q = 1.6 \times 10^{-19}$ C), $n$ is the diode ideality factor, $k$ is the Boltzmann's constant ($k = 1.38 \times 10^{-23}$ $j.K^{-1}$), $R_s$ is the PV cell series resistance in $\Omega$, $R_{sh}$ is the PV cell shunt resistance in $\Omega$, and $I_0$ is the reverse saturation current.

The photo current, $I_{ph}$, and the reverse saturation current, $I_0$, can be expressed as follows [176]:

$$I_{ph} = I_{ph(STC)} \frac{G}{G_{nom}} \tag{2.55}$$

$$I_0 = I_{0(STC)} \left(\frac{T_S}{T}\right)^3 e^{((qV_g\{1+K_v(T_2-T_S)\})/(nkT_S T_2))} \tag{2.56}$$

where $G$ is the solar radiation, $G_{nom}$ is the standard solar radiation level, $I_{ph(STD)}$ is the photo current at the standard solar radiation level, $T_s$ is the temperature of standard level, $V_g$ is the energy band gap, and $K_v$ is temperature coefficient at open circuit voltage.
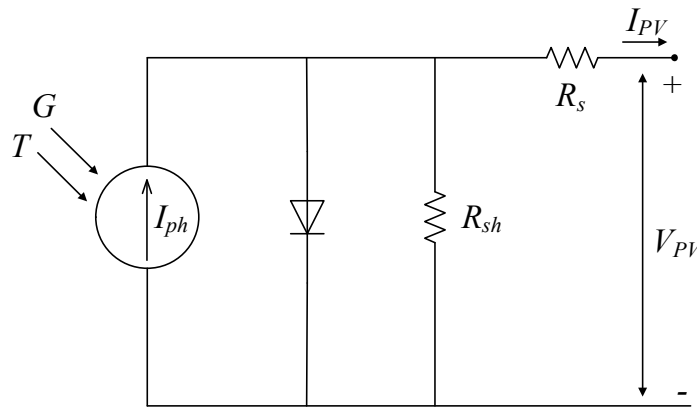


**Figure 2.14: Equivalent circuit of PV cell**

## 2.5.2 Inverter

The PV solar farm inverter converts DC power generated by PV panels to ac power for being injected to the grid. There are two types of inverter used in PV solar systems: Voltage Source Inverter (VSI), and Current Source Inverter (CSI) [108]. The VSI has a capacitor in its dc side and the polarity of dc side voltage remains the same. The direction of inverter average power flow is specified by the polarity of the dc side current [108]. VSI has been used widely, in comparison to CSI, in power system applications and PV solar farms [108].

The PV voltage source inverter comprises six Insulated Gate Bipolar Transistor (IGBT). A large dc capacitor is employed to hold the dc voltage approximately constant at the DC side of the inverter [178]. Various technologies such as Sinusoidal Pulse Width Modulation (SPWM), Space Vector PWM (SVPWM), or Multilevel Selective Harmonic Elimination (SHE) techniques are used to generate the firing pulses for IGBTs in the inverter. Among

all these techniques, the SPWM technique is widely used for high power PV inverter applications [108].

## 2.5.3 Filter

The filter attenuates the VSI ac side switching ripple and provides current and voltage with low distortion for the system through a coupling transformer [179]. Different filter configurations can be used at the inverter output. Among them, L filter is comprised of only a series inductor, LC filter is constituted of a series inductor with a shunt capacitor [180], while the LCL filter includes two series inductors and one capacitor in T configuration [181]. The LCL filter is recommended for grid-connected applications [179]. In this thesis, the LCL filter is chosen to reduce the VSI output switching ripple and provide current and voltage with low distortion to the load. Both LC and LCL filter present resonance phenomena at their characteristic frequency which can cause transient distortions and steady state harmonics around the LC resonant frequency or even affect the overall system stability. This resonance can be suitably damped through a proper resistor, to be placed either in parallel or in series with the inductor or the capacitor. Conventional schemes put this resistor in series with the capacitor [181, 182].

In modeling the filter certain conditions are considered to: (i) avoid excessive voltage drop across the inductors, (ii) maintain better controllability of output current and, (iii) suppress the ripple in the ac side current. These conditions are as follows [181]:

a) The capacitor size should be limited such that it can exchange a maximum reactive power of no more than 5% of the rated active power in order to maintain almost unity power factor.

b) The total value of inductance should be around 0.1 p.u. to limit the ac voltage drop during operation. Otherwise, a higher dc link voltage is required to ensure current controllability.

c) The resonant frequency should be in the range between 10 times the line frequency and one-half of the switching frequency, to avoid amplification of unwanted harmonics in the lower parts and upper parts of the harmonic spectrum.

Figure 2.15 depicts the single phase circuit of an LCL filter [181, 182] where $L_i$ and $R_i$ are the inverter side inductor and resistance, respectively; $L_g$ and $R_g$ are the grid side inductor and resistance, respectively; $C_f$ and $R_f$ are the capacitor filter and damping resistance, respectively.
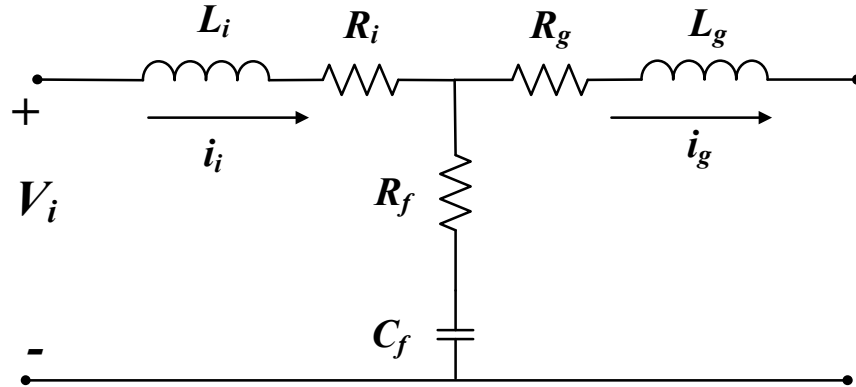


**Figure 2.15: Sigle phase LCL filter circuit**

The values of LCL filter components are calculated through the following equations which are adopted from [181-183]. As stated above, the reactive power of filter capacitor should be less than 5% of the nominal power [181-183]. Therefore, it is important that $C_f$ satisfies the following condition:

$$C_f \leq 0.05 \frac{P_n}{\omega_n E_n^2} \tag{2.57}$$

where $P_n$ is the rated active power, and $E_n$ is line to line RMS voltage. $L_i$ and $L_g$ are obtained as follows:

$$L_i = \frac{V_{DC}}{6 f_{sw} \Delta I_{Lmax}} \tag{2.58}$$

$$\Delta I_{Lmax} = 0.1 I_{max} \tag{2.59}$$

$$I_{max} = \frac{P_n \sqrt{2}}{3 V_{ph}} \tag{2.60}$$

$$L_g = rL_i \tag{2.61}$$

where $V_{DC}$ is DC side voltage, $f_{sw}$ is switching frequency, $\Delta I_{Lmax}$ is the maximum peak to peak current ripple, and $I_{max}$ is the rated current, $V_{ph}$ is the phase voltage, and $r$ is the constant between inverter side inductor and grid side inductor. The resonance frequency is obtained as follows:

$$f_{res} = \frac{1}{2\pi} \sqrt{\frac{L_i + L_g}{L_i L_g C_f}} \tag{2.62}$$

The obtained resonance frequency must satisfy the following condition:

$$10f_0 < f_{res} < 0.5f_{sw} \tag{2.63}$$

Where $f_g$ is the grid frequency. The damping resistance is calculated as follows:

$$R_f = \frac{1}{3\omega_{res}C_f} \tag{2.64}$$

## 2.5.4 Transformer

The transformer in the PV solar system is a step-up transformer to connect the PV system having a low-voltage level to the grid having a high-level voltage. This transformer also works as an isolation transformer to provide galvanic separation of the PV solar system. The Delta-Wye configuration of transformer is widely used in PV solar system for providing galvanic isolation and performing as a harmonic filter for zero-order harmonics. Due to utility connection requirement, the PV side coupling transformer is Delta, while the grid side coupling transformer is Wye grounded. The Delta winding in the PV side allows the zero-order harmonics (3rd, 9th,…) to circulate, and prevents them from flowing into the grid [184, 185].

## 2.6　Conventional PV Inverter Control System

The general schematic of the conventional PV inverter controller is shown in Figure 2.12 which includes *abc* to *qd* transformer block, Phase Locked Loop (PLL) block, current controller, and DC voltage controller. The different components of PV inverter controller are explained in following subsections.

### 2.6.1 *abc* to *dq* Transformation

In this thesis, the PV inverter control is based on *dq*-reference frame model of VSI. In *abc*-frame, controller variables such as references, feedback signals are sinusoidal and high order compensation is, consequently, needed to attain zero steady state error [108]. Therefore, the design of the controller can be complicated. In *dq*-frame, the sinusoidal variables are transformed to dc variables under steady state condition which allows utilization of low order compensator and therefore makes the controller design simpler [108]. Figure 2.16 illustrates the phasor diagram of *dq*-frame with respect to *abc*-frame transformation, while the *q*-axis is leading the *d*-axis [165]. In Figure 2.16, $f$ denotes an electrical space vector such as voltage, or current; $\theta$ is the angle between *q*-axis and *a*-axis, $\omega$ is the rotational speed of the synchronous frame.
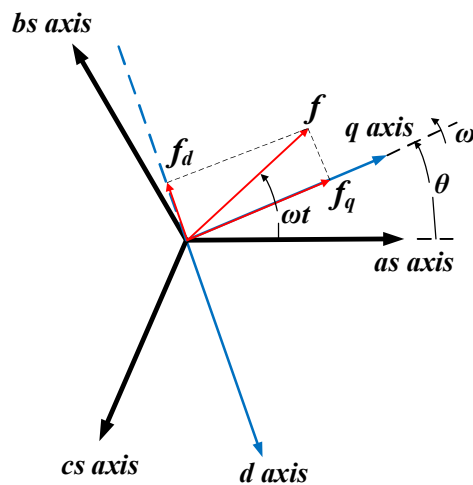


**Figure 2.16 *abc* to *dq* transformation phasor diagram**

The transformation of variables from *abc*-frame to *dq*-frame can be expressed as follows [165]:

$$f_{qd} = K f_{abc} \tag{2.65}$$

where

$$(f_{abc})^T = [f_a \ f_b \ f_c] \tag{2.66}$$

$$(f_{qd})^T = [f_q \ f_d] \tag{2.67}$$

$$K = \frac{2}{3} \begin{bmatrix} \cos\theta & \cos(\theta - \frac{2\pi}{3}) & \cos(\theta + \frac{2\pi}{3}) \\ \sin\theta & \sin(\theta - \frac{2\pi}{3}) & \sin(\theta + \frac{2\pi}{3}) \end{bmatrix} \tag{2.68}$$

$$\omega = \frac{d\theta}{dt} \tag{2.69}$$

Therefore, the space vector $\vec{f}$ can be defined in $dq$-frame by

$$\vec{f} = f_q - j f_d \tag{2.70}$$

## 2.6.2 Phase Locked Loop (PLL)

To convert the variables from $abc$-frame to $dq$-frame, the angle between $q$-axis and $a$-axis, $\theta$, is required. Therefore, a phase locked loop (PLL) block is utilized to obtain $\theta$. PLL is a common method of extracting phase angle and frequency in FACTS devices and inverter-based energy sources. In PV system, the PLL is used by PV controller to synchronize PV system with grid and control the plant. Figure 2.17 depicts the schematic diagram of PLL [108] which includes an $abc/dq$ block, a voltage-controlled oscillator block (VCO), a saturation block, and a compensator block. PLL utilizes the PCC voltage to extract the phase angle. $V_{abc}$ is converted to $V_{dq}$ by $abc/dq$ block. The PLL tries to regulate the rotational angle of $dq$-frame ($\rho$) at $\theta$. Therefore, ($\rho$) is controlled by $H(s)$ in a way that $V_d$ becomes zero. $V_d = 0$ happens when $\rho = \theta$ [108]. In this thesis, a PI controller is used as compensator [108]. The output of compensator is passed through the saturation block to limit $\omega$ within $\pm 377$ rad/s. The VCO block is a resettable integrator which resets if its output reaches $2\pi$.
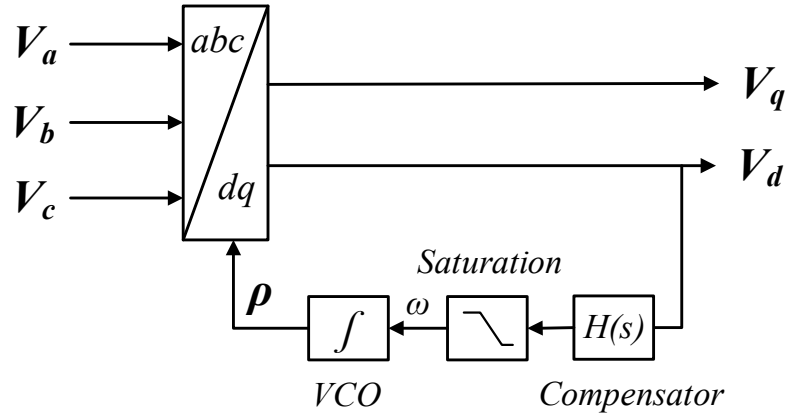
**Figure 2.17: PLL schematic diagram**

## 2.6.3 Current Controller

The function of the current-control loop is to regulate the active and reactive components of the ac side current of VSI by using sinusoidal pulse width modulation (SPWM) strategy [108]. The active and reactive power of inverter in $dq$-frame can be obtained as follows:

$$P = \frac{3}{2}\left(V_q I_q + V_d I_d\right) \tag{2.71}$$

$$Q = \frac{3}{2}\left(V_q I_d - V_d I_q\right) \tag{2.72}$$

where $V_q$, $V_d$, $I_q$, and $I_d$ are the inverter ac side voltage and current at $dq$-frame. (2.71) and (2.72) show that $P$ and $Q$ are coupled in $dq$-frame. However, if the voltage vector ($V$) for $dq$-frame model is aligned with the quadrature axis by PLL, $V_q$ equals $V$ and $V_d$ equals zero. Consequently, (2.71) and (2.72) can be expressed as follows:

$$P = \frac{3}{2}V_q I_q \tag{2.73}$$

$$Q = \frac{3}{2}V_q I_d \tag{2.74}$$

Thus, the reactive and active powers of VSI are independently controlled through the $d$-axis and $q$-axis loops, respectively.

Dynamics of VSI ac-side are depicted in Figure 2.18 .The dynamic model of VSI inverter ac side current in $dq$-frame can be written as follows:

$$L_S \frac{di_d}{dt} = -(R_s + r_{on})i_d + L_s\omega\, i_q + m_d\left(\frac{V_{DC}}{2}\right) - v_d \tag{2.75}$$

$$L_S \frac{di_q}{dt} = -(R_s + r_{on})i_q - L_s\omega\, i_d + m_q\left(\frac{V_{DC}}{2}\right) - v_q \tag{2.76}$$

where $L_s$ is the filter inductance, $R_S$ is the filter resistance, $r_{on}$ is the switched-on resistance of IGBT, $V_{DC}$ is the inverter dc side voltage, $m_d$ and $m_q$ are the $d$-axis and $q$-axis components of modulating signal, respectively.
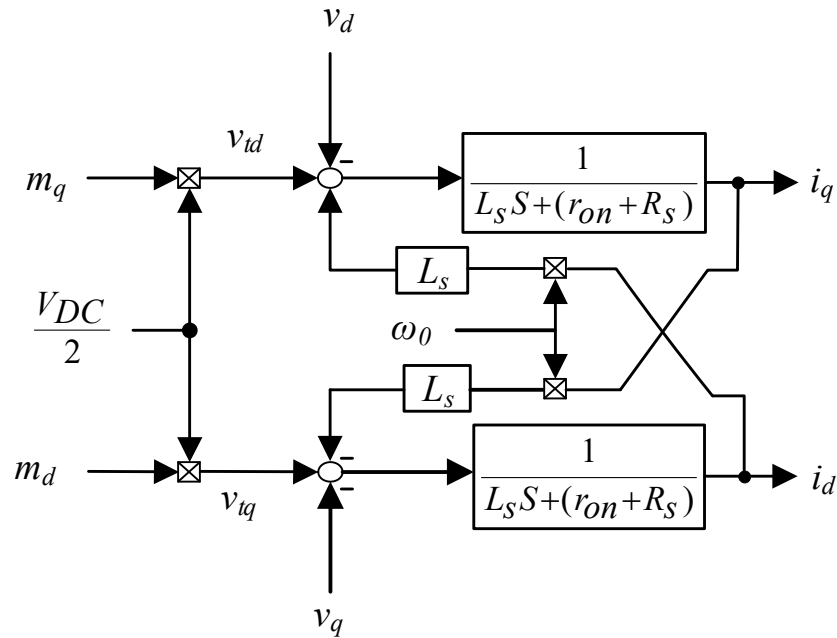


**Figure 2.18: VSI ac-side current dynamic model**

(2.75) and (2.76)show that the dynamics of $i_d$ and $i_q$ are coupled. The decoupling of $i_d$ and $i_q$ dynamics can be achieved by considering $m_d$ and $m_q$, the output of the current controller, as:

$$m_d = \frac{(U_d - L_s \omega i_q + V_d)}{V_{DC}/2} \tag{2.77}$$

$$m_q = \frac{(U_q + L_s \omega i_d + V_q)}{V_{DC}/2} \tag{2.78}$$

Substituting (2.77) and (2.78) in (2.75) and (2.76) we deduce

$$L_S \frac{di_d}{dt} = -(R_s + r_{on})i_d + U_d \tag{2.79}$$

$$L_S \frac{di_q}{dt} = -(R_s + r_{on})i_q + U_q \tag{2.80}$$

In (2.79) and (2.80), the dynamics if $i_d$ and $i_q$ are decoupled and they can be controlled independently by $U_d$ and $U_q$, respectively. The current-control loop as an inner loop is shown in Figure 2.19. According to Figure 2.19, $i_d$ and $i_q$ are first compared with their reference values $i_{d\text{-}ref}$ and $i_{q\text{-}ref}$. The error signals are then processed by Proportional Integral (PI) controllers, and their corresponding outputs ( $U_d$ and $U_q$) are augmented with the decoupled feed-forward signals [108]. A decoupled feed-forward technique is utilized to decouple the dynamics of $d$-axis and $q$-axes and improve the disturbance rejection ability of the closed-loop system [108]. The resulting signals are normalized to produce the modulating indices $m_d$ and $m_q$, which represent the $d$-axis and $q$-axis components of the three-phase PWM modulating signal ($m_{abc}$) respectively. Finally, $m_d$ and $m_q$ are converted to $m_{abc}$ and compared with a high-frequency triangular wave to generate the proper IGBT switching signals (Figure 2.12 ).
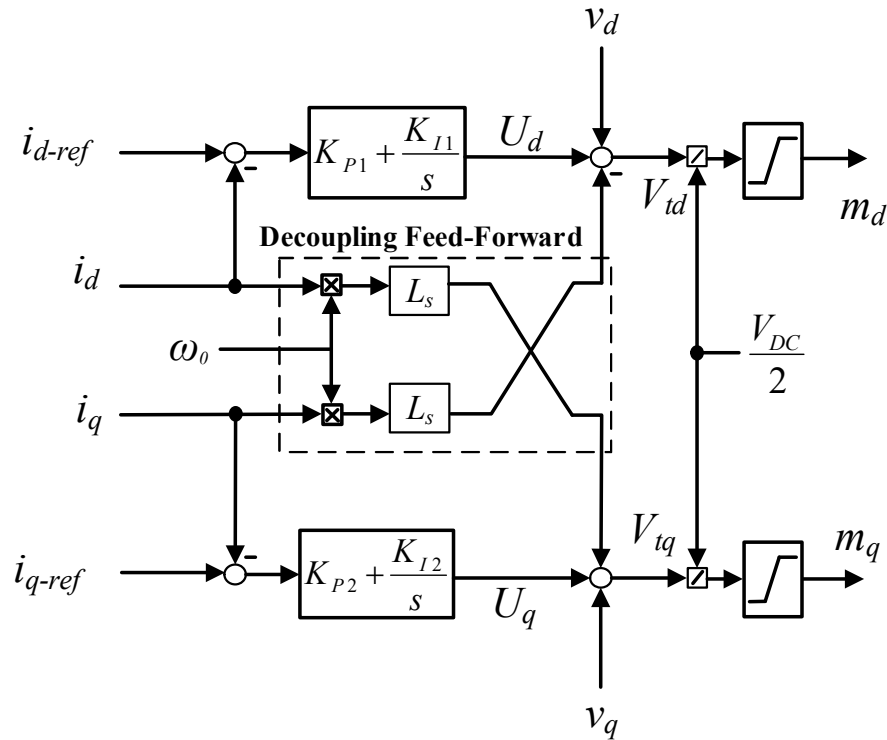
**Figure 2.19: Current control block diagram**

## 2.6.4 DC Voltage Controller

As described in section *2.5.1* the output power of PV panel depends on the dc voltage across it. Therefore, the DC voltage controller controls the PV system output active power by adjusting the dc side voltage. Figure 2.20 illustrates the block diagram of DC voltage controller. It is comprised of the MPPT block, and a PI controller. The MPPT block produces $V_{dc-ref}$ to control the active power generated by PV solar farm. The measured dc voltage is compared with $V_{dc-ref}$ to create an error signal. The PI controller processes this error signal and generates the $q$-axis reference $i_{q-ref}$ for the current loop controller.
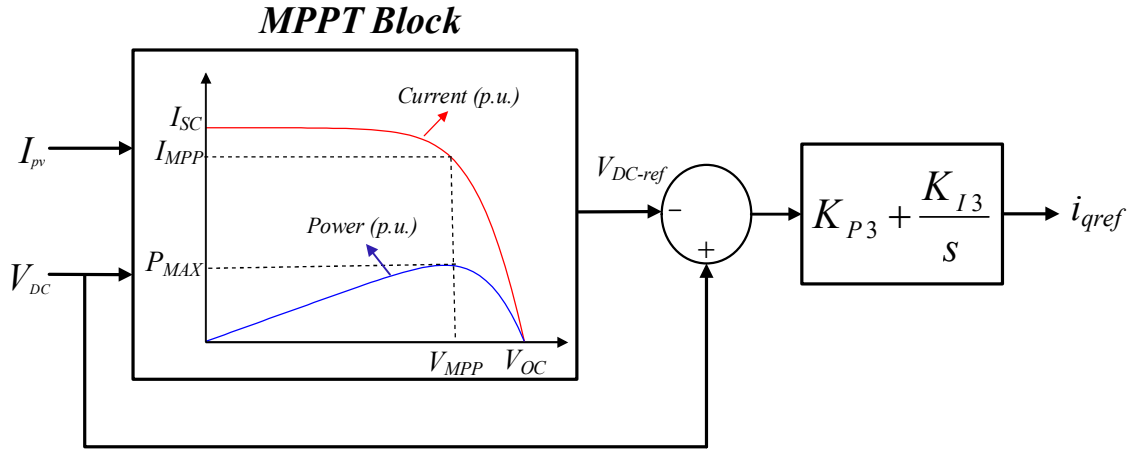
**MPPT Block**



**Figure 2.20: Block diagram of DC voltage controller**

## 2.6.4.1   MPPT Algorithm

The MPPT block produces the reference voltage ($V_{dc\text{-}ref}$) for DC voltage controller in a way that maximum power can be extracted from the PV panels. The MPPT block is simulated based on an incremental conductance algorithm [186-188]. Figure 2.21 depicts the flowchart of the algorithm of MPPT process. The MPPT block monitors the current and voltage of PV panels in a specific time period known as time step. The time step is chosen to be 0.2 sec in this thesis. Then, the deviation of voltage ($dV$) and the deviation of current ($dI$) are calculated. Two scenarios can then happen based on voltage deviation.

In the first scenario, if there is no change in voltage and $dV = 0$, the deviation of current will be examined. If the $dI$ is also zero, it means that PV panels are working at their maximum power point (MPP) and there is no need for changing voltage. But if $dI$ is not zero, it means that PV panels is not working at its MPP. Therefore, a small step change ($\pm delV$) is made in voltage based on the sign of $dI$. $delV$ is selected to be $5$ V in this thesis. This process continues until the PV system reaches its MPPT condition [188].

In the second scenario, $dV$ is not zero. So, it examines the following relation, first:

$$\frac{dI}{dV} + \frac{I_{PV}}{V_{DC}} = 0 \qquad (2.81)$$

If 2.81 is true, it means that the PV panels are operating at MPP. Otherwise, PV panels do not generate their maximum power and their voltage needs to be changed by a step deviation (±*delV*) based on the sign of 2.81. This process continues until reaching the MPP condition of PV panels [188].
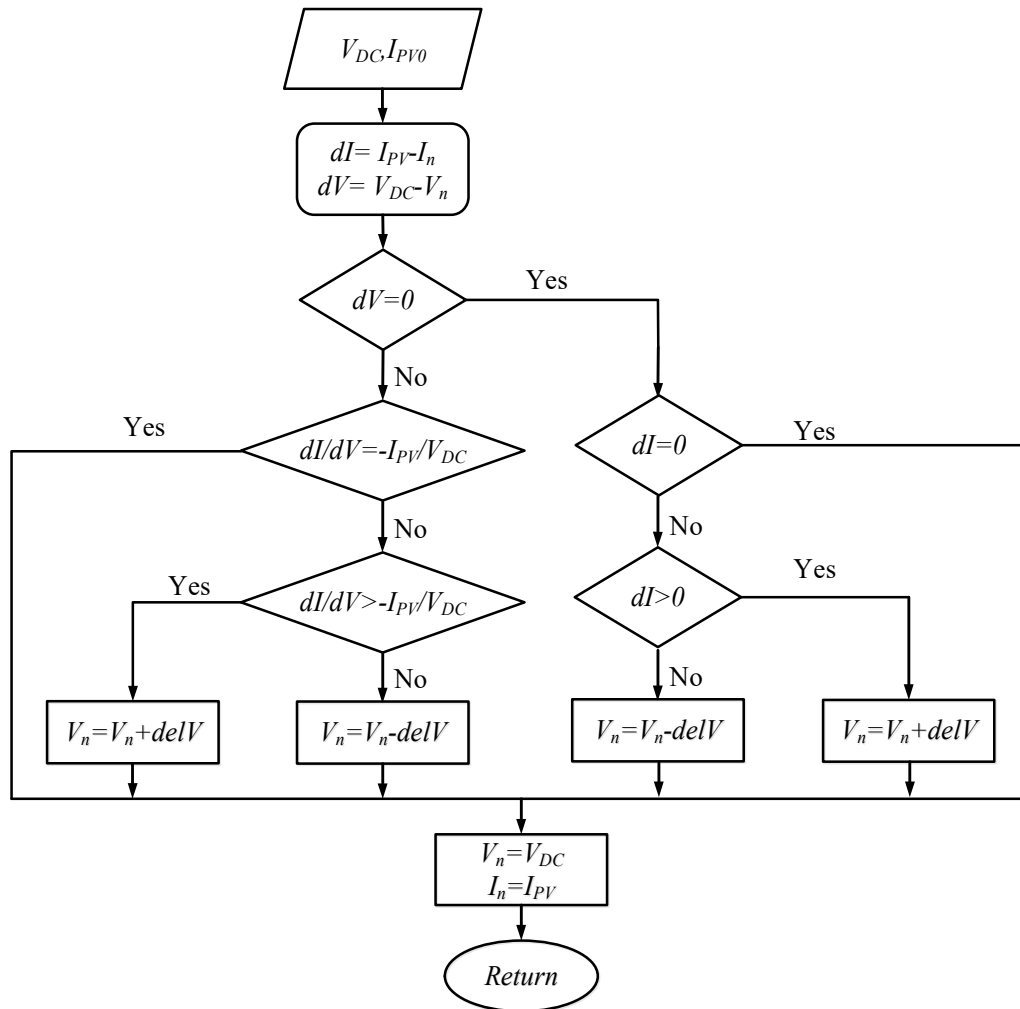


**Figure 2.21 MPPT algorithm flowchart [188]**

## 2.6.5 Conventional Reactive Power Controller

Conventionally, PV solar farm operates at unity power factor. In this mode of operation of the PV solar farm, the MPPT block adjusts dc side voltage to $V_{MPP}$ to generate maximum active power while reactive power generation is zero. As the voltage vector in *dq*-frame is aligned with the quadrature axis and $V_d$ equals zero; zero reactive power generation can be achieved when $i_d$ equals zero, per (2.74). Consequently, $i_{dref}$ is zero in Figure 2.12.

## 2.7   PV-STATCOM Controller

Figure 2.22 depicts a PV solar system with the proposed PV-STATCOM controller. The proposed PV-STATCOM controller is designed for damping SSO in the series compensated transmission system. The PV-STATCOM controller includes a subsynchronous damping controller and a power point tracking (PPT) block as a part of the DC voltage controller.
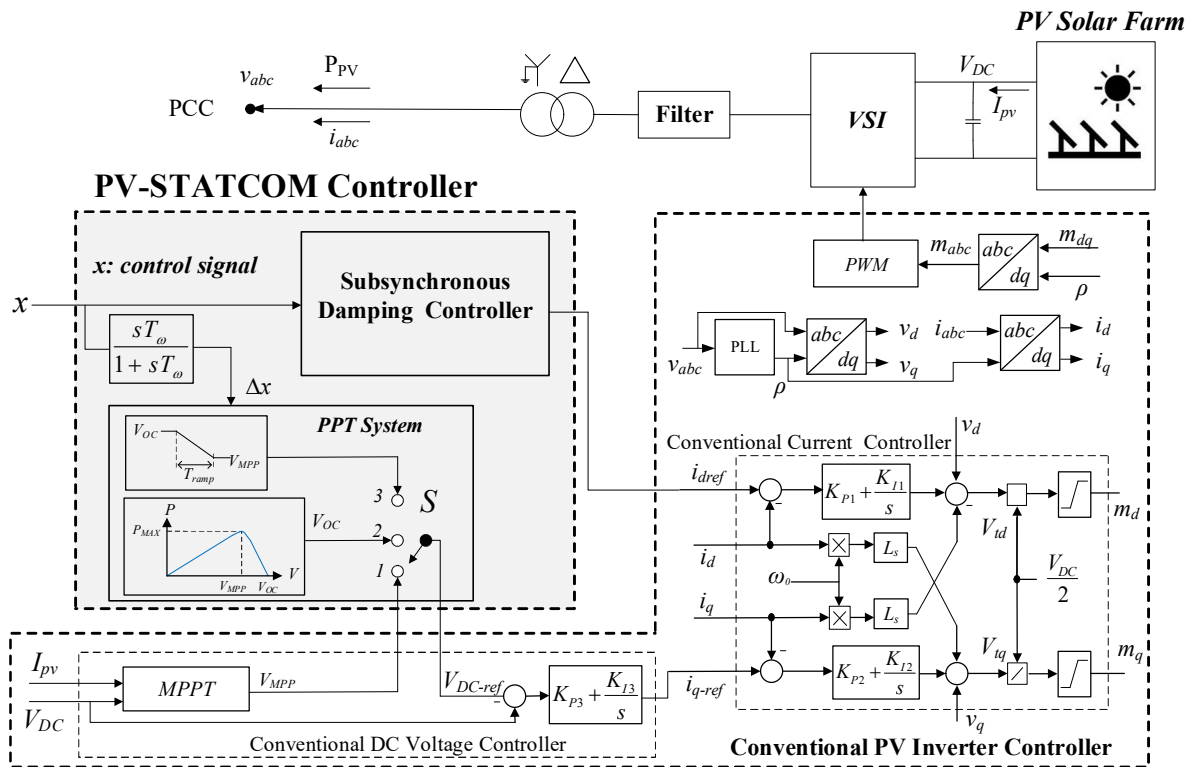


**Figure 2.22: PV solar farm plant with PV-STATCOM controller**

## 2.7.1 Subsynchronous Damping Controller

The subsynchronous damping controller provides SSO damping through dynamic reactive power control. It utilizes a control signal as input and extracts information about subsynchronous oscillations from it. Then, the damping controller generates $i_{def}$ in a manner that the corresponding VSI reactive power exchange can damp the subsynchronous oscillations in the system. The control signal can be any one of generator speed ($\omega$), current of the line, active power flow of the line, etc.

## 2.7.2 Power Point Tracking (PPT) System

The power point tracking (PPT) system, as a part of the new DC voltage controller, controls the active power generation of PV system by controlling the dc side voltage to provide the needed VSI capacity for the damping controller.

The flow chart of PPT system for PV-STATCOM operation is portrayed in Figure 2.23. This flowchart is written for the case when generator speed ($\omega$) is selected as the control signal, however, it applies for any other control signals as well. The PPT block constantly monitors if the system is operating in a healthy manner and no SSO are initiated i.e., the rotor speed deviation $\Delta\omega$ is less than a pre-specified quantity which is chosen to be 1 rad/sec, in this work. In this case, Full PV-STATCOM mode is not activated and the system operates in normal PV power generation mode with $V_{DC-ref}$ sets to $V_{MPP}$, and the switch $S$ stays at position 1 (Figure 2.22). If SSO are caused due to any system disturbance or fault, and the rotor speed deviation $\Delta\omega$ exceeds 1 rad/sec, Full PV-STATCOM mode is initiated. This is accomplished by changing switch $S$ from position $1$ to position 2 and setting $V_{dc-ref}$ to $V_{oc}$ which is the open circuit voltage of the solar panels. The active power generated by the solar panels is made to go to zero and the entire inverter capacity is released for STATCOM operation to damp SSO.

Once SSO are mitigated, i.e., $\Delta\omega$<1 rad/s, the DC voltage controller gradually restores normal solar power generation by decreasing the dc voltage to its pre-fault value $V_{MPP}$ in a ramped manner. For this purpose, the dc controller switches to position 3 of switch $S$ and decreases dc side voltage ($V_{OP}$) from $V_{OC}$ to $V_{MPP}$ gradually in a specific time ($T_{ramp}$). Simultaneously, the Partial PV-STATCOM mode is enabled. In this mode while the real power generation is being ramped up, damping of SSO is continued with the inverter capacity remaining after real power generation. This ensures that the PV power can be restored to its pre-fault value without causing any recurrence of SSR. This ramp-up of power with damping controller in operation is another novel contribution of this thesis. Once $V_{dc}$ becomes equal to $V_{MPP}$, the partial PV-STATCOM operation is disabled and Full PV power generation is resumed.
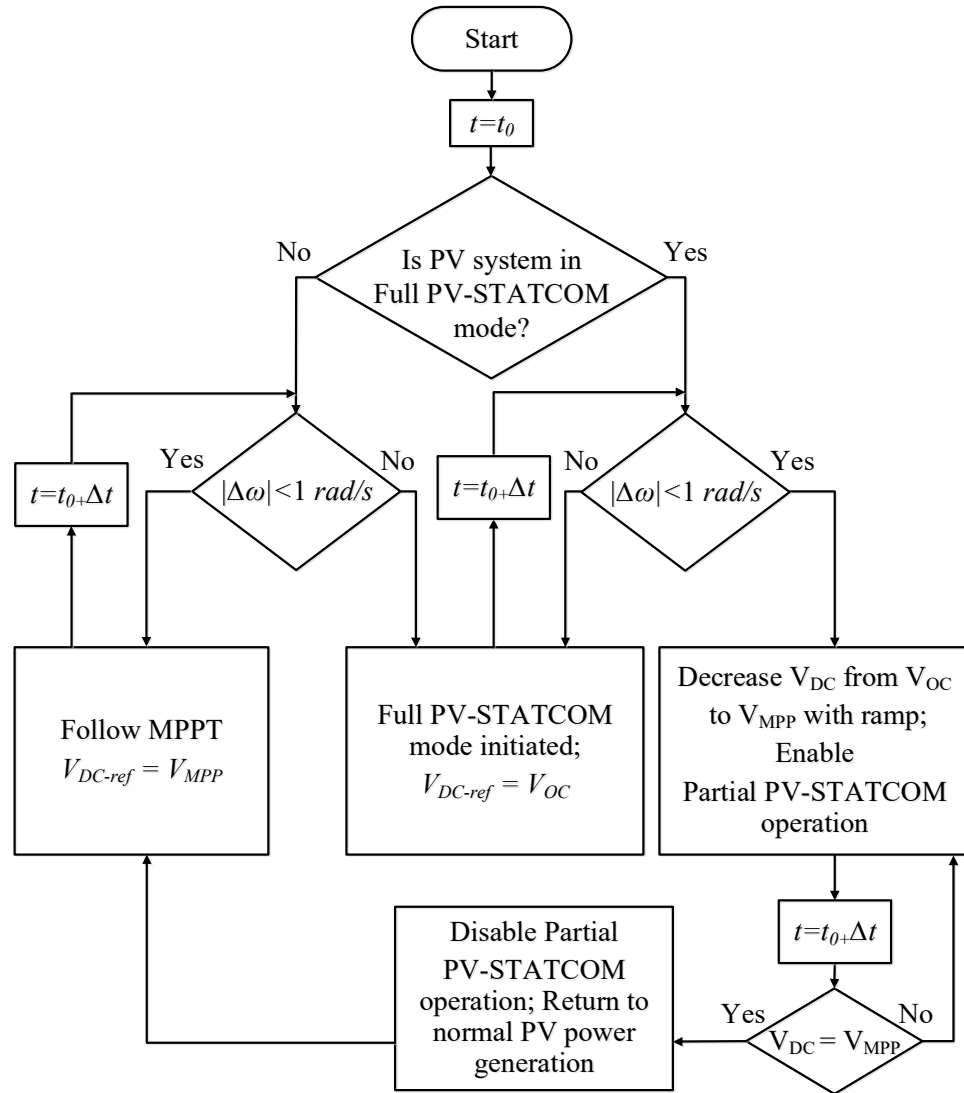
**Figure 2.23: Flowchart of the PPT system (DC voltage controller operation)**

## 2.8 Small-Signal Stability Analysis

Small-signal stability is the ability of the power system to maintain stability when the system is subjected to small disturbances [168]. In small-signal stability analysis, the stability and inherent dynamic characteristics of the power system can be obtained by using linearization techniques and eigenvalue analysis. This information facilitates the design of controllers and their integration into the dynamics of the plant [168, 189].

The behavior of any dynamic system can be expressed by $n$ first-order nonlinear equations as follows [168] :

$$\dot{X} = f(X, u) \tag{2.82}$$

$$y = g(X, u) \tag{2.83}$$

where,

$$X = [x_1 \ x_2 \ x_3 \ ... \ ... \ x_n]^T$$

$$u = [u_1 \ u_2 \ u_3 \ ... \ ... \ u_r]^T$$

$$y = [y_1 \ y_2 \ y_3 \ ... \ ... \ y_m]^T \tag{2.84}$$

$$g = [g_1 \ g_2 \ g_3 \ ... \ ... \ g_m]^T$$

In (2.84), $n$ is the order of the system, $r$ is the number of system input, $m$ is the number of system output, $X$ is state vector which consists of system state variables ($x_i$), $u$ is the input vector, $y$ is the output vector, and $g$ is a vector of nonlinear functions which relates state and input variables to output variables.

The nonlinear equations (2.82) and (2.83) can be linearized around a steady state operating point and written as follows:

$$\Delta\dot{X} = A\Delta X + B\Delta u \tag{2.85}$$

$$\Delta y = C\Delta X + D\Delta u \tag{2.86}$$

where $A$ is the state matrix of size $n \times n$, $B$ is the input matrix of size $n \times m$, $C$ is the output matrix $m \times n$, $D$ is the feedforward matrix of size $m \times r$. The eigenvalues of the linearized system can be obtained from solving the following equation:

$$\det(sI - A) = 0 \tag{2.87}$$

The values of $s$ which satisfy (2.87) are the eigenvalues of the system which provide information related to the stability and dynamic characteristics of the system such as [168, 189]. If the linearized form of the nonlinear system is stable, the nonlinear system is also

stable at the operating point at which the system has been linearized [189]. In this thesis, the linearization toolbox of MATLAB is used to obtain the state-space model and eigenvalues of the study systems which are modeled in MATLAB/Simulink.

## 2.8.1 Investigation of Subsynchronous Oscillation in Synchronous Generator

Figure 2.1 depicts the IEEE First SSR Benchmark system in which an 892-MW synchronous generator is connected to the infinite bus through a 500-kV series compensated transmission line. The parameters of IEEE First SSR Benchmark system are presented in Appendix A. This radial system produces subsynchronous resonances with four torsional modes: 15.71 Hz (Mode 1), 20.21 Hz (Mode 2), 25.55 Hz (Mode 3), and 32.28 Hz (Mode 4) [112]. Each of these modes has its largest destabilization at a specific series compensation level. Series compensation level ($k$) is defined as:

$$k = \frac{X_C}{X_T + X_l + X_{sys}}$$  (2.88)

where $X_C$ is the series capacitive reactance, $X_T$ is the transformer reactance, $X_l$ is the transmission line reactance, and $X_{sys}$ is the equivalent system reactance at the infinite bus. Figure 2.24 depicts the real part of unstable eigenvalues of torsional modes obtained by utilizing the linearization toolbox of MATLAB software. It shows that each torsional mode has its largest destabilization at a certain compensation level:  Mode 1 (67.4%), Mode 2 (54.3%), Mode 3 (40.9%), and Mode 4 (26.4%). Table 2.1 shows the eigenvalues of the system for four critical compensation levels. Figure 2.24 and Table 2.1 show that the system has eigenvalues with positive real part for some compensation level and is consequently unstable at these compensation levels.
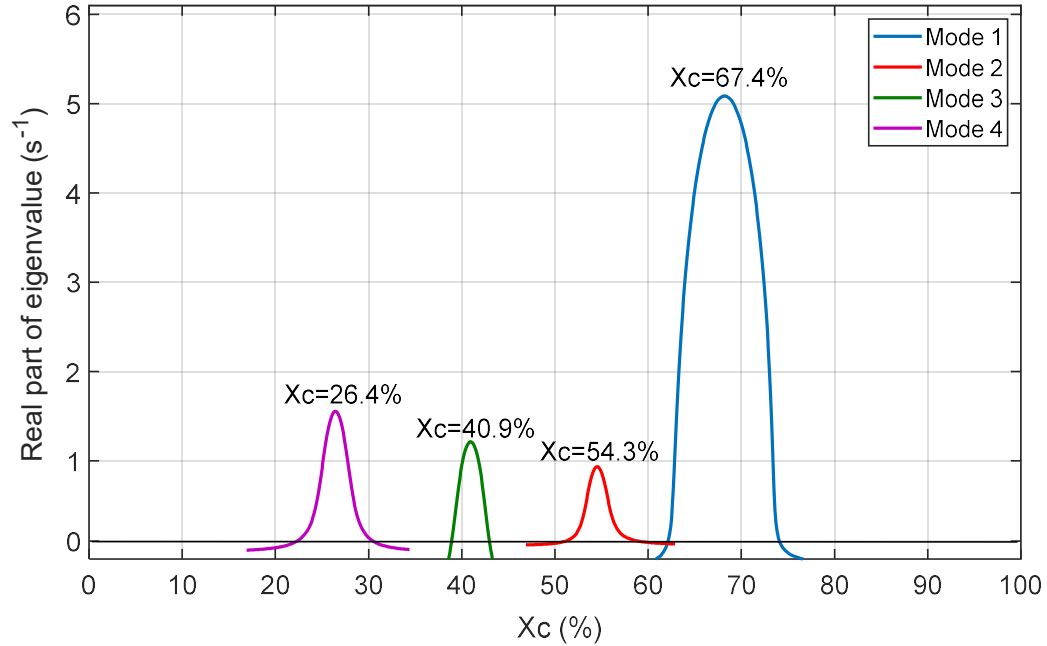
**Figure 2.24: The real part of unstable eigenvalues of torsional modes for the IEEE's First SSR Benchmark System**

It is noticed from Table 2.1, that at each critical compensation level, the frequency of subsynchronous mode is close to the frequency of one of the torsional modes and thus makes the corresponding torsional mode unstable.

**Table 2.1: Eigenvalues of the system for critical compensation levels**

| Modes | Compensation Level (%) | | | |
|---|---|---|---|---|
| | 26.4 | 40.9 | 54.3 | 67.4 |
| 0 | -0.459 ± 8.88 j | -0.557±9.78j | -0.693±10.80j | -0.89±12.065j |
| 1 | -0.181 ±99.22j | -0.18±99.45j | -0.175±100.05j | 5.18±98.81j |
| 2 | -0.03 ±127.03j | -0.029±127.07j | 0.983±126.93j | -0.028±126.98j |
| 3 | -0.396 ±160.7j | 1.32±160.43j | -0.403±160.41j | -0.407±160.5j |
| 4 | 1.51 ± 202.84j | -0.072±202.77j | -0.077±202.85j | -0.078±202.88j |
| 5 | -0.449± 298.18j | -0.449±298.18j | -0.44±298.18j | -0.44±298.18j |
| Network-1 (Sub) | -4.32± 202.77j | -3.704±160.33j | -2.102±126.77j | -5.424±98.7j |
| Network-2 (Super) | -4.964±551.23j | -5.061±594.02j | -5.1±627.38j | -5.183±657.00j |

Time domain investigation of SSR in synchronous generator is now performed using EMTDC/PSCAD software. A three-line-to-ground (3LG) fault for five cycles is initiated at Bus B at $t = 5\ sec$. This fault study is performed for the most critical level of series compensation ($k = 67.4\%$) when the respective torsional oscillatory modes are most undamped, as shown in Figure 2.24.

Figure 2.25 (a)-(c) depict the post-fault behavior of the study system including generator speed ($\omega$), torque between HP-IP ($T_{HP}$), and Fast Fourier transform (FFT) of $T_{HP}$. It is evident from this study that the system becomes highly unstable due to SSR. The system is seen to be unstable due to SSR in $\omega$ and $T_{HP}$. The online FFT block of PSCAD/EMTDC is used to obtain the harmonic magnitude of $T_{HP}$ as a function of time. The FFT analysis of $T_{HP}$ shows that the peak of amplitude happens at frequency of 16 Hz which matches with the results of eigenvalue frequency of 98.81 rad/s,15.73 Hz, of the Mode 1 predicted in Table 2.1. This correlation demonstrates the eigenvalue analysis results in steady state.
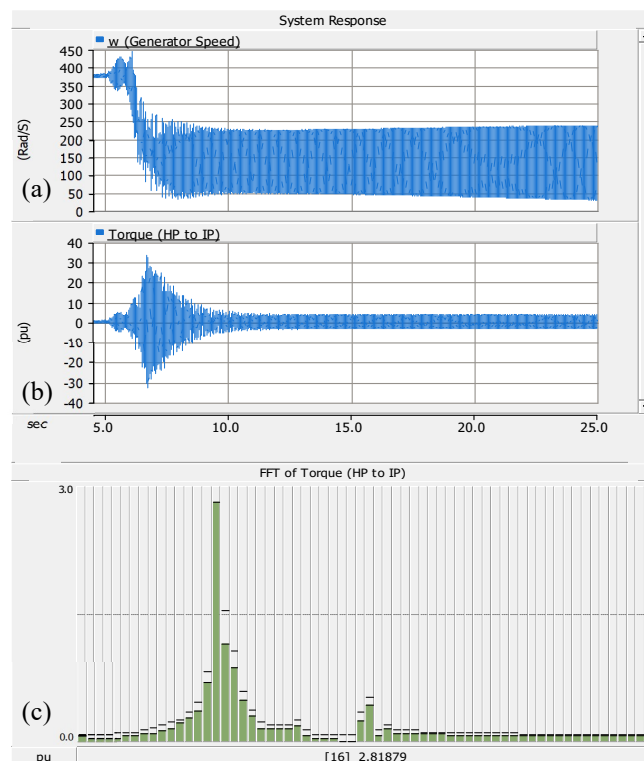


**Figure 2.25: System response while line compensation level is 67.4%**

## 2.8.2 Investigation of Subsynchronous Oscillation in IG-based wind farm

Subsynchronous resonance in IG-based wind farm is comprehensively investigated and explained in [44, 53] for various system conditions. In this section, this phenomenon is investigated for one case study. Figure 2.7 depicts a modified IEEE First SSR Benchmark system in which the synchronous generator is replaced by an IG-based wind farm. Table 2.2 shows the eigenvalues of the system when the size of wind farm in 500 MW and $k =$ 55%, for different wind farm power generation ($P_{WF}$): 100 MW, 300 MW, and 500 MW. This table shows that the system for different wind farm power outputs has an unstable mode with the approximate frequency of 150 rad/s, 24 Hz.

**Table 2.2: Eigenvalues of the system with 500-MW IG-based wind farm, and $k =$ 55%.**

| Modes | Wind farm output power ($P_{WF}$) | | |
|---|---|---|---|
| | 500 MW | 300 MW | 100 MW |
| **Network-1(Sub)** | 0.281± 150.72i | 0.261±150.17i | 0.256±149.92i |
| **Network-2(Super)** | -6.573± 602.49i | -6.558±603.00i | -6.553±603.24i |
| **Electro-mech-1** | -4.31± 30.84i | -3.91±31.53i | -3.738±31.82i |
| **Electro-mech-2** | -59.89± 3.81i | -60.037±2.38i | -60.115±1.04i |
| **Torsional** | -0.617± 3.56i | -0.463±3.53i | -0.412±3.52i |

EMTDC/PSCAD simulation studies are conducted for the case when the 500-MW wind farm generates its rated power, 500 MW, $k =$ 55%, and a three-line-to-ground (3LG) fault is initiated at Bus D (remote from the WF terminals) for 5 cycles at $t =5$ sec. Figure 2.26 (a)-(c) show the post-fault behavior of the system including generator speed ($\omega$), electrical torque ($T_e$), and Fast Fourier Transform (FFT) of $T_e$. The system is seen to be unstable due to growing SSO in $T_e$, and $\omega$. The FFT analysis of $T_e$ shows that the peak torque occurs at the frequency of 24 Hz which matches with the results shown in Table 2.2. This correlation validates the eigenvalue analysis results in steady state.
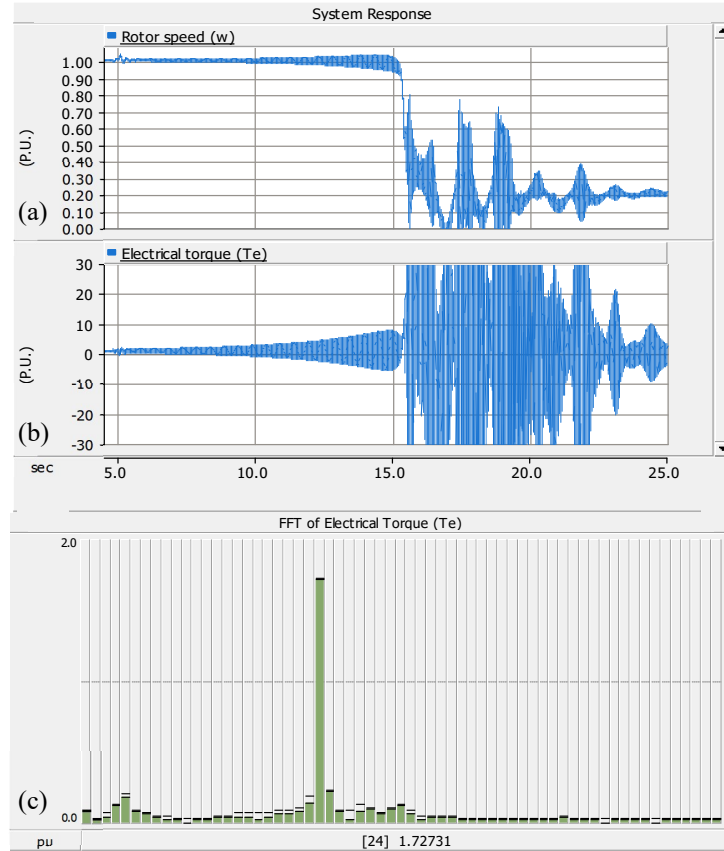
**Figure 2.26: System response for $P_{WF}$=500 MW, and $k$ =55%**

## 2.8.3 Investigation of Subsynchronous Oscillation in DFIG-based windfarm

Subsynchronous resonance in DFIG-based wind farm is mainly due to adverse interaction between the DFIG controller and series compensated transmission system which is termed subsynchronous control interaction (SSCI). SSCI in DFIG-based wind farm is extensively studied in the literature [58-61]. In this section, subsynchronous oscillation in DFIG-based wind farm is studied in MATLAB/Simulink software, for the case which is used in this thesis. Figure 2.9 depicts the series compensated power system which is derived from the IEEE First SSR Benchmark system. In this system, a 100-MW DFIG-based wind farm, comprised of an aggregation of 2-MW units, is connected to a 169-kV series compensated transmission line [58]. The parameters of the system are presented in Appendix A. Table 2.3 depicts the look-up table for the wind speed ($V_{wind}$), the corresponding optimum rotor speed ($\omega_r$), the maximum mechanical power ($P_m$), and corresponding shaft torque ($T_m$) [58, 61].

**Table 2.3: MPPT look-up table for wind speed $V_{wind}$, the rotor speed $\omega_r$ , mechanical power $P_m$, and mechanical torque $T_m$**

| $V_{wind}$ (m/s) | 7 | 8 | 9 |
|---|---|---|---|
| $\omega_r$ (p.u.) | 0.75 | 0.85 | 0.95 |
| $P_m$ (p.u.) | 0.32 | 0.49 | 0.69 |
| $T_m = P_m / \omega_r$ (p.u.) | 0.43 | 0.58 | 0.73 |

Table 2.4 shows the eigenvalues of the system, obtained by linearization toolbox of MATLAB, when the wind speed is 7 m/s and the compensation level is 75% [58]. This table includes network modes (subsynchronous and supersynchronous), electromechanical mode and the shaft mode. It is shown that the subsynchronous mode with frequency of almost 19 Hz is unstable due to having positive real part.

**Table 2.4: Eigenvalues of the system, $V_{wind} = 7$ m/s, and $k = 75\%$.**

| Modes | Eigenvalues |
|---|---|
| **Network-1 (Sub)** | 5.352±121.56i |
| **Network-2 (Super)** | -7.2±630.25i |
| **Electromechanical** | -13.432± 98.69i |
| **Shaft mode** | -1.031 ± 5.94i |

The time domain simulation study is carried out for this case when a three-line-to-ground (3LG) fault is initiated at $t = 5$ sec for 5 cycles. Figure 2.27 (a)-(c) depict the post-fault behavior of the system including rotor speed ($\omega_r$), electrical torque ($T_e$), and Fast Fourier transform (FFT) of $T_e$. Figure 2.27 (a)-(b) show that the $\omega_r$ and $T_e$ are unstable as predicted from eigenvalue analysis in Table 2.4. The FFT analysis of electrical torque, illustrated in Figure 2.27 (c), shows a peak at frequency of 19.33 Hz which matches with the frequency of subsynchronous mode in Table 2.4. This validates the small-signal analysis of the DFIG based study system.
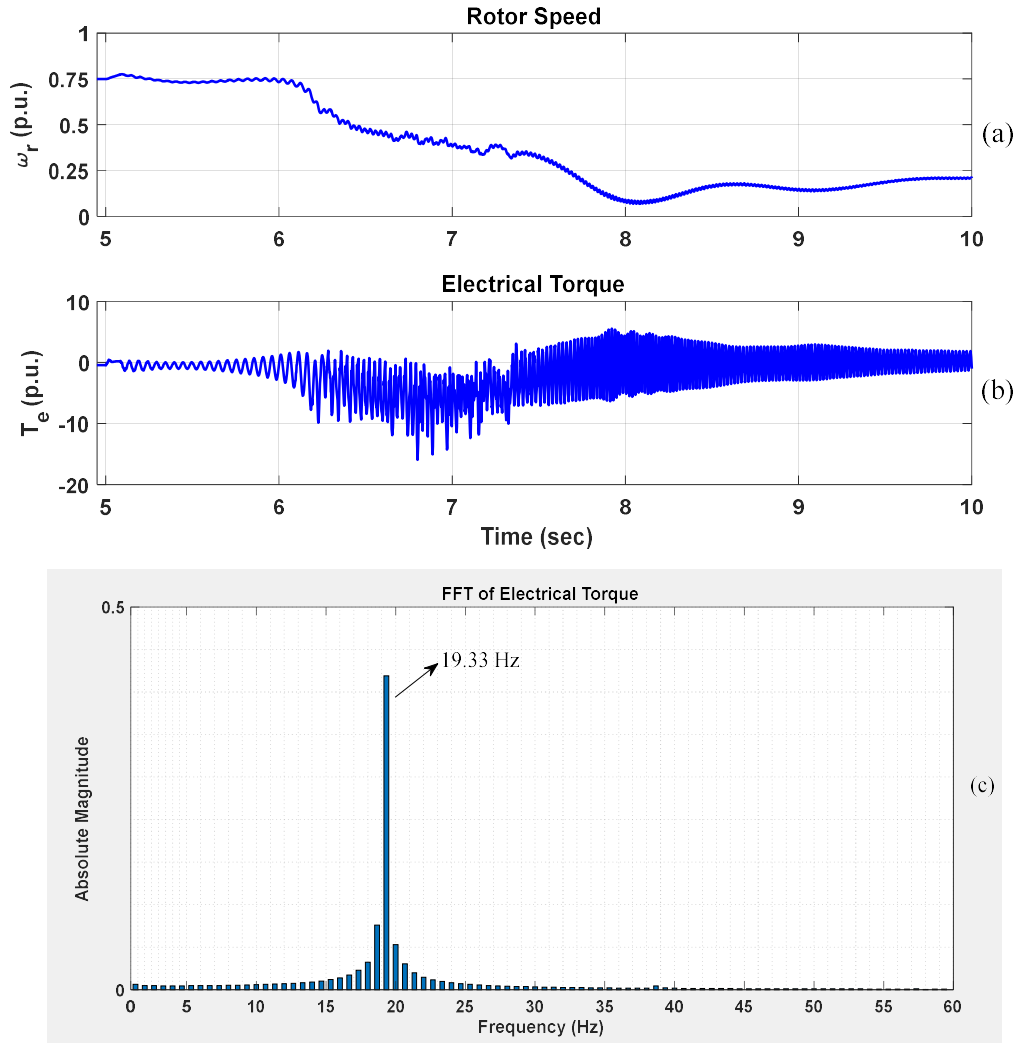
**Figure 2.27: FFT of the electrical torque (T$_e$) while wind speed 7 m/s, and $k$ = 75%**

## 2.9 Conclusion

This chapter describes the model of various power system components which are used in this thesis for SSR mitigation studies. The dynamic model of the IEEE First SSR Benchmark system including synchronous generator with its subcomponents and series compensated transmission line are developed in *dq*-frame. Wind farm models including IG-based wind farm and DFIG-wind farm are presented. The PV solar farm system and its conventional controller are described, and then the proposed PV-STATCOM controller is presented. The SSR phenomena is investigated in the synchronous generator, IG-based wind farm, and DFIG-based wind farm through eigenvalue analysis and validated through

electromagnetic transient simulation in MATLAB/Simulink and PSCAD/EMTDC software.

Chapter 3

# 3    SSR Mitigation with PV-STATCOM connected at Synchronous Generator Terminal

## 3.1  Introduction

This chapter presents a novel control of a large-scale PV solar farm as STATCOM, termed PV-STATCOM, for alleviation of subsynchronous resonance (SSR) in a steam turbine driven synchronous generator connected to a series compensated transmission line. During nighttime, the PV solar farm can operate as a STATCOM with its entire inverter capacity for SSR mitigation. During daytime, if a system fault triggers SSR, the solar farm autonomously discontinues its normal active power generation and releases its entire inverter capacity to operate as PV-STATCOM for SSR prevention. Once the subsynchronous oscillations are damped, the solar farm returns to its normal real power production. Electromagnetic transients studies using EMTDC/PSCAD are performed to demonstrate that a solar farm connected at the terminals of synchronous generator in the IEEE First SSR Benchmark system can damp all the four torsional modes at all the four critical levels of series compensation, and return to normal PV power production in less than half a minute.  This proposed PV-STATCOM technology can either obviate or reduce the need of an expensive FACTS device to accomplish the same objective.

## 3.2   Study System

Figure 3.1 illustrates the study system in which the IEEE First SSR Benchmark system [112] is augmented with a PV solar farm at the generator bus. The mechanical system is modeled fully by its six mass-spring system: the high pressure turbine (HP), the intermediate pressure turbine (IP), the low pressure turbines (LPA and LPB), the Generator (GEN), and the exciter (EXC). The mechanical damping is considered zero in all modes to represent the worst damping condition [81]. This radial system produces subsynchronous resonances with four torsional modes: 15.71 Hz (Mode 1), 20.21 Hz (Mode 2), 25.55 Hz (Mode 3), and 32.28 Hz (Mode 4).

The synchronous generator and the entire network are modeled in EMTDC/PSCAD software according to parameters provided in Appendix A, based on [112]. No AVR is

considered on the synchronous generator [112]. The synchronous generator although rated at 892.4 MVA [112] is operated at 500 MW. However, a 300 MVA PV solar system is connected at generator bus to make the total power generation at the generating end match with that in [112]. The series capacitive reactance ($X_C$) of the system is changed to excite the different torsional modes. The values of $X_C$ (p.u.) for which different torsional modes have their largest destabilization are as follows:  Mode 1 (0.47 p.u.), Mode 2 (0.38 p.u.), Mode 3 (0.285 p.u.), and Mode 4 (0.185 p.u.) [112].

The PV solar system is modeled with an equivalent voltage source inverter (VSI) comprising six insulated gate bipolar transistor (IGBT) switches, and a dc current source which follows the I-V characteristics of PV panels of the PV solar farm system [15, 176]. With the utilization of a Maximum Power Point Tracking (MPPT) algorithm, the PV solar farm operates at its maximum power point in normal operation [108, 190]. A large dc capacitor is employed to hold the dc voltage approximately constant at the dc side of the inverter [178].

## 3.3  Inverter Control System

The proposed control of the PV solar farm as PV-STATCOM is illustrated in Figure 3.1. It is known that a STATCOM with voltage control alone is unable to damp the torsional SSR oscillations and hence an auxiliary damping controller is required [78, 79, 81, 82]. It is possible to mitigate SSR by damping controllers utilizing electrical signals from the PCC, such as, PCC voltage [83] and line current [86, 191]. However, in this study, rotor speed deviation is selected as the control signal for the auxiliary SSR damping controller for the PV-STATCOM. This is because rotor speed contains information about all the torsional modes of oscillation [79, 81]. It has further been shown to be an effective signal to mitigate SSR by SVCs and STATCOMs connected at the terminals of the turbine generator [77, 79, 81, 82, 99, 100].
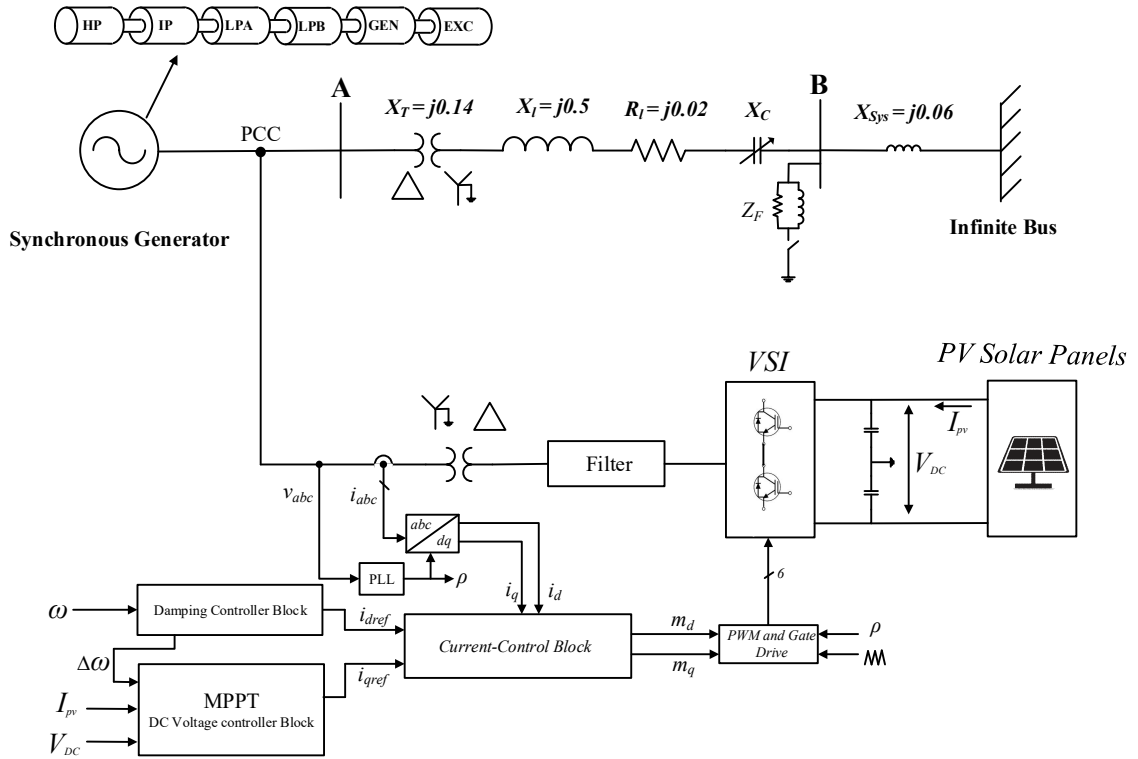
**Figure 3.1: Study system with a PV solar farm as PV-STATCOM connected at the synchronous generator terminal in the IEEE First SSR Benchmark system**

The PV inverter control is based on the *dq*-reference frame model of VSI [15, 108, 190]. The phase-locked loop (PLL) block is utilized to estimate the angle of the grid voltage [108]. The voltage vector for *dq*-frame modeling is aligned with the quadrature axis, and therefore $V_d$ equals zero. Thus, the reactive and active powers of VSI are independently controlled through the *d*-axis and *q*-axis loops, respectively.

The DC voltage controller block including the Power Point Tracking (PPT) subsystem adjusts the dc side voltage of inverter to the desired value as described in section 2.6.4. The damping controller block utilizes the generator speed signal to produce the *d*-axis reference current $i_{d-ref}$ for current controller. By employing the dc side voltage and current, the DC Voltage controller block provides the *q*-axis reference current $i_{q-ref}$. The current control block subsequently controls the output current of the inverter, as described in section 2.6.3. The PI controller parameters in current controller and DC voltage controller are tuned by a systematic hit-and-trial method to achieve the fastest step response, least settling time, and an overshoot less than 10% [15].

## 3.3.1 Damping Controller

Figure 3.2 illustrates the configuration of the proposed SSR damping controller of the PV-STATCOM. Since it is intended to utilize the entire STATCOM inverter capacity only for damping SSR, the voltage controller typically employed in the STATCOM is not implemented.

The PV-STATCOM is connected at the terminals of the turbine driven synchronous generator. It is therefore expected that the generator rotor speed signal obtained from speed measurement devices will become available to the PV-STATCOM control without any appreciable delay. This is the approach adopted by almost all the studies dealing with SSR mitigation by Flexible AC Transmission System (FACTS) devices connected at the terminals of the turbine generators [79, 81, 82, 89, 100, 192]. Hence, the same approach has also been adopted in this thesis.

The generator speed is continuously measured and passed through the washout block to obtain the generator speed deviation which reflects the SSO occurring in the generator. It is enhanced by a gain factor K and phase shifted by 180º to produce the $d$-axis reference $i_{d\text{-}ref}$ for the current loop controller. This controller produces $i_{d\text{-}ref}$ in a manner that the corresponding PV-STATCOM reactive power exchange can damp the subsynchronous oscillations.

The best controller parameters are obtained through a systematic hit-and-trial method to result in a minimal settling time and acceptable over shoot (less than 10%) in generator speed [15]. There are analytical approaches to design damping controllers of FACTS devices such as [82, 83, 86, 193, 194] which are more efficient than gain selection through trial and error. However, as the objective of this chapter is to demonstrate a new concept of SSR mitigation by PV solar farms control as STATCOM (PV-STATCOM), a simpler controller parameter selection through systematic trial-and-error method was chosen.

Washout

$$\omega \rightarrow \boxed{\dfrac{sT_\omega}{1+sT_\omega}} \xrightarrow{\Delta\omega} \boxed{K} \rightarrow \boxed{\begin{array}{c}180^{\text{o}}\text{ phase}\\ \text{shift}\end{array}} \rightarrow \boxed{\phantom{/}} \rightarrow i_{dref}$$
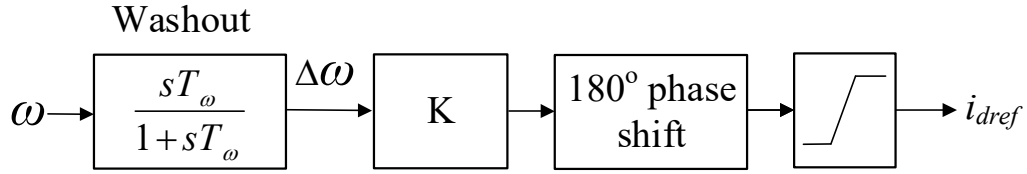
**Figure 3.2: Damping controller configuration**

## 3.4 Eigenvalue Analysis and Electromagnetic Transients Study of SSR Damping

Studies for damping subsynchronous oscillations using PV-STATCOM control are now performed using EMTDC/PSCAD and MATLAB/Simulink software. These studies are reported for the most stringent case when the synchronous generator is producing 500 MW and PV solar system is producing 300 MW, therefore the line power flow is 800 MW and representing a similar power flow as in [112].

The eigenvalues of the system without the proposed controller are shown in Table 3.1. The eigenvalues of the system are obtained by linearization toolbox of MATLAB. This table includes torsional Modes 0 to 5, and network modes (subsynchronous and supersynchronous). Table 3.1 shows that the system has unstable modes at critical compensation levels pertaining to the IEEE First SSR Benchmark system. It can be seen in this table that the frequency of subsynchronous mode in each compensation level is close to the frequency of one of the torsional modes making the torsional mode unstable. Comparison of Table 3.1 and Table 2.1 reveals that the integration of PV solar farm does not affect the stability of torsional modes generally. It improves or decreases the damping of the modes only marginally, but it does not change the stability status of the system, either stable or unstable.

A three-line-to-ground (3LG) fault for five cycles is initiated at Bus B at $t = 5\ sec$. These fault studies are performed for four critical levels of series compensation when the four respective torsional oscillatory modes are most undamped, as described in [81, 112] and showed in section *2.8.1*.

**Table 3.1: Eigenvalues of the system with conventional PV system at SG bus**

| Modes | Compensation Level (%) | | | |
|---|---|---|---|---|
| | 26.4 | 40.9 | 54.3 | 67.4 |
| 0 | -0.68±8.91i | -0.861±9.77i | -1.087±10.71i | -1.39± 11.89i |
| 1 | -0.139±99.24i | -0.142±99.47i | -0.144±100.06i | 4.96± 99.03i |
| 2 | -0.021±127.04i | -0.020±127.07i | 0.837±127.01i | -0.015±126.95i |
| 3 | -0.252±160.71i | 1.289±160.52i | -0.248±160.42i | -0.255±160.51i |
| 4 | 1.397±202.89i | -0.052±202.79i | -0.058±202.86i | -0.059±202.89i |
| 5 | -0.280±298.18i | -0.280±298.18i | -0.280±298.18i | -0.28±298.18i |
| Network-1(Sub) | -4.476±202.83i | -3.910±160.37i | -2.465±126.84i | -5.714± 98.63i |
| Network-2(Super) | -5.155±551.32i | -5.34±594.16i | -5.48±627.57i | -5.611±657.23i |

Figure 3.3 depicts the post-fault behavior of the study system when the solar farm functions conventionally and is *not controlled* as the proposed PV-STATCOM. This figure illustrates the system response for the series compensation level when Mode 1 is critically excited. The responses of the PCC rms voltage, PV-STATCOM reactive power; generator real and reactive powers, rotor speed, and the torque in the LPB-GEN section are depicted in Figure 3.3 (a)-(f). It is evident from this study that the system becomes highly unstable due to SSR.

According to the Voltage Ride Through criteria of existing grid codes and Standards, the PV solar farm *must be disconnected* due to its large voltage excursions. For instance, NERC standard "PRC-024-2" [155] requires the generating unit to have the capability of Voltage Ride-Through (VRT). Based on voltage ride-through time duration curve and Table in Attachment 2 of this Standard, whenever the PCC voltage goes under 0.65 p.u. for a duration more than 0.3 sec the generating unit should be disconnected from the grid. Furthermore, whenever the voltage goes above 1.2 p.u. the generating unit should be tripped instantaneously. As evident from Figure 3.3, the PCC voltage after fault occurrence goes under 0.65 p.u. for a duration of 0.8 second. Therefore, the PV solar farm should be disconnected at $t = 5.835$ sec. In addition, the voltage goes above
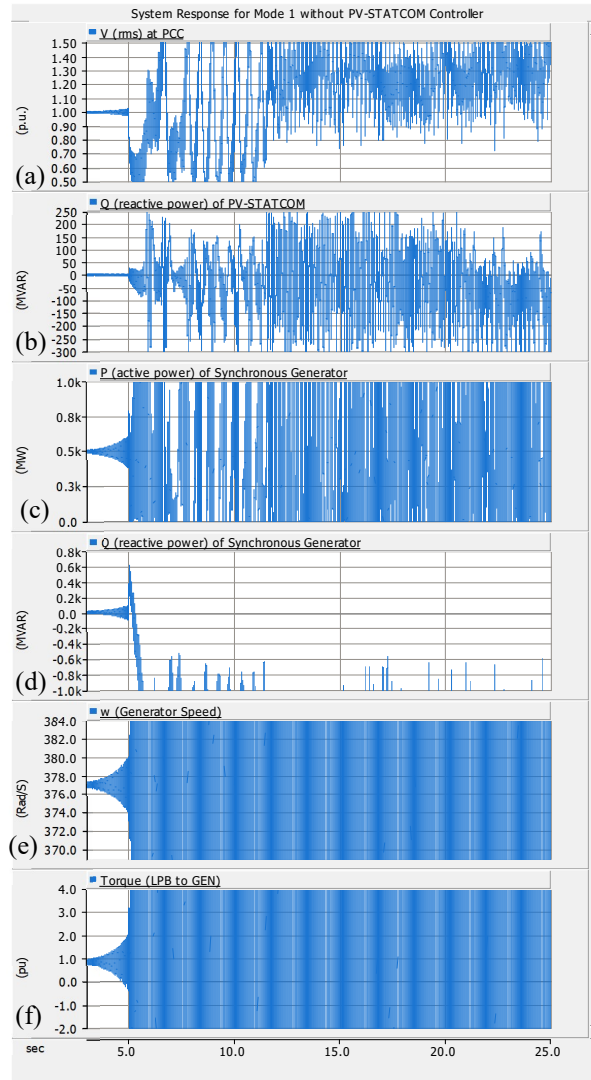
**Figure 3.3: System response for Mode 1 SSR without PV-STATCOM controller.**

1.2 p.u. at $t = 5.86$ sec, which is another criterion for the solar farm to be disconnected at $t = 5.86$ sec, although the previous criterion will take precedence for disconnection.

ERCOT Nodal Operating Guides [195] requires all Intermittent Renewable Resources (IRR) to conform to Voltage Ride Through requirements. Based on Figure 1 of section 2 of this operating guide, the IRR shall be disconnected whenever the PCC voltage goes under 0.6 p.u. for 1.25 sec, or immediately whenever it goes above 1.2 pu. Therefore, based on ERCOT Nodal Operating Guides and Figure 3.3, the PV solar farm shall be disconnected at $t = 5.86$ sec when the PCC voltage goes above 1.2 pu.

It is therefore emphasized that the solar farm will *anyway be disconnected* due to the VRT criterion of the grid codes, and not because of the proposed PV-STATCOM control. The issues of load frequency control will arise, but that will need to be addressed by the system operator. This is outside the scope of this thesis.

It is shown in this chapter that the proposed novel PV-STATCOM control goes a step beyond, and instead of remaining idle in the disconnected mode, utilizes its inverter capacity to successfully damp SSR. This control further returns the solar farm to its normal pre-fault power production and restores the system frequency to its nominal value. It performs this function autonomously without any communication from the system operator. Without this proposed control, the system will become unstable and the system operator will have to take due measures to restores system stability and frequency.

The stabilizing impact of SSR damping control of the PV-STATCOM is now investigated. The system eigenvalues for four critical series compensation levels with the proposed PV-STATCOM controller are shown in Table 3.2. Comparison between Table 3.2 and Table 3.1 shows that PV-STATCOM controller significantly improves the damping of torsional Modes 1 to 4 at all the four critical compensation levels and thereby makes the system stable. The damping of Mode 0 is noticeably improved when the compensation level is 26.5%, 40.9%, and 54.3%. However, its damping is slightly decreased when $k$ equals 67.4%. The damping of subsynchronous mode is decreased, while the damping of supersynchronous mode is increased in all four critical compensation levels. The PV-STATCOM controller does not have any significant effect on Mode 5 as its modal inertia is very high [86]. This eigenvalue study clearly demonstrates the effectiveness of the proposed PV-STATCOM controller with SSR damping controller in alleviation of SSO.

**Table 3.2: Eigenvalues of the system with PV at SG bus, and with PV-STATCOM**

| Modes | Compensation Level (%) | | | |
|---|---|---|---|---|
| | 26.4 | 40.9 | 54.3 | 67.4 |
| 0 | -1.167±8.09i | -1.189±8.88i | -1.24±9.73i | -1.325±10.76i |
| 1 | -1.516±98.6i | -1.398±97.84i | -1.138±95.84i | -0.367±88.34i |
| 2 | -0.150±126.93i | -0.140±126.76i | -0.255±125.35i | -0.305±127.75i |
| 3 | -0.787±159.91i | -1.105±155.21i | -0.990±162.58i | -0.885±161.95i |
| 4 | -1.413±196.56i | -1.341±205.47i | -1.202±204.81i | -1.146±204.61i |
| 5 | -0.280±298.180i | -0.280±298.18i | -0.280±298.18i | -0.280±298.18i |
| Network-1(Sub) | -2.62±213.21i | -1.83±168.53i | -1.482±133.43i | -1.471±111.74i |
| Network-2(Super) | -5.184±550.12i | -5.410±592.78i | -5.585±626.11i | -5.74±j655.70i |

## 3.4.1 SSR Damping with First Critical Level of Compensation

Figure 3.4 (a)-(e) depict the different PV-STATCOM variables which include Inverter active power $P$, reactive power $Q$, apparent power $S$, dc side current $I_{PV}$ and the dc side voltage $V_{DC}$, respectively. Figure 3.5 (a)-(h) illustrate the different synchronous generator variables for this case, which include active power, reactive power, generator speed $\omega$, and torques between HP-IP, IP-LPA, LPA-LPB, LPB-GEN, and GEN-EXC sections, respectively. The corresponding transmission system parameters for this case study are portrayed in Figure 3.6 (a)-(c) which consist of rms voltage at PCC, active power flow and reactive power flow, respectively.

As soon as the onset of SSO in rotor speed is sensed at $t = 5$ sec by the damping controller, the dc voltage controller increases the dc bus voltage to its open circuit value $V_{OC}$ to make the inverter active power $P$ and the dc current $I_{PV}$ go to zero, however, with a slight delay based on the time constant of the involved controllers. The entire capacity of the inverter is thereby made available for Full-STATCOM operation to damp SSR. The rotor oscillations are successfully damped to within 1 rad /sec at $t = 9.68$ sec. Once this occurs, the PV solar farm restarts power generation by decreasing the dc voltage in a ramped manner, while continuing to damp SSR in the Partial-STATCOM mode of operation. The pre-fault level of power generation is achieved without any voltage/power oscillations in

about 5 seconds at $t = 14.68$ sec. The entire process of damping Mode 1 SSR takes only 9.68 sec utilizing a maximum of 200 Mvar STATCOM capacitive reactive power.

It is observed from Figure 3.5 (d)-(h) that torsional oscillations occur in all the mechanical sections, however, the highest torque in excess of 4 p.u. is experienced in the LPA-LPB shaft section. The PV-STATCOM successfully damps the SSR in the entire torsional system. It is noted from Figure 3.6 that during the damping of Mode 1 by PV-STATCOM, the line active power reduces as the power output of the solar farm is made to go to zero but subsequently returns to the pre-fault value. The PCC voltage rises slightly above 1 p.u. during the transient.
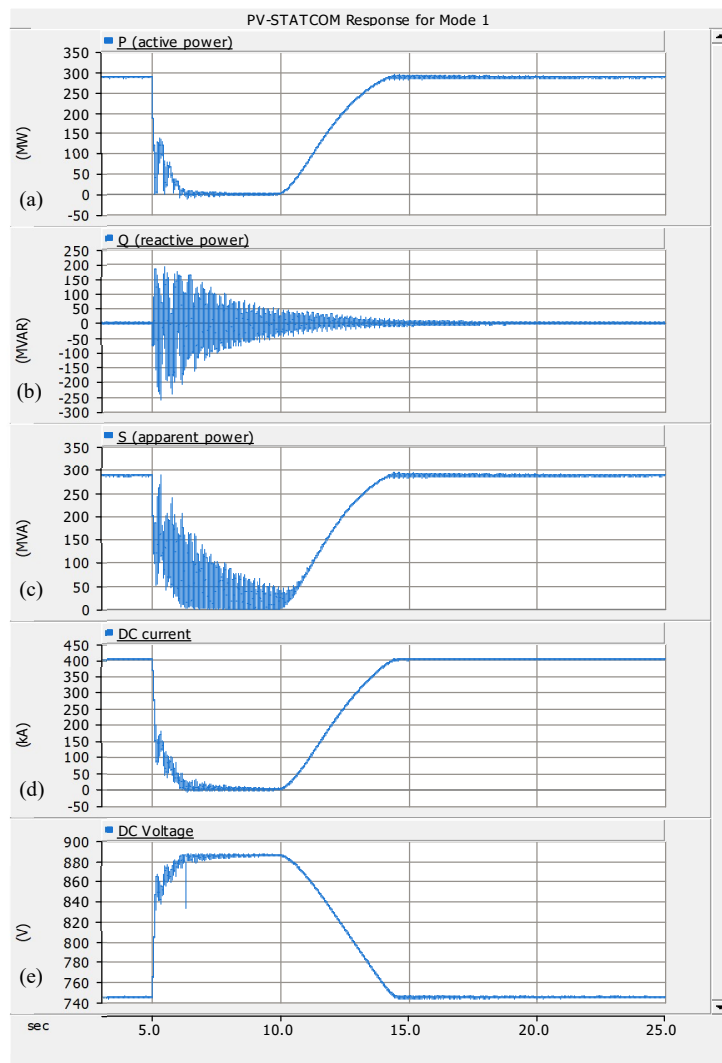


**Figure 3.4: PV-STATCOM response for damping of Mode 1 SSR.**
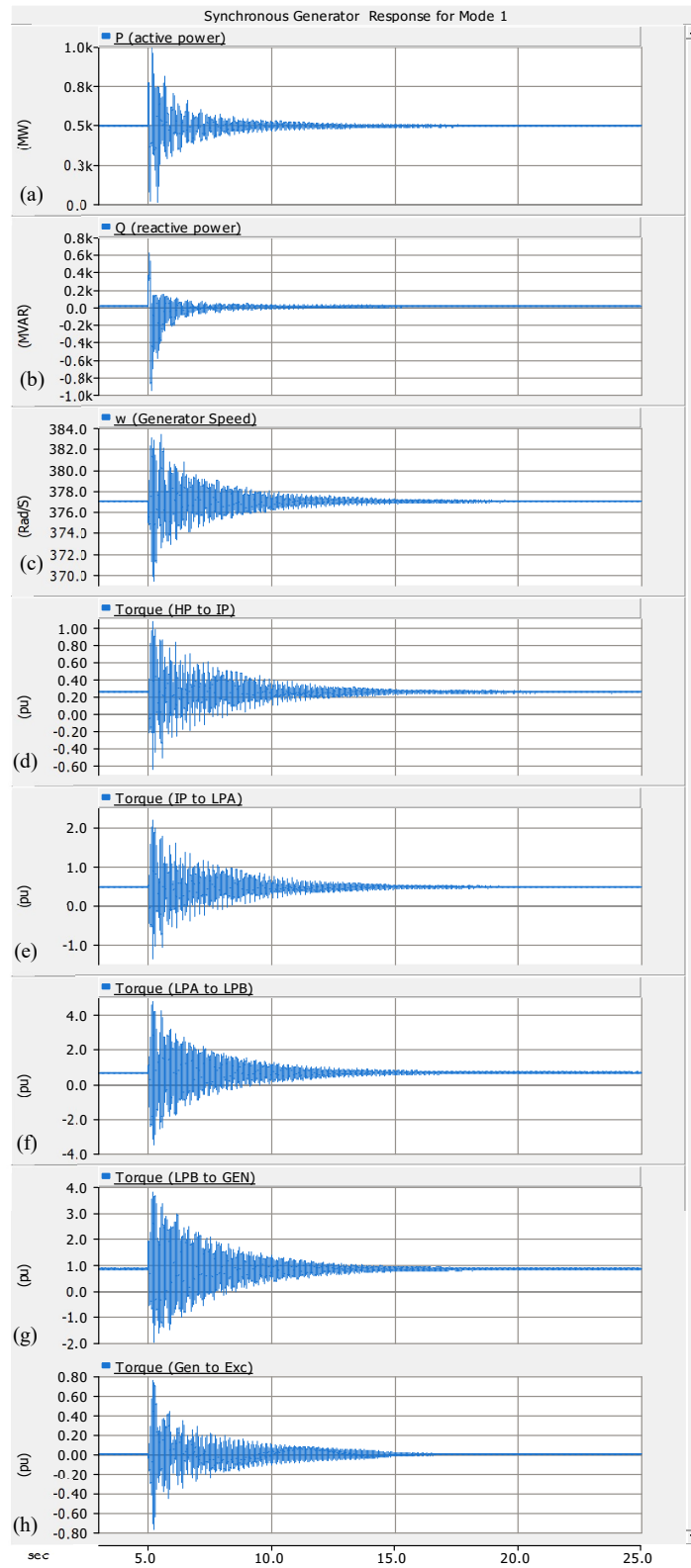
**Figure 3.5: Synchronous generator response for damping of Mode 1 SSR**
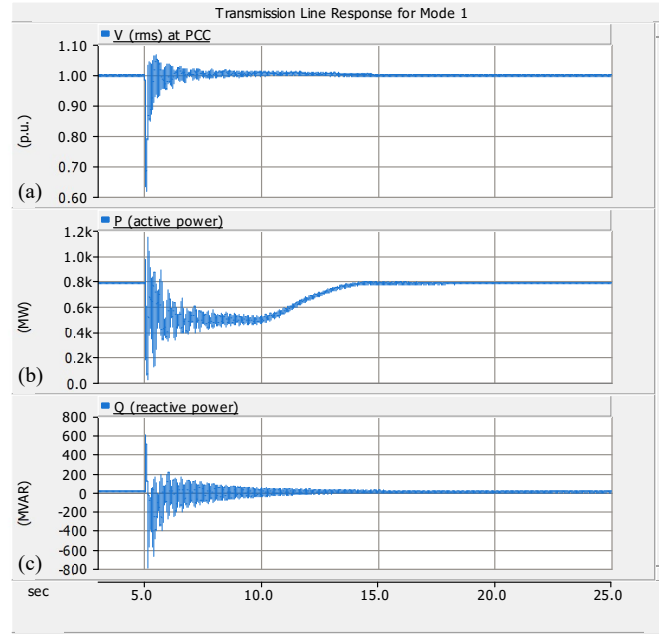
**Figure 3.6: Transmission system response for damping of Mode 1 SSR**

## 3.4.2 Ramp-up without the Proposed PV-STATCOM Control

Grid codes such as [125, 154, 196] stipulate that active power sources including PV solar farms should ramp-up their power output slowly during the connection process in order to avoid voltage or power oscillations due to the sudden injection of a large amount of active power into the grid.

The grid codes further specify a range for the rate at which the power may be ramped up depending upon system characteristics. A typical specification is that the increase in active power supplied to the network by the power source must not exceed a maximum gradient of 10% of the agreed active connection power per minute [154]. The appropriate ramp-rate for a specific system may be determined from off-line system studies.

This thesis has therefore proposed a novel fast method of reconnection of PV solar farm while keeping the PV-STATCOM SSR damping function activated. It is demonstrated from Figure 3.4 and Figure 3.5 that with this proposed technique the active power can be ramped up from zero to 300 MW in about 5 seconds without resumption of SSR.

To demonstrate the effectiveness of this proposed technique a new study is performed. In this study, after SSR has been mitigated and generator rotor speed stabilized to within

acceptable limits at $t = 10$ sec in Figure 3.4 and Figure 3.5, the power ramping up is performed without the PV-STATCOM damping function. The ramp-up rate is slowed down three times, i.e. the power is ramped up from zero to 300 MW over 15 sec instead of 5 sec as in Figs.7-8 with PV-STATCOM damping control in operation. Figure 3.7 (a)-(c) portray the response of real power of the synchronous generator, the active power of solar farm, and generator rotor speed, respectively. The system is seen to become unstable due to recurrence of SSR. This clearly shows the efficacy of the proposed ramp-up with PV-STATCOM damping control active.
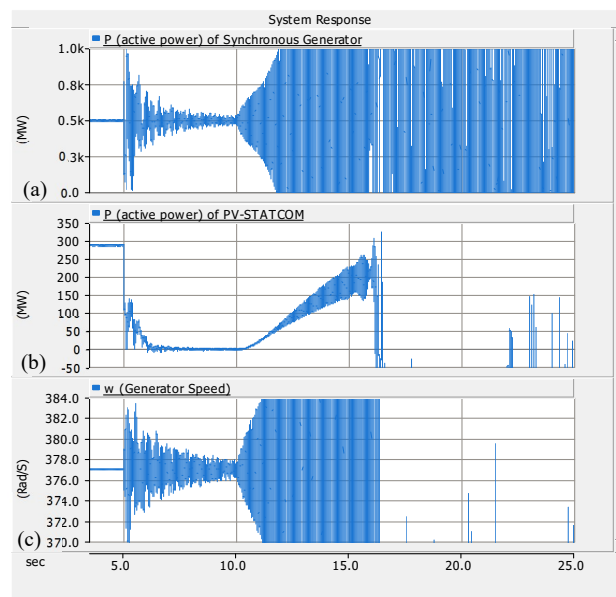


**Figure 3.7: System response for Mode 1 SSR without damping controller during ramp-up**

## 3.4.3 SSR Damping for Second Critical Level of Compensation

Figure 3.8 (a)-(f) illustrate the system parameters for mode 2 which consist of the PCC rms voltage, PV-STATCOM reactive power; generator real and reactive powers, rotor speed, and the torque in the LPB-GEN section, respectively. The results shown in this figure validate the efficacy of PV-STATCOM in alleviation SSR for the second critical compensation level of 54.3%. In this case study, the fault is initiated as before at $t = 5$ sec. The PV-STATCOM damps the torsional oscillations ($\Delta\omega<1$ rad/s) at $t = 7.96$ sec, and the solar power output is restored to its pre-fault value at $t = 12.96$ sec without any recurrence

of SSR. Thus, the total time required for SSR alleviation is 7.96 sec. The maximum PV-STATCOM capacitive reactive power needed for this purpose is about 200 Mvar.
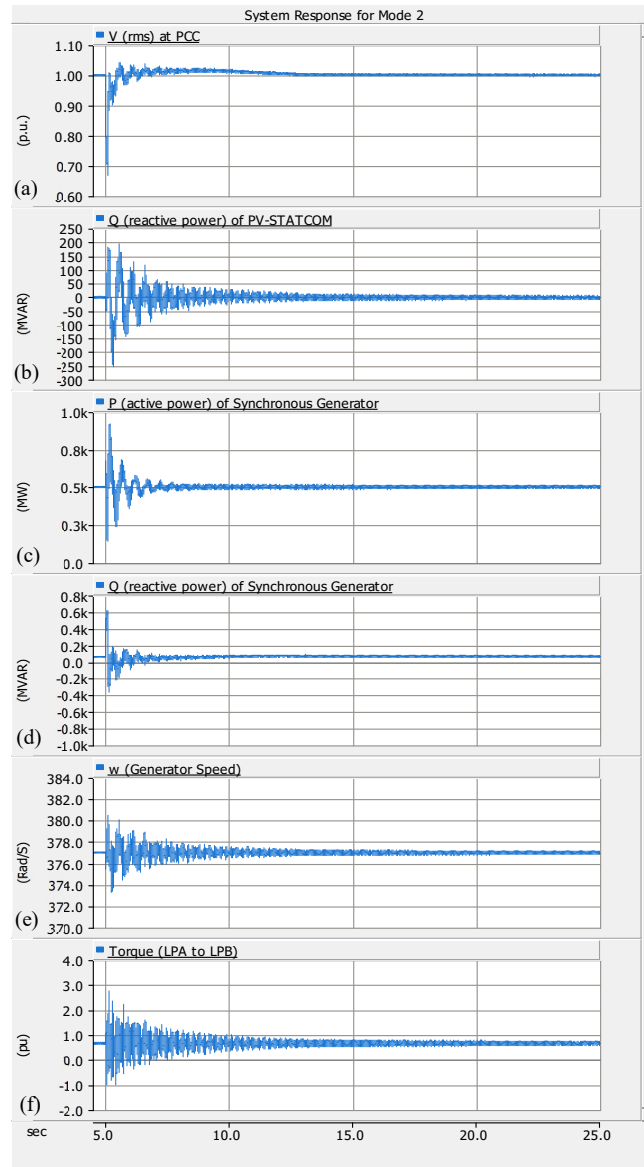


**Figure 3.8: System response for damping of Mode 2 SSR**

## 3.4.4 SSR Damping for Third Critical Level of Compensation

The effectiveness of PV-STATCOM in damping SSR for the third critical compensation level $k = 41\%$, is described in this section. Figure 3.9 (a)-(f) depicts the PCC rms voltage, PV-STATCOM reactive power; generator real and reactive powers, rotor speed, and the torque in the LPB-GEN section, respectively. In this case study, the fault is initiated as

before at $t$ = 5 sec. The PV-STATCOM damps the torsional oscillations ($\Delta\omega<1$ rad/s) at $t$ = 6.81 sec, and the solar power output is reinstated to its pre-fault value without any SSR at $t$ = 11.81 sec. Thus the total time required for SSR alleviation is 6.81 sec. The maximum PV-STATCOM capacitive reactive power needed for this purpose is also about 200 Mvar.
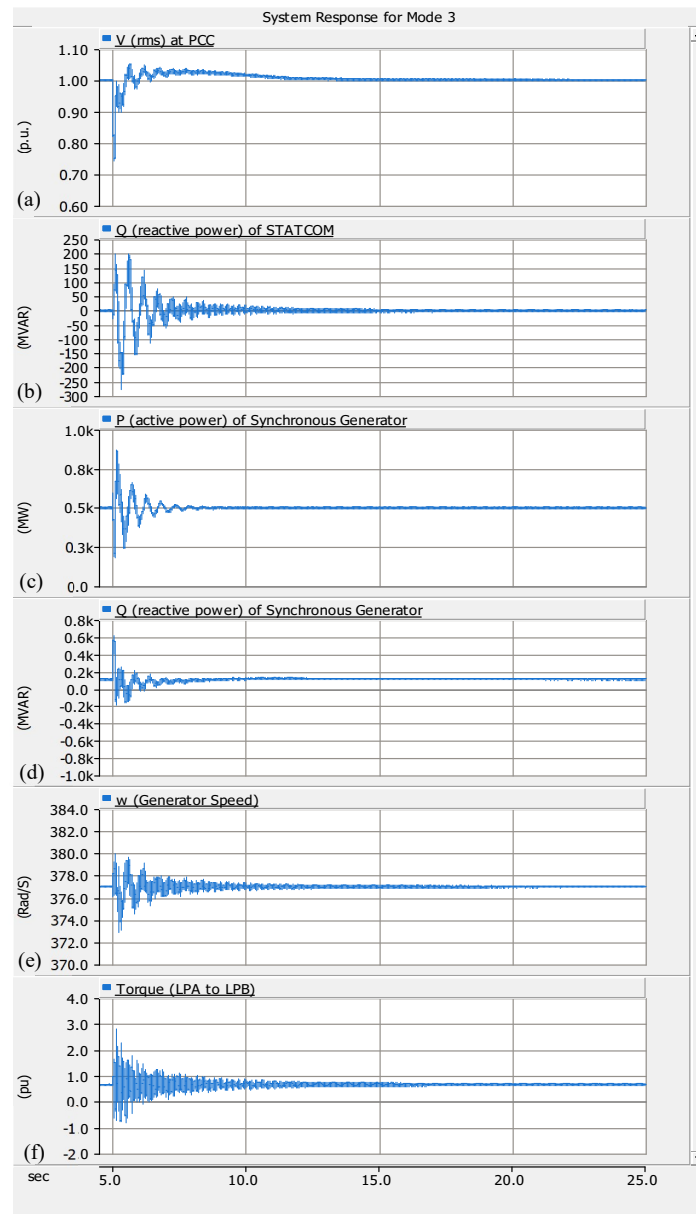


**Figure 3.9: System response for damping of Mode 3 SSR**

## 3.4.5 SSR Damping for Fourth Critical Level of Compensation

For this case, Figure 3.10 (a)-(f) illustrate the PCC rms voltage, PV-STATCOM reactive power, generator real and reactive powers, rotor speed, and the torque in the LPB-GEN section, respectively. The PCC bus voltage is about 1.05 pu, which is higher than in the case of Mode 1 damping (Figure 3.6). This is because during PV-STATCOM operation, when PV solar system does not generate any real power, the synchronous generator reactive power is largely capacitive, as opposed to being largely inductive as in case of Mode 1 damping (Figure 3.5).

A maximum subsynchronous torque of about 3 p.u. is experienced in the LPB-GEN section. The PV-STATCOM successfully mitigates all the torsional oscillations ($\Delta\omega < 1$ rad/s) at $t = 6.77$ sec, and the solar power output is restored to its pre-fault value without any SSR at $t = 11.77$ sec. Thus, the total time required for SSR alleviation is 6.77 sec. The maximum PV-STATCOM capacitive reactive power needed for this purpose is about 200 Mvar.

## 3.4.6 Discussion

A. *Impact of PV Solar Farm Shutdown and Ramp-up on Grid Frequency during PV-STATCOM operation*

In general, both the outage and ramping up of a large amount of PV solar power may potentially impact the frequency of the grid. However, these impacts will depend upon the size of the PV solar system in comparison to the overall power generation in the grid, the duration of the outage of solar power, and the rate of ramping up (in case of reconnection). These impacts can only be determined after due studies are performed for the concerned power system.

A significant number of research studies on SSR mitigation including [81, 82] have been conducted on the IEEE First SSR Benchmark system [112]. In this thesis also, the effectiveness of the proposed PV-STATCOM for SSR alleviation has been examined on a system similar to the IEEE First SSR Benchmark system. For this system, the size of PV
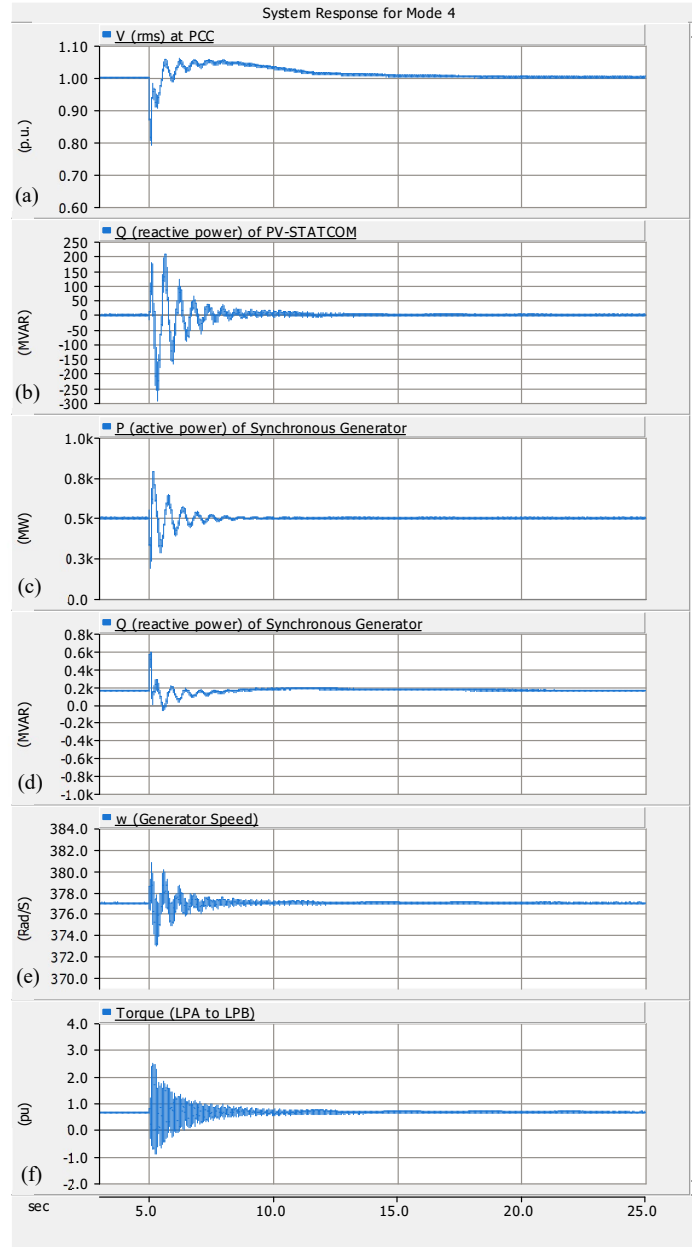
**Figure 3.10: System response for damping of Mode 4 SSR**

solar farm (300 MW) is about a third in comparison to the rating of synchronous generator (892 MVA). With the large voltage deviations experienced during the onset of SSR, the PV solar farm will need to be shut down in accordance with the transmission grid codes such as [154] and wait for reconnection till the SSR has been mitigated by other mechanisms. This thesis proposes a novel concept that instead of being shut down the solar farm performs SSR mitigation and returns to its full pre-fault solar power production within a period of less than 10 sec.

It is clearly seen that the shutdown of the PV solar farm to transform into a PV-STATCOM does not have any significant effect on the grid frequency. It is evident from Figure 3.5 that the maximum deviation of the generator speed (representative of the system frequency) caused by the combined effect of SSR in synchronous generator and outage of 300 MW solar power output for a duration of 10 seconds is just about 7 rad/s.

It is however recommended to check that the PV-STATCOM control while damping SSR does not cause any adverse impact on system frequency if implemented in any other large power system.

While it is recommended that adequate studies be conducted to determine frequency deviations in study systems in question, it is concluded based on this study that a PV solar farm equipped with PV-STATCOM control can provide a valuable service of SSR mitigation without causing any appreciable impact on the system frequency in the IEEE First SSR Benchmark system.

## B. *Potential of Utilizing Large-scale PV Solar Farms for Damping Subsynchronous Resonance*

With increasing electrical power generation to meet the load demand, series compensation of lines is expected to be increasingly considered as an economical alternative to construction of new transmission lines, worldwide. This is likely to make the associated generation systems more prone to SSR issues. On the other hand, due to the rapid adoption of renewable energy systems coupled with the drop in PV panel prices, large-scale PV solar farms with rating in excess of 100 MW are increasingly being deployed in transmission systems worldwide [12-14, 197]. Furthermore, these sizes of large utility scale solar farms are becoming comparable to transmission level shunt connected FACTS devices such as, Static Var Compensators and STATCOMs. It is understood that large-scale PV solar farms may be installed at locations which will be determined from non-technical considerations, such as availability of cheap land, etc. However, it is quite a possibility that such transmission connected solar farms may be connected in networks that are series compensated and also may be in close vicinity of synchronous generators that may be SSR prone. For instance, the 290 MW Agua Caliente Solar Project constructed by First Solar is

connected to Hassayampa-North Gila 500 kV transmission line that is series compensated [197].

Considering the above growing developments of large solar farms and their possible connection in series compensated lines, such large solar farms can potentially become candidates for implementation of PV-STATCOM SSR damping function.

## 3.5  Conclusion

Rapidly emerging, large utility scale PV solar farms are likely to find themselves being connected in transmission systems that are series compensated. This chapter presents a novel patent-pending concept of autonomously controlling such large utility scale PV solar farms as STATCOM, termed PV-STATCOM, for mitigating subsynchronous resonance (SSR) in steam turbine driven synchronous generators connected to series compensated transmission line. The proposed PV-STATCOM control provides solar farm the capability to mitigate SSR both in the night and anytime during the day. In the night, since the solar farm is idle, the entire inverter capacity is utilized for PV-STATCOM operation. During the day, at any time, if SSR is triggered due to any system disturbance, the solar farm autonomously discontinues its normal real power generation function and transforms into a STATCOM with the full inverter capacity for SSR mitigation. Once the subsynchronous resonances are reduced below an acceptable level, the solar farm autonomously returns to its pre-fault real power generation level in a ramped manner.

Studies are conducted on the IEEE First SSR Benchmark system [112] having a large 300 MVA solar farm connected at the generator terminals producing its rated power, to simulate similar study conditions as in [112]. The PV-STATCOM SSR damping control utilizing generator rotor speed as the control signal is developed in *d-q* frame of reference. PSCAD/EMTDC based electromagnetic transients simulation studies are conducted for all the four critical levels of series compensation [112]. The following conclusions are drawn:

1) The PV-STATCOM successfully mitigates all the four torsional modes at all the four critical levels of series compensation.

2) The total time taken by the PV-STATCOM from the autonomous initiation of damping control to mitigate the different subsynchronous mode oscillations and return to pre-fault normal solar power production is: 9.68 sec for Mode 1, 7.96 sec for Mode 2, 6.81 sec for Mode 3 and 6.77 sec for Mode 4, oscillations respectively.

This time of interruption of PV solar power generation is comparable to a cloud passing event.

3) The PV-STATCOM capacitive reactive power required to damp SSR for all the critical series compensation levels in this study is less than 200 Mvar.

4) The novel concept of ramping up keeping the SSR damping function of PV-STATCOM activated allows a ramp-up rate much faster than that specified in grid codes without resurgence of SSR.

The studies demonstrate that the proposed PV-STATCOM control on large utility scale PV solar farms can successfully mitigate potentially dangerous subsynchronous resonances in synchronous generators connected to series compensated lines. The PV-STATCOM control can potentially obviate the need for installation of an expensive SVC or STATCOM connected to the generator terminals for the same purpose.

Under the current power market situation, the owner of synchronous generator normally may not want to share such confidential information about rotor oscillations to other generation owner such as the PV solar farm which is a competitor in the market. However, this chapter proposes a new concept by which the PV solar farm can provide SSR mitigation for the synchronous generator in a highly cost effective manner as compared to the installation of a FACTS device exclusively for the purpose of SSR alleviation, assuming both are connected close to the terminals of the synchronous generator.

In the proposed concept, the solar farm is not acting as a competitor to the synchronous generator. Instead it is providing a very valuable service in form of protection against shaft damages in the synchronous generator due to SSR. The synchronous generator will therefore not be averse to sharing its rotor oscillation information with the PV solar farm. It is expected and also proposed that appropriate agreements among the synchronous

generator owner, concerned utility, system operator, solar farm owner and the inverter manufacturer may be made to implement such a cost-effective solution.

Chapter 4

# 4 SSR Mitigation with PV-STATCOM connected at Line Midpoint

## 4.1 Introduction

This chapter presents the efficacy of PV-STATCOM control in damping SSR in a synchronous generator when the solar farm is connected at the line midpoint, i.e., quite far from the synchronous generator which is experiencing SSR. A modified IEEE First SSR Benchmark system is considered with the PV system integrated at line midpoint where maximum voltage excursions are experienced. The PV-STATCOM subsynchronous damping controller utilizes a local control signal i.e. the line active power, to avoid the communication delay if the generator speed were to be selected as the control signal. By using a local signal as the control signal, not only the communication delay is avoided but also the SSR alleviation service of PV-STATCOM becomes independent from PV solar farm location. Results of small-signal modal analysis and electromagnetic transients' studies validate the effectiveness of PV-STATCOM for alleviation of SSR in SG. This novel method of utilizing existing PV system as PV-STATCOM to alleviate SSO can obviate the need for installing expensive FACTS devices such as STATCOM or SVC to achieve this objective.

## 4.2 Study System

The study system shown in Figure 4.1 is a modified IEEE First SSR Benchmark system [112] augmented with a 300-MW PV solar farm which is connected to line midpoint (Bus C). In previous chapter, the PV system is located at synchronous generator terminal, which is the closest location to synchronous generator. In this chapter, PV solar farm is located at line midpoint where maximum voltage excursions are experienced to investigate the effectiveness of PV-STATCOM in SSR alleviation when PV system in located remotely from synchronous generator. Both the synchronous generator and PV solar farm are connected to the infinite bus through a series capacitive compensated transmission line. While the 892-MW SG operates at 500 MW, PV solar farm operates at its rated power, i.e. 300 MW. The entire system is modeled in MATLAB/Simulink software. The parameters

of the system are given in Appendix A. To represent the dynamics of mechanical system, an aggregated six-mass turbine is considered, while the mechanical damping is assumed to be zero to study the worst-case damping situation [81]. The series capacitive reactance ($X_C$) of the system is changed to excite the different torsional modes. The values of $X_C$ (p.u.) for which different torsional modes have their largest destabilization are as follows:  Mode 1 (0.47 p.u.), Mode 2 (0.38 p.u.), Mode 3 (0.285 p.u.), and Mode 4 (0.185 p.u.) [112]. The PV panels are represented by a controlled current source as a dc source which follows the I-V characteristic of PV panels. This dc source is connected to a voltage source inverter (VSI) which is linked to the transmission line through a filter and a coupling transformer. The PV solar system utilizes maximum power point tracking (MPPT) system to generate its maximum power at its normal operation [15].
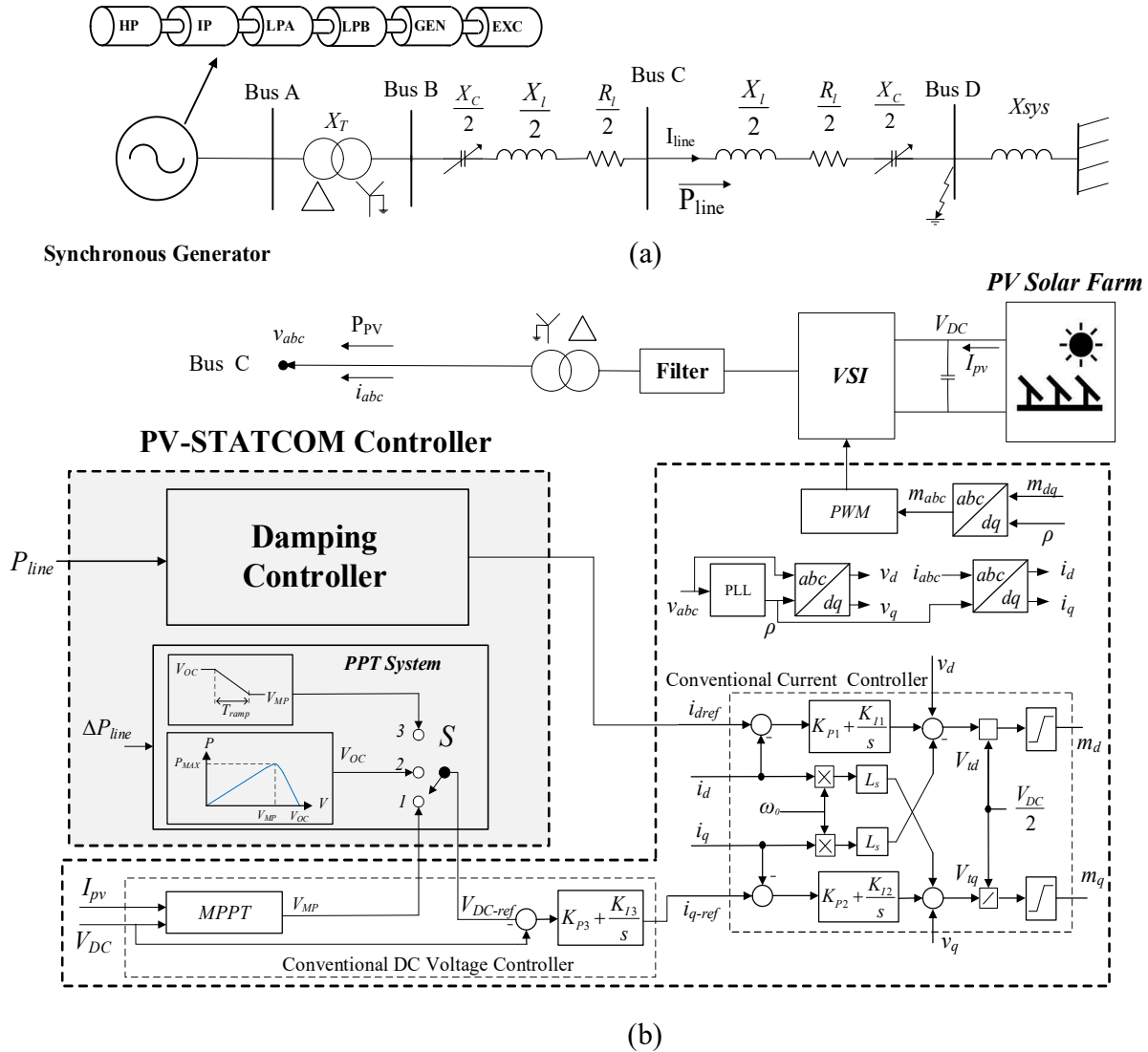
**Figure 4.1: Study system: (a) modified IEEE First SSR Benchmark system with PV plant connected at line midpoint (b) PV-STATCOM and its control system**

## 4.3 Inverter Control System

Figure 4.1(b) depicts the PV system controller augmented with PV-STATCOM controller. It consists of a damping controller, dc voltage controller with PPT system (section 2.7.2), and the conventional PV current controller. The PV inverter control is based on the $dq$-reference frame model of VSI [108]. The voltage vector is aligned with the quadrature axis and $V_d$ equals zero in this paper. Therefore, the $d$-axis control loop controls the reactive power of the VSI and the $q$-axis control loop controls the active power of the VSI. The current controller regulates the output current of VSI by providing appropriate modulation

indexes $m_d$ and $m_q$, as explained in section 2.6.3. The DC voltage controller including PPT system controls the active generation of PV panels by producing reference of dc voltage ($V_{DC\_ref}$) as explained in section 2.6.4.

## 4.3.1 Damping Controller

Various control signals have been used in the literature for subsynchronous damping controller such as generator speed [81], PCC voltage [83], line current [191], and active power flow of the line [97]. In this chapter, active power flow of the line (*Pline*) is used as a local control signal for damping controller. The choice of this signal avoids communication delay if generator speed were to be chosen as the control signal. Figure 4.2 depicts the damping controller configuration which includes band-pass filters, gain blocks, phase compensators (lead-lag compensators), and a limiter block. In this chapter, a multi-band SSR damping controller is used which is different from the other damping controllers used in this thesis. This damping controller deals with 4 unstable modes. The control signal, i.e. $P_{Line}$, is passed through band-pass filters to extract the subsynchronous frequency components of $P_{Line}$. The band-pass filters are designed based on the generator torsional frequencies, Mode 1 to 4. Since the modal inertia of the Mode 5 is high and this mode hardly excites, a filter for this mode is not needed [86]. The torsional mode frequency $f_{Mi}$ representing the frequency of $i^{th}$ torsional mode, is taken as the center of the band-pass filters [86]. The band-pass filter only extracts the relevant oscillations and improves the damping of corresponding torsional mode to which it has been set. The output of each filter is amplified with an appropriate gain. The output of each gain block is passed through proper phase compensator. After that, the output of phase compensators are added together to provide $i_{dref}$ for the current controller. The damping controller mitigates SSO in the system by generating appropriate $i_{dref}$ and consequently reactive power output of PV solar farm ($Q_{PV}$).

The MATLAB optimization block, Genetic Algorithm (GA), is used to determine the SSR damping controller parameters. An Objective Function (OF) is defined to accomplish maximum damping for the system. In (4.1), $\xi_i$ is the damping ratio of $i^{th}$ eigenvalue of the system. This OF ensures that the eigenvalues of the system have positive damping ratio. To avoid convergence to a local minima, the GA is run for 50 times and the minimum value

of objective function corresponding to all the runs is chosen. The obtained parameters of the damping controller are given in Appendix B.

$$OF = \sum_{j=1}^{n} (1 - |\xi_i|), \qquad \xi_i > 0 \qquad (4.1)$$
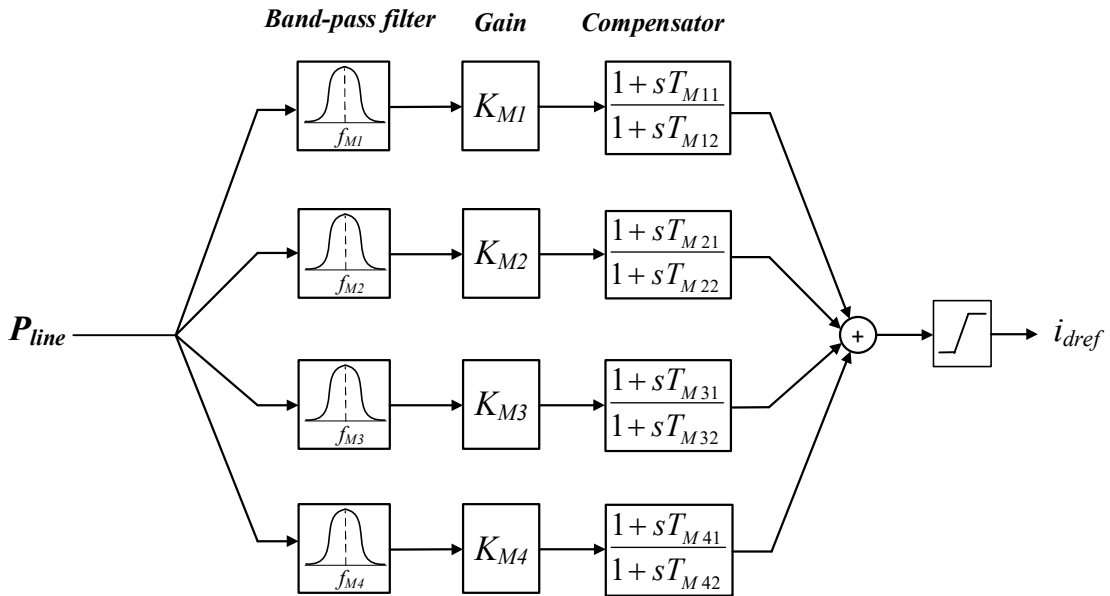


**Figure 4.2: Damping controller configuration**

## 4.4 Eigenvalue Analysis and Electromagnetic Transients Study of SSR Damping

In this section, the effectiveness of SSO alleviation by PV-STATCOM is studied when PV solar farm is connected at line midpoint. The system under study is modeled in MATLAB/Simulink software. While the 892-MW SG is assumed to generate 500 MW the PV solar farm produces $P_{PV}$ of 300 MW. This simulates the most stringent case of the IEEE First SSR Benchmark system [112]. The linearization toolbox of MATLAB software is utilized to obtain the state-space model of the system and consequently the eigenvalues of the system. Also, electromagnetic transient studies through MATLAB/Simulink are carried out for a three-phase to ground fault at $t = 5$ sec for 5 cycles at Bus D.

Table 4.1 illustrates the eigenvalues of the system without PV-STATCOM controller for four critical compensation levels. This table consists of torsional Modes 0 to 5, and network modes (subsynchronous and supersynchronous). Table 4.1 shows that the system has an unstable mode for each critical compensation level and is unstable in the same manner as the IEEE First SSR Benchmark system, as explained in section *2.8.1*. It should be noted that the system is unstable due to the interaction between the subsynchronous mode and one of the torsional mode at each critical compensation when their frequencies get aligned with each other.

**Table 4.1: Eigenvalues of the system with PV system at line midpoint, and without PV-STATCOM control**

| Modes | Compensation Level (%) | | | |
|---|---|---|---|---|
| | 26.4 | 40.9 | 54.3 | 67.4 |
| **0** | -0.869±9.75i | -1.075± 10.48i | -1.3374±11.32i | -1.708 + 12.39i |
| **1** | -0.113±99.33i | -0.108±99.58i | -0.146± 100.08i | 4.726± 98.99i |
| **2** | -0.018±127.04i | -0.015± 127.08i | 0.732±126.97i | -0.012± 126.93i |
| **3** | -0.239±160.73i | 1.134± 160.48i | -0.242±160.38i | -0.252± 160.48i |
| **4** | 1.548±202.81i | -0.045± 202.75i | -0.052±202.83i | -0.053± 202.87i |
| **5** | -0.28± 298.18i | -0.28± 298.18i | -0.28± 298.18i | -0.28± 298.18i |
| **Network-1(Sub)** | -4.874±202.82i | -4.501± 160.48i | -3.373±126.97i | -7.102±98.75i |
| **Network-2(Super)** | -5.206±551.27i | -5.413± 594.10i | -5.692± 627.49i | -5.701± 657.15i |

Figure 4.3 (a)-(d) illustrate the SG rotor speed ($\omega_r$), torque between LPA-LPB ($T_{AB}$), torque between GEN-EXC ($T_{GE}$), and active power flow of the line ($P_{line}$), respectively, for $k$ = 67.4%, representing Mode 1 SSR, when PV-STATCOM controller is not implemented in the PV system. The growing SSO in these variables clearly show the instability of the system and corroborate the results of the eigenvalue study, shown in Table 4.1.
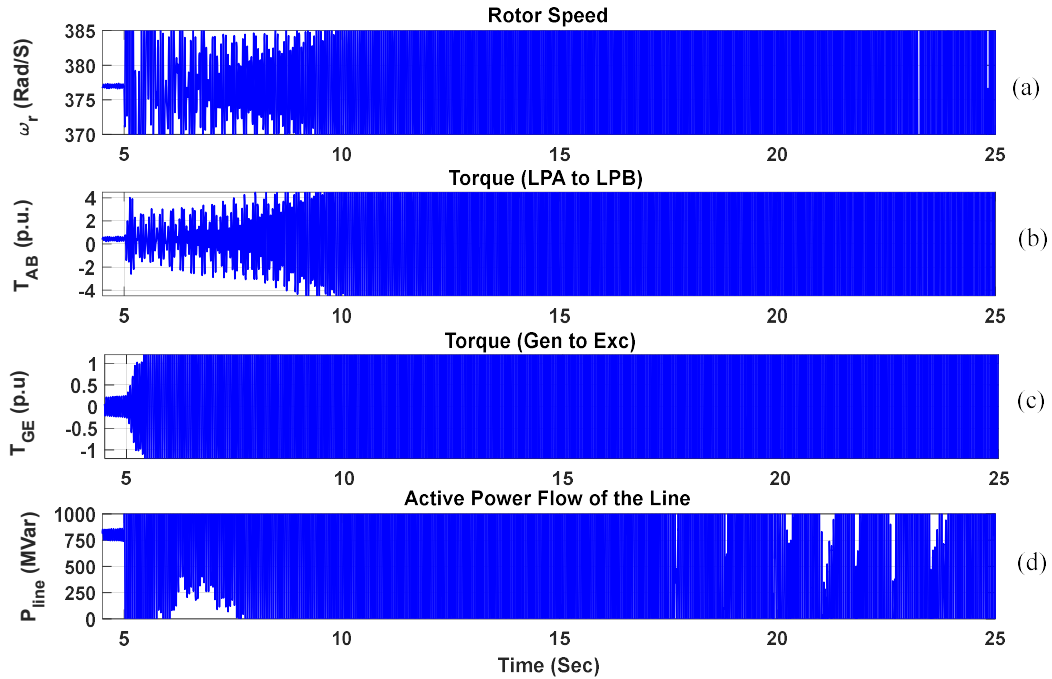
**Figure 4.3: System response for Mode 1 SSR, PV located at line midpoint, without PV-STATCOM controller**

Table 4.2 shows the eigenvalues of the system when PV-STATCOM controller is implemented in the PV system and active power flow of the line ($P_{line}$) is employed as the SSR damping control signal. As shown in Table 4.2, the PV-STATCOM damping controller successfully stabilizes the unstable modes.

Comparison between Table 4.1 and Table 4.2 shows that implementation of PV-STATCOM controller noticeably increases the damping of Mode 2 and Mode 4 in all the critical compensation levels. But, the damping of Mode 0 and supersynchronous mode are slightly decreased in all the cases. The damping of Mode 1 is significantly improved in its corresponding compensation level, i.e. 67.4%, but it is decreased at other series compensation levels. Damping of Mode 3 is also noticeably increased in its corresponding compensation level, i.e. 40.9%, but it is decreased in $k = 54.3\%$ and 67.4%. However, the damping of Mode 3 is barely changed when the compensation level is 26.4%. The damping of subsynchronous mode noticeably increases when the compensation level is 26.4% and 40.9%, but it decreases while the compensation level is 54.3% and 67.4%. Due to high modal inertia, damping of Mode 5 does not change remarkably.

**Table 4.2: Eigenvalues of the system with PV at line midpoint, and with PV-STATCOM**

| Modes | Compensation Level (%) | | | |
|---|---|---|---|---|
| | 26.4 | 40.9 | 54.3 | 67.4 |
| 0 | -0.847± 9.822i | -1.056±10.58i | -1.326± 11.45i | -1.698±12.59i |
| 1 | -0.106± 98.78i | -0.102± 98.78i | -0.096± 98.744i | -0.143± 98.702i |
| 2 | -0.097± 127.03i | -0.112±126.99i | -0.114±126.99 i | -0.112± 126.93i |
| 3 | -0.266± 160.62i | -0.2114± 160.643i | -0.1599± 160.6i | -0.151± 160.52i |
| 4 | -0.104±203.23 i | -0.2208± 202.36i | -0.126± 202.83i | -0.103± 202.90i |
| 5 | -0.28± 298.18i | -0.28± 298.18i | -0.28± 298.18i | -0.28± 298.18i |
| Network-1(Sub) | -7.516± 221.61i | -9.681± 194.875i | -1.588± 115.36i | -2.562± 63.20i |
| Network-2(Super) | -4.721±545.24 i | -5.122± 587.17i | -5.453±620.04 i | -5.686± 649.33i |

## 4.4.1 SSR Damping with First Critical Level of Compensation

Figure 4.4 (a)-(e) depict the different PV-STATCOM variables which include Inverter active power ($P_{PV}$), reactive power ($Q_{PV}$), apparent power ($S_{PV}$), the dc side voltage ($V_{DC}$), and dc side current ($I_{PV}$), respectively, when PV-STATCOM controller is implemented in PV system and $k = 67.4\%$ corresponding to Mode 1 SSR. Figure 4.5 (a)-(d) illustrate SG rotor speed ($\omega_r$), torque between LPA-LPB ($T_{AB}$), torque between GEN-EXC ($T_{GE}$), and active power flow of the line ($P_{line}$), respectively.

As shown in Figure 4.4 (a), before the fault occurrence, PV solar farm operates in its conventional mode and extracts maximum power from PV panels ($P_{PV} = 300$ MW). Once fault occurs and undamped SSO are detected by the PV-STATCOM controller, the DC voltage controller increases the dc side voltage ($V_{OP}$) to $V_{OC}$, as shown in Figure 4.4 (d). Consequently, $I_{DC}$ and $P_{PV}$ go to zero with a slight delay based on the controller time constant. The entire inverter capacity is now available to operate in Full-STATCOM mode. Once the SSR in $P_{line}$ are damped to within 0.01 p.u. at $t = 9.733$ sec, PV solar farm restores its $P_{PV}$ gradually. The gradual increment of $P_{PV}$ is required to avert initiation of low frequency oscillations based on grid codes [135, 154, 198]. To achieve this, DC voltage controller increases $V_{op}$ from $V_{OC}$ to $V_{MPP}$ in 5 seconds in ramped manner. During $P_{PV}$

ramp-up, the remaining capacity of VSI is used by damping controller in Partial-STATCOM mode to prevent any recurrence of SSO. It can be seen from Figure 4.4 (b), that there are some damped oscillations during ramp-up which demonstrate PV-STATCOM operation in Partial-STATCOM mode to prevent the recurrence of SSO in the system. The PV system goes back to its pre-fault level of power generation in about 5 seconds at $t$ = 14.733 sec. It can be seen in Figure 4.4 (b) that the maximum $Q_{PV}$ needed to damp SSR in this case is 268 Mvar.
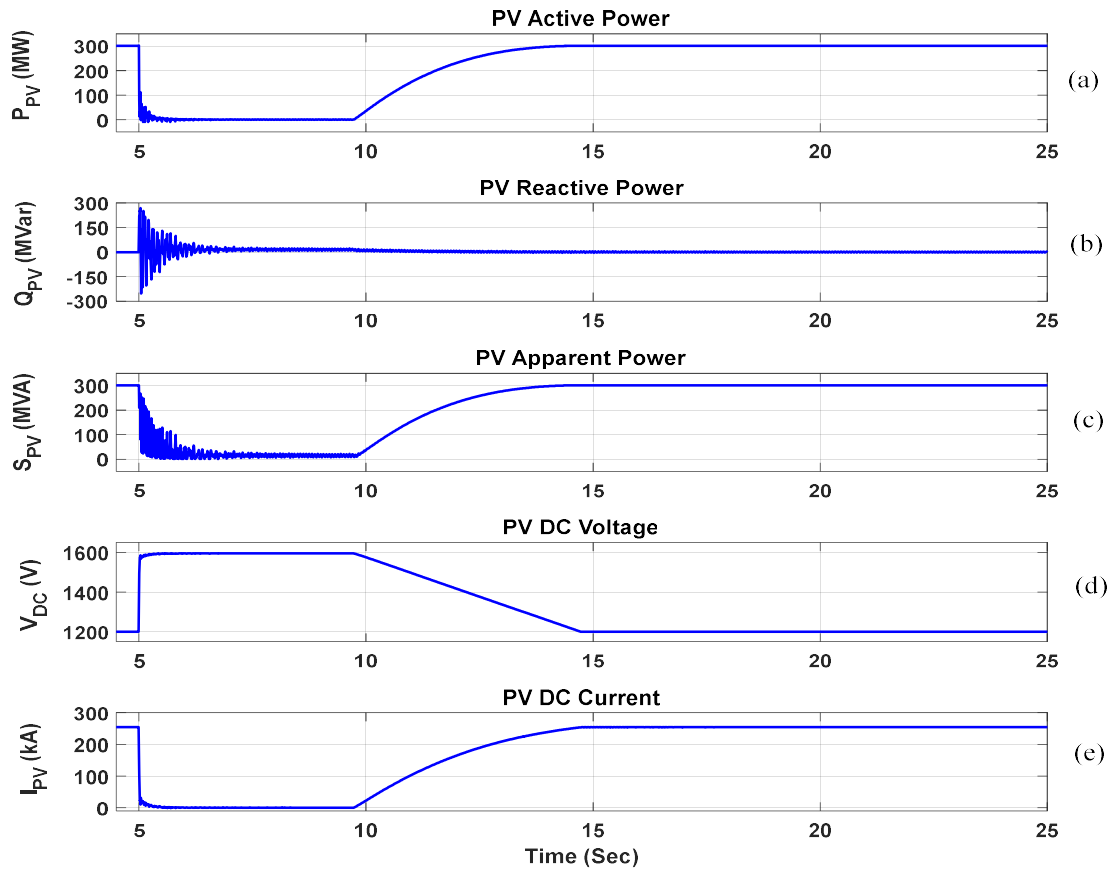


**Figure 4.4: PV solar farm response for Mode 1 SSR, PV system located at line midpoint, with PV-STATCOM controller**

As shown in Figure 4.5 (a)-(c), the PV-STATCOM successfully damps SSO in rotor speed ($\omega_r$), torque between LPA-LPB ($T_{AB}$), torque between GEN-EXC ($T_{GE}$). Figure 4.5 (d) illustrates that once fault occurs at $t$ = 5 sec, $P_{line}$ decreases to 500 MW because $P_{PV}$ is made zero. At $t$ = 9.73 sec, when SSO is successfully damped by PV-STATCOM, the PV system

starts restoring $P_{PV}$. $P_{line}$ subsequently returns to its pre-fault generation level at $t = 14.73$ sec.
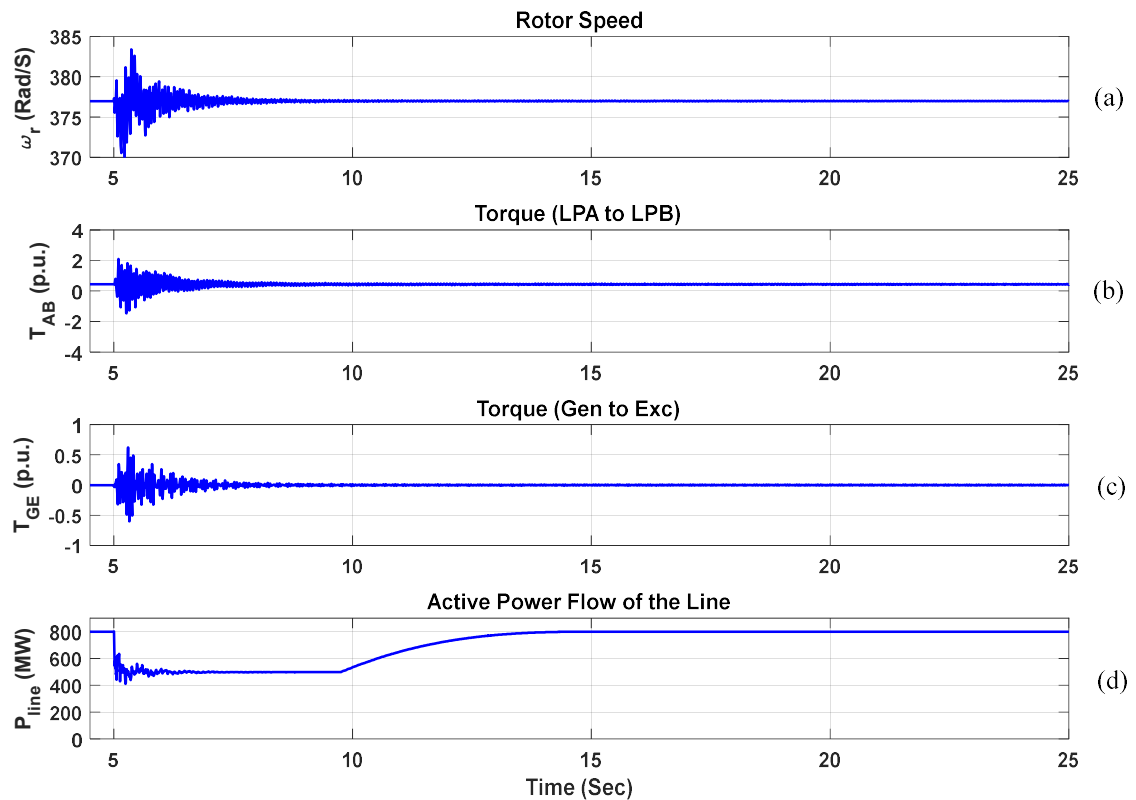


**Figure 4.5: System response for Mode 1 SSR, PV located at line midpoint, with PV-STATCOM controller**

## 4.4.2 SSR Damping with Second Critical Level of Compensation

In this section, the effectiveness of PV-STATCOM with local line power based damping control for SSR alleviation is demonstrated while the compensation level of the line is 54.3%, which is the second critical level of compensation. Figure 4.6 (a)-(e) depict different system variables which include SG rotor speed ($\omega_r$), torque between LPA-LPB ($T_{AB}$), torque between GEN-EXC ($T_{GE}$), active power flow of the line ($P_{line}$), and PV reactive power ($Q_{PV}$), respectively. As shown in Figure 4.6, at the occurrence of fault at $t = 5$ sec, the PV real power generation is ceased. Consequently $P_{line}$ reduces to 500 MW and the entire capacity of PV inverter is made available to operate in Full-STATCOM mode.

Once the SSO in active power flow of the line are damped to less than 0.01 p.u. at $t = 8.11$ sec, the PV system start restoring $P_{PV}$ in a ramped manner while keeping the subsynchronous damping function activated in Partial-STATCOM mode to prevent recurrence of SSR. The PV solar farm returns to its normal operation in 8.11 sec after fault occurrence, at $t = 13.11$ sec. The PV-STATCOM reactive power $Q_{PV}$ for SSR damping is about 251 Mvar in this case.
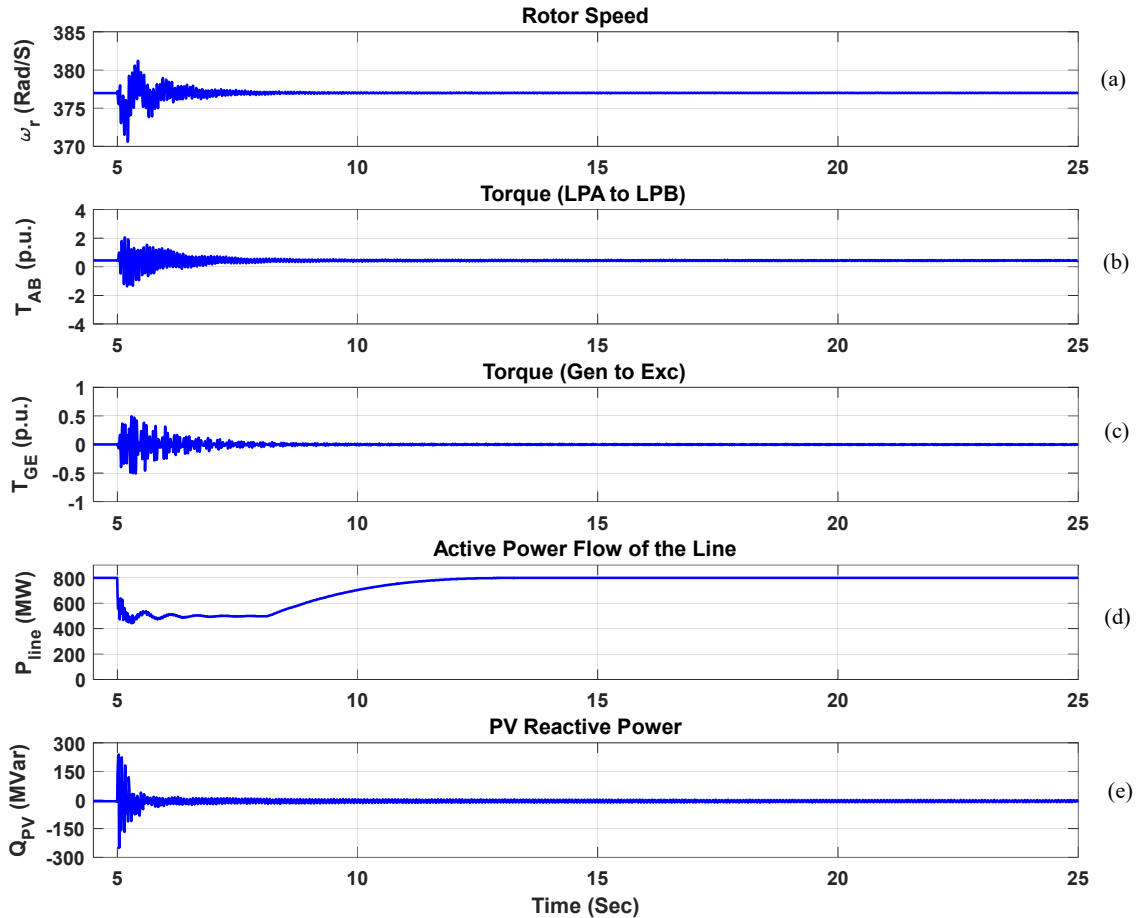


**Figure 4.6: System response for Mode 2 SSR, PV system located at line midpoint, with PV-STATCOM controller**

## 4.4.3 SSR Damping for Third Critical Level of Compensation

Figure 4.7 (a)-(e) depict the system parameters for Mode 3 which represent SG rotor speed ($\omega_r$), torque between LPA-LPB ($T_{AB}$), torque between GEN-EXC ($T_{GE}$), and active power flow of the line ($P_{line}$), respectively. Figure 4.7 (a)-(c) show that PV-STATCOM successfully alleviates subsynchronous resonance in the synchronous generator. Once

growing SSO is detected at $t = 5$ sec by PV-STATCOM controller, it reduces $P_{PV}$ to zero thereby making the entire PV inverter capacity available for Full STATCOM operation. This can be noticed from Figure 4.7 (d) in which $P_{line}$ reduces to 500 MW at $t = 5$ sec. Then, the damping controller utilizes the entire capacity of the PV inverter and modulates the reactive power of PV system $Q_{PV}$ to damp SSR as shown in Figure 4.7 (e). When SSR in $P_{line}$ are damped to within 0.01 p.u. at $t = 7.23$ sec, the PV-STATCOM stops functioning in Full-STATCOM mode and starts increasing active power generation of PV solar farm in a ramped manner while operating in Partial-STATCOM mode, as described earlier. Figure 4.7 (e) shows damped oscillations in $Q_{PV}$ during ramp-up which demonstrate PV-STATCOM operation in Partial-STATCOM mode to prevent the recurrence of SSO in. Restoration of PV real power to its pre-fault condition is achieved at $t = 12.23$ sec, i.e., 7.23 sec after fault initiation. The PV inverter reactive power needed to damp SSR is 265 Mvar in this case.
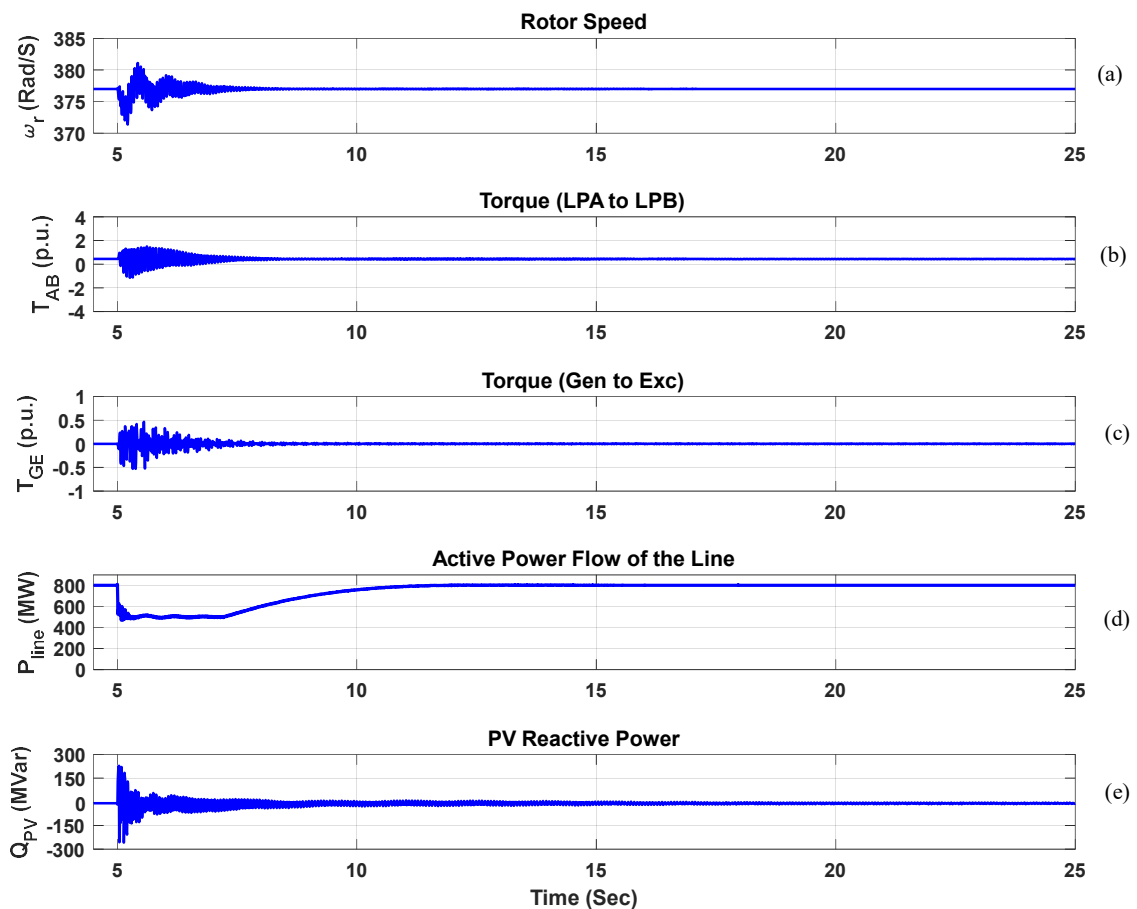
**Figure 4.7: System response for Mode 3 SSR, PV system located at line midpoint, with PV-STATCOM controller**

## 4.4.4 SSR Damping for Fourth Critical Level of Compensation

In this section, the effectiveness of PV-STATCOM in SSR alleviation is investigated while the series compensation level of the line is 26%, which is the fourth critical level of compensation. Figure 4.8 (a)-(e) depict the SG rotor speed ($\omega_r$), torque between LPA-LPB ($T_{AB}$), torque between GEN-EXC ($T_{GE}$), and active power flow of the line ($P_{line}$), respectively. When fault happens at $t = 5$ sec, $P_{line}$ decreases to 500 MW because $P_{PV}$ is made zero by PV-STATCOM controller, as seen from Figure 4.8 (d). Therefore, the entire capacity of PV inverter can be used as a STATCOM to damp SSR. At $t = 6.98$ sec, when SSO is successfully damped by PV-STATCOM, the PV system starts ramping up its real power output. $P_{PV}$ is eventually restored to its pre-fault generation level at $t = 11.98$ sec. The damped oscillations in $Q_{PV}$, shown in Figure 4.8 (e), during ramp-up demonstrate the PV-STATCOM operation in Partial-STATCOM mode to avoid recurrence of SSR in the system. The required $Q_{PV}$ for SSR mitigation is this case is 258 Mvar.
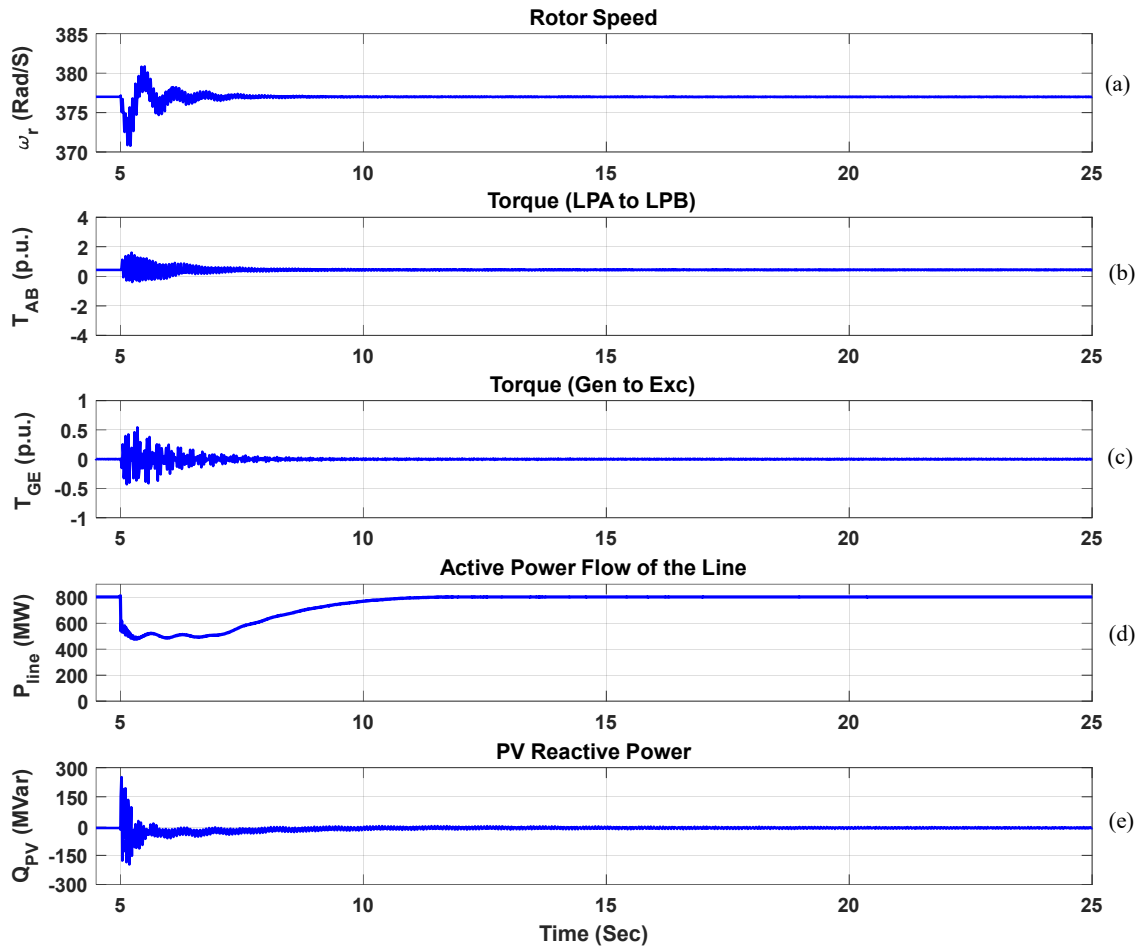
**Figure 4.8: System response for Mode 4 SSR, PV system located at line midpoint, with PV-STATCOM controller**

## 4.5  Conclusion

In this section, a new concept is demonstrated of using a remotely connected PV solar farm as STATCOM to mitigate SSR in a synchronous generator connected to a series compensated line. A modified IEEE First SSR Benchmark system with an integrated 300-MW PV solar farm is employed to study the effectiveness of PV-STATCOM in SSR alleviation. Studies are performed while the PV solar farm is connected at line midpoint for all four critical compensation levels of IEEE First SSR Benchmark system. The process of SSO damping by PV-STATCOM during daytime is similar to the one described in previous chapter when the PV solar system is connected at generator terminals. However in this case, active power flow of the line ($P_{Line}$) is used as the local control signal for

subsynchronous damping controller. This choice of damping control signal avoids any communication delay which would be incurred if a remote signal like generator speed were to be selected.

The following conclusions are obtained:

1) Eigenvalue studies of the system show that implementation of PV-STATCOM controller in PV system successfully improves the damping of the unstable modes and makes them stable at all the critical compensation levels.

2) The time domain results also validate the effectiveness of PV-STATCOM in damping SSR for all the critical compensation levels.

3) The entire process of SSO instability alleviation from fault occurrence until restoration of PV solar farm to its pre-fault condition takes place in less than half a minute: 9.73 sec for Mode 1, 8.11 sec for Mode 2, 7.23 sec for Mode 3 and 6.98 sec for Mode 4 oscillations, respectively.

4) The maximum reactive power needed to damp SSR when PV system is located at line midpoint is 268 Mvar. In comparison to the case when it is located at SG bus, it is noted that PV-STATCOM needs slightly more reactive power and time to alleviate SSO.

5) During active power ramp-up the damping controller of PV-STATCOM uses the remaining capacity of the solar inverter and operates in Partial-STATCOM mode to prevent the recurrence of SSO while achieving a fast ramp-up. This is a novel functionality during the power ramp-up proposed in this thesis, which is not specified in existing grid codes.

Chapter 5

# 5 Alleviating Subsynchronous Oscillations in Type 1 Induction Generator-Based Wind Farm by PV Solar Farm controlled as PV-STATCOM

## 5.1 Introduction.

In this chapter, a new concept of controlling a PV solar farm as STATCOM, termed PV-STATCOM, is presented for alleviation of subsynchronous oscillations (SSO) induced instability in induction generator (IG)-based Type-1 wind farm (WF). This concept is demonstrated in a modified IEEE First SSR Benchmark system in which the solar farm may be located either at WF terminal or remotely from the WF, wherein the SSO damping controller is based on WF generator speed and local transmission line current, respectively. During daytime, at the occurrence of SSO, the PV system ceases active power generation and utilizes the entire inverter capacity to operate as STATCOM. At nighttime, the entire PV inverter is utilized as STATCOM for SSO alleviation. Thus PV-STATCOM provides SSO alleviation on a 24/7 basis like a STATCOM. SSO damping controller is designed through eigenvalue analysis of the system with MATLAB/Simulink software. Detailed electromagnetic transient studies using PSCAD/EMTDC software are performed for wide ranging system conditions to demonstrate PV-STATCOM efficacy.

## 5.2 Study System

The IEEE First SSR Benchmark System [112] is modified by replacing the 892.4 MW synchronous generators by a 500-MW IG-based Type-1 WF. This modified system is considered to be the study system for this chapter and is depicted in Figure 5.1 (a). The WF is connected to the infinite bus through a series compensated transmission line. Figure 5.1 (b) illustrates the 300-MW PV plant and its control system for operation as PV-STATCOM. The PV plant is connected to the series compensated network of Figure 5.1(a) at either of the two locations: i) at the WF generator (Bus A), or ii) at the middle of

(a)

(b)
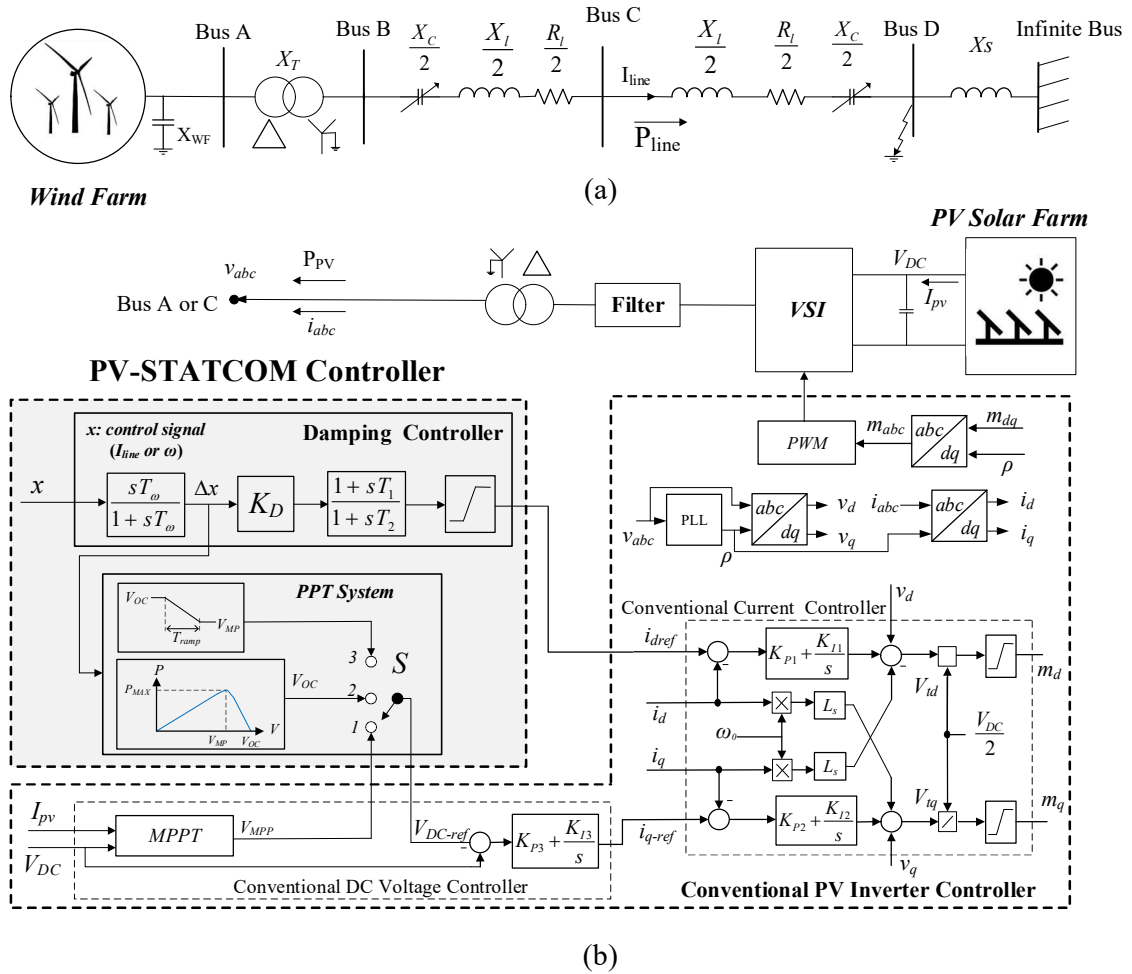
**Figure 5.1: Study system: (a) modified IEEE First SSR Benchmark System with integrated wind farm (b) PV solar farm plant and its control system**

transmission line (Bus C). The entire system is modeled in PSCAD/EMTDC and MATLAB/Simulink software according to the data provided in [55, 112].

The 500-MW WF is constituted of an aggregation of 217 identical 2.3-MW double-cage induction generators. It is assumed that all the generators are of the same type and size and are subjected to the same wind speed [55]. To model the dynamics of mechanical system, an aggregated two-mass wind turbine is considered. The mechanical damping is assumed to be zero to represent the worst-case scenario [55]. Unlike synchronous generator, the IG does not have any source of excitation and needs to absorb inductive reactive power for its operation. A shunt capacitor ($X_{WF}$) is therefore connected at the terminal of the wind farm to keep its power factor close to unity.

The PV solar farm model includes a voltage source inverter (VSI) which is connected to a capacitor and a controlled current source on its dc side. The dc current source follows the I-V characteristic of PV panels of the solar farm. The ac side of the VSI is connected to the transmission line through an LCL filter and a coupling transformer. The PV system utilizes a Power Point Tracking (PPT) system which provides the DC link voltage reference $V_{DC\text{-}ref}$ for the current loop controller.

## 5.3 Inverter Control System

Figure 5.1 (b) illustrates the proposed PV-STATCOM control system for damping SSO. This control system includes a damping controller, dc voltage controller with PPT system (section2.7.2 ), and the conventional PV current controller [108]. All the controllers are modeled in $dq$-reference frame. The angle of the grid voltage is estimated and provided by a phase-locked loop (PLL) block [108]. In this thesis, the voltage vector is aligned with the quadrature axis and $V_d$ equals zero. Thus, reactive power of the VSI ($Q_{PV}$) is controlled with $d$-axis control loop whereas active power generation of PV solar farm ($P_{PV}$) is controlled by the $q$-axis loop. The current controller regulates the output current of VSI by generating appropriate switching signals for VSI's switches as explained in section 2.6.3. As Figure 5.1 (b) illustrates, the dc voltage controller includes a PPT block and a PI controller. The PPT block provides the reference voltage ($V_{DC\_ref}$) to control PV-STATCOM real power output $P_{PV}$ as described in *section 2.6.4.*

### 5.3.1 Damping Controller

As shown in Figure 5.1 (b), the proposed SSO damping controller consists of a washout filter block, controller gain block, phase compensator (lead-lag compensator) and a limiter block. When the PV system is connected at WF terminal i.e. at Bus A, the generator speed is utilized as the control signal for damping controller of PV-STATCOM. However, when the PV system is connected at line midpoint i.e. at Bus C, the local line current ($I_{line}$) is employed as a control signal. This signal further helps avoid the impact of communication delay if wind turbine generator rotor speed $\omega$ were to be selected as the control signal. The damping control signal, $\omega$ or $I_{line}$, is measured and passed through the washout filter. The output of the washout filter contains the oscillatory component of the control signal which reflects SSO in the system. This signal is amplified with the controller gain, and its phase

is compensated by the phase compensator to provide $i_{d\text{-}ref}$ for current controller. The damping controller modulates the reactive power $Q_{PV}$ of PV-STATCOM to damp SSO by controlling $i_{d\text{-}ref}$, appropriately.

## 5.3.2 Damping Controller Design

MATLAB/Simulink software is utilized to develop the state-space model of the system, and to design the SSO damping controller. A sixth-order model is used to represent the IG stator and rotor current dynamics, while shaft system is represented by a third-order model [55]. The series compensated transmission line is represented with a fourth-order model. A first-order differential equation is used to model the WF terminal capacitor. The high-frequency switching dynamics of the PV inverter is neglected for this part while the dynamics of the current controller, dc voltage controller, and SSO damping controller are considered. The dc bus capacitor is modeled by a first-order differential equation.

With the help of MATLAB linearization toolbox, the state-space model of the study system is developed, and the eigenvalues of the system are computed. Table 5.1 illustrates the system eigenvalues when PV system is connected at the terminal of 500-MW wind farm and the compensation level is 55%, as this is a realistic level of series compensation in transmission systems [20]. This compensation level excites SSO with a frequency of 24 Hz in this radial system for different levels of $P_{WF}$ as described in section 2.8.2 and also explained in [55].

Table 5.1 consists of two network modes (supersynchronous and subsynchronous), torsional mode, and electromechanical mode 1 and 2. Without PV-STATCOM controller, it is seen that eigenvalues related to subsynchronous mode are located in the right half-plane (RHP) of the complex plane. This indicates an unstable system with negative damping.

**Table 5.1: Eigenvalues of the system without and with PV-STATCOM controller,**
**$P_{WF}$ = 500 MW, PV system at Bus A, and $k$ = 55%.**

| Modes | Without PV-STATCOM | With PV-STATCOM |
|---|---|---|
| Network-1(Sub) | 0.09 ± 151.11i | -4.89 ± 151.95 i |
| Network-2(Super) | -6.84 ± 602.19i | -4.32 ± 600.42i |
| Electro-mech-1 | -4.30 ± 30.67i | -5.24 ± 29.79 i |
| Electro-mech-2 | -59.82 ± 3.82i | -59.80 ± 3.89 i |
| Torsional | -0.609 ± 3.54i | -0.58 ± 3.56 i |

Generator speed ($\omega$) is considered as the input signal for SSO damping controller when the PV system is connected at WF terminal [81, 82]. The structure of SSO damping controller is shown in Figure 5.1(b). To remove the dc part of $\omega$ and obtain $\Delta\omega$, generator speed is passed through a washout filter. The time constant of washout filter ($T_W$) is considered to be 10 sec which is big enough to allow the signal associated to subsynchronous mode pass without any changes.

A residue-based approach [189] is used to design the phase compensator (lead-lag compensator). The residue of subsynchronous mode is calculated as follows:

$$\begin{cases} \dot{\Delta x} = A\Delta x + B\Delta u \\ y = C\Delta x + D\Delta u \end{cases}$$

$$\text{(5.1)}$$

$$R_i = C\phi_i\psi_i B$$

where $\Delta x$ is the state vector, $\Delta y$ is the output vector, $A$ is the state matrix, $B$ is input matrix, $C$ is the output matrix, $D$ is the feedforward matrix, $R_i$ is the residue corresponding to $i^{th}$ mode, $\phi_i$ is the left eigenvector, and $\psi_i$ is the right eigenvector. The residue of each mode is a complex number which indicates the direction and the angles of the closed-loop eigenvalues leaving the corresponding pole in the root locus diagram [189]. Therefore, the angle required to be added to the subsynchronous mode for moving it to left half-plane (LHP) is calculated as follows [189]:

$$\angle\,\theta = \begin{cases} 180 - \angle R_i & 0 < \angle R_i < 180 \\ -180 - \angle R_i & -180 < \angle R_i < 0 \end{cases} \qquad \textbf{(5.2)}$$

The parameters of the phase compensator ($T_1$ and $T_2$) are designed to satisfy (5.2). After this step, the gain of the SSO damping controller ($K_D$) is tuned. Figure 5.2 is the root loci with increasing gain ($K_D = 0$ to 30) when the PV system is located at WF terminal and $\omega$ is used as the input signal for SSO damping controller. It is seen that increasing $K_D$ moves the subsynchronous mode to LHP and enhances the stability of this mode. $K_D$ has an adverse effect on supersynchronous mode which moves towards RHP but does not cross the imaginary axis.

Figure 5.2 also shows that an increase in $K_D$ improves the stability of electromechanical mode 1. Being far from the imaginary axis and in LHP, electromechanical mode 2 is not shown here to have better visibility of other modes. It is also noticed that $K_D$ variation does not cause any significant changes in damping of torsional mode. The system eigenvalues when PV-STATCOM controller is incorporated in the PV plant and with $K_D = 12$ are shown in Table 5.1. It is seen that the SSO damping controller stabilizes the subsynchronous mode. It is noticed that increasing $K_D$ improves the damping of subsynchronous mode but reduces the damping of supersynchronous mode. However, it does not notably affect electromechanical mode 2 and the torsional mode.
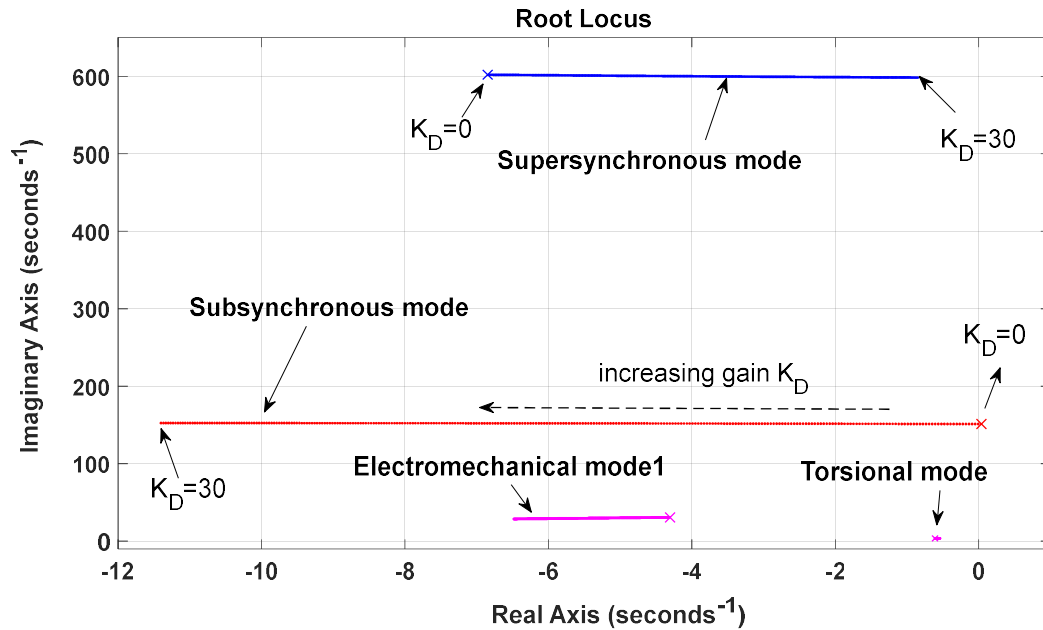
**Figure 5.2: Root locus diagram when PV located at WF terminal and as ω is the control signal**

The same procedure is conducted to design the SSO damping controller when PV plant is connected at line midpoint, and local transmission line current is considered as the input signal for SSO damping controller [83, 191]. Eigenvalues are obtained for this case with and without PV-STATCOM controller and depicted in Table 5.2. It is noted that without PV-STATCOM controller, system is unstable due to the subsynchronous mode instability. Figure 5.3 depicts the root locus diagram with increasing gain while the compensator is designed to satisfy (5.2). In Figure 5.3, $K_D$ various from 0 to 1. It shows that increasing $K_D$ has a stabilizing effect on subsynchronous mode whereas it has an adverse effect on supersynchronous mode and moves it towards RHP.

Unlike the previous case (Figure 5.2), increasing $K_D$ decreases the damping of Electromechanical mode 1 in this case (Figure 5.3). The torsional mode does not significantly move with the variation of $K_D$ in Figure 5.3. Eigenvalues of under-study modes are shown in Table 5.2. while PV plant is enhanced with PV-STATCOM controller and $K_D = 0.3$. It is seen that increasing $K_D$ improves the damping of subsynchronous mode but reduces the damping of supersynchronous mode. However, it does not quite affect electromechanical mode 1 and the torsional mode.

**Table 5.2: Eigenvalues of the system without and with PV-STATCOM controller,**
**$P_{WF}$ = 500 MW, PV system at Bus C, and $k$ = 55%.**

| Modes | Without PV-STATCOM | With PV-STATCOM |
|---|---|---|
| Network-1 (Sub) | 0.18 ± 150.8i | -2.58 ± 150.13i |
| Network-2 (Super) | -6.67 ± 602.43 | -3.79 ± 602.86i |
| Electro-mech-1 | -4.29 ± 31.12i | -4.1 ± 30.24 i |
| Electro-mech-2 | -58.93 ± 3.81i | -59.85 ± 3.95 i |
| Torsional | -0.619 ± 3.58i | -0.616 ± 3.52 i |
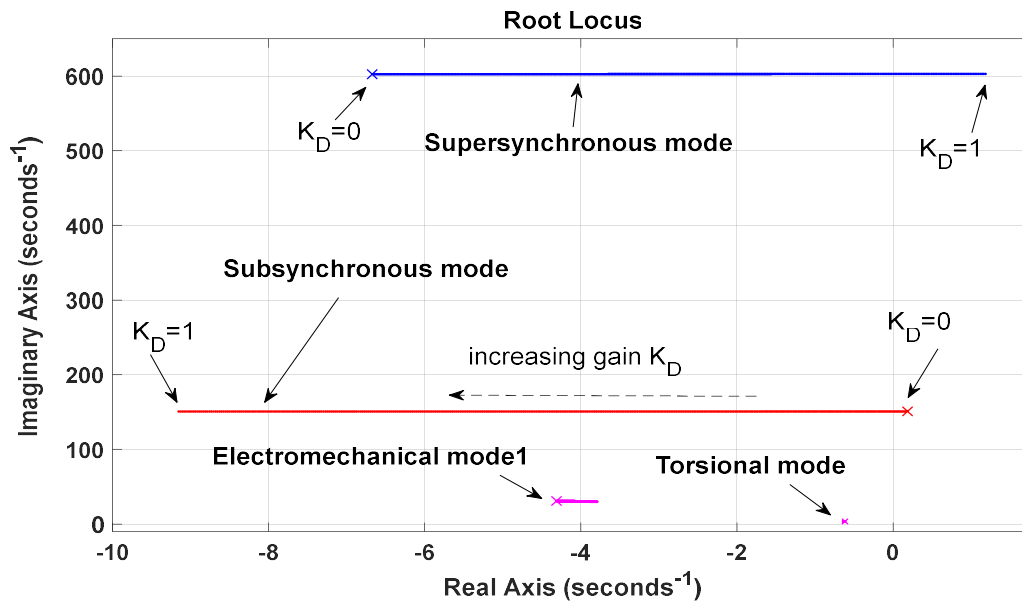


**Figure 5.3: Root locus diagram when PV located at line midpoint and as $I_{line}$ is the control signal**

## 5.4 Daytime Application of PV-STATCOM: PV System Connected at Wind Farm Terminal

This section presents the daytime performance of PV-STATCOM in alleviation of SSO. EMTDC/PSCAD simulation studies are conducted for: i) different power outputs of wind farm, ii) different sizes of wind farm, iii) different levels of series compensation, and iv) different locations of fault. A three-line-to-ground (3LG) fault is initiated at Bus D (remote

from the WF terminals) for 5 cycles at $t = 5$ sec. For all the studies, the size of the PV plant is 300 MW, i.e. $P_{PV} = 300$ MW.

## 5.4.1 Impact of PV-STATCOM Damping Controller

Figure 5.4 (a)-(d) depict the electrical torque ($T_e$) of wind farm, shaft torque ($T_{sh}$), rotor speed ($\omega$), and PCC voltage ($V_A$), respectively, when wind farm power output $P_{WF}$ is 500 MW, without PV-STATCOM damping control. $k$ is selected to be 55%. The system is seen to be unstable due to growing SSO in $T_e$, $\omega$, and $V_A$. Although SSO is reflected in $T_{sh}$, but it does not make $T_{sh}$ unstable in a similar time frame as $T_e$.
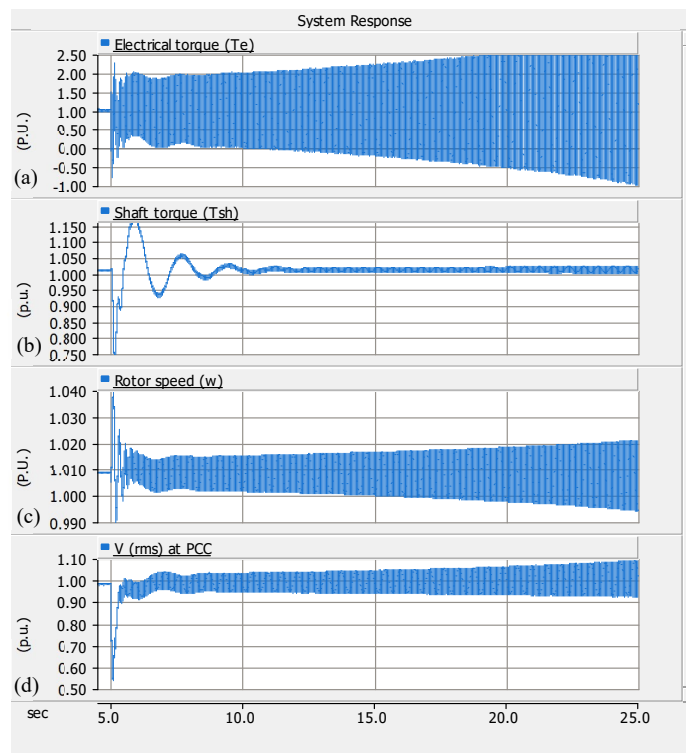


**Figure 5.4: System response, without PV-STATCOM controller, $P_{WF} = 500$ MW, PV system at Bus A, and $k = 55\%$**

Figure 5.5 (a)-(d) illustrate the system variables when the PV-STATCOM damping controller is implemented in PV system. The variables shown are correspondingly similar to Figure 5.4 (a)-(d). Comparison of these figures clearly validates the effectiveness of PV-STATCOM in damping SSO.

Figure 5.6 presents different variables of the system when $P_{WF}$ = 500 MW, $k$ = 55%, and PV-STATCOM control is implemented on the PV plant. Figure 5.6 (a)-(d) depict active power generation of PV system ($P_{PV}$), dc side current $I_{PV}$, dc side voltage ($V_{DC}$), reactive power generation of PV system ($Q_{PV}$), respectively. Before fault occurrence, the PV system operates in its conventional MPPT mode and $P_{PV}$ = 300 MW (Figure 5.6 (a)). Once fault takes place in the system at $t$ = $5$ sec, the dc voltage controller increases the dc voltage to $V_{OC}$ and makes $I_{PV}$ and $P_{PV}$ go to zero although with a slight delay based on the controller time constant. Consequently, the entire VSI capacity is made available for Full-STATCOM operation. Once SSO are damped and $\Delta\omega$ becomes less than 1 rad/sec at $t$ = $7.53$ sec, the PV system starts increasing $P_{PV}$ gradually to its pre-fault value in 4 sec. Based on grid codes [135, 154, 198], a gradual increment of $P_{PV}$ is required to prevent initiation of low frequency oscillations. The dc voltage controller commences power restoration process by decreasing the dc voltage in a ramped manner. During power ramp-up the PV plant continues to operate in Partial-STATCOM mode utilizing the remaining capacity of the VSI to avoid recurrence of SSO. The PV plant resumes its pre-fault power generation at $t$ = $11.53$ sec, i.e. just 6.53 sec after fault occurrence. After fault is initiated, the PCC voltage and reactive power undergo a short transient but stabilize quickly.
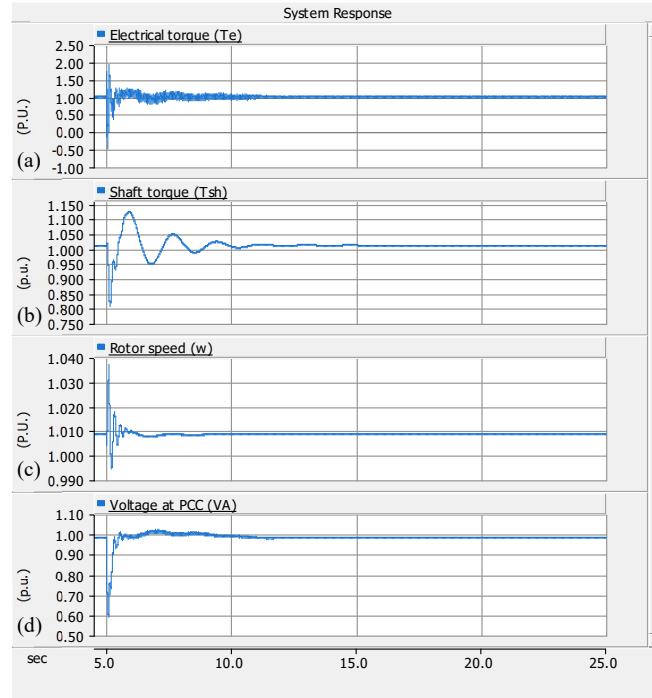
**Figure 5.5: System response, with PV-STATCOM controller, $P_{WF}$=500 MW, PV system at Bus A, and $k = 55\%$.**
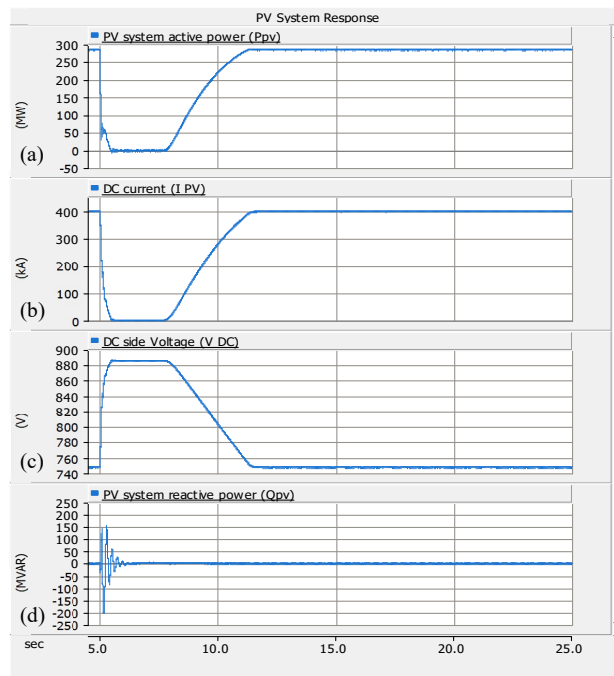


**Figure 5.6: System response, with PV-STATCOM controller, $P_{WF}$= 500 MW, PV system at Bus A, and $k = 55\%$.**

## 5.4.2 Impact of Wind Farm Power Generation

In this section, the effectiveness of PV-STATCOM in damping SSO for different levels of $P_{WF}$ (300 MW and 100 MW) for a 500-MW rated wind farm is demonstrated.

Figure 5.7 (a)-(d) illustrate different system variables for $P_{WF}$ = 300 MW. Figure 5.7 (a) depicts the electrical torque ($T_e$) without PV-STATCOM damping controller. It is seen that SSR occurs even when WF operates below its rated power. Figure 5.7 (b)-(d) depict electrical torque ($T_e$), active power flow of line ($P_{line}$), and reactive power exchanged by PV-STATCOM ($Q_{PV}$) with PV-STATCOM control in operation. Figure 5.7 (b) demonstrates that PV-STATCOM successfully stabilizes SSO in $T_e$ for $P_{WF}$ = 300 MW. Figure 5.7 (c) shows that when fault occurs at $t$ = *5* sec, $P_{line}$ decreases to 300 MW because $P_{PV}$ is made zero. At $t$ = *7.69* sec, when SSO is successfully damped by PV-STATCOM, the PV system starts restoring $P_{PV}$ and returns to its pre-fault generation level at $t$ = *11.69* sec. It can be seen in Figure 5.7 (d), that there are some damped oscillations during ramp-up which demonstrate PV-STATCOM operation in Partial-STATCOM mode to prevent the recurrence of SSO in the system.
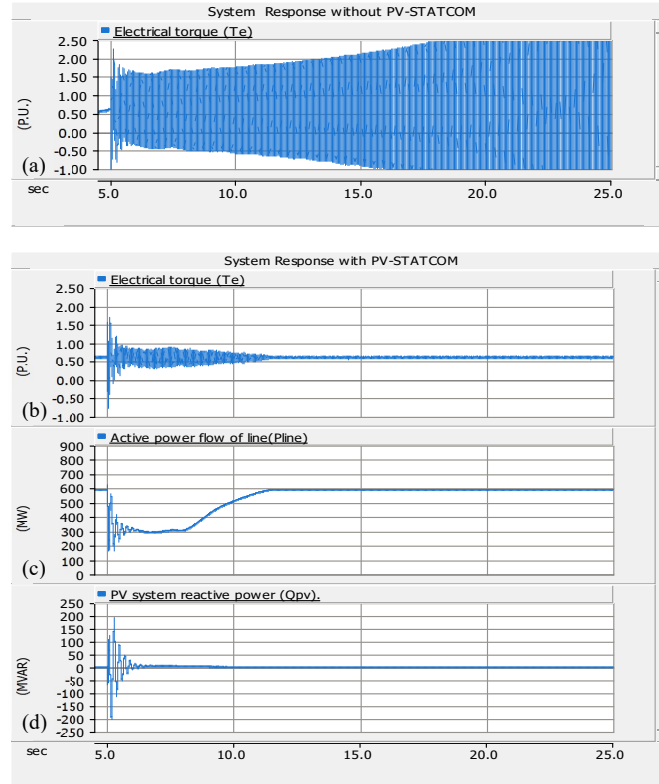
**Figure 5.7: System response, without and with PV-STATCOM controller, $P_{WF}$=300 MW, PV system at Bus A, $k = 55\%$.**

Figure 5.8 (a)-(d) illustrate various system variables when $P_{WF}$ is 100 MW. The variables shown are correspondingly similar to Figure 5.7 (a)-(d). The behavior of $T_e$, in Figure 5.8 (a), demonstrates that system without PV-STATCOM controller is unstable due to undamped SSO. Figure 5.8 (b) however illustrates that the PV-STATCOM successfully damps SSO.

As shown in Figure 5.8 (c), $P_{line}$ increases in a ramped manner after SSR mitigation at $t = 7.62$ sec, and reaches its pre-fault level at $t = 11.62$ sec. It is noted from Figure 5.8 (d) that the required $Q_{PV}$ for SSR mitigation is almost 150 Mvar when $P_{WF} = 100$ MW whereas it was almost 200 Mvar when $P_{WF} = 300$ MW (Figure 5.7 (d)).

Comparing the PV-STATCOM performance for different levels of $P_{WF}$ (500 MW, 300 MW, 100 MW) of a 500-MW WF, in Figure 5.6, Figure 5.7, and Figure 5.8, it is seen that the maximum $Q_{PV}$ which is required to alleviate SSR is 200 Mvar. The time needed for damping SSO and the power restoration time for all the cases is almost the same.
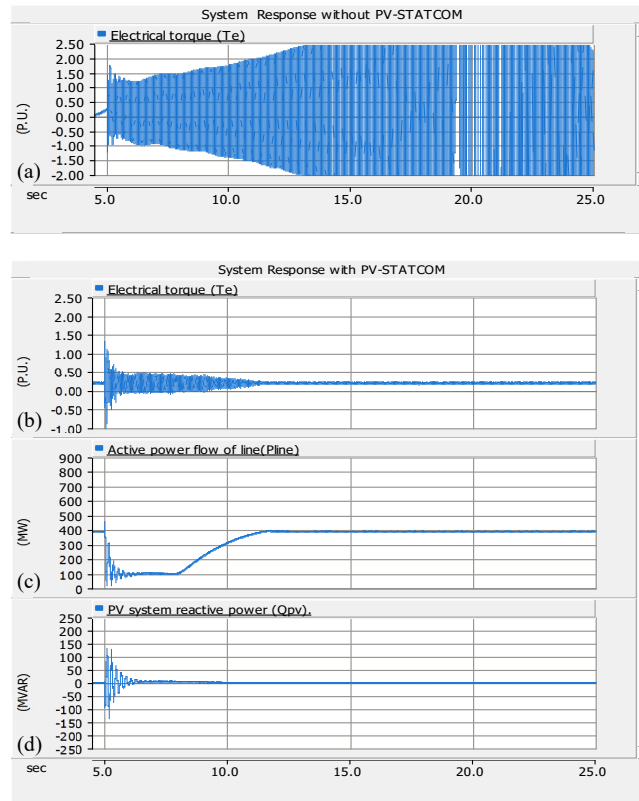
**Figure 5.8: System response, without and with PV-STATCOM controller, $P_{WF}$ = 100 MW, PV system at Bus A, $k$ = 55%.**

## 5.4.3 Impact of Wind Farm Size

The ability of PV-STATCOM in damping SSO for wind farms of different sizes/ratings, is investigated in this section. Figure 5.9 (a)-(d) show the system variables when wind farm size is 300 MW. The variables shown are correspondingly similar to Figure 5.7 (a)-(d). For this system, $k$ is considered to be 50% which excites 29-Hz SSO in the system [55]. Figure 5.9 (a) demonstrates that the system is unstable due to growing SSO in $T_e$, without PV-STATCOM. However, the behavior of $T_e$ and $P_{PV}$ in Figure 5.9 (b)-(c), respectively, demonstrate the ability of PV-STATCOM to mitigate SSO, successfully.

It is shown in Figure 5.9 (d) that PV-STATCOM alleviates SSO by using a maximum $Q_{PV}$ of 140 Mvar for the 300 MW rated WF producing $P_{WF}$ = 300 MW for $k$ = 50%. In comparison with Figure 5.7 (d), this amount is about 200 Mvar to stabilize a 500-MW rated WF generating $P_{WF}$ = 300 MW for $k$ = 55%
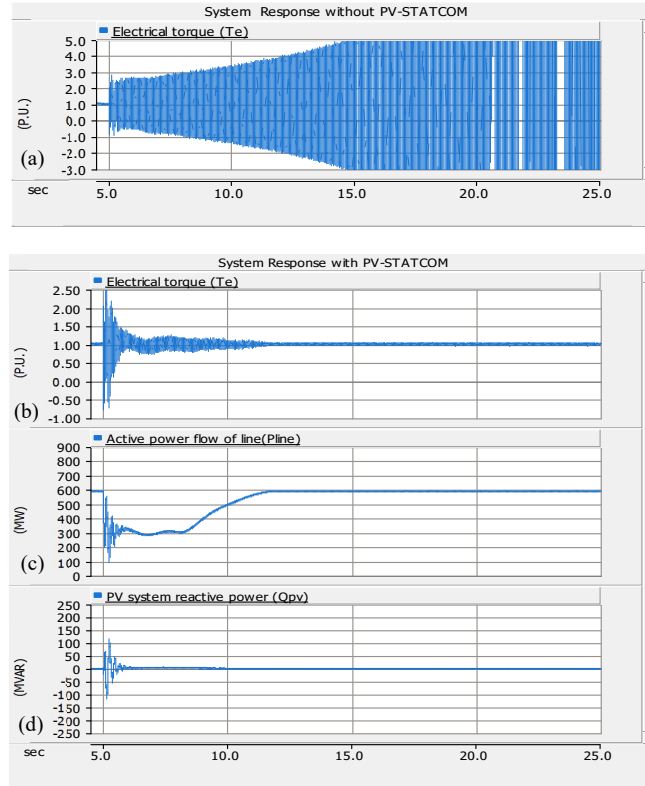
**Figure 5.9: System response, without and with PV-STATCOM controller, for *300-MW* wind farm, *k* = 50%, and PV system at Bus A.**

Studies are now conducted for a 100 MW rated WF. A higher series compensation level $k = 60\%$ is considered, which excites 35.63-Hz SSO in this system [55]. Figure 5.10 (a)-(d) depict system variables with 100-MW WF. The variables shown are correspondingly similar to Figure 5.7 (a)-(d). Furthermore, the behavior of these variables is also similar to those in Figure 5.8 (a)-(d), as already explained earlier.  It is shown in Figure 5.10 (d) that PV-STATCOM alleviates SSO by using a maximum $Q_{PV}$ of 90 Mvar for the 100 MW rated WF producing $P_{WF} = 100$ MW for $k = 60\%$. In comparison, this amount is about 140 Mvar to stabilize a 500-MW rated WF generating $P_{WF} = 100$ MW for $k = 55\%$.
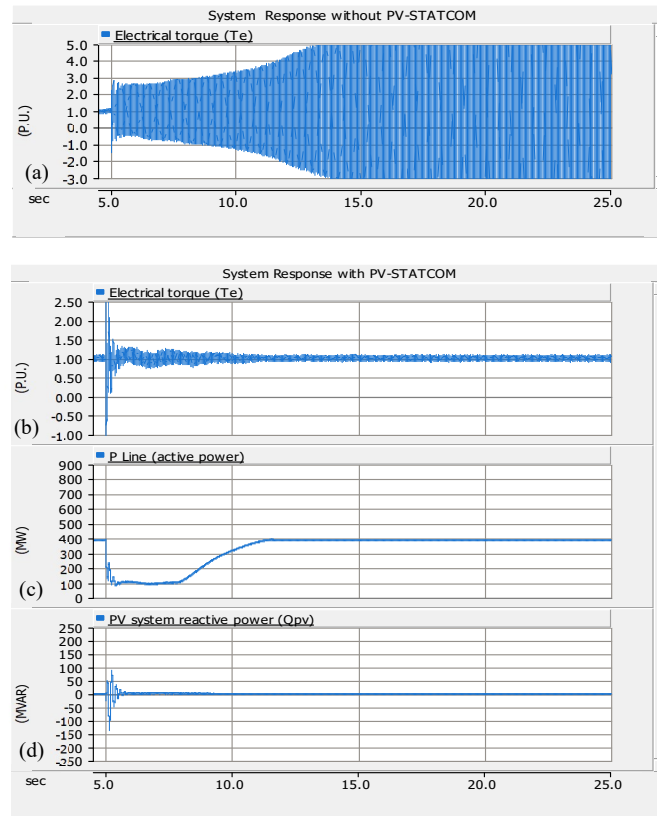
**Figure 5.10: System response, without and with PV-STATCOM controller, for *100-MW* wind farm, *k* = 60%, and PV system at Bus A.**

## 5.4.4 Impact of Fault Location

The fault location is now moved to the terminals of the WF. Studies are conducted for the same three-line-to-ground (3LG) fault at Bus B for 5 cycles at $t = 5$ sec. In this study, $k = 55\%$ and the size of WF is 500 MW with $P_{WF} = 500$ MW.

Figure 5.11 (a) depicts $T_e$ without PV-STATCOM control, whereas Figure 5.11 (b)-(d) represent $T_e$, $P_{line}$ and $Q_{PV}$, all with PV-STATCOM control. The PV-STATCOM is seen to be successful in damping SSO in this case. When the fault is at WF terminal, a higher component of WF rotor mode oscillations is exhibited in $T_e$ as compared to the case when the fault is at remote Bus D, as evident from Figure 5.5 (a). This is expected as the terminal fault is likely to have a bigger impact on the rotor torsional modes.

As depicted in Figure 5.11 (d), the maximum $Q_{PV}$ required to damp SSO is 150 Mvar which is less than the corresponding amount of 200 Mvar required for SSO damping when the

fault was at Bus D (Figure 5.6 (d)). The total time required to damp SSO and restoration of power is 7.56 sec which is almost the same as when the fault was at Bus D ($t = 7.53$ sec).
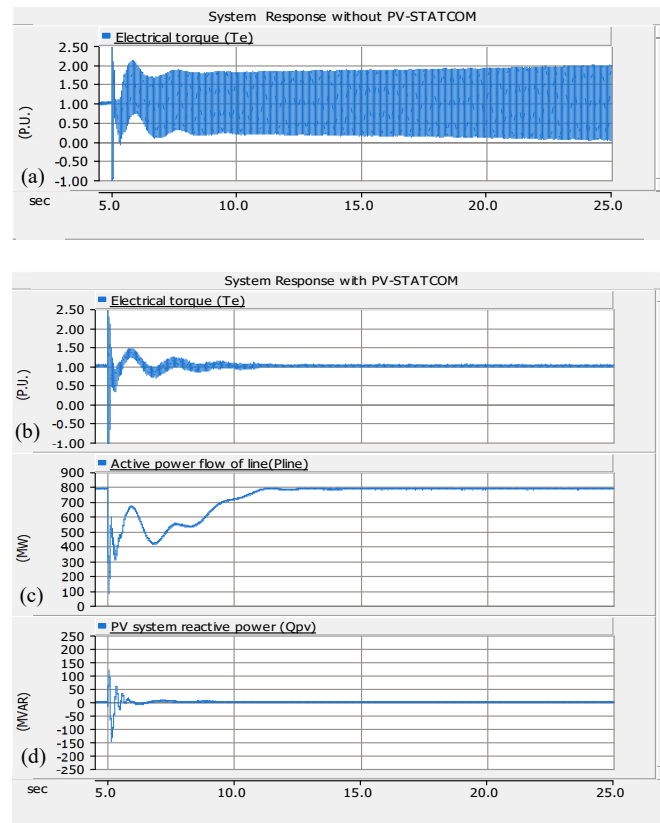


**Figure 5.11: System response, without and with PV-STATCOM controller, $P_{WF} = 500$ MW, $k = 55\%$, for different fault location (Bus B)**

## 5.4.5 Impact of Series Compensation Level

The performance of PV-STATCOM in alleviating SSR for different series compensation level $k$ is investigated in this section. Figure 5.12 (a)-(d) depict the system variables for a high series compensation level $k = 80\%$. The variables shown are correspondingly similar to those in Figure 5.7 (a)-(d). Without PV-STATCOM control, it is seen in Figure 5.12 (a) that $T_e$ increases over 120 p.u. which is significantly more than that in Figure 5.4 (a) for $k = 55\%$. However, Figure 5.12 (b)-(d) confirm that PV-STATCOM can successfully damp SSO even for this high level of $k$. In this case, $Q_{PV}$ exchanged to alleviate SSO (Figure 5.12 (d)), is about 250 Mvar which is more than 200 Mvar reported for the case of $k = 55\%$ (Figure 5.6 (d)).
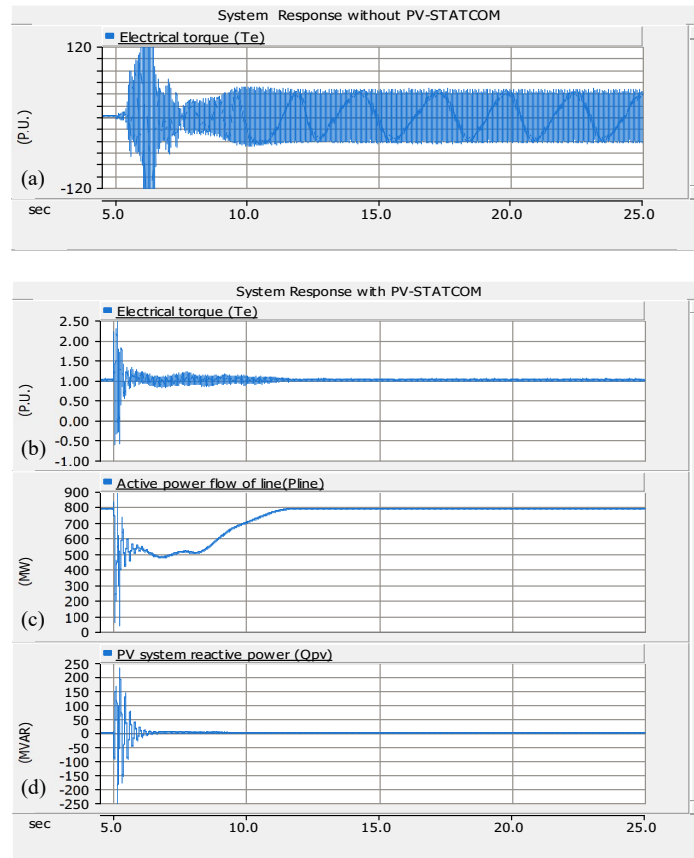
**Figure 5.12: System response, without and with PV-STATCOM controller; $P_{WF}$ = 500 *MW*, for $k$ = 80%.**

## 5.5  Daytime Application of PV-STATCOM: PV System Connected at Line Midpoint

The SSO damping performance of PV-STATCOM when PV system is connected to the middle of the line is studied here. To avoid communication delays, line current (as a local signal) is chosen as the damping control signal. EMTDC/PSCAD studies are conducted for 500 MW rated WF producing $P_{WF}$ = 500 MW and $P_{WF}$ = 300 MW when $k$ = 55%.

Figure 5.13 (a)-(d) depict the system variables for the case $P_{WF}$ = 500 MW, whereas Figure 5.14 (a)-(d) depict the system variables when $P_{WF}$ = 300 MW. The variables shown are correspondingly similar to those in Figure 5.7 (a)-(d). It is seen from Figure 5.13 (a) and Figure 5.14 (a) that without PV-STATCOM controller, the system is unstable due to both relatively large and undamped SSO in $T_e$. However, Figure 5.13 (b) and Figure 5.14 (b) demonstrate that the PV-STATCOM with local line current based damping control can

successfully mitigate these large magnitude SSO. At the occurrence of fault, the PV real power generation is ceased and reduces $P_{line}$ (Figure 5.13 (c) and Figure 5.14 (c)). Once the SSO in the line current are damped to less than 2% of current magnitude, the PV power is restored in a ramped manner while keeping the SSO damping function activated in the Partial-STATCOM mode, as explained in earlier sections. The PV-STATCOM reactive power $Q_{PV}$ for SSO damping is about 250 Mvar for both $P_{WF} = 500$ MW and $P_{WF} = 300$ MW, as seen in Figure 5.13 (d) and Figure 5.14 (d), respectively. It is noted that the corresponding $Q_{PV}$ for SSO damping is about 200 Mvar, when the PV system is located at WF terminal.
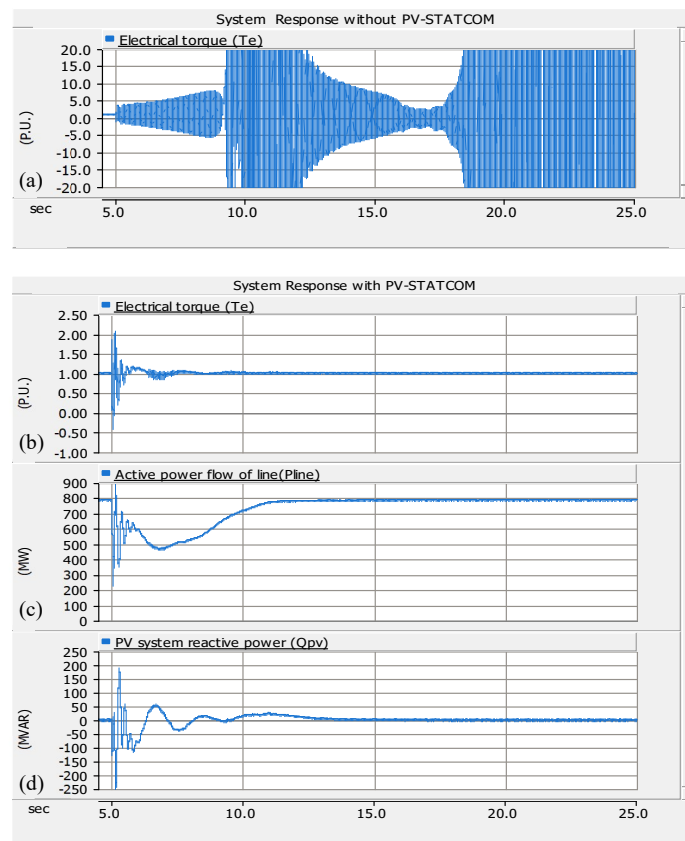


**Figure 5.13: System response, without and with PV-STATCOM controller, $P_{WF} =$ 500 MW, PV system located at line midpoint, and $k = 55\%$**
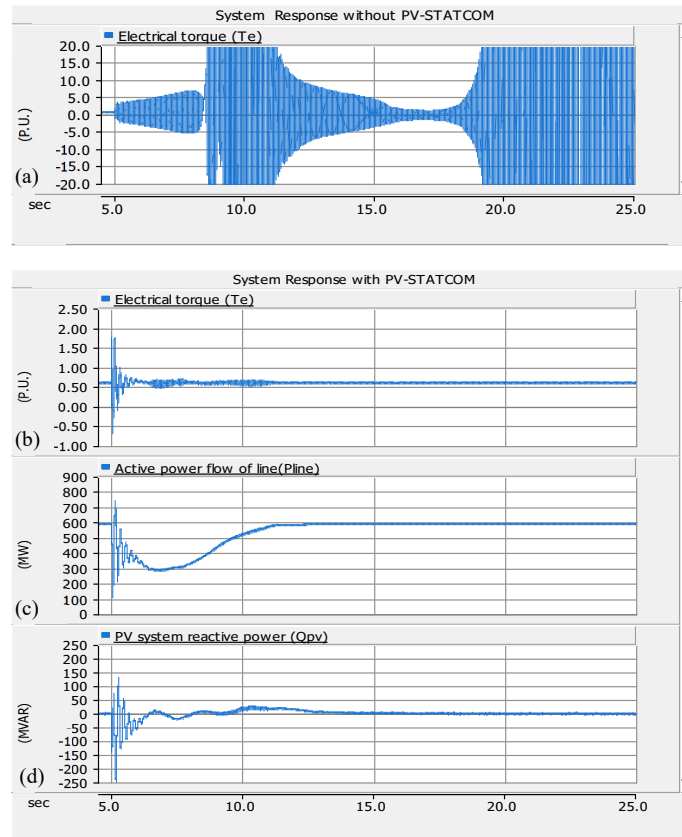
**Figure 5.14: System response, without and with PV-STATCOM controller, $P_{WF}$ = 300 MW, PV system located at line midpoint, and $k$ = 55%**

## 5.6   Nighttime Application of PV-STATCOM

The nighttime performance of PV-STATCOM for SSO damping is now investigated for a three-line-to-ground fault at Bus D (remote from WF terminals) for 5 cycles at $t$ = 5 sec.

Figure 5.15 (a)-(d) and Figure 5.16 (a)-(d) depict the system variables when PV plant is located at Bus A and Bus C, respectively. The variables shown are correspondingly similar to those in Figure 5.7 (a)-(d).

At fault occurrence, the system becomes unstable due to undamped SSO, which get stabilized with PV-STATCOM. Some initial transients and wind farm torsional mode oscillations are seen in line power flow $P_{line}$. The magnitude of torsional mode oscillations is slightly higher when the PV system is connected at line midpoint instead of at WF terminal. This difference is attributed to the use of local line current as damping signal with

a different controller when PV system is located midline, compared to the use of generator speed as damping control signal when PV system is connected at WF terminal.

Comparing Figure 5.15 (d) and Figure 5.16 (d), it is noted that a larger $Q_{PV}$ of 200 Mvar is needed to damp SSO when PV system is located at midline than $Q_{PV}$ of 150 Mvar when PV system is connected at WF terminal. At nighttime, the SSO damping process takes less than 10 seconds and is faster than daytime because no real power cessation and subsequent restoration is involved.
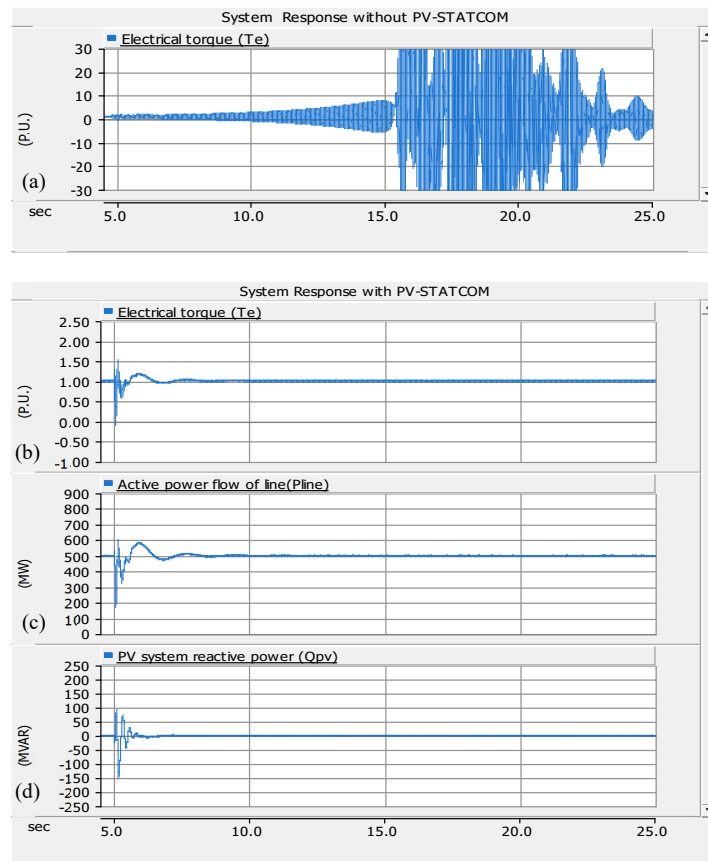


**Figure 5.15: System response, without and with PV-STATCOM controller, nighttime, PV system is connected at Bus A, $P_{WF}$ = 500 MW, and $k$ = 55%.**
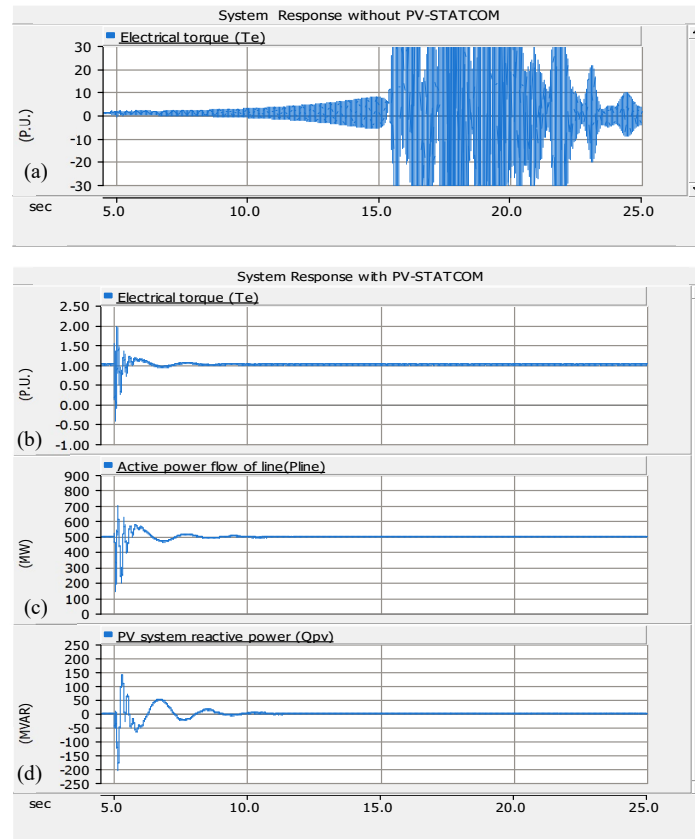
**Figure 5.16: System response, without and with PV-STATCOM controller, nighttime, PV system is connected at Bus C, $P_{WF}$ = 500 MW, and $k$ = 55%.**

## 5.7 Discussions

Nowadays, a large number of PV solar farms rated more than 100 MW are already commissioned and increasingly being developed around the world [12, 14]. Some examples of large-scale PV plants are: Tengger Desert Solar Park (1500 MW) in China, Kurnool Ultra Mega Solar Park (1000 MW) in India, Yanchi Solar PV Station (1000 MW) in China, Longyangxia Dam Solar Park (850 MW) in China, Kamuthi Solar Power Project (648 MW) in India, Solar Star I and II (579 MW) in USA, Desert Sunlight Solar Farm and Topaz Solar Farm (550 MW each) in USA [12, 14].

The typical size of STATCOM required for SSR damping in power transmission systems is about 200 Mvar [55, 82, 83, 107]. Hence, given a need, large solar farms can provide PV-STATCOM functionality for mitigation of SSO.

Some other key developments that may be conducive for the above novel application of solar farms are: i) PV farms are being connected to series compensated lines, e.g. 290 MW Agua Caliente Solar Project in USA is connected to a series compensated 500 kV line [197], ii) some IG-based Type-1 WFs are connected to series compensated lines , e.g., 300 MW Stateline wind farm in USA is connected to a series and shunt-compensated network in BPA transmission network [55], and iii) a trend of co-locating wind farms and PV farms is also happening, e.g. in Ontario [163] and Australia [164].

## 5.8 Conclusion

This chapter presents the concept of utilizing large-scale PV solar farms as a STATCOM on 24/7 basis, named PV-STATCOM, to alleviate instability caused by subsynchronous oscillations in IG-based Type-1 wind farm connected to a series compensated line.

A modified IEEE First SSR Benchmark system including a 500 MW IG-based wind farm and a 300-MW PV solar farm is employed to study the effectiveness of PV-STATCOM in SSO mitigation. Wind generator speed is used as the control signal for damping controller when PV plant is connected at the WF terminal, whereas line current, a local signal, is utilized when PV plant is located at line midpoint. The PV-STATCOM performance is demonstrated through small-signal modal analysis utilizing MATLAB/Simulink and electromagnetic transient studies using PSCAD/EMTDC software. The following conclusion are made:

1) Daytime: PV-STATCOM effectively alleviates SSO for:

- Different levels of wind farm power output ($P_{WF}$ = 100 MW, 300 MW, and 500 MW). Higher $P_{WF}$ requires larger PV system reactive power $Q_{PV}$ for SSO mitigation.
- Various sizes of wind farms: 100 MW, 300 MW, and 500 MW. Higher $Q_{PV}$ is needed for stabilizing SSO in larger WFs.
- Different fault locations - either remote from WF (Bus D) or at terminal of WF (Bus B). Less $Q_{PV}$ is required to mitigate SSO when fault occurs at Bus B.
- Various series compensation levels. Higher $k$ causes more severe SSO which requires larger $Q_{PV}$ for SSO alleviation.
- Different locations of PV plant - WF terminal (Bus A) or line midpoint (Bus C). Higher

$Q_{PV}$ is required for stabilizing SSO when PV system is located at Bus C than at Bus A.

2) Nighttime: PV-STATCOM successfully mitigates SSO in 500-MW IG-based WF for different PV plant locations: Bus A or Bus C.

The entire process of SSO instability mitigation from the instant of fault to restoration of PV solar farm power to its pre-fault condition takes place in less than half a minute.

This novel application of PV solar farm as PV-STATCOM for SSO mitigation in Type-1 WFs can obviate the need of installing expensive STATCOMs or SVCs for same objective.

Chapter 6

# 6 Control Coordination of PV-STATCOM and DFIG-Based Wind Farm for Subsynchronous Oscillation Damping

## 6.1 Introduction

SSR damping controls in Doubly-Fed Induction Generator (DFIG) based Type 3 wind farms have already been proposed and implemented [56, 62, 96, 115]. Moreover, the efficacy of new controls on PV solar farms as PV-STATCOM for SSR mitigation have been described in previous chapters. With the rapid growth of wind and PV solar plants worldwide, it is quite likely that PV solar farms and wind farms may be located in close vicinity, and may be connected to already quite prevalent series compensated transmission lines. Since the SSR controls on both PV solar farms and wind farms are based on power electronic converters and operate at similar response speeds, there is a potential for them to interact in an adverse manner. This chapter presents a study of the need and development of a coordinated control of PV-STATCOM and DFIG converter to damp subsynchronous oscillations in DFIG-based wind farm connected to a series compensated transmission line. Line current is considered as a local control signal for the SSR damping controllers. The optimization block of MATLAB software, Genetic Algorithm (GA), is utilized to obtain the optimal parameters for the subsynchronous damping controllers. The performance of the designed controllers is validated through MATLAB/Simulink simulation studies.

## 6.2 Study System Model

Figure 6.1 depicts the study system which is derived from the IEEE First SSR Benchmark system. Most of the recent studies on SSR investigation and alleviation in wind farms (IG-based or DFIG-based) are conducted on systems which are modified versions of IEEE First SSR Benchmark system [44, 55, 56, 58, 59, 65, 90, 94, 95, 115].

The DFIG-based wind farm, shown in Figure 6.1, is rated 100 MW which is an aggregation of 50 identical wind turbine units, each with a power rating of 2 MW [58, 61]. The wind farm is connected to infinite bus through a 161-kV series compensated transmission line. A PV solar farm, which is rated 100 MW, is also connected to the series compensated

network of Figure 6.1 at the wind farm terminal (Bus A). The parameters of the study system in this chapter are presented in Appendix A.

The DFIG-based wind farm model is explained in Section 2.4 which includes shaft system, wound-rotor induction generator, rotor-side converter (RSC) and grid-side converter (GSC). The converters of the DFIG system are approximately rated 30% of the nominal power of the induction generator [9]. The reactance of the GSC transformer is denoted by $X_{tg}$ in Figure 6.1. An aggregated two-mass wind turbine is considered to model the dynamics of the shaft system, described in Section 2.3.3. The wind speed is considered 7 m/s. It is found from Table 2.3 that the corresponding optimum rotor speed is $\omega_r = 0.75$ p.u., the maximum mechanical power is $P_m = 0.32$ p.u., and the corresponding shaft torque is $T_m = 0.43$ p.u.

The PV solar farm model explained in Section 2.5, comprises a voltage source inverter (VSI) which is connected to a capacitor and a controlled current source on its dc side. The 100-MW PV system uses a 111 MVA inverter [150]. Due to grid codes such as IEEE Standard 1547-2018 [135], PV inverters are required to provide reactive power even when PV solar farm generates its rated active power. Therefore, the MVA rating of PV inverter is considered higher than its MW rating. On its ac side, the VSI is linked to the transmission line through a filter and a coupling transformer. The dc source follows the I-V characteristic of PV panels of the solar farm. To extract maximum power from PV panels, the PV system employs maximum power point tracking (MPPT) system [15].
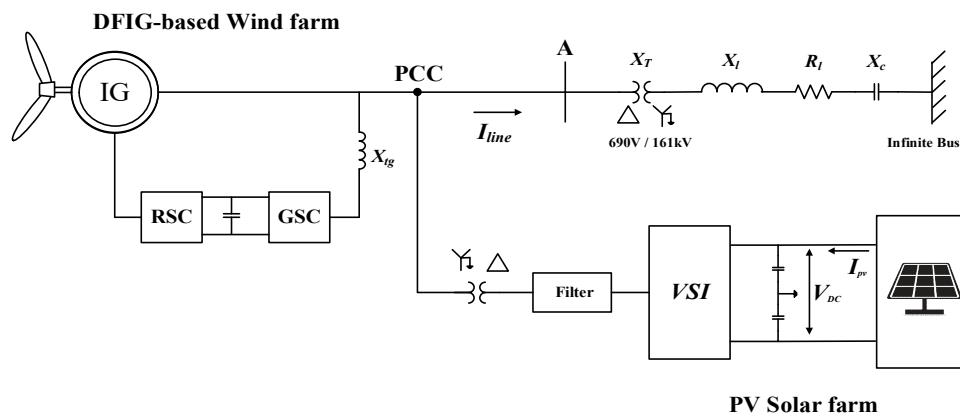


**Figure 6.1: Study system: DFIG-based wind farm and PV solar farm connected to a series compensated transmission line**

## 6.3  Study of Subsynchronous Oscillations

In this section, the MATLAB/Simulink software is employed to investigate subsynchronous oscillations in the study system. Subsynchronous oscillations in DFIG-based wind farm are mainly due to adverse interactions between the controller of DFIG and the series compensated transmission system which is called subsynchronous control interaction (SSCI) [27-37].

Table 6.1 illustrates eigenvalues of the system when the wind speed ($V_{wind}$) is 7 m/s, the series compensation level ($k$) is 75%, and active power generation of the PV system ($P_{PV}$) is 100 MW. It is observed from Table 6.1 that the system is unstable due to its subsynchronous mode.

**Table 6.1: Eigenvalues of the system, $V_{wind}$ = 7 m/s, $P_{PV}$=100 MW, $k$ = 75%, and without subsynchronous damping controller**

| Modes | Eigenvalues |
|---|---|
| **Network-1(Sub)** | 4.737 ± 122.18i |
| **Network-2(Super)** | -7.659 ± 630.90i |
| **Electromechanical** | -14.007 ± 98.67i |
| **Shaft mode** | -1.349 ± 5.88i |

A three-line-to-ground (3LG) fault for 5 cycles is initiated at the end of the transmission line at *t = 5 sec*. The fault studies are performed for $V_{wind}$= 7 m/s, $P_{PV}$= 100 MW, and $k$ = 75%. The post-fault behavior of the system is shown in Figure 6.2 (a)-(c) depicting electrical torque ($T_e$), voltage at PCC ($V_{PCC}$), and line current ($I_{line}$), respectively. The system is seen to be unstable due to growing subsynchronous oscillations in system parameters which validates the results of Table 6.1. Figure 6.3 illustrates the results of FFT analysis of the electrical torque. It shows that there is a peak at frequency of 19.47 Hz (122.33 rad/sec) which matches with the frequency of subsynchronous  mode in Table 6.1.
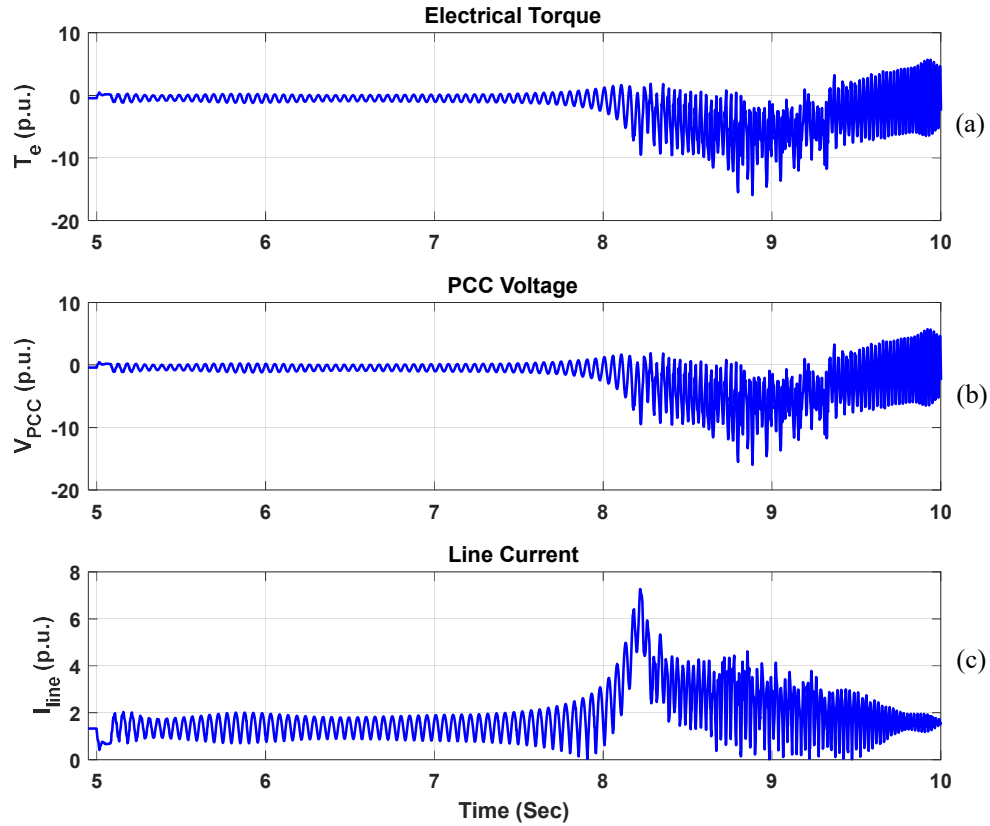
**Figure 6.2: System response, $V_{wind}$ = 7 m/s, $P_{PV}$ =100 MW, $k$ = 75%, and without subsynchronous damping controller**
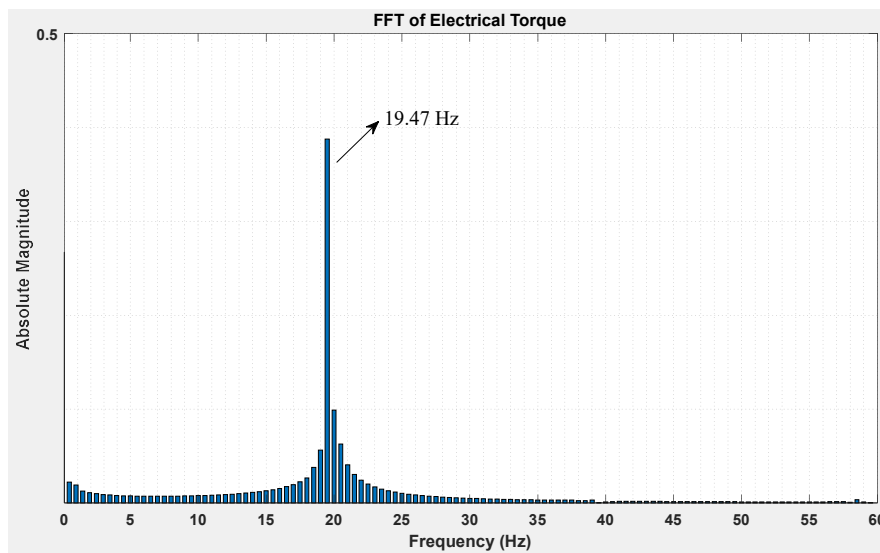


**Figure 6.3: FFT of the electrical torque (T$_e$) while $V_{wind}$ = 7 m/s, $P_{PV}$ =100 MW, $k$ = 75%, and without subsynchronous damping controller**

In the following sections, the damping of SSR in DFIG-based wind farm by utilizing DFIG-converter and/or PV-STATCOM is presented.

## 6.4  SSR Damping by DFIG Converter

Figure 2.10 (a)-(c) depict the configuration of RSC controller, GSC controller, and subsynchronous damping controller considered for DFIG converter, respectively. All the controllers are modeled in *dq*-reference frame. The voltage vector is aligned with quadrature axis and $V_d$ equals zero. Thus, the reactive powers of the converters are controlled with the *d*-axis control loop whereas their active powers are controlled by the *q*-axis loop.

### 6.4.1 Damping Controller

Various signals such as output active power of wind farm ($P_{DFIG}$), line real power ($P_{line}$), voltage across the series capacitor ($V_c$), and line current ($I_{line}$) are used to damp SSR in DFIG-based wind farm [56, 62, 96, 115]. In this chapter, $I_{line}$ is considered as a local control signal for subsynchronous damping controller. The configuration of subsynchronous damping controller is depicted in Figure 6.4 which includes a washout filter block, controller gain block, phase compensator (lead-lag compensator) and a limiter block. This controller is connected at point G of GSC controller [56, 94], i.e. at wind farm terminal voltage ($V_S$ or $V_{PCC}$) controller. The control signal ($I_{line}$) is passed through the washout filter to obtain line current deviation which reflects the subsynchronous oscillations in the system. The output of the damping controller is added to the point $G$ of GSC to modulate the reactive power of GSC ($Q_g$) to mitigate SSCI in the system.
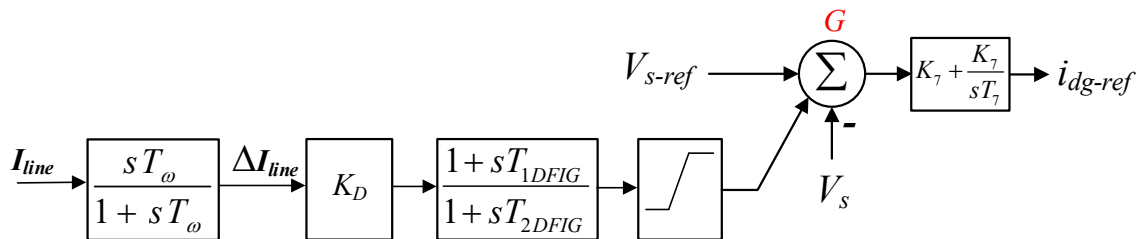


**Figure 6.4: Subsynchronous damping controller of DFIG converter**

The parameters of the damping controller are obtained by employing the optimization toolbox of MATLAB software, based on genetic algorithm (GA). The objective function (OF) which has to be minimized to find the optimal parameters of the controller is defined in (6.1) where $\xi_i$ is the damping ratio of the $i^{th}$ eigenvalue of the system.

$$OF = \sum_{j=1}^{n} (1 - |\xi_i|), \qquad \xi_i > 0 \tag{6.1}$$

subject to constraints that system eigenvalues of the are located in LHP and have positive damping ratio. The obtained parameters of the damping controller are given in Appendix B.

## 6.4.2 Eigenvalue Analysis and Electromagnetic Transients Study of SSR Damping by DFIG

Table 6.2 shows the eigenvalues of the system utilizing optimized damping controller obtained by the linearization toolbox of MATLAB software. It is seen that the damping controller successfully stabilizes the subsynchronous mode and thus the overall system. Comparison between Table 6.2 and Table 6.1 shows that while the damping controller stabilizes the subsynchronous mode, it decreases the damping of supersynchronous mode and electromechanical mode. The subsynchronous damping controller however does not affect the shaft mode.

**Table 6.2: Eigenvalues of the system, $V_{wind}$ = 7 m/s, $P_{PV}$ =100 MW, $k$ = 75%, and with subsynchronous damping controller on DFIG Converter**

| Modes | Eigenvalues |
|---|---|
| Network-1 (Sub) | -9.808± 121.54i |
| Network-2 (Super) | -2.380 ± 626.89i |
| Electromechanical | -13.668 ± 100.79i |
| Shaft mode | -1.356 ± 5.90i |

The effectiveness of the subsynchronous damping controller is also investigated through the time domain simulation studies for the same operating conditions. Figure 6.5 (a)-(d)

depict electrical torque ($T_e$), voltage at PCC ($V_{PCC}$), line current ($I_{line}$), and reactive power of GSC ($Q_g$), respectively. It is apparent from these figures that SSR in the system is successfully alleviated through reactive power modulation provided by the damping controller.
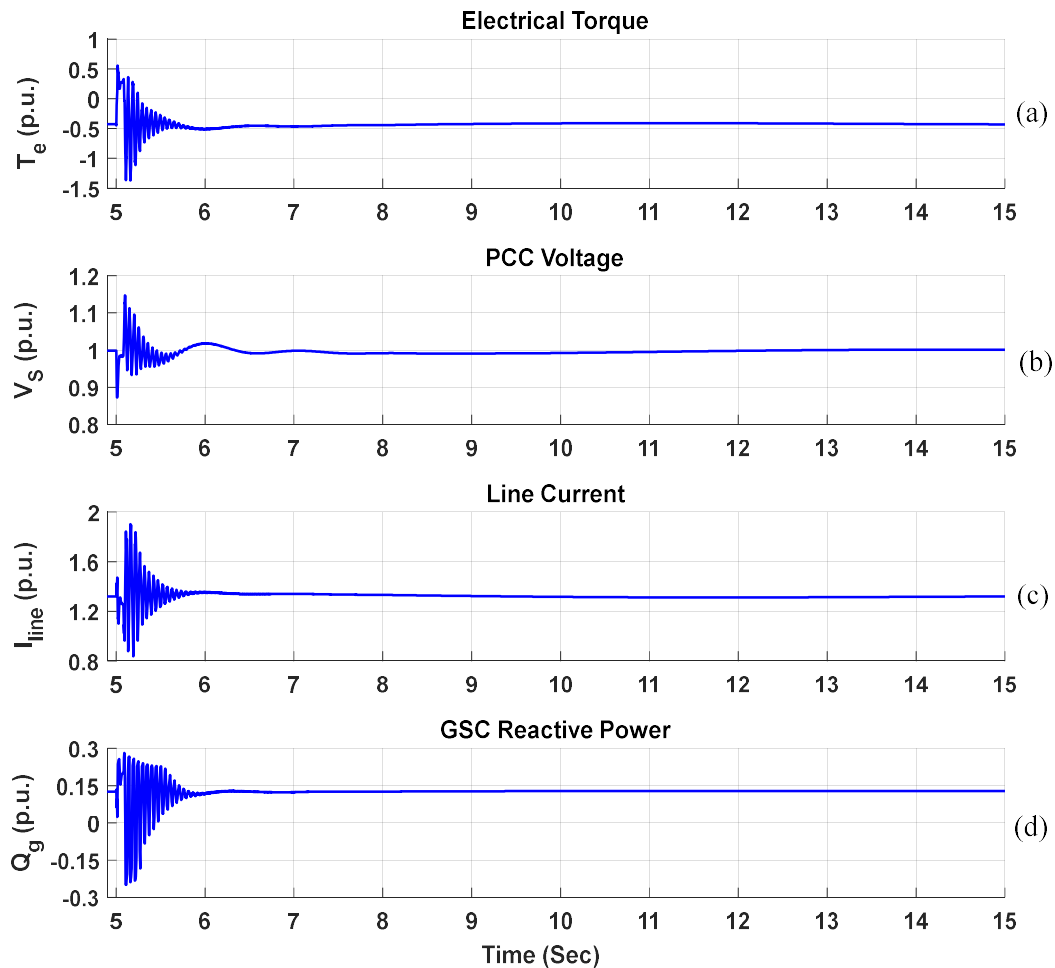


**Figure 6.5: System response, $V_{wind}$ = 7 m/s, $P_{PV}$ =100 MW, $k$ = 75%, and with subsynchronous damping controller on DFIG Converter**

## 6.5  SSR Damping by PV-STATCOM

Studies for damping SSR in DFIG-based wind farm by utilization of PV inverter as PV-STATCOM is presented in this section. Figure 6.6 depicts the PV inverter controller augmented by PV-STATCOM controller which consists of a damping controller, DC voltage controller with PPT system, and the conventional PV current controller. The PV inverter controller, like DFIG converters controller, is based on the *dq*-reference frame

model of VSI. The voltage vector is aligned with the quadrature axis and $V_d$ equals zero. Consequently, the reactive power of the VSI is controlled by $d$-axis control loop, and its active power is controlled by the $q$-axis control loop.

The current control block, as explained in section 2.6.3, controls the output current of the PV inverter based on the references provided by the DC voltage controller and the damping controller. As described in section 2.6.4, the DC voltage controller including the PPT block adjusts the active power generation of the PV system ($P_{PV}$) based on the system condition by providing $i_{q\text{-}ref}$ for current controller.

## 6.5.1 Damping Controller

The damping controller modulates the reactive power output of PV inverter ($Q_{PV}$) to alleviate SSR in the system by providing $i_{d\text{-}ref}$ for current controller. As shown in Figure 6.6, the damping controller consists of a washout filter block, controller gain block, phase compensator (lead-lag compensator) and a limiter block. Similar to the damping controller of DFIG converter, the proposed damping controller for PV system also utilizes line current as of the control signal. The damping controller measures $I_{line}$ continuously and passes it through the washout filter. Then, the output of the washout filter ($\Delta I_{line}$), which reflects the subsynchronous components of the line current, is adjusted by a gain factor ($K_{PV}$). Subsequently, the phase of the controller gain block output is compensated by a lead-lag compensator. The output of the damping controller, $i_{d\text{-}ref}$, is then passed to the current controller. Consequently, the output reactive power of the PV system gets modulated to mitigate SSR in the system by the damping controller.

To attain maximum damping, the parameters of the damping controller are obtained through the same optimization procedure which is used to achieve the parameters of the damping controller of the DFIG converter in section *6.4.1*. The parameters of the damping controller are presented in Appendix B.
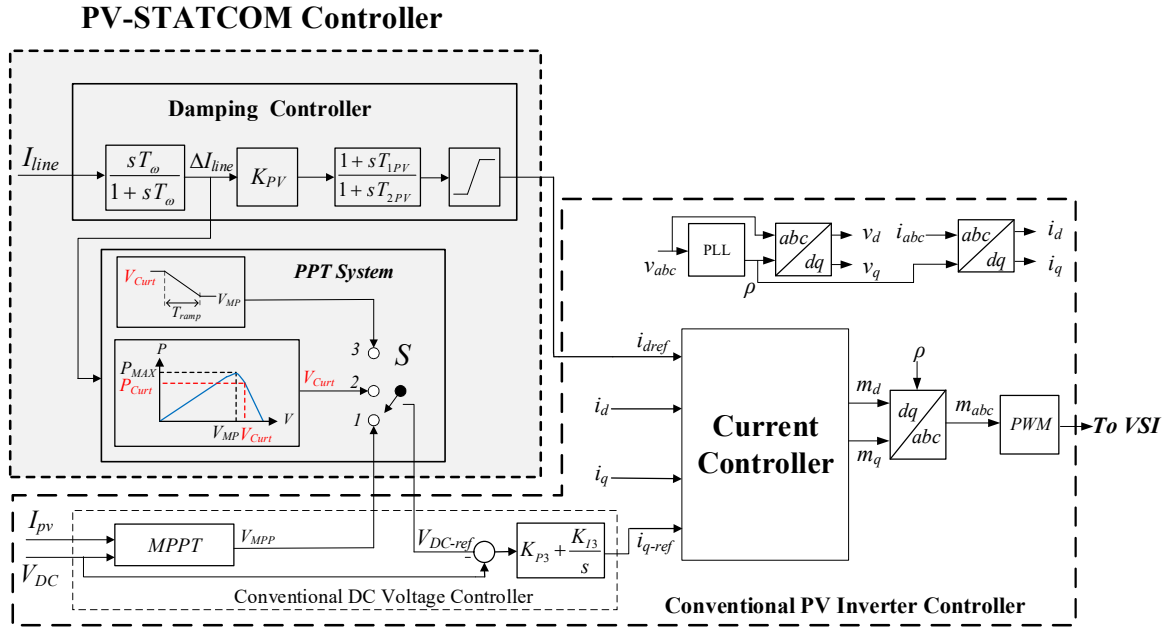
**Figure 6.6: PV inverter controller configuration**

## 6.5.2 Eigenvalue Analysis and Electromagnetic Transients Study of SSR Damping by PV-STATCOM

Table 6.4 shows the eigenvalues of the system with PV-STATCOM controller implemented in the PV system, $P_{PV}$ =100 MW, $V_{wind}$ = 7 m/s, and $k$ = 75%. Comparison between Table 6.4, Table 6.2, and Table 6.1 shows that PV-STATCOM damping controller successfully stabilizes the subsynchronous mode while keeping the other modes stable. PV-STATCOM controller significantly improves the damping of subsynchronous mode, even more than the GSC damping controller. PV-STATCOM decreases the damping of supersynchronous mode similar to GSC damping controller but only slightly. The PV-STATCOM, slightly decreases the damping of electromechanical mode like the DFIG converter damping controller. The PV-STATCOM controller does not impact the shaft mode similar to DFIG converter damping controller.

**Table 6.3: Eigenvalues of the system, $V_{wind}$ = 7 m/s, $P_{PV}$ =100 MW, $k$ = 75%, and with PV-STATCOM**

| Modes | Eigenvalues |
|---|---|
| Network-1(Sub) | -11.93 ± 134.72i |
| Network-2(Super) | -6.30 ± 625.92i |
| Electromechanical | -11.879 ± 99.75i |
| Shaft mode | -1.36 ± 5.91i |

Figure 6.7 (a)-(c) depict electrical torque ($T_e$), voltage at PCC ($V_{PCC}$), and line current ($I_{line}$), respectively. The post-fault behavior of $T_e$, $V_{PCC}$, and $I_{line}$ show that the PV-STATCOM successfully alleviates SSO in the system.
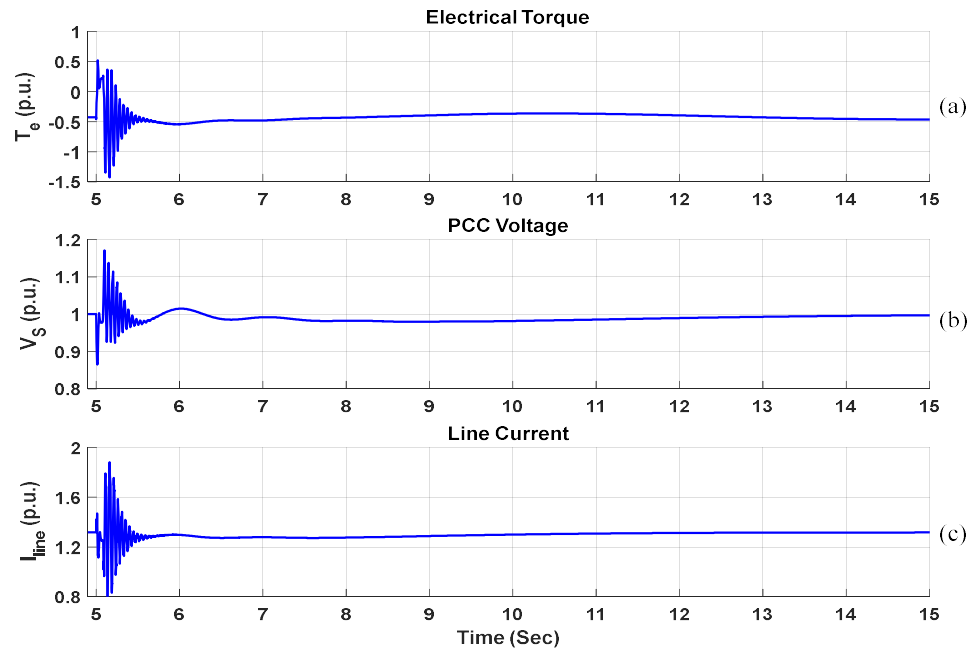


**Figure 6.7: System response, $V_{wind}$ = 7 m/s, $P_{PV}$ =100 MW, $k$ = 75%, and with PV-STATCOM**

Figure 6.8 (a)-(d) illustrate the active power generation of PV system ($P_{PV}$), dc side voltage ($V_{DC}$), reactive power generation of PV system ($Q_{PV}$), and apparent power of PV system ($S_{PV}$), respectively.
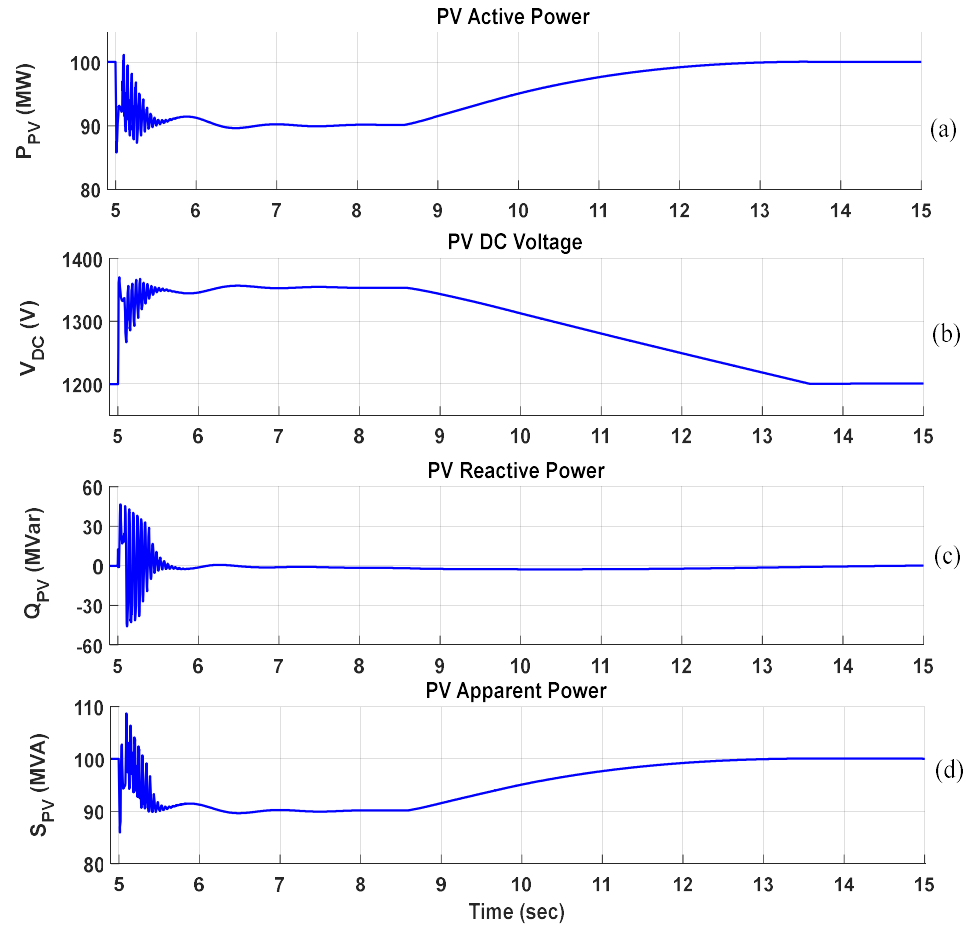
**Figure 6.8: PV solar farm response, $V_{wind}$ = 7 m/s, $P_{PV}$ =100 MW, $k$ = 75%, and with PV-STATCOM**

Once the fault is triggered in the system, the DC voltage controller increases the dc side voltage from $V_{MPP}$ *to* $V_{Curt}$, the voltage corresponding to the curtailed power generation level ($P_{Curt}$). Therfore, $P_{PV}$ goes from 100 MW to 90 MW, although with a slight delay based on the controller time constant, to provide enough capacity for the damping controller. Then, the damping controller utilizes this capacity of inverter in Full-STATCOM mode and mitigates SSR in the system by modulation of $Q_{PV}$, as seen from Figure 6.8 (c). When the line current oscillations are alleviated successfully to within 2% at $t$ = 8.58 sec, PV system starts increasing $P_{PV}$ by decreasing the dc side voltage from $V_{Curt}$ to $V_{MPP}$ gradually in 5 sec, to avoid initiation of low frequency oscillations. By utilizing the remaining capacity of PV inverter after active power generation, PV-STATCOM controller operates in its Partial-STATCOM mode during the power ramp-up to prevent

the recurrence of SSO instability. The PV solar farm resumes its pre-fault active power generation at $t = 13.58$ sec, almost 8.5 sec after fault occurrence. PV-STATCOM alleviates SSR by using a maximum $Q_{PV}$ of 47 Mvar which is much less than the MVA rating of PV inverter, i.e. 111MVA.

As noted from Figure 6.7 (c), the maximum reactive power from PV-STATCOM required to damp SSO is about 47 Mvar, which is much less than the total inverter capacity of 111 MVA. This demonstrates that the PV system does not need to fully curtail its active power generation. Consequently, the active power generation of the PV system is partially curtailed, i.e. by 10-MW, to provide enough reactive power for the damping controller to act.

## 6.6 Simultaneous Alleviation of SSR by DFIG Converter and PV-STATCOM

In this section, SSO mitigation in DFIG-based wind farm is performed while both PV system and DFIG-based wind farm are augmented by subsynchronous damping controller. The studies are performed for two cases: 1) PV-STATCOM and DFIG converter with uncoordinated controllers, 2) PV-STATCOM and DFIG converter with coordinated controllers.

### 6.6.1 PV-STATCOM and DFIG Converter with Uncoordinated Controllers

In this section, the SSR alleviation is performed by concurrent utilization of DFIG converter and PV-STATCOM with damping controllers which independently designed in sections 6.4.1 and 6.5.1, respectively.

Table 6.4 shows the eigenvalues of the system while both DFIG-based wind farm and PV system are augmented by subsynchronous damping controllers, simultaneously (although uncoordinated).

**Table 6.4: Eigenvalues of the system, $V_{wind}$ = 7 m/s, $P_{PV}$=100 MW, $k$ = 75%, with uncoordinated controllers of PV-STATCOM and DFIG**

| Modes | Eigenvalues |
|---|---|
| Network-1(Sub) | -33.021 ± 146.74i |
| Network-2(Super) | -0.207 ± 620.14i |
| Electromechanical | -10.72 ± 99.34i |
| Shaft mode | -1.366 ± 5.94i |

Comparison of Table 6.2, Table 6.3 and Table 6.4 reveals that the two independently optimized but uncoordinated controllers: i) increase the damping of subsynchronous mode, but ii) decrease the damping of supersynchronous mode, as compared to either of the two controllers implemented alone.

Figure 6.9 (a)-(c) show electrical torque ($T_e$), voltage at PCC ($V_{PCC}$), and line current ($I_{line}$), respectively, while the uncoordinated damping controllers of PV-STATCOM and DFIG converter are employed. Figure 6.10 (a)-(c) depict reactive power of GSC ($Q_g$), reactive power generation of PV system ($Q_{PV}$), active power generation of PV system ($P_{PV}$), respectively. It is seen that with uncoordinated controllers:

i)     The overall GSC reactive power exchange is more than that of PV-STATCOM. This implies that the damping effort provided by the GSC of wind farm is larger than that provided by PV-STATCOM.

ii)    SSO is damped in about 11 sec (at t=16.5 sec)
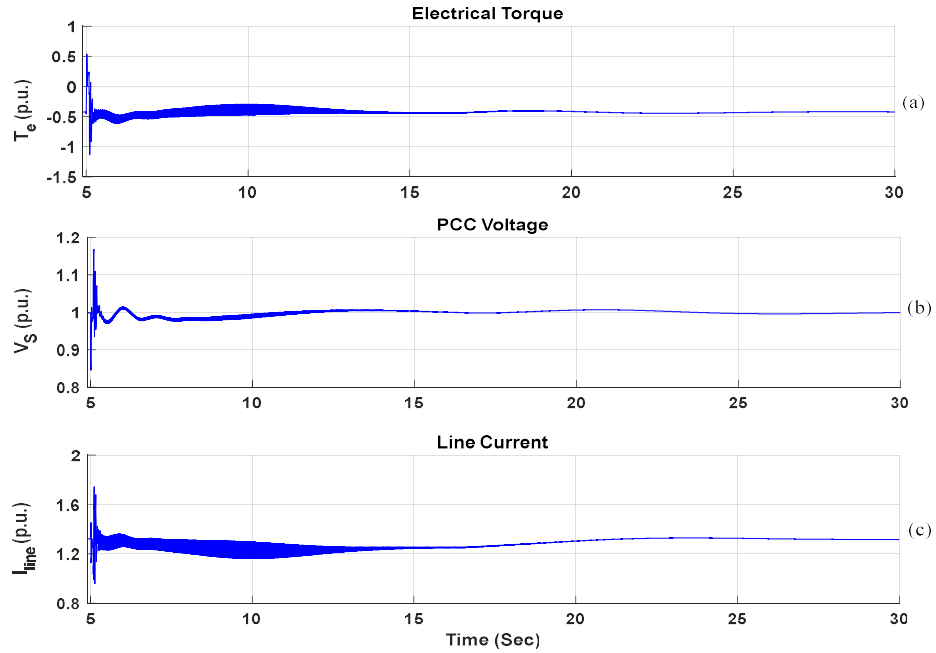
**Figure 6.9: System response, $V_{wind}$ = 7 m/s, $P_{PV}$ = 100 MW, $k$ = 75%, and with uncoordinated controllers of PV-STATCOM and DFIG**
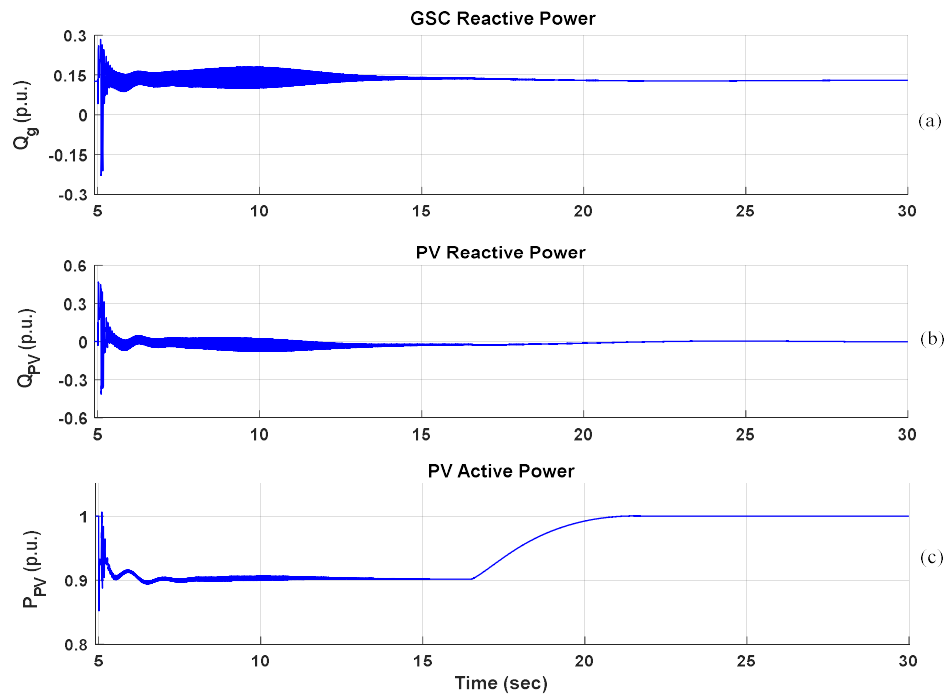


**Figure 6.10: DFIG and PV system responses, $V_{wind}$ = 7 m/s, $P_{PV}$ = 100 MW, $k$ = 75%, with uncoordinated controllers of PV-STATCOM and DFIG**

Figure 6.11 depicts the results of FFT analysis of the electrical torque between $t = 7$ sec and $t = 13$ sec. It shows that there is a peak at frequency of 98.8 Hz (620.77 rad/sec) which matches with the frequency of supersynchronous mode in Table 6.4.
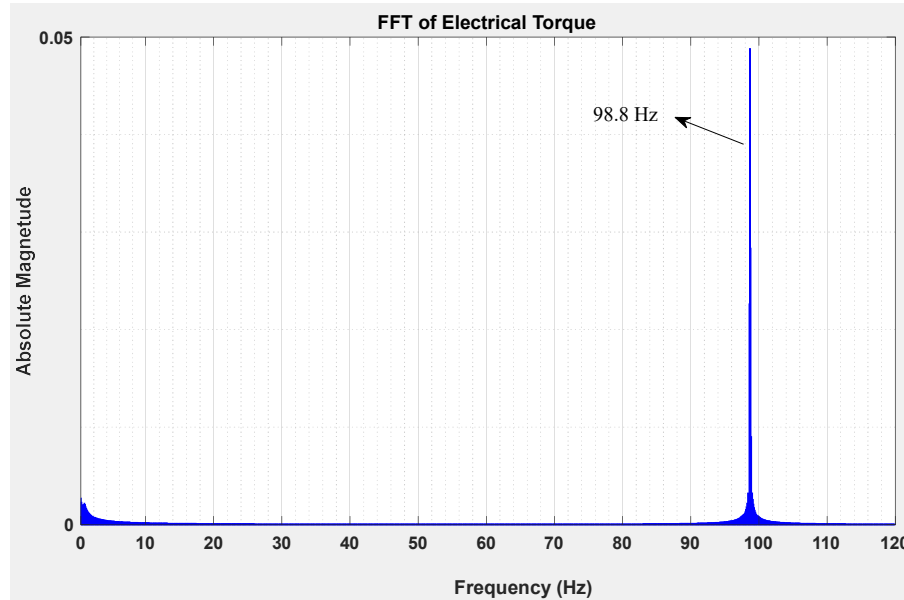


**Figure 6.11: FFT of the electrical torque ($T_e$) while $V_{wind} = 7$ m/s, $P_{PV}$=100 MW, $k = 75\%$, with uncoordinated controllers of PV-STATCOM and DFIG**

A comparison is now performed of the SSR damping controller performances of the individual DFIG-GSC, PV-STATCOM and both of them combined (but uncoordinated).

Figure 6.12 and Figure 6.13, show the electrical torque ($Te$) and line current ($I_{line}$), respectively, for the cases in which 1) just DFIG damping controller is implemented,  2) just PV-STATCOM damping controller is implemented, 3) simultaneous SSR alleviation by DFIG converter and PV-STATCOM while their controllers are not coordinated.

The results depicted in Figure 6.12 and Figure 6.13 demonstrate the following:

1) PV-STATCOM damps SSO faster than DFIG-GSC. However, the combined controllers damp SSO faster than each of them acting individually.
2) The combined controllers are unable to damp the supersynchronous mode as fast as any of the individual controllers.

Both the above observations correlate with the results of the eigenanalysis of the damping controllers presented in Table 6.2, Table 6.3, and Table 6.4
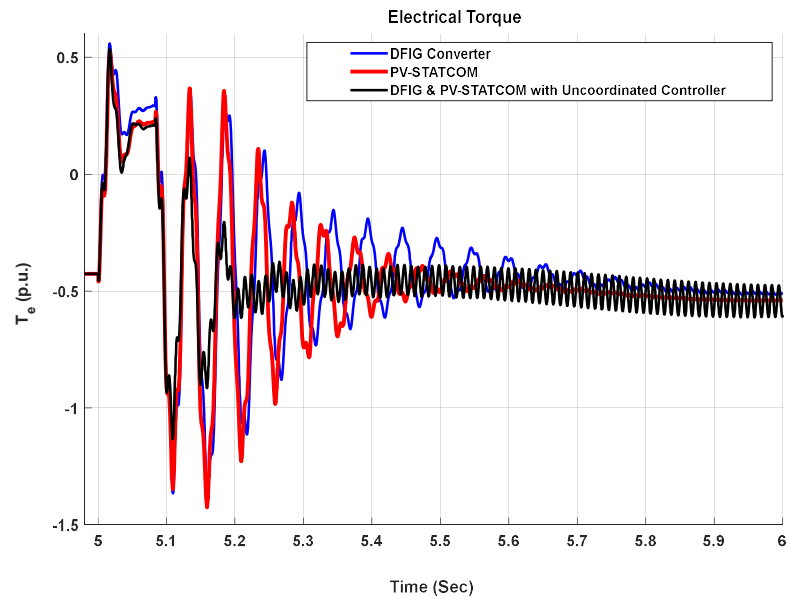


**Figure 6.12: The electrical torque (T$_e$) while $V_{wind}$ = 7 m/s, $P_{PV}$ = 100 MW, $k$ = 75%, with uncoordinated controllers of PV-STATCOM and DFIG**
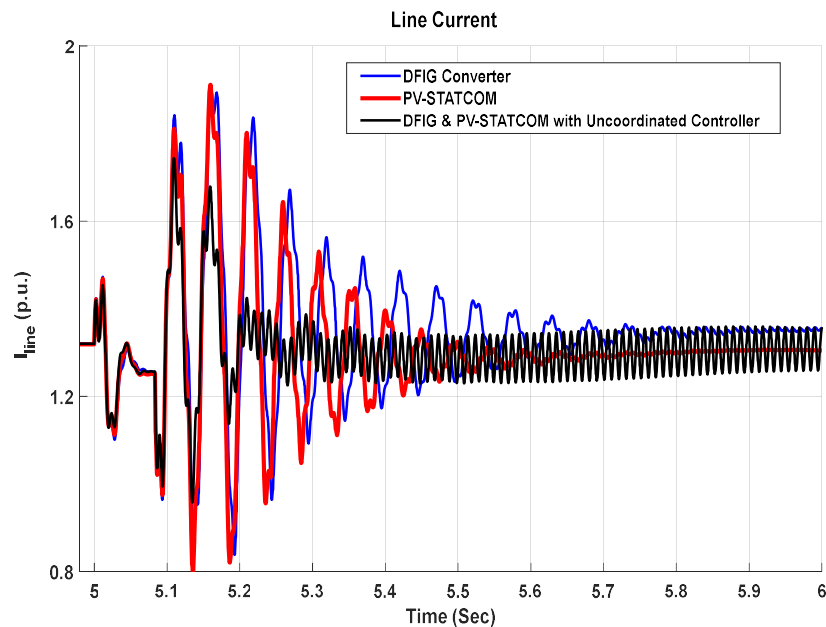


**Figure 6.13: The line current (I$_{line}$) while $V_{wind}$ = 7 m/s, $P_{PV}$ = 100 MW, $k$ = 75%, with uncoordinated controllers of PV-STATCOM and DFIG**

## 6.6.2 PV-STATCOM and DFIG Converter with Coordinated Controls

It is seen from studies in the previous section that simultaneous utilization of individually designed, but uncoordinated, damping controls of PV-STATCOM and DFIG converter substantially decrease the damping of supersynchronous mode. It therefore becomes imperative to design both the damping controllers in a coordinated manner. To achieve this objective, the optimization method explained in Section 6.4.1 is used to obtain the parameters of PV-STATCOM damping controller and GSC damping controller simultaneously in a coordinated manner. These coordinated parameters of the damping controllers are given in Appendix B.

Table 6.5 shows the eigenvalues of the system with coordinated controllers of PV-STATCOM and DFIG converter.

**Table 6.5: Eigenvalues of the system, $V_{wind}$ = 7 m/s, $P_{PV}$ =100 MW, $k$ = 75%, with coordinated controllers of PV-STATCOM and DFIG**

| Modes | Eigenvalues |
|---|---|
| **Network-1 (Sub)** | -16.196 ± 131.67i |
| **Network-2 (Super)** | -3.956± 625.18i |
| **Electromechanical** | -11.90 ± 100.16i |
| **Shaft mode** | -1.365 ± 5.91i |

It is seen that the coordinated damping controllers: i) increase the damping of the subsynchronous mode more than either controller acting alone, and ii) improve the damping of supersynchronous mode much more than uncoordinated controllers. The supersynchronous mode damping is now brought to a level higher than that with DFIG-GSC but slightly lower than that with PV-STATCOM.

Figure 6.14 (a)-(c) depict electrical torque ($T_e$), voltage at PCC ($V_{PCC}$), and line current ($I_{line}$), respectively, while the coordinated damping controllers of PV-STATCOM and DFIG converter are employed. Figure 6.15 (a)-(c) show reactive power of GSC ($Q_g$),

reactive power generation of PV system ($Q_{PV}$), active power generation of PV system ($P_{PV}$), respectively. It is seen that with coordinated controllers:

i) The overall GSC reactive power exchange is for a longer duration than that of PV-STATCOM. This implies that the damping effort provided by the GSC of wind farm is larger than that provided by PV-STATCOM.

ii) SSO is damped in about 3 sec (at t=7.92 sec). This is significantly faster than the case with uncoordinated controllers.
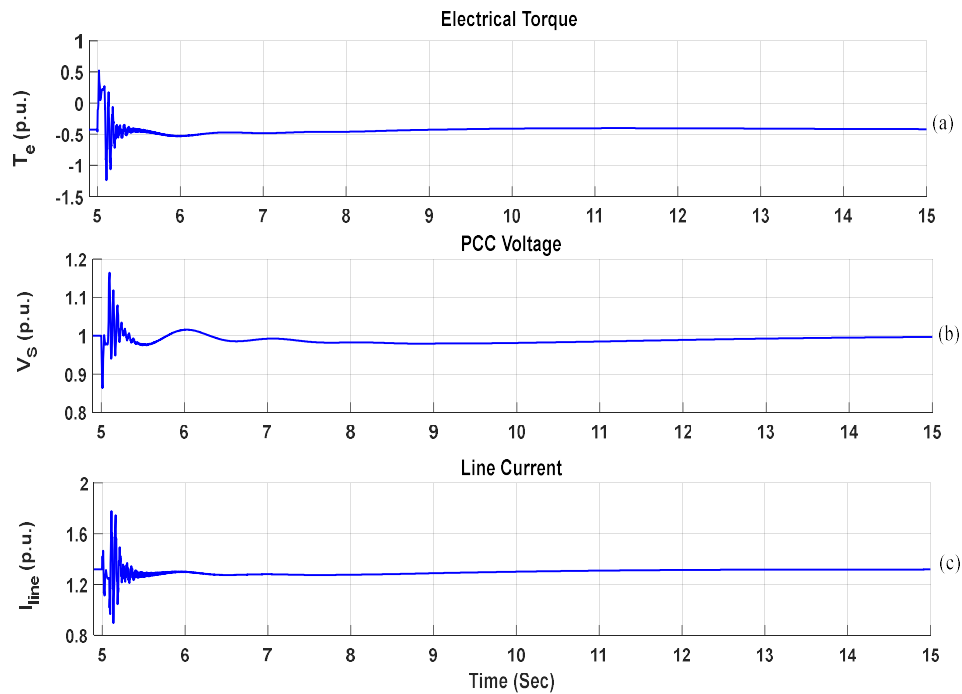


**Figure 6.14: System response, $V_{wind}$ = 7 m/s, $P_{PV}$=100 MW, $k$ = 75%, with coordinated controllers of PV-STATCOM and DFIG**
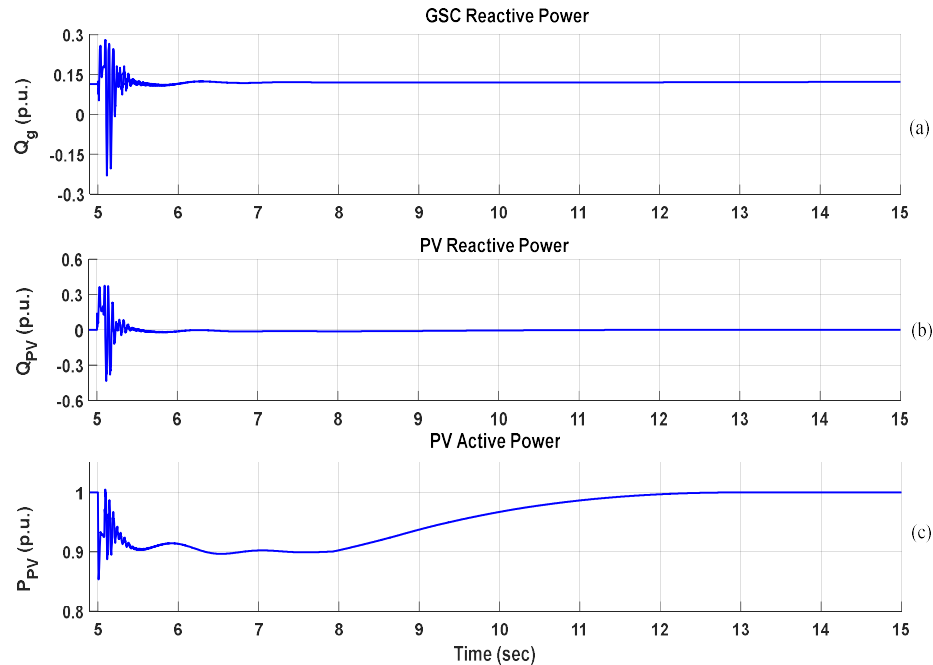
**Figure 6.15: : DFIG and PV system responses, $V_{wind}$ = 7 m/s, $P_{PV}$ =100 MW, $k$ = 75%, with coordinated controllers of PV-STATCOM and DFIG**

A comparison is now performed of the SSR damping controller performances of the individual DFIG-GSC, PV-STATCOM and both of them coordinated.

Figure 6.16 and Figure 6.17 depict the electrical torque ($Te$) and line current ($I_{line}$), respectively, for the cases in which 1) just DFIG damping controller is implemented, 2) just PV-STATCOM damping controller is implemented, 3) coordinated damping controllers of DFIG converter and PV-STATCOM are implemented.

The results shown in Figure 6.16 and Figure 6.17 demonstrate the following:

1) PV-STATCOM damps SSO faster than DFIG-GSC. However, the combined controllers damp SSO faster than each of them acting individually.
2) The combined controllers damp both the subsynchronous and supersynchronous modes faster than each of them acting individually.
3) The time taken to damp SSO with coordinated controllers is about 3 sec, which is significantly faster than the case with uncoordinated controllers.

The above observations correlate with the results of the eigenanalysis of the damping controllers presented in Table 6.2, Table 6.3, and 6.5.
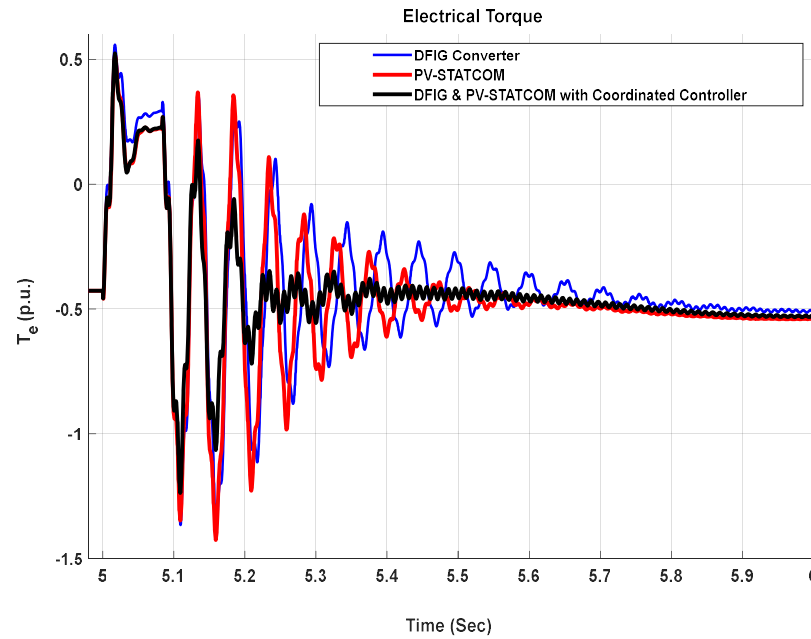


**Figure 6.16: The electrical torque ($T_e$) while $V_{wind}$ = 7 m/s, $P_{PV}$ =100 MW, $k$ = 75%, with coordinated controllers of PV-STATCOM and DFIG**
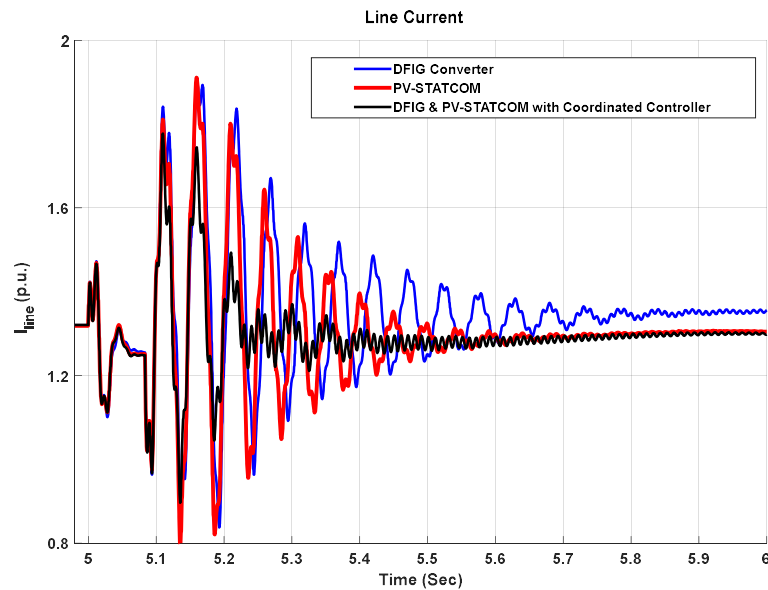


**Figure 6.17: The line current ($I_{line}$) while $V_{wind}$ = 7 m/s, $P_{PV}$ =100 MW, $k$ = 75%, with coordinated controllers of PV-STATCOM and DFIG**

## 6.7  Conclusion

This chapter presents a coordinated control of PV solar farm inverter as STATCOM, called PV-STATCOM, with DFIG converter for mitigation of SSR in DFIG-based wind farm connected to a series compensated transmission line.

The study system is a modified version of IEEE First SSR Benchmark system with the synchronous generator replaced by a combination of 100-MW DFIG-based wind farm and 100-MW PV solar farm. Line current is chosen as a local control signal for the subsynchronous damping controllers for both DFIG and PV-STATCOM. MATLAB/Simulink is utilized to perform eigenvalue analysis and time domain simulations of the study system. The optimization block of MATLAB software is employed to optimally design the damping controllers of DFIG and PV-STATCOM.

The SSR alleviation studies are carried out with: i) DFIG damping controller alone, ii) PV-STATCOM damping controller alone, iii) uncoordinated damping controllers of DFIG and PV-STATCOM acting together, and iv) coordinated damping controllers of DFIG and PV-STATCOM implemented together.

The following conclusions are made:

- The system is inherently unstable due to the instability of subsynchronous mode.
- The SSO damping controller of DFIG stabilizes the subsynchronous mode but reduces the damping of supersynchronous mode, although stabilizing the overall system
- The SSO damping controller of PV-STATCOM stabilizes the subsynchronous mode but reduces the damping of supersynchronous mode to a lesser extent than the DFIG damping control, while stabilizing the overall system
- PV-STATCOM damps SSO faster than DFIG.
- The combined but uncoordinated damping control of DFIG and PV-STATCOM increases the stability of subsynchronous mode but substantially reduces the damping of supersynchronous mode. The reactive power exchange from DFIG is higher than PV-STATCOM in stabilizing the system.

- The coordinated damping control of DFIG and PV-STATCOM provides significant damping to both the subsynchronous and supersynchronous modes.

- The coordinated controllers damp SSO faster than each of them acting individually.

- In case of coordinated controllers, the entire process of PV solar farm active power reduction, mitigation of SSR simultaneously by PV-STATCOM and DFIG converter, and PV solar farm restoration to its pre-fault condition takes place in 7.92 sec.

Chapter 7

# 7 Conclusion

## 7.1 General

Transmission lines across the world are extensively compensated by series capacitors to increase their power transfer capacity. However, series compensation can potentially cause subsynchronous resonance (SSR) which can lead to significant damage in shafts of synchronous generators and induction generator based wind farms. Actual incidents of such damages have already been reported in generators and wind farms causing a serious concern for the safety of such power generating systems. Dynamic reactive power compensators such as STATCOM and SVCs are typically used for mitigation of SSR, but these are quite expensive.

Large scale PV solar farms are growing at a very rapid rate across the world. Therefore, it is quite likely that they may get installed near synchronous generators or wind farms which are themselves directly or indirectly interfaced with series compensated transmission lines.

For the first time, novel SSR damping controls for the patented technology of PV solar farm controlled as STATCOM (PV-STATCOM) are presented in this thesis for mitigating SSR both during night and day in synchronous generators connected to series compensated transmission lines. The effectiveness of PV-STATCOM is investigated for mitigating SSR whether the solar farm is located at generator terminals or remotely from it.

New SSR alleviation controls are also developed for PV-STATCOM for mitigating SSR in wind farms connected to series compensated networks, during night and day, irrespective of the location of PV-STATCOM. The SSR damping control is based on wind farm speed when PV solar system is sited at wind farm terminals and on local line active power signal when the PV solar farm is remotely located.

As soon as a system disturbance is detected, the solar farm discontinues its real power generation and makes available its entire inverter capacity for dynamic reactive power exchange as STATCOM, for SSR mitigation. As soon as subsynchronous oscillations are damped the solar farm utilizes a novel ramp-up technique according to which the SSR

damping function is kept activated with remaining inverter capacity during power ramp-up. The effectiveness of such a novel technique for ramp-up is examined.

A novel coordinated control of PV-STATCOM and DFIG-based Type 3 wind farms is developed for faster and effective SSR damping, when both are connected to series compensated lines.

MATLAB based eigenvalue analysis is validated by nonlinear simulations through SIMULINK and PSCAD software to confirm the effectiveness of the proposed SSR damping controls for a wide variation in system conditions.

The broad review and the major contributions of this thesis are presented below. Also, the suggestions for future work are included in this section.

## 7.2   System Modeling

In Chapter 2, the modeling of study systems and their components is presented. The study systems, in this thesis, are either modified versions of, or are derived from IEEE First SSR Benchmark system which is a well-established study system for SSR phenomena analysis in power systems. The dynamics of system components including synchronous generator, induction generator based Type 1 wind farm, doubly-fed induction generator based Type 3 wind farm, series compensated transmission line, PV solar farm, and the proposed controller of PV-STATCOM are explained. Then, the SSR phenomena in synchronous generator, IG-based wind farm, and DFIG-based wind farm connected to a series compensated transmission system are studied through small-signal analysis and electromagnetic transient simulations utilizing MATLAB/Simulink and PSCAD/EMTDC software.

## 7.3   SSR Mitigation with PV-STATCOM connected at Synchronous Generator Terminal

In Chapter 3, the PV-STATCOM technology is employed for SSR alleviation in steam turbine driven synchronous generator (SG) connected to a series compensated transmission line. A modified IEEE First SSR Benchmark system with a 300-MW PV solar farm connected to SG terminal is adopted as the study system. The 892-MW synchronous

generator operates at 500 MW. The corresponding line power flow is 800 MW which resembles the power flow in IEEE First SSR Benchmark system. The generator rotor speed is considered as the control signal for PV-STATCOM damping controller.

The eigenvalue analysis and electromagnetic transient simulations using EMTDC/PSCAD software demonstrate that the PV-STATCOM controller effectively damps all four critical subsynchronous torsional modes at all the four critical series compensation levels in the IEEE First SSR Benchmark system. The process of SSR alleviation by PV-STATCOM from autonomous active power cessation, operation in Full-STATCOM mode to power restoration to its pre-fault condition takes place in less than half a minute. This momentary interruption in active power generation of PV system can be compared with a cloud passing event. Another novel power ramp-up concept is presented in which SSR damping is continuously performed with remaining capacity of PV inverter after active power generation in Partial-STATCOM mode. This enables a faster ramp-up than that specified in grid codes while preventing recurrence of subsynchronous oscillations. Such a novel ramp-up control is not envisaged in existing grid codes and Standards.

## 7.4  SSR Mitigation with PV-STATCOM connected at Line Midpoint

In Chapter 4, the effectiveness of PV-STATCOM in alleviating SSR in a synchronous generator in the modified IEEE First SSR Benchmark system is investigated when the 300-MW PV solar farm is located remotely from the synchronous generator at line midpoint. Locally available line active power flow ($P_{line}$) is considered as the control signal for a multi-band SSR damping controller. This choice of local control signal avoids the communication delay if generator speed were to be selected as the control signal.

The results obtained through eigenvalue analysis and validated through time domain simulations demonstrate the efficacy of the proposed damping controller. All the four torsional modes of the synchronous generator are successfully damped by the proposed PV-STATCOM controller at all the four critical series compensation levels. In this chapter too, the PV-STATCOM utilizes the novel ramp-up technique of continuing to damp SSR in Partial-STATCOM mode during active power ramp-up. This ensures a faster ramp-up than that specified by grid codes and Standards. The entire time from the PV-STATCOM

autonomous initiation of damping controller for SSR mitigation to restoration the pre-fault power generation of PV system is less than half a minute for all system configurations.

As compared to the case when PV-STATCOM is located at SG bus, it is noted that the mid-line located PV-STATCOM needs slightly more reactive power and time to alleviate SSO.

## 7.5 Alleviating Subsynchronous Oscillations in Type 1 Induction Generator-Based Wind Farm by PV Solar Farm controlled as PV-STATCOM

In Chapter 5, the proposed novel PV-STATCOM control is utilized to damp SSR in IG-based Type 1 wind farm on a night and day basis. The studies are performed on a modified IEEE First SSR Benchmark system including a 500 MW IG-based wind farm. The 300-MW PV solar farm may be located either at wind farm terminal or remotely at line midpoint. Wind farm generator speed and local transmission line current are used as damping control signals in the above two cases, respectively.

The PV-STATCOM efficacy in alleviation SSR is successfully demonstrated through small-signal analysis and validated by time domain simulation for wide ranging system conditions both during daytime and nighttime. It is seen that PV-STATCOM uses more reactive power for SSR alleviation: i) at higher levels of output power from a given size wind farm, and ii) for higher rated (larger-size) wind farms, iii) at increased levels of series compensation, iv) when three-phase fault occurs at the wind farm terminals rather than remotely from wind farm at the end of transmission line, and v) when PV system is located at line midpoint instead of at wind farm terminals. It is also shown that the entire process of damping SSR in IG-based wind farm by PV-STATCOM takes place in less than half a minute.

## 7.6 Coordination of PV-STATCOM and DFIG-Based Wind Farm for Subsynchronous Oscillation Damping

In Chapter 6, a coordinated control of PV-STATCOM and DFIG-based Type 3 wind farm converter is presented to mitigate SSR in DFIG-based wind farm connected to a series compensated transmission line. The study system is derived from the IEEE First SSR

Benchmark system in which the synchronous generator is replaced by a combination of 100-MW DFIG-based Type 3 wind farm and 100-MW PV solar system. Local line current is chosen as the control signal for subsynchronous damping controllers. The optimization block of MATLAB software is utilized to obtain optimal parameters for the damping controllers in each study case.

SSR alleviation studies are performed for four different cases: i) DFIG damping controller alone, ii) PV-STATCOM damping controller alone, iii) uncoordinated damping controllers of DFIG and PV-STATCOM acting together, and iv) coordinated damping controllers of DFIG and PV-STATCOM implemented together.

The results obtained through eigenvalue analysis and validated by time domain simulations conclude that: i) damping controllers of DFIG and PV-STATCOM, operating alone, mitigate SSO but PV-STATCOM performs faster, ii) individual operation of PV-STATCOM damping controller and DFIG damping controller reduces the damping of super synchronous mode, iii) the combined but uncoordinated damping controllers of PV-STATCOM and DFIG improves the damping of subsynchronous mode but considerably decreases the damping of super synchronous mode, iv) the coordinated controllers of PV-STATCOM and DFIG provide substantial damping to both subsynchronous and supersynchronous modes, while damping SSO faster than each of them operating alone. It is further seen that the entire process of damping SSR by coordinated controllers takes place in less than half minute. The PV-STATCOM controller combined with the DFIG damping controller, i.e. coordinated controllers, improves the SSR alleviation

## 7.7 Discussion

### 7.7.1 Benefits

The PV-STATCOM technology has the following benefits:
1) Considering: i) the rapid growth of PV solar farms rated over 100 MW around the world, ii) the high likelihood of their being directly or indirectly connected to series compensated transmission lines, and iii) the typical size of STATCOM required for SSR alleviation in power transmission systems being around 200

Mvar, large solar farms can potentially provide PV-STATCOM functionality for mitigation of SSR in both synchronous generators and wind farms.

2) While synchronous generator based devices and other mechanisms for damping SSR do exist, FACTS device based SSR mitigation measures have been widely utilized and reported in literature [16, 78-84, 86, 88, 89, 98-100, 102, 192]. Therefore, in cases where generator-based SSR damping devices are not found to be inadequate, the PV-STATCOM technology can be an effective solution for SSR mitigation.

3) The proposed PV-STATCOM is expected to be significantly cheaper than a conventional STATCOM. This is because only an incremental PV-STATCOM SSR damping controller with its associated measurement circuitry needs to be installed on the existing infrastructure (the substation, bus-work, transformers, circuit breakers, protection systems, etc.) of a PV solar farm to transform it into a full scale STATCOM of similar size. This makes PV-STATCOM at least 50-100 times cheaper than an equivalent size STATCOM.

4) Grid codes are presently being revised to accommodate smart inverter functions. SSR damping using solar farms as PV-STATCOM is a novel smart inverter function. It is recommended that this smart SSR alleviation function be incorporated in the emerging grid codes.

5) Mechanisms may also be evolved for compensating the PV solar farms financially for providing this important service of SSR mitigation.

## 7.7.2 Limitations

1) It is understood that a simplistic approach has been adopted in this thesis by considering an equivalent 300 MVA inverter instead of possibly hundreds of inverters present in an actual solar farm of such size with their associated controls, communication and protection systems. However, the objective of this thesis is to demonstrate the concept of a novel technology of alleviating SSR with PV solar systems. However, more studies are needed to see the impact of detailed modeling of PV solar farms. It is expected that even with detailed models, the PV-STATCOM can still provide SSR damping, although the time taken for SSR mitigation may be slightly more than half minute.

2) The significant potential financial saving in adoption of PV-STATCOM in lieu of an actual STATCOM can certainly be a motivation to overcome the intricacies involved in implementation of this novel technology in a coordinated manner on the multiples of inverters in an actual solar farm of similar size.

## 7.8   Contribution and Significance of this Thesis

The contributions and significance of this thesis are as follows:

1) A novel patented control of PV solar farm inverter as STATCOM, termed PV-STATCOM, is developed for alleviating SSR, on a night and day basis, in synchronous generators connected to a series compensated transmission line. The PV-STATCOM successfully damps SSR whether it is located at the terminal of the synchronous generator or located remotely at line midpoint.
   *Such a novel control of PV solar farms for damping SSR in synchronous generators is being proposed for the first time in literature to best of author's knowledge.*

2) A new PV-STATCOM control is proposed for SSR alleviation in Type-1 IG-based wind farms connected to series compensated lines for a wide range of system conditions. The PV-STATCOM effectively mitigates SSR in wind farms irrespective of its distance from the wind farm.
   *This new control of PV solar farms for damping SSR in Type 1 wind farms is demonstrated for the first time in literature to best of author's knowledge.*

3)  A coordinated SSR damping control of PV-STATCOM and DFIG based Type 3 wind farm converter is demonstrated which effectively increases the overall damping of subsynchronous oscillations in series compensated systems.

*This novel control coordination of PV solar farms and Type 3 wind farms for SSR alleviation is being proposed for the first time in literature known to the author.*

## 7.9  Future Work

The suggestions for the future work are as follows:

1) An actual large-scale PV solar farm consists of possibly hundreds of inverters instead of one equivalent aggregated inverter. Therefore, further research needs to be performed considering individual inverters with associated controls, and communication delays.

2) Both real-time and hardware-in-loop studies on Real Time Digital Simulator (RTDS) may be performed to further validate the effectiveness of the proposed PV-STATCOM controls for SSR alleviation.

3) Control coordination between multiple PV solar farms as PV-STATCOM, DFIG-based wind farms, and FACTS devices for alleviating SSR in realistic power systems may be performed

## 7.10 Publications from this Thesis

**A. Refereed Journal Papers:**

[1] R. K. Varma and **R. Salehi**, "SSR Mitigation With a New Control of PV Solar Farm as STATCOM (PV-STATCOM)," *IEEE Trans. on Sustainable Energy, vol.8, pp. 1473-1483, 2017.*

[2] R. K. Varma and **R. Salehi**, "Alleviating Subsynchronous Oscillations in Induction Generator-Based Wind Farms by Solar Farms controlled as PV-STATCOM," ready for submission to IET Renewable Power Generation

[3] R. K. Varma and **R. Salehi**, "Control Coordination of PV-STATCOM and DFIG-Based Wind Farm for Subsynchronous Oscillation Damping," ready for submission to IEEE Transactions on Sustainable Energy

**B. Refereed Conference Papers:**

[1] R. Salehi and R. K. Varma, "PV Solar Farm Control as STATCOM (PV-STATCOM) for Alleviating Subsynchronous Oscillations," accepted in *2019 CIGRE Canada Conference*.

[2] Rajiv K. Varma, Ehsan Siavashi, Hesamaldin Maleki, Reza Salehi, Sibin Mohan, Mahendra A.C., S. Arifur Rahman and T. Vanderheide, "PV-STATCOM: A Novel Smart Inverter for Transmission and Distribution System Applications", Poster at the *7th International Conference on Integration of Renewable and Distributed Energy Resources*, Niagara Falls, Canada, Oct. 24-28, 2016

[3] S. B. Subramanian, S. Mohan, M. Akbari, H. Maleki, R. Salehi, W. H. Litzenberger, et al., "Control of STATCOMs – A Review," in 2018 *IEEE Power & Energy Society General Meeting (PESGM)*, 2018, pp. 1-5.

# Appendices

## Appendix A: Study system parameters

### A.1. IEEE First SSR Benchmark system [112, 167]

Table A. 1: Transmission line

| | | | |
|---|---|---|---|
| $X_T$ | 0.14 p.u. | $R_l$ | 0.02 p.u. |
| $X_l$ | 0.5 p.u. | $X_c$ | 0.06 p.u. |

Table A. 2: 892-MW Synchronous generator

| | | | |
|---|---|---|---|
| $r_s$ | 0 | $X_{ls}$ | 0.13 p.u. |
| $r_{kq1}$ | 0.0123 p.u. | $X_{kq1}$ | 1.63 p.u. |
| $r_{kq2}$ | 0.0179 p.u. | $X_{kq2}$ | 1.90 p.u. |
| $r_{fd}$ | 0.0012 p.u. | $X_{fd}$ | 1.73 p.u. |
| $r_{kd}$ | 0.0295 p.u. | $X_{kd}$ | 1.71 p.u. |
| $X_{md}$ | 1.66 p.u. | $X_{mq}$ | 1.58 p.u. |

Table A. 3: Exciter system

| | | | |
|---|---|---|---|
| $K_F$ | 2 | $T_A$ | 0.04 sec |
| $K_A$ | 0.03 | $T_E$ | 0.01 sec |
| $K_E$ | 1 | $T_F$ | 1 sec |
| $V_{Rmax}$ | 4.75 p.u. | $V_{Rmax}$ | -4.75 p.u. |

Table A. 4: Turbine generator mechanical system

| $H_H$ | 0.092897 sec | $K_{HI}$ | 19.303 p.u./rad |
|---|---|---|---|
| $H_I$ | 0.155589 sec | $K_{IA}$ | 34.929 p.u./rad |
| $H_A$ | 0.858670 sec | $K_{AB}$ | 52.038 p.u./rad |
| $H_B$ | 0.884215 sec | $K_{BG}$ | 70.858 p.u./rad |
| $H_G$ | 0.868495 sec | $K_{GE}$ | 2.822 p.u./rad |
| $H_E$ | 0.0342165 sec | | |

Table A. 5: Turbine generator governor

| $F_A$ | 0.22 | $K_G$ | 25 |
|---|---|---|---|
| $F_B$ | 0.22 | $T_{SM}$ | 0.1 sec |
| $F_I$ | 0.26 | $T_{ch}$ | 0.4 sec |
| $F_H$ | 0.3 | $T_{rh}$ | 7 sec |
| $C_{VOPEN}$ | 4 p.u./sec | $T_{co}$ | 0.6 sec |
| $C_{VCLOSE}$ | -4 p.u./sec | | |

## A.2. IG-based wind farm parameters [44]

Table A. 6: 2.3-MW double-cage induction generator

| $r_s$ | 0.00506 p.u. | $X_{lr1}$ | 0 p.u. |
|---|---|---|---|
| $r_{r1}$ | 0.01199 p.u. | $X_{lr2}$ | 0.21172 p.u. |
| $r_{r2}$ | 0.0192 p.u. | $X_M$ | 3.8892 p.u. |
| $X_{ls}$ | 0.1317 p.u. | $X_{rM}$ | 0.07217 p.u. |

Table A. 7: Drive train

| $H_t$ | 4 sec | $K_{tg}$ | 0.3 p.u./rad |
|---|---|---|---|
| $H_g$ | 0.5 sec | | |

## A.3. DFIG-based wind farm parameters [59, 61]

Table A. 8: 2-MW Doubly-fed induction generator

| $r_s$ | 0.00488 p.u. | $X_{lr}$ | 0.09955 p.u. |
|---|---|---|---|
| $r_r$ | 0.00549 p.u. | $X_M$ | 3.95279 p.u. |
| $X_{ls}$ | 0.09231 p.u. | $X_{tg}$ | 0.3 p.u. |

Table A. 9: RSC and GSC Controller

| $K_1$ | 0.0001 | $T_1$ | 0.05 |
|---|---|---|---|
| $K_2$ | 0.0001 | $T_2$ | 0.005 |
| $K_3$ | 0.0001 | $T_3$ | 0.025 |
| $K_4$ | 0.0001 | $T_4$ | 0.0025 |
| $K_5$ | 0.1 | $T_5$ | 0.05 |
| $K_6$ | 1 | $T_6$ | 0.01 |
| $K_7$ | 0.1 | $T_7$ | 0.05 |
| $K_8$ | 1 | $T_8$ | 0.01 |

Table A. 10: Drive train

| $H_t$ | 4.29 sec | $K_{tg}$ | 0.15 p.u./rad |
|---|---|---|---|
| $H_g$ | 0.9 sec | $D_{tg}$ | 1.5 p.u. |

## A.4. PV solar farm parameters [188]

Table A. 11: PV module parameters

| | |
|---|---|
| Nominal Power (±5%) ($P_{MPP}$) | 72.6 W |
| Voltage at P$_{MPP}$ ($V_{ms}$) | 66.6 V |
| Current at P$_{MPP}$ ($I_{ms}$) | 1.09 A |
| Open Circuit Voltage ($V_{OC}$) | 88.7 V |
| Short Circuit Current ($I_{SC}$) | 1.23 A |
| Temperature Co-efficient of $V_{OC}$ high tem>25 ˚C ($K_V$) | -0.25 %/˚C |
| Temperature Co-efficient of $V_{OC\ low}$ tem>25 ˚C ($K_V$) | -0.2 %/˚C |
| Temperature Co-efficient of $I_{SC}$ ($K_I$) | 0.045 %/˚C |

Table A. 12: PV controller parameters

| $K_{P1}$ | 1 | $T_{I1}$ | 0.0015 |
|---|---|---|---|
| $K_{P2}$ | 1 | $T_{I2}$ | 0.001 |
| $K_{P3}$ | 2 | $T_{I3}$ | 0.05 |

# Appendix B: SSR damping controller parameters

Table B. 1: PV-STATCOM damping controller parameters in chapter 3

| $T_\omega$ | 0.006631 | $K$ | 150 |
|---|---|---|---|

Table B. 2 : PV-STATCOM damping controller parameters in chapter 4

| $K_{M1}$ | 138.38 | $K_{M2}$ | 84.35 |
|---|---|---|---|
| $K_{M4}$ | 5.24 | $K_{M3}$ | 1.067 |
| $T_{M11}$ | 6.705 | $T_{M12}$ | 1.224 |
| $T_{M21}$ | 12.654 | $T_{M22}$ | 1.087 |
| $T_{M31}$ | 1.384 | $T_{M32}$ | 7.518 |
| $T_{M41}$ | 7.846 | $T_{M42}$ | 4.328 |

Table B. 3: PV-STATCOM damping controller parameters in chapter 5

| PV connected at wind farm terminal | | | |
|---|---|---|---|
| $T_\omega$ | 10 | $K_D$ | 12 |
| $T_1$ | 0.023 | $T_2$ | 0.0021 |
| PV connected at line midpoint | | | |
| $T_\omega$ | 0.2 | $K_D$ | 0.3 |
| $T_1$ | 0.054 | $T_2$ | 0.081 |

Table B. 4: Subsynchronous damping controller parameters in chapter 6

| DFIG converter damping controller | | | |
|---|---|---|---|
| $T_\omega$ | 0.1 | $K_D$ | 9.64 |
| $T_{1DFIG}$ | 0.00099 | $T_{2DFIG}$ | 0.0038 |
| PV-STATCOM damping controller | | | |
| $T_\omega$ | 0.1 | $K_{PV}$ | 1.87 |
| $T_{1PV}$ | 0.00047 | $T_{2PV}$ | 0.009 |
| Coordinated damping controllers of DFIG converter and PV-STATCOM | | | |
| $K_D$ | 7.12 | | |
| $T_{1DFIG}$ | 0.0009 | $T_{2DFIG}$ | 0.0044 |
| $K_{PV}$ | 1.14 | | |
| $T_{1PV}$ | 0.00032 | $T_{2PV}$ | 0.0096 |

# References

[1]     *The Wind Power wind energy market intelligence. [Online]*. Available: https://www.thewindpower.net/

[2]     *List of offshore wind farms. [Online]*. Available: https://en.wikipedia.org/wiki/List_of_offshore_wind_farms

[3]     *STATISTICS.[Online]*. Available: http://www.wwindea.org/information-2/information/

[4]     *European statistics archive.[Online]*. Available: http://www.ewea.org/statistics/european/

[5]     *Global statistics.[Online]*. Available: http://www.gwec.net/global-figures/graphs/

[6]     E. Hau, *Wind Turbines-Fundamentals, Technologies, Application, Economics*: Springer Science & Business Media, 2013.

[7]     V. Akhmatov, *Induction Generators for Wind Power*: Essex, U.K.: Multi-Science Publication, 2007.

[8]     Z. Lubosny, *Wind turbine operation in electric power systems: advanced modeling*: Springer Heidelberg, 2003.

[9]     T. Ackermann, *Wind power in power systems*: John Wiley and Sons, 2005.

[10]    S. J. Chapman, *Electric Machinery Fundamentals*: 4th ed. Toronto,ON, Canada: McGraw-Hill,, 2005.

[11]    I. Boldea, *Variable speed generators*: CRC press, 2005.

[12]    *PV Resources, Large scale photovoltaic power plants ranking 1-50. [Online]*. Available: http://www.pvresources.com/en/pvpowerplants/top50pv.php#notes

[13]    *Sunpower,Solar Projects,Solar Star Projects.[Online]*. Available: http://us.sunpower.com/utility-scale-solar-power-plants/solar-energy-projects/solar-star-projects/

[14]    *First Solar,Projects. [Online]*. Available: http://www.firstsolar.com/About-Us/Projects.aspx

[15]    R. K. Varma, S. A. Rahman, and T. Vanderheide, "New Control of PV Solar Farm as STATCOM (PV-STATCOM) for Increasing Grid Power Transmission Limits During Night and Day," *IEEE Trans. on Power Delivery,* vol. 30, pp. 755-763, 2015.

[16]   N. G. Hingorani and L. Gyugi, *Understanding FACTS*: Piscataway, NJ, USA: IEEE Press, 2000.

[17]   P. M. Anderson and R. G. Farmer, *Series compensation of power systems*: PBLSH, 1996.

[18]   *Series compensation: boosting transmission capacity.[Online]*. Available: http://new.abb.com/facts/fixed-series-compensation

[19]   D. H. R. Suriyaarachchi, U. D. Annakkage, C. Karawita, and D. A. Jacobson, "A Procedure to Study Sub-Synchronous Interactions in Wind Integrated Power Systems," *IEEE Transactions on Power Systems,* vol. 28, pp. 377-384, 2013.

[20]   K. R. Padiyar, *Analysis of subsynchronous resonance in power systems*: Norwell,MA,USA:Kluwer, 1999.

[21]   J. W. Ballance and S. Goldberg, "Subsynchronous Resonance in Series Compensated Transmission Lines," *IEEE Trans. Power Apparatus and Systems,* vol. PAS-92, pp. 1649-1658, 1973.

[22]   P. M. Anderson, B. L. Agrawal, and J. E. Van Ness, *Subsynchronous resonance in power systems*: Piscataway, NJ, USA: IEEE Press, 1990.

[23]   IEEE Committee Report, "Reader's guide to subsynchronous resonance," *IEEE Trans. on Power Systems,* vol. 7, pp. 150-157, 1992.

[24]   IEEE Subsynchronous Resonance Working Group, "Terms, Definitions and Symbols for Subsynchronous Oscillations," *IEEE Trans. Power Apparatus and Systems,* vol. PAS-104, pp. 1326-1334, 1985.

[25]   J. Adams, C. Carter, and S. H. Huang, "ERCOT experience with Sub-synchronous Control Interaction and proposed remediation," in *PES T&D*, 2012, pp. 1-5.

[26]   W. Ren and E. Larsen, "A Refined Frequency Scan Approach to Sub-Synchronous Control Interaction (SSCI) Study of Wind Farms," *IEEE Transactions on Power Systems,* vol. 31, pp. 3904-3912, 2016.

[27]   H. Liu, X. Xie, J. He, T. Xu, Z. Yu, C. Wang, *et al.*, "Subsynchronous Interaction Between Direct-Drive PMSG Based Wind Farms and Weak AC Networks," *IEEE Transactions on Power Systems,* vol. 32, pp. 4708-4720, 2017.

[28]   L. Wang, X. Xie, Q. Jiang, H. Liu, Y. Li, and H. Liu, "Investigation of SSR in Practical DFIG-Based Wind Farms Connected to a Series-Compensated Power System," *IEEE Transactions on Power Systems,* vol. 30, pp. 2772-2779, 2015.

[29]   J. Adams, V. A. Pappu, and A. Dixit, "Ercot experience screening for Sub-Synchronous Control Interaction in the vicinity of series capacitor banks," in *2012 IEEE Power and Energy Society General Meeting*, 2012, pp. 1-5.

[30]   Y. Chen, Y. Liu, H. Sun, B. Huang, and L. Wang, "SSCI Problem of D-PMSGs Based Wind Farm Considering Frequency Characteristics of Grid Impedance," in *2018 International Conference on Power System Technology (POWERCON)*, 2018, pp. 1826-1831.

[31]   C. Karawita and U. D. Annakkage, "Control block diagram representation of an HVDC system for sub-synchronous frequency interaction studies," in *9th IET International Conference on AC and DC Power Transmission (ACDC 2010)*, 2010, pp. 1-5.

[32]   X. Xie, W. Liu, H. Liu, Y. Du, and Y. Li, "A System-Wide Protection Against Unstable SSCI in Series-Compensated Wind Power Systems," *IEEE Transactions on Power Delivery,* vol. 33, pp. 3095-3104, 2018.

[33]   T. Joseph, C. E. Ugalde-Loo, S. Balasubramaniam, and J. Liang, "Real-Time Estimation and Damping of SSR in a VSC-HVDC Connected Series-Compensated System," *IEEE Transactions on Power Systems,* vol. 33, pp. 7052-7063, 2018.

[34]   N. Prabhu and K. R. Padiyar, "Investigation of Subsynchronous Resonance With VSC-Based HVDC Transmission Systems," *IEEE Transactions on Power Delivery,* vol. 24, pp. 433-440, 2009.

[35]   K. M. Alawasa, Y. A. I. Mohamed, and W. Xu, "Active Mitigation of Subsynchronous Interactions Between PWM Voltage-Source Converters and Power Networks," *IEEE Transactions on Power Electronics,* vol. 29, pp. 121-134, 2014.

[36]   D. Shu, X. Xie, H. Rao, X. Gao, Q. Jiang, and Y. Huang, "Sub- and Super-Synchronous Interactions Between STATCOMs and Weak AC/DC Transmissions With Series Compensations," *IEEE Transactions on Power Electronics,* vol. 33, pp. 7424-7437, 2018.

[37]   Y. Xu and Y. Cao, "Sub-synchronous oscillation in PMSGs based wind farms caused by amplification effect of GSC controller and PLL to harmonics," *IET Renewable Power Generation,* vol. 12, pp. 844-850, 2018.

[38]   R. J. Piwko and E. V. Larsen, "HVDC System Control for Damping of Subsynchronous Oscillations," *IEEE Trans. Power Apparatus and Systems,* vol. PAS-101, pp. 2203-2211, 1982.

[39]   H. A. Mohammadpour and E. Santi, "Analysis of sub-synchronous resonance (SSR) in doubly-fed induction generator (DFIG)-based wind farms," *Synthesis Lectures on Power Electronics,* vol. 5, pp. 1-64, 2015.

[40]   B. L. Agrawal and R. G. Farmer, "Use of Frequency Scanning Techniques for Subsynchronous Resonance Analysis," *IEEE Transactions on Power Apparatus and Systems,* vol. PAS-98, pp. 341-349, 1979.

[41]    M. El-Marsafawy, "Use of frequency-scan techniques for subsynchronous-resonance analysis of a practical series-capacitor compensated AC network," *IEE Proceedings C - Generation, Transmission and Distribution,* vol. 130, pp. 28-40, 1983.

[42]    S. Gupta, A. Moharana, and R. K. Varma, "Frequency scanning study of sub-synchronous resonance in power systems," in *2013 26th IEEE Canadian Conference on Electrical and Computer Engineering (CCECE)*, 2013, pp. 1-6.

[43]    M. R. Iravani and A. Edris, "Eigen analysis of series compensation schemes reducing the potential of subsynchronous resonance," *IEEE Transactions on Power Systems,* vol. 10, pp. 876-883, 1995.

[44]    R. K. Varma and A. Moharana, "SSR in Double-Cage Induction Generator-Based Wind Farm Connected to Series-Compensated Transmission Line," *IEEE Trans. on Power Systems,* vol. 28, pp. 2573-2583, 2013.

[45]    A. Moharana and R. K. Varma, "Subsynchronous resonance in single-cage self-excited-induction-generator-based wind farm connected to series-compensated lines," *IET Generation, Transmission & Distribution,* vol. 5, pp. 1221-1232, 2011.

[46]    M. L. Crow, *Computational methods for electric power systems*: Crc Press, 2009.

[47]    *Series Compensation Systems.[Online]*. Available: http://www.gegridsolutions.com/products/brochures/powerD_vtf/SeriesCompensation_GEA12785C_LR.pdf

[48]    J. W. Butler and C. Concordia, "Analysis of Series Capacitor Application Problems," *Transactions of the American Institute of Electrical Engineers,* vol. 56, pp. 975-988, 1937.

[49]    D. N. Walker, C. E. J. Bowler, R. L. Jackson, and D. A. Hodges, "Results of subsynchronous resonance test at Mohave," *IEEE Trans. Power Apparatus and Systems,* vol. 94, pp. 1878-1889, 1975.

[50]    D. Duc Tung, L. Van Dai, and L. Cao Quyen, "Subsynchronous Resonance and FACTS-Novel Control Strategy for Its Mitigation," *Journal of Engineering,* vol. 2019, p. 14, 2019.

[51]    P. Pourbeik, R. J. Koessler, D. L. Dickmander, and W. Wong, "Integration of large wind farms into utility grids (part 2 - performance issues)," in *IEEE Power Engineering Society General Meeting, 2003*, 2003, pp. 1-1525 Vol. 3.

[52]    R. K. Varma, S. Auddy, and Y. Semsedini, "Mitigation of Subsynchronous Resonance in a Series-Compensated Wind Farm Using FACTS Controllers," *IEEE Trans. Power Delivery,* vol. 23, pp. 1645-1654, 2008.

[53] A. K. Moharana, "Subsynchronous Resonance in Wind Farms," Ph.D. dissertation, Dept. ECE, Univ. of Western Ontario, London, ON, 2012.

[54] A. Tabesh and R. Iravani, "Small-signal dynamic model and analysis of a fixed-speed wind farm - a frequency response approach," *IEEE Trans. Power Delivery,* vol. 21, pp. 778-787, 2006.

[55] A. Moharana, R. K. Varma, and R. Seethapathy, "SSR Alleviation by STATCOM in Induction-Generator-Based Wind Farm Connected to Series Compensated Line," *IEEE Trans. Sustainable Energy,* vol. 5, pp. 947-957, 2014.

[56] L. Fan and Z. Miao, "Mitigating SSR Using DFIG-Based Wind Generation," *IEEE Transactions on Sustainable Energy,* vol. 3, pp. 349-358, 2012.

[57] A. Ostadi, A. Yazdani, and R. K. Varma, "Modeling and Stability Analysis of a DFIG-Based Wind-Power Generator Interfaced With a Series-Compensated Line," *IEEE Trans. Power Delivery,* vol. 24, pp. 1504-1514, 2009.

[58] L. Fan, R. Kavasseri, Z. L. Miao, and C. Zhu, "Modeling of DFIG-Based Wind Farms for SSR Analysis," *IEEE Transactions on Power Delivery,* vol. 25, pp. 2073-2082, 2010.

[59] L. Fan, H. Yin, and Z. Miao, "On Active/Reactive Power Modulation of DFIG-Based Wind Generation for Interarea Oscillation Damping," *IEEE Transactions on Energy Conversion,* vol. 26, pp. 513-521, 2011.

[60] G. D. Irwin, A. K. Jindal, and A. L. Isaacs, "Sub-synchronous control interactions between type 3 wind turbines and series compensated AC transmission systems," in *2011 IEEE Power and Energy Society General Meeting*, 2011, pp. 1-6.

[61] H. A. Mohammadpour, A. Ghaderi, and E. Santi, "Analysis of sub-synchronous resonance in doubly-fed induction generator-based wind farms interfaced with gate-controlled series capacitor," *IET Generation, Transmission & Distribution,* vol. 8, pp. 1998-2011, 2014.

[62] A. E. Leon and J. A. Solsona, "Sub-Synchronous Interaction Damping Control for DFIG Wind Turbines," *IEEE Transactions on Power Systems,* vol. 30, pp. 419-428, 2015.

[63] M. Sahni, D. Muthumuni, B. Badrzadeh, A. Gole, and A. Kulkarni, "Advanced screening techniques for Sub-Synchronous Interaction in wind farms," in *Transmission and Distribution Conference and Exposition (T&D), 2012 IEEE PES*, 2012, pp. 1-9.

[64] M. Sahni, B. Badrzadeh, D. Muthumuni, Y. Cheng, H. Yin, S. Huang, *et al.*, "Sub-synchronous interaction in Wind Power Plants- part II: An ercot case study," in *2012 IEEE Power and Energy Society General Meeting*, 2012, pp. 1-9.

[65]    H. A. Mohammadpour and E. Santi, "Sub-synchronous resonance analysis in DFIG-based wind farms: Definitions and problem identification-Part I," in *2014 IEEE Energy Conversion Congress and Exposition (ECCE)*, 2014, pp. 812-819.

[66]    E. V. Larsen, "Wind generators and series-compensated AC transmission lines," in *2012 IEEE Power and Energy Society General Meeting*, 2012, pp. 1-4.

[67]    K. Narendra, D. Fedirchuk, R. Midence, N. Zhang, A. Mulawarman, P. Mysore*, et al.*, "New microprocessor based relay to monitor and protect power systems against sub-harmonics," in *IEEE Electrical Power and Energy Conference (EPEC)*, 2011, pp. 438-443.

[68]    X. Zhang, X. Xie, H. Liu, and Y. Li, "Robust subsynchronous damping control to stabilise SSR in series-compensated wind power systems," *IET Generation, Transmission & Distribution,* vol. 13, pp. 337-344, 2019.

[69]    *Why HVDC?.[Online]*. Available: http://new.abb.com/systems/hvdc/why-hvdc

[70]    Y. Y. Hsu and L. Wang, "Modal control of an HV DC system for the damping of subsynchronous oscillations," *IEE Proceedings C - Generation, Transmission and Distribution,* vol. 136, pp. 78-86, 1989.

[71]    M. Bahrman, E. V. Larsen, R. J. Piwko, and H. S. Patel, "Experience with HVDC - Turbine-Generator Torsional Interaction at Square Butte," *IEEE Trans. Power Apparatus and Systems,* vol. PAS-99, pp. 966-975, 1980.

[72]    I. S. Benko, B. Bhargava, and W. N. Rothenbuhler, "Prototype NGH Subsynchronous Resonance Damping Scheme. Part II-Switching and Short Circuit Tests," *IEEE Power Engineering Review,* vol. PER-7, pp. 48-48, 1987.

[73]    N. G. Hingorani, B. Bhargava, G. F. Garrigue, and G. D. Rodriguez, "Prototype NGH Subsynchronous Resonance Damping Scheme. Part I-Field Installation and Operating Experience," *IEEE Power Engineering Review,* vol. PER-7, pp. 47-48, 1987.

[74]    A. Yan and Y.-n. Yu, "Multi-Mode Stabilization of Torsional Oscillations Using Output Feedback Excitation Control," *Power Engineering Review, IEEE,* vol. PER-2, pp. 43-44, 1982.

[75]    L. Wang and Y. Y. Hsu, "Damping of subsynchronous resonance using excitation controllers and static VAr compensations: a comparative study," *IEEE Transactions on Energy Conversion,* vol. 3, pp. 6-13, 1988.

[76]    X. Xiaorong, W. Liang, and H. Yingduo, "Combined Application of SEDC and GTSDC for SSR Mitigation and Its Field Tests," *IEEE Trans. Power Systems,* vol. 31, pp. 769-776, 2016.

[77] IEEE Subsynchronous Resonance Working Group, "Countermeasures to subsynchronous resonance problems," *IEEE Transactions on Power Apparatus and Systems,* vol. PAS-99, pp. 1810-1818, 1980.

[78] R. M. Mathur and R. K. Varma, *Thyristor-based FACTS controllers for electrical transmission systems*: John Wiley & Sons, 2002.

[79] N. C. Abi-Samra, R. F. Smith, T. E. McDermott, and M. B. Chidester, "Analysis of Thyristor-Controlled Shunt SSR Countermeasures," *IEEE Trans. Power Apparatus and Systems,* vol. PAS-104, pp. 583-597, 1985.

[80] L. Gyugyi, "Reactive power generation and control by thyristor circuits," in *Power Electronics Specialists Conference, 1976 IEEE*, 1976, pp. 174-184.

[81] A. E. Hammad and M. El-Sadek, "Application of a Thyristor Controlled Var Compensator for Damping Subsynchronous Oscillations in Power Systems," *IEEE Trans. Power Apparatus and Systems,* vol. PAS-103, pp. 198-212, 1984.

[82] K. V. Patil, J. Senthil, J. Jiang, and R. M. Mathur, "Application of STATCOM for damping torsional oscillations in series compensated AC systems," *IEEE Trans. Energy Conversion,* vol. 13, pp. 237-243, 1998.

[83] K. R. Padiyar and N. Prabhu, "Design and performance evaluation of subsynchronous damping controller with STATCOM," *IEEE Trans. Power Delivery,* vol. 21, pp. 1398-1405, 2006.

[84] W. Zhu, R. Spee, R. R. Mohler, G. C. Alexander, W. A. Mittelstadt, and D. Maratukulam, "An EMTP study of SSR mitigation using the thyristor controlled series capacitor," *IEEE Trans. Power Delivery,* vol. 10, pp. 1479-1485, 1995.

[85] G. N. Pillai, A. Ghosh, and A. Joshi, "Robust control of SSSC to improve torsional damping," in *2001 IEEE Power Engineering Society Winter Meeting. Conference Proceedings (Cat. No.01CH37194)*, 2001, pp. 1115-1120 vol.3.

[86] R. Thirumalaivasan, M. Janaki, and N. Prabhu, "Damping of SSR Using Subsynchronous Current Suppressor With SSSC," *IEEE Trans. Power Systems,* vol. 28, pp. 64-74, 2013.

[87] M. Bongiorno, J. Svensson, and L. Angquist, "Single-Phase VSC Based SSSC for Subsynchronous Resonance Damping," *IEEE Transactions on Power Delivery,* vol. 23, pp. 1544-1552, 2008.

[88] M. Bongiorno, L. Angquist, and J. Svensson, "A novel control strategy for subsynchronous resonance mitigation using SSSC," *IEEE Transactions on Power Delivery,* vol. 23, pp. 1033-1041, 2008.

[89] R. M. I. Hamouda, M. R.; Hackam, R., "Torsional oscillations of series capacitor compensated AC/DC systems," *IEEE Trans. Power Systems,* vol. 4, pp. 889-896, 1989.

[90]     H. A. Mohammadpour, M. M. Islam, E. Santi, and Y. J. Shin, "SSR Damping in Fixed-Speed Wind Farms Using Series FACTS Controllers," *IEEE Trans. on Power Delivery,* vol. 31, pp. 76-86, 2016.

[91]     B. Gao and Y. Hu, "Sub-synchronous resonance mitigation by a STATCOM in doubly fed induction generator-based wind farm connected to a series-compensated transmission network," *The Journal of Engineering,* vol. 2019, pp. 812-815, 2019.

[92]     C. Wu and Y. Lee, "Application of simultaneous active and reactive power modulation of superconducting magnetic energy storage unit to damp turbine-generator subsynchronous oscillations," *IEEE Transactions on Energy Conversion,* vol. 8, pp. 63-70, 1993.

[93]     W. Li, L. Shin-Muh, and L. Ching-Huei, "Application of superconductive magnetic energy storage unit on damping subsynchronous resonance," in *IEEE Region 10 Conf.  Control and Power Engineering.1993* 1993, pp. 141-144 vol.5.

[94]     H. A. Mohammadpour and E. Santi, "Optimal adaptive sub-synchronous resonance damping controller for a series-compensated doubly-fed induction generator-based wind farm," *IET Renewable Power Generation,* vol. 9, pp. 669-681, 2015.

[95]     H. A. Mohammadpour, A. Ghaderi, H. Mohammadpour, and E. Santi, "SSR damping in wind farms using observed-state feedback control of DFIG converters," *Electric Power Systems Research,* vol. 123, pp. 57-66, 2015.

[96]     S. O. Faried, I. Unal, D. Rai, and J. Mahseredjian, "Utilizing DFIG-Based Wind Farms for Damping Subsynchronous Resonance in Nearby Turbine-Generators," *IEEE Transactions on Power Systems,* vol. 28, pp. 452-459, 2013.

[97]     U. Karaagac, S. O. Faried, J. Mahseredjian, and A. A, "Coordinated Control of Wind Energy Conversion Systems for Mitigating Subsynchronous Interaction in DFIG-Based Wind Farms," *IEEE Transactions on Smart Grid,* vol. 5, pp. 2440-2449, 2014.

[98]     O. Wasynczuk, "Damping Subsynchronous Resonance Using Reactive Power Control," *IEEE Trans.  Power Apparatus and Systems,* vol. PAS-100, pp. 1096-1104, 1981.

[99]     T. H. Putman and D. G. Ramey, "Theory of the modulated reactance solution for subsynchronous resonance," *IEEE Transactions on Power Apparatus and Systems,* vol. PAS-101, pp. 1527-1535, 1982.

[100]   D. G. Ramey, D. S. Kimmel, J. W. Dorney, and F. H. Kroening, "Dynamic Stabilizer Verification Tests at the San Juan Station," *IEEE Power Engineering Review,* vol. PER-1, pp. 48-49, 1981.

[101] N. Kakimoto and A. Phongphanphanee, "Calculation of damping torque of power systems compensated with TCSC," *Electrical Engineering in Japan (English translation of Denki Gakkai Ronbunshi),* vol. 143, pp. 39-49, 2003.

[102] G. N. Pillai, A. Ghosh, and A. Joshi, "Torsional interaction studies on a power system compensated by SSSC and fixed capacitor," *IEEE Trans. Power Delivery,* vol. 18, pp. 988-993, 2003.

[103] Y. M. Alharbi, A. Abu Siada, and A. F. Abdou, "Application of UPFC on stabilizing torsional oscillations and improving transient stability," in *2013 Australasian Universities Power Engineering Conference, AUPEC 2013*, Hobart, TAS, 2013.

[104] H. Hosseini, A. Boudaghi, A. Mehri, S. F. Torabi, and H. Farshbar, "Mitigating SSR in hybrid system with steam and wind turbine by UPFC," in *17th Electrical Power Distribution Network Conference, EPDC 2012*, Tehran, 2012.

[105] S. Golshannavaz, F. Aminifar, and D. Nazarpour, "Application of UPFC to Enhancing Oscillatory Response of Series-Compensated Wind Farm Integrations," *IEEE Trans. Smart Grid,* vol. 5, pp. 1961-1968, 2014.

[106] S. A. Khaparde and V. Krishna, "Simulation of unified static VAr compensator and power system stabilizer for arresting subsynchronous resonance," *IEEE Trans. Power Systems,* vol. 14, pp. 1055-1062, 1999.

[107] M. S. El-Moursi, B. Bak-Jensen, and M. H. Abdel-Rahman, "Novel STATCOM Controller for Mitigating SSR and Damping Power System Oscillations in a Series Compensated Wind Park," *IEEE Transactions on Power Electronics,* vol. 25, pp. 429-441, 2010.

[108] A. Yazdani and R. Iravani, *Voltage-sourced converters in power systems: modeling, control, and applications*: John Wiley & Sons, 2010.

[109] A. Abu-Siada, "Damping of large turbo-generator subsyncronous resonance using superconducting magnetic energy storage unit," in *Universities Power Engineering Conference (AUPEC), 2010 20th Australasian*, 2010, pp. 1-4.

[110] A. Abu-Siada, S. Islam, and W. B. Lawrance, "Stabilizing control of series capacitor power system using a Superconducting Magnetic Energy Storage unit under unequal α-mode," *International Energy Journal,* vol. 6, pp. 197-1110, 2005.

[111] C. J. Wu and Y. S. Lee, "Application of Simultaneous Active and Reactive Power Modulation of Superconducting Magnetic Energy Storage Unit to Damp Turbine-Generator Subsynchronous Oscillations," *IEEE Transactions on Energy Conversion,* vol. 8, pp. 63-70, 1993.

[112] IEEE Subsynchronous Resonance Task Force, "First benchmark model for computer simulation of subsynchronous resonance," *IEEE Trans. Power Apparatus and Systems,* vol. 96, pp. 1565-1572, 1977.

[113] IEEE Subsynchronous Resonance Working Group, "Second Benchmark Model for Computer Simulation of Subsynchronous Resonance," *IEEE Transactions on Power Apparatus and Systems,* vol. PAS-104, pp. 1057-1066, 1985.

[114] M. Anju and R. Rajasekaran, "Co-ordination of SMES with STATCOM for mitigating SSR and damping power system oscillations in a series compensated wind power system," in *2013 International Conference on Computer Communication and Informatics, ICCCI 2013*, 2013.

[115] H. A. Mohammadpour and E. Santi, "SSR Damping Controller Design and Optimal Placement in Rotor-Side and Grid-Side Converters of Series-Compensated DFIG-Based Wind Farm," *IEEE Transactions on Sustainable Energy,* vol. 6, pp. 388-399, 2015.

[116] L. Gerin-Lajoie, G. Scott, S. Breault, E. V. Larsen, D. H. Baker, and A. F. Imece, "Hydro-Quebec multiple SVC application control stability study," *IEEE Transactions on Power Delivery,* vol. 5, pp. 1543-1551, 1990.

[117] K. Clark, B. Fardanesh, and R. Adapa, "Thyristor controlled series compensation application study-control interaction considerations," *IEEE Transactions on Power Delivery,* vol. 10, pp. 1031-1037, 1995.

[118] M. Szechtman, *Coordination of Controls of Multiple FACTS/HVDC Links in the Same System*: CIGRÉ, 1999.

[119] L. J. Cai and I. Erlich, "Simultaneous coordinated tuning of PSS and FACTS controller for damping power system oscillations in multimachine systems," in *2003 IEEE Bologna Power Tech Conference Proceedings*, 2003, p. 6 pp. Vol.2.

[120] T. T. Nguyen and R. Gianto, "Optimisation-based control coordination of PSSs and FACTS devices for optimal oscillations damping in multi-machine power system," *IET Generation, Transmission & Distribution,* vol. 1, pp. 564-573, 2007.

[121] N. Mithulananthan, C. A. Canizares, and J. Reeve, "Tuning, performance and interactions of PSS and FACTS controllers," in *IEEE Power Engineering Society Summer Meeting*, 2002, pp. 981-987 vol.2.

[122] M. J. Gibbard, D. J. Vowles, and P. Pourbeik, "Interactions between, and effectiveness of, power system stabilizers and FACTS device stabilizers in multimachine systems," *IEEE Transactions on Power Systems,* vol. 15, pp. 748-755, 2000.

[123] P. Pourbeik and M. J. Gibbard, "Simultaneous coordination of power system stabilizers and FACTS device stabilizers in a multimachine power system for

enhancing dynamic performance," *IEEE Transactions on Power Systems,* vol. 13, pp. 473-479, 1998.

[124] X. Lei, E. Lerch, and D. Povh, "Optimization and coordination of damping controls for improving system dynamic performance," in *2001 Power Engineering Society Summer Meeting. Conference Proceedings (Cat. No.01CH37262)*, 2001, p. 777 vol.2.

[125] "Common functions for smart inverters:4th edition," EPRI 3002008217, Dec. 2016.

[126] W. Peng, C. Hicks, O. Gonzalez, B. Blackstone, and Y. Baghzouz, "Experimental test on some autonomous functions of advanced PV inverters," in *2016 IEEE Power and Energy Society General Meeting (PESGM)*, 2016, pp. 1-5.

[127] M. J. Reno, R. J. Broderick, and S. Grijalva, "Smart inverter capabilities for mitigating over-voltage on distribution systems with high penetrations of PV," in *2013 IEEE 39th Photovoltaic Specialists Conference (PVSC)*, 2013, pp. 3153-3158.

[128] J. W. Smith, W. Sunderman, R. Dugan, and B. Seal, "Smart inverter volt/var control functions for high penetration of PV on distribution systems," in *2011 IEEE/PES Power Systems Conference and Exposition*, 2011, pp. 1-6.

[129] K. S. Tey and S. Mekhilef, "Modified incremental conductance MPPT algorithm to mitigate inaccurate responses under fast-changing solar irradiation level," *Solar Energy,* vol. 101, pp. 333-342, 2014/03/01/ 2014.

[130] R. Shah, N. Mithulananthan, and K. Y. Lee, "Large-Scale PV Plant With a Robust Controller Considering Power Oscillation Damping," *IEEE Transactions on Energy Conversion,* vol. 28, pp. 106-116, 2013.

[131] B. Mather and R. Neal, "Integrating high penetrations of PV into Southern California: Year 2 project update," in *2012 38th IEEE Photovoltaic Specialists Conference*, 2012, pp. 000737-000741.

[132] M. A. Shuvra and B. H. Chowdhury, "Autonomous control of smart inverters in grid connected and islanded mode," in *2017 IEEE Power & Energy Society Innovative Smart Grid Technologies Conference (ISGT)*, 2017, pp. 1-5.

[133] H. Vallecha and Shivam, "Smart utilization of solar and wind power farm inverters as SSSC in grid connected renewable energy system," in *2016 IEEE 6th International Conference on Power Systems (ICPS)*, 2016, pp. 1-5.

[134] "Advanced Inverter Functions To Support High Levels Of Distributed Solar," *National Renewable Energy Laboratory, [Online]. Available: http://www. nrel. gov/docs/fy15osti/62612. pdf,* 2014.

[135] IEEE Standard 1547, "IEEE Standard for Interconnection and Interoperability of Distributed Energy Resources with Associated Electric Power Systems Interfaces," ed, 2018, pp. 1-138.

[136] M. Morjaria, D. Anichkov, V. Chadliev, and S. Soni, "A Grid-Friendly Plant: The Role of Utility-Scale Photovoltaic Plants in Grid Stability and Reliability," *IEEE Power and Energy Magazine,* vol. 12, pp. 87-95, 2014.

[137] B. Mather, "NREL/SCE High-Penetration PV Integration Project: Report on Field Demonstration of Advanced Inverter Functionality in Fontana, CA," NREL, Golden, CO, USA, Rep. NREL/TP-5D00-62483,2014.

[138] T. Stetz, F. Marten, and M. Braun, "Improved low voltage grid-integration of photovoltaic systems in Germany," in *2013 IEEE Power & Energy Society General Meeting*, 2013, pp. 1-1.

[139] A. Beekmann, J. Marques, E. Quitmann, and S. Wachtel, "Wind energy converters with FACTS Capabilities for optimized integration of wind power into transmission and distribution systems," in *2009 CIGRE/IEEE PES Joint Symposium Integration of Wide-Scale Renewable Resources Into the Power Delivery System*, 2009, pp. 1-1.

[140] N. W. Miller and K. Clark, "Advanced controls enable wind plants to provide ancillary services," in *IEEE PES General Meeting*, 2010, pp. 1-6.

[141] A. E. Leon, J. M. Mauricio, and J. A. Solsona, "Subsynchronous resonance mitigation using variablespeed wind energy conversion systems," *IET Generation, Transmission & Distribution,* vol. 7, pp. 511-525, 2013.

[142] R. G. Wandhare and V. Agarwal, "Reactive Power Capacity Enhancement of a PV-Grid System to Increase PV Penetration Level in Smart Grid Scenario," *IEEE Transactions on Smart Grid,* vol. 5, pp. 1845-1854, 2014.

[143] R. A. Walling and K. Clark, "Grid support functions implemented in utility-scale PV systems," in *IEEE PES T&D 2010*, 2010, pp. 1-5.

[144] D. T. Rizy, Y. Xu, H. Li, F. Li, and P. Irminger, "Volt/Var control using inverter-based distributed energy resources," in *2011 IEEE Power and Energy Society General Meeting*, 2011, pp. 1-8.

[145] R. K. Varma, V. Khadkikar, and R. Seethapathy, "Nighttime Application of PV Solar Farm as STATCOM to Regulate Grid Voltage," *IEEE Trans. Energy Conversion,* vol. 24, pp. 983-985, 2009.

[146] R. K. Varma, S. A. Rahman, A. C. Mahendra, R. Seethapathy, and T. Vanderheide, "Novel nighttime application of PV solar farms as STATCOM (PV-STATCOM)," in *2012 IEEE Power and Energy Society General Meeting*, 2012, pp. 1-8.

[147]  R. K. Varma and E. M. Siavashi, "PV-STATCOM: A New Smart Inverter for Voltage Control in Distribution Systems," *IEEE Transactions on Sustainable Energy,* vol. 9, pp. 1681-1691, 2018.

[148]  R. K. Varma and E. M. Siavashi, "Enhancement of Solar Farm Connectivity With Smart PV Inverter PV-STATCOM," *IEEE Transactions on Sustainable Energy,* vol. 10, pp. 1161-1171, 2019.

[149]  R. K. Varma and H. Maleki, "PV Solar System Control as STATCOM (PV-STATCOM) for Power Oscillation Damping," *IEEE Transactions on Sustainable Energy,* pp. 1-1, 2018.

[150]  R. K. Varma and M. A. Kelishadi, "Simultaneous Fast Frequency Control and Power Oscillation Damping by Utilizing PV Solar System as PV-STATCOM," *IEEE Transactions on Sustainable Energy,* pp. 1-1, 2019.

[151]  R. K. Varma, "Multivariable Modulator Controller for Power Generation Facility," U.S. Provisional Patent, PCT Application (PCT/CA2014/051174) filed on December , 2014.

[152]  R. K. Varma and V. Khadkikar, "Utilization of solar farm inverter as STATCOM," U.S. Provisional Patent Patent, PCT Patent application PCT/CA2010/001419,diled on  Sep. 15, 2010.

[153]  IEEE Standard 1547, "IEEE Standard for Interconnecting Distributed Resources with Electric Power Systems," *IEEE Std 1547-2003,* pp. 1-28, 2003.

[154]  BDEW:, "Technical Guideline: Generating Plants Connected to the Medium Voltage Network," ed, 2008.

[155]  "Reliability Standards for the Bulk Electric Systems of North America," *National Renewable Energy Laboratory, [Online]. Available: https://www.nerc.com/pa/Stand/Reliability%20Standards%20Complete%20Set/RSCompleteSet.pdf,* 2019.

[156]  *P2800-Standard for Interconnection and Interoperability of Inverter-Based Resources Interconnecting with Associated Transmission Electric Power Systems. [Online].* Available: https://standards.ieee.org/project/2800.html

[157]  R. K. Varma, V. Khadkikar, and S. A. Rahman, "Utilization of Distributed Generator Inverters as STATCOM," U.S. Provisional Patent Patent, PCT Patent application PCT/CA2010/001419 filed on 15 September, 2010.

[158]  R. K. Varma and R. Salehi, "SSR Mitigation With a New Control of PV Solar Farm as STATCOM (PV-STATCOM)," *IEEE Trans. on Sustainable Energy,* vol. 8, pp. 1473-1483, 2017.

[159]  R. K. Varma, E. M. Siavashi, S. Mohan, and T. Vanderheide, "First in Canada, Night and Day Field Demonstration of a New Photovoltaic Solar Based Flexible

AC Transmission System (FACTS) Device PV-STATCOM for Stabilizing Critical Induction Motor," *IEEE Access,* pp. 1-1, 2019.

[160] *Western Engineering research demonstrated in Sarnia [Online]*. Available: https://www.theobserver.ca/2016/12/13/western-engineering-research-demonstrated-in-sarnia/wcm/48d61f85-3b6c-7e4c-751f-1d896f277fb4

[161] H. Maleki and R. K. Varma, "Coordinated control of PV solar system as STATCOM (PV-STATCOM) and Power System Stabilizers for power oscillation damping," in *2016 IEEE Power and Energy Society General Meeting (PESGM)*, 2016, pp. 1-5.

[162] "Rule 21 – Generating Facility Interconnections," ed: California Public Utilities Commission, July 2014.

[163] *GRAND RENEWABLE Energy Park, Haldimand County, Ontario. [Online]*. Available: https://www.power-technology.com/projects/ grand-renewable-energy-park-haldimand-county-ontario/

[164] *Australia's first hybrid wind-solar farm to be built near Canberra. [Online]*. Available: https://www.theguardian.com/environment/2016/jul/26/renewable-energy-australias-first-hybrid-wind-solar-farm-gets-funded

[165] P. C. Krause, O. Wasynczuk, S. D. Sudhoff, and S. Pekarek, *Analysis of electric machinery and drive systems* vol. 2: Wiley Online Library, 2002.

[166] IEEE Power Engineering Society, "IEEE Recommended Practice for Excitation System Models for Power System Stability Studies," *IEEE Std 421.5,* pp. 1-207, 2005.

[167] G. Tang, "Damping Subsynchronous Resonance Oscillations Using a VSC HVDC Back-To-Back System," Ph.D. dissertation, Department of Electrical Engineering, Univ. of Saskatchewan, Saskatoon, Saskatchewan, 2006.

[168] P. Kundur, *Power system stability and control*: McGraw-hill, USA, 1994.

[169] IEEE Commitee Report, "Dynamic Models for Steam and Hydro Turbines in Power System Studies," *IEEE Transactions on Power Apparatus and Systems,* vol. PAS-92, pp. 1904-1915, 1973.

[170] K. W. Louie, "Aggregating Induction Motors in a Power System Based on their Standard Specifications," in *2006 International Conference on Power System Technology*, 2006, pp. 1-8.

[171] K. W. Louie and P. Wilson, "Aggregation of Induction Motors Based on their Specifications," in *2006 Canadian Conference on Electrical and Computer Engineering*, 2006, pp. 803-806.

[172]   S. M. Chan, D. H. Curtice, and R. L. Cresap, "Wind Turbine Cluster Model,"
        *IEEE Power Engineering Review,* vol. PER-4, pp. 41-41, 1984.

[173]   R. Piwko, N. Miller, J. Sanchez-Gasca, Y. Xiaoming, D. Renchang, and J. Lyons,
        "Integrating Large Wind Farms into Weak Power Grids with Long Transmission
        Lines," in *2005 IEEE/PES Transmission & Distribution Conference &
        Exposition: Asia and Pacific*, 2005, pp. 1-7.

[174]   T. Ackerman, *Wind Power in Power Systems*: NewYork,NY,USA: Wiley, 2005.

[175]   Y. N. Sudhakar, M. Selvakumar, and D. K. Bhat, "Chapter 4 - Biopolymer
        Electrolytes for Solar Cells and Electrochemical Cells," in *Biopolymer
        Electrolytes*, Y. N. Sudhakar, M. Selvakumar, and D. K. Bhat, Eds., ed: Elsevier,
        2018, pp. 117-149.

[176]   S. A. Rahman, R. K. Varma, and T. Vanderheide, "Generalised model of a
        photovoltaic panel," *IET Renewable Power Generation,* vol. 8, pp. 217-229, 2014.

[177]   C. Carrero, J. Amador, and S. Arnaltes, "A single procedure for helping PV
        designers to select silicon PV modules and evaluate the loss resistances,"
        *Renewable Energy,* vol. 32, pp. 2579-2589, 2007.

[178]   P. A. Dahono, Y. Sato, and T. Kataoka, "Analysis and minimization of ripple
        components of input current and voltage of PWM inverters," *IEEE Trans.
        Industry Applications,* vol. 32, pp. 945-950, 1996.

[179]   J. L. Agorreta, M. Borrega, Lo, x, J. pez, and L. Marroyo, "Modeling and Control
        of N-Paralleled Grid-Connected Inverters With LCL Filter Coupled Due to Grid
        Impedance in PV Plants," *IEEE Trans. Power Electronics,* vol. 26, pp. 770-785,
        2011.

[180]   G. L. Calzo, A. Lidozzi, L. Solero, and F. Crescimbini, "LC filter design for on-
        grid and off-grid distributed generating units," in *2013 IEEE Energy Conversion
        Congress and Exposition*, 2013, pp. 713-720.

[181]   B. Liu and B. Song, "Modeling and analysis of an LCL filter for grid-connected
        inverters in wind power generation systems," in *2011 IEEE Power and Energy
        Society General Meeting*, 2011, pp. 1-6.

[182]   S. Jayalath and M. Hanif, "Generalized LCL-Filter Design Algorithm for Grid-
        Connected Voltage-Source Inverter," *IEEE Transactions on Industrial
        Electronics,* vol. 64, pp. 1905-1915, 2017.

[183]   A. Reznik, M. G. Simões, A. Al-Durra, and S. M. Muyeen, "LCL filter design and
        performance analysis for small wind turbine systems," in *2012 IEEE Power
        Electronics and Machines in Wind Applications*, 2012, pp. 1-7.

[184] W. S. Moon, J. Hur, and J. Kim, "A Protection of interconnection transformer for DG in Korea distribution power system," in *2012 IEEE Power and Energy Society General Meeting*, 2012, pp. 1-5.

[185] C. J. Mozina, "Interconnect protection of dispersed generators," in *2001 IEEE/PES Transmission and Distribution Conference and Exposition. Developing New Perspectives (Cat. No.01CH37294)*, 2001, pp. 709-723 vol.2.

[186] K. H. Hussein, I. Muta, T. Hoshino, and M. Osakada, "Maximum photovoltaic power tracking: an algorithm for rapidly changing atmospheric conditions," *IEE Proceedings - Generation, Transmission and Distribution,* vol. 142, pp. 59-64, 1995.

[187] S. A. Rahman and R. K. Varma, "PSCAD/EMTDC model of a 3-phase grid connected photovoltaic solar system," in *2011 North American Power Symposium*, 2011, pp. 1-7.

[188] S. A. Rahman, "Novel Controls of Photovoltaic (PV) Solar Farms," Ph.D. dissertation, Dept. ECE, Univ. of Western Ontario, London, ON, 2012.

[189] M. J. Gibbard, D. J. Vowles, and P. Pourbeik, *Small-signal stability, control and dynamic performance of power systems*: University of Adelaide press, 2015.

[190] M. H. Rashid, *Power electronics handbook*: Butterworth-Heinemann, 2017.

[191] C. Chen, O. Wasynczuk, and N. A. Anwah, "Stabilizing subsynchronous resonance using transmission current feedback," *IEEE Trans. on Power Systems,* vol. 1, pp. 34-41, 1986.

[192] W. Chi-Jui and Y. S. Lee, "Application of simultaneous active and reactive power modulation of superconducting magnetic energy storage unit to damp turbine-generator subsynchronous oscillations," *IEEE Trans. Energy Conversion,* vol. 8, pp. 63-70, 1993.

[193] E. V. Larsen, J. J. Sanchez-Gasca, and J. H. Chow, "Concepts for design of FACTS controllers to damp power swings," *IEEE Trans.  Power Systems,* vol. 10, pp. 948-956, 1995.

[194] C. C. Yu, Z.; Ni, Y.; Zhong, J., "Generalised eigenvalue and complex-torque-coefficient analysis for SSR study based on LDAE model," *IEE Proceedings: Generation, Transmission and Distribution,* vol. 153, pp. 25-34, 2006.

[195] "ERCOT Nodal Operating Guides," *Electric Reliability Council of Texas, [Online]. Available: http://www.ercot.com/mktrules/guides/noperating/cur,* 2018.

[196] Smart Inverter Working Group Recommendations,"*Recommendations for Updating the Technical Requirements for Inverters in Distributed Energy Resources"*, 2014.

[197]   *First Solar,Projects, Agua Caliente Solar Project . [Online]*. Available: http://www.firstsolar.com/Resources/Projects/Agua-Caliente-Solar-Project

[198]   "Reliability Standards for the Bulk Electric Systems of North America," *National Renewable Energy Laboratory, [Online]. Available: https://www.nerc.com/pa/Stand/Reliability%20Standards%20Complete%20Set/RSCompleteSet.pdf,* 2017.

# Curriculum Vitae

**Name:**              Reza Salehi Sharafdarkolaee

**Post-secondary**     Iran University of Science and Technology
**Education and**      Tehran, Tehran, Iran
**Degrees:**           2003-2008 B.Sc. Electrical Engineering

                       Amirkabir University of Technology
                       Tehran, Tehran, Iran
                       2008-2011 M.Sc. Electrical Engineering

                       The University of Western Ontario
                       London, Ontario, Canada
                       2014-2019 Ph.D. Electrical Engineering

**Honours and**        Western Graduate Research Scholarship (WGRS-ECE)
**Awards:**            2014-2019

**Related Work**       Teaching Assistant
**Experience**         The University of Western Ontario
                       2014-2019

                       Research Assistant
                       The University of Western Ontario
                       2014-2019

**Publications:**

[1] R. K. Varma and **R. Salehi**, "SSR Mitigation With a New Control of PV Solar Farm as STATCOM (PV-STATCOM)," IEEE Trans. on Sustainable Energy, vol. 8, pp. 1473-1483, 2017.

[2] **R. Salehi** and R. K. Varma, "PV Solar Farm Control as STATCOM (PV-STATCOM) for Alleviating Subsynchronous Oscillations," *Proc. 2019 CIGRE Canada Conference.*

[3] Rajiv K. Varma, Ehsan Siavashi, Hesamaldin Maleki, **Reza Salehi**, Sibin Mohan, Mahendra A.C., S. Arifur Rahman and T. Vanderheide, "PV-STATCOM: A Novel Smart Inverter for Transmission and Distribution System

Applications", Poster at the 7th International Conference on Integration of Renewable and Distributed Energy Resources", Niagara Falls, Canada, Oct. 24-28, 2016

[4] S. B. Subramanian, S. Mohan, M. Akbari, H. Maleki, **R. Salehi**, W. H. Litzenberger, et al., "Control of STATCOMs – A Review," *in 2018 IEEE Power & Energy Society General Meeting* (PESGM), 2018, pp. 1-5.

[5] H. Gharavi, F. Mohammadi, H. Gharoei, S. Ghanbari-Tichi, and **R. Salehi**, "Optimal fuzzy multi-objective design of a renewable energy system with economics, reliability, and environmental emissions considerations," *Journal of Renewable and Sustainable Energy*, vol. 6, p. 053125, 2014.

[6] H. Aalami and **R. Salehi**, "Extended Modulation Index with more Eliminated Low Order Harmonics at Cascaded Multilevel Inverters," *in Applied Mechanics and Materials*, 2014, pp. 123-127.

[7] A. Kavousi, B. Vahidi, **R. Salehi**, M. K. Bakhshizadeh, N. Farokhnia, and S. H. Fathi, "Application of the Bee Algorithm for Selective Harmonic Elimination Strategy in Multilevel Inverters," *IEEE Trans. Power Electronics*, vol. 27, pp. 1689-1696, 2012.

[8] N. Farokhnia, S. H. Fathi, **R. Salehi**, G. B. Gharehpetian, and M. Ehsani, "Improved selective harmonic elimination pulse-width modulation strategy in multilevel inverters," *IET Power Electronics*, vol. 5, pp. 1904-1911, 2012.

[9] **R. Salehi**, N. Farokhnia, M. Abedi, and S. H. Fathi, "Elimination of low order harmonics in multilevel inverters using genetic algorithm," *Journal of Power Electronics*, vol. 11, pp. 132-139, 2011.

[10] **R. Salehi**, B. Vahidi, N. Farokhnia, and M. Abedi, "Harmonic elimination and optimization of stepped voltage of multilevel inverter by bacterial foraging algorithm," *Journal of Electrical Engineering and Technology*, vol. 5, pp. 545-551, 2010.